ECOLE CENTRALE MARSEILLE

N° attribué par la bibliothèque

TITRE
3D digital imaging with tomographic diffractive microscopy

Thèse
Pour obtenir le grade de DOCTEUR
délivré par
L'ECOLE CENTRALE MARSEILLE

Discipline : *Optique, Photonique et Traitement d'image*

présentée et soutenue publiquement par Yi RUAN
le 22 Octobre 2012

Laboratoire d'accueil: *Institut Fresnel UMR 7249, équipe* S.E.M.O
Ecole doctorale: *ED 352*

Membres du jury:

Olivier HAEBERLÉ	*rapporteur*
Frédérique DE FORNEL	*rapporteur*
Natalie DESTOUCHES	*examinateur*
Hugues GIOVANNINI	*examinateur*
Guillaume MAIRE	*codirecteur de thèse*
Patrick Christian CHAUMET	*directeur de thèse*

2012

Contents

Lists of the figures **vii**

Résumé en Français **xvii**
1 Le mot du directeur de thèse . . . xvii
2 Généralités . . . xvii
3 Quelques mots sur la résolution . . . xviii
4 Quelques mots sur la la sphère d'Ewald . . . xix
5 La tomographie optique . . . xix

General introduction **1**

1 Principles of tomographic diffractive microscopy (TDM) **3**
1.1 Introduction . . . 3
1.2 Principles of conventional wide-field optical microscopy . . . 4
1.3 Principles of TDM under the Born approximation . . . 6
1.3.1 Modelling of tomographic diffractive microscopy . . . 6
1.3.1.1 Position of the problem . . . 6
1.3.1.2 Electromagnetic scattering by an object of volume V and relative permittivity $\varepsilon(\boldsymbol{r})$ . . . 8
1.3.1.3 TDM in the case of the Born approximation . . . 9
1.3.2 Synthetic aperture . . . 10
1.3.2.1 One normal incidence working in transmission: $k_{\mathrm{inc;z}} = k_0$ and $k_z > 0$ . . . 10
1.3.2.2 The complete configuration . . . 12
1.3.2.3 The transmission configuration: $k_{\mathrm{inc;z}} > 0$ and $k_z > 0$ . . . 13
1.3.2.4 The reflection configuration: $k_{\mathrm{inc;z}} < 0$ and $k_z > 0$ . . . 13
1.3.3 Linear inversion with an inverse Fourier transform . . . 14
1.4 State-of-the-art results obtained by TDM under linear approximations . . . 18

2 Tomographic diffractive microscopy with non-linear inversion procedures **21**
2.1 Description of the tomographic diffractive microscopy set-up . . . 21
2.2 The phase measurement techniques . . . 23
2.2.1 Phase shifting interferometry . . . 24
2.2.1.1 Principle of the method . . . 24
2.2.1.2 Calibration of the phase-stepper . . . 24
2.2.1.3 Limitations of phase-shifting interferometry . . . 25
2.2.2 Off-axis holography . . . 25
2.2.3 Phase measurement with a wavefront sensor . . . 26
2.2.3.1 Choice of the wavefront sensor . . . 26

2.2.3.2 Principle of lateral shearing interferometry . . . 27
2.3 Rigorous nonlinear inversion procedures in 3D . . . 30
2.3.1 The direct problem . . . 30
2.3.1.1 Computation of the scattered field: the coupled dipole method . . 30
2.3.1.2 Strengths and drawbacks of the coupled dipole method . . . 32
2.3.2 The nonlinear inversion algorithm for 3D imaging . . . 32

3 3D experimental reconstructions with non-linear inversion procedures 37
3.1 Data treatment procedures . . . 37
3.1.1 Angular calibration . . . 37
3.1.2 Normalization procedure of the measurements . . . 38
3.1.2.1 Amplitude normalization . . . 38
3.1.2.2 Phase normalization . . . 41
3.1.3 Determination of the phase origin mismatch . . . 42
3.2 Experimental results . . . 43
3.2.1 Resin cylinders with diameter 1 μm. . . . 44
3.2.1.1 Comparison of the measurement by phase-shifting interferometry and the simulated scattered field . . . 44
3.2.1.2 Comparison of the data set measured by PSI and with a wavefront sensor (WFS) . . . 47
3.2.1.3 Application of the non-linear inversion algorithm to the experimental data for different sizes of investigation domain . . . 49
3.2.1.4 Comparison of the non-linear inversions obtained with the WFS and the PSI data sets . . . 52
3.2.1.5 Comparison of the reconstructions obtained with the non-linear inversion procedure and the linear inversion valid for the Born approximation . . . 52
3.2.1.6 Iterative process of the inversion algorithm applied on the WFS data set . . . 54
3.2.2 Resin cylinders with diameter 500 nm . . . 56
3.2.2.1 Comparison of the PSI data set with the theory . . . 57
3.2.2.2 Measurement of the field by off-axis holography . . . 58
3.2.2.3 Application of the non-linear inversion algorithm to the PSI data set for different sizes of investigation domain . . . 61
3.2.2.4 Application of the non-linear inversion algorithm to the off-axis data set . . . 63
3.2.2.5 Reconstructions obtained with the linear inversion valid under the Born approximation . . . 64
3.2.2.6 Influence of the number of illumination angles on the reconstructions 65
3.2.2.7 Spatial filtering of the scattered field for the selective reconstruction of objects . . . 67
3.2.2.8 Comparison of different sample heights . . . 70
3.2.3 Resin cylinders with diameter 200 nm . . . 72
3.2.3.1 Comparison of the data set measured by PSI with the theory . . . 72
3.2.3.2 Data set obtained by off-axis holography . . . 74
3.2.3.3 Reconstructions obtained with the non-linear inversion procedure on the PSI and off-axis data sets . . . 76
3.2.4 Resin cylinders with diameter 150 nm . . . 79
3.2.4.1 Comparison of the data set measured by PSI with the theory . . . 79
3.2.4.2 Data set measured by off-axis holography . . . 81
3.2.4.3 Comparison of the reconstructions obtained with the non-linear inversion procedure on the PSI and off-axis data sets . . . 81

4 Polarization resolved measurements for tomographic diffractive microscopy 85
4.1 Introduction . . . 85
4.2 Measurement of the vectorial scattered field with the experimental set-up . . . 88
4.3 Amplitude and phase normalization . . . 89
4.3.1 Correction on the measured field . . . 89
4.3.2 Decomposition in TM and TE polarizations . . . 89
4.4 Experimental results with polarization resolved measurements . . . 90
4.4.1 Samples with diameter 200 nm . . . 90
4.4.2 Samples with diameter 150 nm . . . 93
4.5 Some final remarks on the reconstructions . . . 96

General conclusion and perspectives 97

A The dyadic Green's functions 99
A.1 Wave equation . . . 99
A.2 The scalar Green's function . . . 100
A.3 The dyadic Green's function . . . 100

B The approximation of scalar Green's function in far field 103

C The measured scattered fields under $\widehat{h}\widehat{h}$ polarization 105
C.1 Samples with diameter 200 nm . . . 105
C.2 Samples with diameter 150 nm . . . 106

D The measured four groups of data set to retrieve the vectorial scattered fields 109
D.1 Samples with diameter 200 nm . . . 109
D.2 Samples with diameter 150 nm . . . 111

References 115

List of Figures

1 Schéma du montage utilisé. Le laser émet à 633 nm; M miroir ajustable; PL polariseur; L_1 lentille objectif du microscope; $L_{2,\cdots,6}$ lentilles; f_i, $f_i^{'}$ focales objet et image de la lentille L_i; B_1, B_2, B_3, séparateur de faisceaux; BE_1, BE_2 systèmes afocaux; TM, pinhole ; PM, modulateur de phase; D_1, D_2, diaphragmes. xx

2 Vue de dessus de l'échantillon par un microscope électronique: les cylindres sont de diamètre D et séparés d'une distance D. xxi

3 Profil de l'échantillon par un microscope électronique. Les cylindres sont de hauteur h. xxi

4 Image de reconstruction obtenue avec la méthode itérative. Les plots ont les caractéristiques géométriques suivantes: $D = 1$ μm et $h = 150$ nm. (a) Carte dans le plan (x, y) pour $z = 125$ nm. (b) Carte dans le plan (x, z) pour $y = 1$ μm. xxi

5 Image de reconstruction obtenue avec la transformée de Fourier 3D inverse du champ diffracté mesuré. Les plots ont les caractéristiques géométriques suivantes: $D = 1$ μm et $h = 150$ nm. (a) Carte dans le plan (x, y) pour $z = 125$ nm. (b) Carte dans le plan (x, z) pour $y = 1$ μm. xxii

6 Image de reconstruction obtenue avec la méthode itérative. Les plots ont les caractéristiques géométriques suivantes: $D = 1$ μm et $h = 150$ nm. (a) Carte dans le plan (x, y) pour $z = 125$ nm. (b) Carte dans le plan (x, z) pour $y = 500$ nm. xxii

7 Image de reconstruction obtenue avec la méthode itérative. Nous faisons l'hypothèse que le champ diffracté est parallèle au champ électrique incident et que le champ électrique incident est toujours suivant la même direction. Les plots ont les caractéristiques géométriques suivantes: $D = 150$ nm et $h = 150$ nm. (a) Carte dans le plan (x, y) pour $z = 125$ nm. (b) Carte dans le plan (x, z). xxiii

8 Image de reconstruction obtenue avec la méthode itérative. Nous faisons l'hypothèse que le champ diffracté est parallèle au champ électrique incident par contre le champ électrique incident possède deux orientations orthogonales. Les plots ont les caractéristiques géométriques suivantes: $D = 150$ nm et $h = 150$ nm. (a) Carte dans le plan (x, y) pour $z = 125$ nm. (b) Carte dans le plan (x, z). xxiv

9 Image de reconstruction obtenue avec la méthode itérative. Le champ électrique incident possède deux orientations orthogonales et le champ diffracté est mesuré vectoriellement. Les plots ont les caractéristiques géométriques suivantes: $D = 150$ nm et $h = 150$ nm. (a) Carte dans le plan (x, y) pour $z = 125$ nm. (b) Carte dans le plan (x, z). xxiv

10 Image de reconstruction obtenue avec la méthode itérative. Le champ électrique incident est en polarisation TE et le champ diffracté est mesuré vectoriellement. Les plots ont les caractéristiques géométriques suivantes: $D = 150$ nm et $h = 150$ nm. (a) Carte dans le plan (x, y) pour $z = 125$ nm. (b) Carte dans le plan (x, z). xxv

11 Image de reconstruction obtenue avec la méthode itérative. Le champ électrique incident est en polarisation TM et le champ diffracté est mesuré vectoriellement. Les plots ont les caractéristiques géométriques suivantes: $D = 150$ nm et $h = 150$ nm. (a) Carte dans le plan (x, y) pour $z = 125$ nm. (b) Carte dans le plan (x, z). xxv

1.1 The schematic diagram of wide-field microscopy 5
1.2 Intensity distributions of Airy disks. (a) is a hypothetical Airy disk, (b) shows two Airy disks and their intensity distributions. 6
1.3 The principle diagram of tomographic diffractive microscopy. $\boldsymbol{E}_{inc}$ denotes the incident field in the direction $\boldsymbol{k}_{inc}$, $\boldsymbol{E}_d$ denotes the incident field in the direction $\boldsymbol{k}_d$, x, y, z is the orientation of the spatial coordinates. 7
1.4 The schematic diagram of tomographic diffractive microscopy 7
1.5 Accessible 3D Fourier domain for one incidence 10
1.6 Optical transfer function (OTF) for one normal incidence in transmission 11
1.7 Transverse cut at $z = 0$ of the PSF for one normal incidence in transmission and scattered field detected in transmission with NA = 1. 11
1.8 Longitudinal cut at $y = 0$ of the PSF for one normal incidence in transmission and scattered field detected in transmission with NA = 1. 11
1.9 OTF for the complete configuration 12
1.10 Transverse cut of the complete configuration PSF at $z = 0$ 12
1.11 Longitudinal cut of the complete configuration PSF at $y = 0$ 12
1.12 OTF for the transmission configuration 13
1.13 Transverse cut of the transmission PSF at $z = 0$ 13
1.14 Longitudinal cut of the transmission PSF at $y = 0$ 13
1.15 OTF for the reflection configuration 14
1.16 Longitudinal cut of the real part of the reflection PSF at $y = 0$ 14
1.17 Longitudinal cut of the imaginary part of the reflection PSF at $y = 0$ 14
1.18 The sample geometry : resin blocks deposited on a silicon substrate. h is the height of the cylinders and D their diameter and side to side distance. The configuration used is the reflection configuration. 15
1.19 Overview of the sample imaged by electron microscopy 16
1.20 Profile of the sample imaged by electron microscopy 16
1.21 Diagram for the different illumination angles used with four azimuthal angles ϕ. . . 16
1.22 Modulus of the field scattered by the sample for an illumination angle of 31° and the four possible azimuthal angles: (a)$\phi = 0°$, (b)$\phi = 90°$, (c)$\phi = 180°$, (d)$\phi = 270°$; k_x and k_y are the spatial frequencies of the field. 17
1.23 Transverse cut of the modulus of the reconstruction at a height $z = 53$ nm under Born approximation, the tested sample with diameter 1 μm. 18
1.24 Longitudinal cut of the modulus of the reconstructions at $y = 1$ μm under Born approximation, the tested sample with diameter 1 μm. 18

2.1 Sketch of the experimental TDM set-up, laser source emitting at 633 nm; M, adjustable mirror; PL, polarizer; L_1, microscope objective; $L_{2,\cdots,6}$, lenses; f_i, $f_i^{'}$, object and image focal planes of lens L_i; B_1, B_2, B_3, beam splitters; BE_1, BE_2 beam expanders; P, pinhole; PM, phase modulator; D_1, D_2, diaphragms. 22
2.2 The image of diaphragm D_1 obtained on the CCD camera when a reflective substrate is placed in the vicinity of the object focal plane of L_1. This kind of setting is usually accurate enough. 23
2.3 The image of diaphragm D_2, optically conjugated with the CCD camera. 23
2.4 Sketch of the TDM set-up in off-axis configuration. The phase modulator has been suppressed and the reference wave propagates with an angle with respect to the optical axis. 26
2.5 Principle of quadri-wave lateral shearing interferometry. 27

2.6 Sketch of the experimental setup using wavefront sensor SID4-HR. M, adjustable mirror; PL, polarizer; L_1, L_2, L_3, L_4, lenses; f_i, $f_i^{'}$, object and image focal planes of lenses; B_1, beam splitters; BE_1, beam expander; D_1, diaphragms. 28
2.7 Schematic used to evaluate the axial component of a wave vector for a small perturbation α' of its transverse wave vector around $\frac{\pi}{p}$. 29
2.8 Discretization diagram for direct problem. The permittivity of sample is $\varepsilon(\boldsymbol{r})$ and volume V, the object under study is discretized into small cubic units. 31
2.9 Sketch of the illumination and detection configuration of TDM, the large discretized box is the investigation domain for the inverse problem, the blue points are the observation points in far-field. 33

3.1 Intensity image of a grating (1200 grooves per mm) used as reference object 38
3.2 Fresnel amplitude reflection coefficient as a function of the illumination angle : TE case in blue and TM case in red. 39
3.3 Sketch of the reference object used to test the validity of the amplitude normalization factor : a transparent parallelepiped of refractive index $n_s = 1.01$ and dimensions 2 μm $\times$ 2 μm $\times$ 25 nm. 40
3.4 Modulus of the far field scattered by the reference object depicted on Figure 3.3 for different polar and azimuthal illumination angles θ_l and ϕ_l, respectively. (a) $\theta_l = 55°$, $\phi_l = 0°$; (b) $\theta = 9°$, $\phi_l = 0°$; (c) $\theta_l = 57°$, $\phi_l = 90°$; (d) $\theta_l = 9°$, $\phi_l = 90°$ 40
3.5 Positions of the theoretical and experimental phase origins with respect to the object, and indication of the additional phase shifts due to the shift of the phase origin from the theoretical position to the experimental one. 41
3.6 Polar angle distribution within the discretized numerical aperture in the Fourier space. 44
3.7 Modulus (first line) and phases (second line) of the field in the image space obtained by PSI on resin cylinders with diameter 1 μm and height 125 nm. (a) and (e) $\theta_l = 32°$, $\phi_l = 0°$, TE polarization; (b) and (f) $\theta_l = 10°$, $\phi_l = 0°$, TE polarization; (c) and (g) $\theta_l = 31°$, $\phi_l = 90°$, TM polarization; (d) and (h) $\theta_l = 10°$, $\phi_l = 90°$, TM polarization. 45
3.8 Mask function applied to the data in the image space to isolate the sample region and suppress artefacts created by the discrete 2D FT^{-1} for the transfer to Fourier space. 45
3.9 Modulus (first line) and phases (second line) of the field in the Fourier space obtained by PSI on resin cylinders with diameter 1 μm and height 125 nm. (a) and (e) $\theta_l = 32°$, $\phi_l = 0°$, TE polarization; (b) and (f) $\theta_l = 10°$, $\phi_l = 0°$, TE polarization; (c) and (g) $\theta_l = 31°$, $\phi_l = 90°$, TM polarization; (d) and (h) $\theta_l = 10°$, $\phi_l = 90°$, TM polarization. 46
3.10 Modulus (first line) and phases (second line) of the theoretical far field (Fourier space) scattered by resin cylinders with diameter 1 μm and height 125 nm. (a) and (e) $\theta_l = 32°$, $\phi_l = 0°$, TE polarization; (b) and (f) $\theta_l = 10°$, $\phi_l = 0°$, TE polarization; (c) and (g) $\theta_l = 31°$, $\phi_l = 90°$, TM polarization; (d) and (h) $\theta_l = 10°$, $\phi_l = 90°$, TM polarization. 47
3.11 Modulus (first line) and phases (second line) of the field in the image space measured with a WFS on resin cylinders with diameter 1 μm and height 125 nm. (a) and (e) $\theta_l = 32°$, $\phi_l = 0°$, TE polarization; (b) and (f) $\theta_l = 10°$, $\phi_l = 0°$, TE polarization; (c) and (g) $\theta_l = 31°$, $\phi_l = 90°$, TM polarization; (d) and (h) $\theta_l = 10°$, $\phi_l = 90°$, TM polarization. 48
3.12 Modulus (first line) and phases (second line) of the field in the Fourier space measured with a WFS on resin cylinders with diameter 1 μm and height 125 nm. (a) and (e) $\theta_l = 32°$, $\phi_l = 0°$, TE polarization; (b) and (f) $\theta_l = 10°$, $\phi_l = 0°$, TE polarization; (c) and (g) $\theta_l = 31°$, $\phi_l = 90°$, TM polarization; (d) and (h) $\theta_l = 10°$, $\phi_l = 90°$, TM polarization. 49
3.13 Transverse cut at $z = 100$ nm of the reconstruction with 200 nm meshing of 1 μm large resin cylinders with 125 nm height (WFS data set) 50

3.14 Longitudinal cut at $y = 1\mu$m of the reconstruction with 200 nm meshing of 1 μm large resin cylinders with 125 nm height (WFS data set) 50
3.15 Transverse cut at $z = 100$ nm of the reconstruction with 200 nm meshing of 1 μm large resin cylinders with 125 nm height (WFS data set) 50
3.16 Longitudinal cut at $y = 1\mu$m of the reconstruction with 200 nm meshing of 1 μm large resin cylinders with 125 nm height (WFS data set) 50
3.17 Transverse cut at $z = 150$ nm of the reconstruction with 100 nm meshing of 1 μm large resin cylinders with 125 nm height (WFS data set) 51
3.18 Longitudinal cut at $y = 1\mu$m of the reconstruction with 100 nm meshing of 1 μm large resin cylinders with 125 nm height (WFS data set) 51
3.19 Transverse cut at $z = 125$ nm of the reconstruction with 50 nm meshing of 1 μm large resin cylinders with 125 nm height (WFS data set) 51
3.20 Longitudinal cut at $y = 1\mu$m of the reconstruction with 50 nm meshing of 1 μm large resin cylinders with 125 nm height (WFS data set) 51
3.21 Transverse cut at $z = 125$ nm of the reconstruction with 50 nm meshing of 1 μm large resin cylinders with 125 nm height (PSI data set) 52
3.22 Longitudinal cut at $y = 1\mu$m of the reconstruction with 50 nm meshing of 1 μm large resin cylinders with 125 nm height (PSI data set) 52
3.23 Comparison of the reconstructions of the 1 μm large resin cylinders with the non-linear inversion procedure and the 3D FT^{-1}, applied on the WFS data set. 53
3.24 Comparison of the reconstructions of the 1 μm large resin cylinders with the non-linear inversion procedure and the 3D FT^{-1}, applied on the PSI data set. 54
3.25 The 1^{st} iteration, transverse cut at $z = 125$ nm of the reconstruction with 50 nm meshing of 1 μm large resin cylinders with 125 nm height (WFS data set) 55
3.26 The 1^{st} iteration, longitudinal cut at $y = 1$ μm of the reconstruction with 50 nm meshing of 1 μm large resin cylinders with 125 nm height (WFS data set) 55
3.27 The 2^{nd} iteration, transverse cut at $z = 125$ nm of the reconstruction with 50 nm meshing of 1 μm large resin cylinders with 125 nm height (WFS data set) 55
3.28 The 2^{nd} iteration, longitudinal cut at $y = 1\mu$m of the reconstruction with 50 nm meshing of 1 μm large resin cylinders with 125 nm height (WFS data set) 55
3.29 The 3^{rd} iteration, transverse cut at $z = 125$ nm of the reconstruction with 50 nm meshing of 1 μm large resin cylinders with 125 nm height (WFS data set) 56
3.30 The 3^{rd} iteration, longitudinal cut at $y = 1\mu$m of the reconstruction with 50 nm meshing of 1 μm large resin cylinders with 125 nm height (WFS data set) 56
3.31 The final iteration, transverse cut at $z = 125$ nm of the reconstruction with 50 nm meshing of 1 μm large resin cylinders with 125 nm height (WFS data set) 56
3.32 The final iteration, longitudinal cut at $y = 1\mu$m of the reconstruction with 50 nm meshing of 1 μm large resin cylinders with 125 nm height (WFS data set) 56
3.33 Modulus (first line) and phases (second line) of the field in the image space measured by PSI on resin cylinders with diameter 500 μm and height 125 nm. (a) and (e) $\theta_l = 55°$, $\phi_l = 0°$, TE polarization; (b) and (f) $\theta_l = 8.8°$, $\phi_l = 0°$, TE polarization; (c) and (g) $\theta_l = 55°$, $\phi_l = 90°$, TM polarization; (d) and (h) $\theta_l = 9°$, $\phi_l = 90°$, TM polarization. 57
3.34 Modulus (first line) and phases (second line) of the field in the Fourier space measured by PSI on resin cylinders with diameter 500 μm and height 125 nm. (a) and (e) $\theta_l = 55°$, $\phi_l = 0°$, TE polarization; (b) and (f) $\theta_l = 8.8°$, $\phi_l = 0°$, TE polarization; (c) and (g) $\theta_l = 55°$, $\phi_l = 90°$, TM polarization; (d) and (h) $\theta_l = 9°$, $\phi_l = 90°$, TM polarization. 58
3.35 Modulus (first line) and phases (second line) of the theoretical field in the Fourier space scattered by resin cylinders with diameter 500 μm and height 125 nm. (a) and (e) $\theta_l = 55°$, $\phi_l = 0°$, TE polarization; (b) and (f) $\theta_l = 8.8°$, $\phi_l = 0°$, TE polarization; (c) and (g) $\theta_l = 55°$, $\phi_l = 90°$, TM polarization; (d) and (h) $\theta_l = 10°$, $\phi_l = 90°$, TM polarization. 58

3.36 Intensity of the field in the image space measured by off-axis holography on resin cylinders with diameter 500 μm and height 98 nm. (a) $\theta_l = 58°$, $\phi_l = 0°$, TE polarization; (b) $\theta_l = 10°$, $\phi_l = 0°$, TE polarization; (c) $\theta_l = 57°$, $\phi_l = 90°$, TM polarization; (d) $\theta_l = 9°$, $\phi_l = 90°$, TM polarization. 59
3.37 Modulus of the far field propagation of the intensity images measured by off-axis holography on resin cylinders with diameter 500 μm and height 98 nm. (a) $\theta_l = 58°$, $\phi_l = 0°$, TE polarization; (b) $\theta_l = 9°$, $\phi_l = 0°$, TE polarization; (c) $\theta_l = 58°$, $\phi_l = 90°$, TM polarization; (d) $\theta_l = 10°$, $\phi_l = 90°$, TM polarization. 59
3.38 The kept term modulus of the far field propagation of the intensity images measured by off-axis holography on resin cylinders with diameter 500 μm and height 98 nm. (a) $\theta_l = 58°$, $\phi_l = 0°$, TE polarization; (b) $\theta_l = 9°$, $\phi_l = 0°$, TE polarization; (c) $\theta_l = 58°$, $\phi_l = 90°$, TM polarization; (d) $\theta_l = 10°$, $\phi_l = 90°$, TM polarization. . . . 60
3.39 Modulus and phase of the field in the image space retrieved from the off-axis data set on resin cylinders with diameter 500 μm and height 98 nm. (a) and (e) $\theta_l = 58°$, $\phi_l = 0°$, TE polarization; (b) and (f) $\theta_l = 9°$, $\phi_l = 0°$, TE polarization; (c) and (g) $\theta_l = 58°$, $\phi_l = 90°$, TM polarization; (d) and (h) $\theta_l = 10°$, $\phi_l = 90°$, TM polarization. 60
3.40 Modulus (first line) and phases (second line) of the field in the Fourier space measured by off-axis holography on resin cylinders with diameter 500 μm and height 98 nm. (a) and (e) $\theta_l = 58°$, $\phi_l = 0°$, TE polarization; (b) and (f) $\theta_l = 9°$, $\phi_l = 0°$, TE polarization; (c) and (g) $\theta_l = 58°$, $\phi_l = 90°$, TM polarization; (d) and (h) $\theta_l = 10°$, $\phi_l = 90°$, TM polarization. 61
3.41 Transverse cut at $z = 200$ nm of the reconstruction with 200 nm meshing of 500 nm large resin cylinders with 125 nm height (PSI data set) 62
3.42 Longitudinal cut at y =500 nm of the reconstruction with 200 nm meshing of 500 nm large resin cylinders with 125 nm height (PSI data set) 62
3.43 Transverse cut at $z = 100$ nm of the reconstruction with 100 nm meshing of 500 nm large resin cylinders with 125 nm height (PSI data set) 62
3.44 Longitudinal cut at y =500 nm of the reconstruction with 100 nm meshing of 500 nm large resin cylinders with 125 nm height (PSI data set) 62
3.45 Transverse cut at $z = 125$ nm of the reconstruction with 50 nm meshing of 500 nm large resin cylinders with 125 nm height (PSI data set) 63
3.46 Longitudinal cut at y =500 nm of the reconstruction with 50 nm meshing of 500 nm large resin cylinders with 125 nm height (PSI data set) 63
3.47 Transverse cut at $z = 75$ nm of the reconstruction with 50 nm meshing of 500 nm large resin cylinders with 98 nm height (Off-axis data set) 63
3.48 Longitudinal cut at y =500 nm of the reconstruction with 50 nm meshing of 500 nm large resin cylinders with 98 nm height (Off-axis data set) 63
3.49 Transverse cut at $z = 53$ nm of the reconstruction under Born approximation with 53 nm meshing of 500 nm large resin cylinders with 125 nm height (PSI data set) . 64
3.50 Longitudinal cut at y =500 nm of the reconstruction under Born approximation with 53 nm meshing of 500 nm large resin cylinders with 125 nm height (PSI data set) 64
3.51 Transverse cut at $z = 53$ nm of the reconstruction under Born approximation with 53 nm meshing of 500 nm large resin cylinders with 98 nm height (Off-axis data set) 65
3.52 Longitudinal cut at y =500 nm of the reconstruction under Born approximation with 53 nm meshing of 500 nm large resin cylinders with 98 nm height (Off-axis data set) 65
3.53 Transverse cut at $z = 125$ nm of the reconstruction with 50 nm meshing of 500 nm large resin cylinders with 150 nm height (Off-axis data set, double incidences) . . . 66
3.54 Longitudinal cut at y =500 nm of the reconstruction with 50 nm meshing of 500 nm large resin cylinders with 150 nm height (PSI data set, 40 incidences) 66
3.55 Transverse cut at $z = 125$ nm of the reconstruction with 50 nm meshing of 500 nm large resin cylinders with 150 nm height (PSI data set, 10 incidences in TE polarization) 66

3.56 Longitudinal cut at y =500 nm of the reconstruction with 50 nm meshing of 500 nm large resin cylinders with 150 nm height (PSI data set, 10 incidences in TE polarization) . . . 66
3.57 Transverse cut at z = 125 nm of the reconstruction with 50 nm meshing of 500 nm large resin cylinders with 150 nm height (PSI data set, 10 incidences in TM polarization) . . . 67
3.58 Longitudinal cut at y =500 nm of the reconstruction with 50 nm meshing of 500 nm large resin cylinders with 150 nm height (PSI data set, 10 incidences in TM polarization) . . . 67
3.59 The upper two rows are the modulus and phases of the field scattered by one cylinder detected on the CCD camera, the lowers are the modulus and phases of the field scattered by one cylinder in Fourier domain, respectively. Data set obtained by PSI. (a, e, i, m) $\theta_l = 55°$, $\phi_l = 0°$, TE polarization; (b, f, j, n) $\theta_l = 8.8°$, $\phi_l = 0°$, TE polarization; (c, g, k, o) $\theta_l = 55°$, $\phi_l = 90°$, TM polarization; (d, h, l, p) $\theta_l = 9°$, $\phi_l = 90°$, TM polarization. . . . 68
3.60 The upper two rows are the modulus and phases of the field scattered by two diagonal cylinders detected on the CCD camera, the lowers are the modulus and phases of the field scattered by two diagonal cylinders in Fourier domain, respectively. Data set obtained by PSI. (a, e, i, m) $\theta_l = 55°$, $\phi_l = 0°$, TE polarization; (b, f, j, n) $\theta_l = 8.8°$, $\phi_l = 0°$, TE polarization; (c, g, k, o) $\theta_l = 55°$, $\phi_l = 90°$, TM polarization; (d, h, l, p) $\theta_l = 9°$, $\phi_l = 90°$, TM polarization. . . . 69
3.61 Transverse cut at $z = 125$ nm of the reconstruction with 50 nm meshing of one 500 nm large resin cylinders with 150 nm height (PSI data set) . . . 70
3.62 Longitudinal cut at y =-500 nm of the reconstruction with 50 nm meshing of one 500 nm large resin cylinders with 150 nm height (PSI data set) . . . 70
3.63 Transverse cut at $z = 125$ nm of the reconstruction with 50 nm meshing of two 500 nm large resin cylinders with 150 nm height (PSI data set) . . . 70
3.64 Longitudinal cut at y =-500 nm of the reconstruction with 50 nm meshing of two 500 nm large resin cylinders with 150 nm height (PSI data set) . . . 70
3.65 Transverse cut at $z = 120$ nm of the reconstruction with 10 nm meshing of 500 nm large resin cylinders with 150 nm height (PSI data set) . . . 71
3.66 Longitudinal cut at y =0 nm of the reconstruction with 10 nm meshing of one 500 nm large resin cylinders with 150 nm height (PSI data set) . . . 71
3.67 Transverse cut at $z = 80$ nm of the reconstruction with 10 nm meshing of 500 nm large resin cylinders with 98 nm height (Off-axis data set) . . . 71
3.68 Longitudinal cut at y =-30 nm of the reconstruction with 10 nm meshing of one 500 nm large resin cylinders with 98 nm height (Off-axis data set) . . . 71
3.69 A line cut map along z with $150nm$ height sample at $x = 0nm$ . . . 72
3.70 A line cut map along z with $98nm$ height sample at $x = 50nm$ . . . 72
3.71 Modulus [(a)-(d)] and phases [(e)-(h)] of the data set obtained by PSI, respectively. Samples diameter $200nm$, height $150nm$. (a) and (e) $\theta_l = 53°$, $\phi_l = 0°$, TE polarization; (b) and (f) $\theta_l = 11°$, $\phi_l = 0°$, TE polarization; (c) and (g) $\theta_l = 54°$, $\phi_l = 90°$, TM polarization; (d) and (h) $\theta_l = 9°$, $\phi_l = 90°$, TM polarization. . . . 73
3.72 Modulus (first line) and phases (second line) of the far field (Fourier space) scattered by resin cylinders with diameter 200 nm and height 150 nm, obtained by PSI. (a) and (e) $\theta_l = 53°$, $\phi_l = 0°$, TE polarization; (b) and (f) $\theta_l = 11°$, $\phi_l = 0°$, TE polarization; (c) and (g) $\theta_l = 54°$, $\phi_l = 90°$, TM polarization; (d) and (h) $\theta_l = 9°$, $\phi_l = 90°$, TM polarization. . . . 73
3.73 Modulus (first line) and phases (second line) of the theoretical far field (Fourier space) scattered by resin cylinders with diameter 200 nm and height 150 nm. (a) and (e) $\theta_l = 53°$, $\phi_l = 0°$, TE polarization; (b) and (f) $\theta_l = 11°$, $\phi_l = 0°$, TE polarization; (c) and (g) $\theta_l = 54°$, $\phi_l = 90°$, TM polarization; (d) and (h) $\theta_l = 9°$, $\phi_l = 90°$, TM polarization. . . . 74

3.74 Intensity in the image space measured by off-axis holography on samples with diameter 200 nm and height 150 nm. (a) $\theta_l = 52°$, $\phi_l = 0°$, TE polarization; (b) $\theta_l = 10°$, $\phi_l = 0°$, TE polarization; (c) $\theta_l = 54°$, $\phi_l = 90°$, TM polarization; (d) $\theta_l = 10°$, $\phi_l = 90°$, TM polarization. 74
3.75 Modulus of the far field (Fourier space) scattered by resin cylinders with diameter 200 nm and height 150 nm, obtained by off-axis method. (a) $\theta_l = 52°$, $\phi_l = 0°$, TE polarization; (b) $\theta_l = 10°$, $\phi_l = 0°$, TE polarization; (c) $\theta_l = 54°$, $\phi_l = 90°$, TM polarization; (d) $\theta_l = 10°$, $\phi_l = 90°$, TM polarization. 75
3.76 Modulus of the selected interference order of the far field (Fourier space) scattered by resin cylinders with diameter 200 nm and height 150 nm, obtained by off-axis method. (a) $\theta_l = 52°$, $\phi_l = 0°$, TE polarization; (b) $\theta_l = 10°$, $\phi_l = 0°$, TE polarization; (c) $\theta_l = 54°$, $\phi_l = 90°$, TM polarization; (d) $\theta_l = 10°$, $\phi_l = 90°$, TM polarization. 75
3.77 Modulus of the field in the image space retrieved from the off-axis holography data set on samples with diameter 200 nm and height 150 nm. (a) $\theta_l = 52°$, $\phi_l = 0°$, TE polarization; (b) $\theta_l = 10°$, $\phi_l = 0°$, TE polarization; (c) $\theta_l = 54°$, $\phi_l = 90°$, TM polarization; (d) $\theta_l = 10°$, $\phi_l = 90°$, TM polarization. 76
3.78 Modulus (first line) and phase (second line) of the field in the Fourier space retrieved from the off-axis holography data set on samples with diameter 200 nm and height 150 nm. (a) and (e) $\theta_l = 53°$, $\phi_l = 0°$, TE polarization; (b) and (f) $\theta_l = 11°$, $\phi_l = 0°$, TE polarization; (c) and (g) $\theta_l = 54°$, $\phi_l = 90°$, TM polarization; (d) and (h) $\theta_l = 9°$, $\phi_l = 90°$, TM polarization. 76
3.79 Transverse cut at $z = 53$ nm of the reconstruction under Born approximation with 53 nm meshing of 200 nm large resin cylinders with 150 nm height (PSI data set) . 77
3.80 Longitudinal cut at y =0 nm of the reconstruction under Born approximation with 53 nm meshing of 200 nm large resin cylinders with 150 nm height (PSI data set) . 77
3.81 Transverse cut at $z = 53$ nm of the reconstruction under Born approximation with 53 nm meshing of 200 nm large resin cylinders with 150 nm height (Off-axis data set) 77
3.82 Longitudinal cut at y =0 nm of the reconstruction under Born approximation with 53 nm meshing of 200 nm large resin cylinders with 150 nm height (Off-axis data set) 77
3.83 Transverse cut at $z = 125$ nm of the reconstruction with 50 nm meshing of 200 nm large resin cylinders with 150 nm height (PSI data set) 78
3.84 Longitudinal cut at y =200 nm of the reconstruction with 50 nm meshing of 200 nm large resin cylinders with 150 nm height (PSI data set) 78
3.85 Transverse cut at $z = 125$ nm of the reconstruction with 50 nm meshing of 200 nm large resin cylinders with 150 nm height (Off-axis data set) 79
3.86 Longitudinal cut at y =300 nm of the reconstruction with 50 nm meshing of 200 nm large resin cylinders with 150 nm height (Off-axis data set) 79
3.87 Modulus (first line) and phases (second line) of the data set obtained by PSI. Samples diameter 150 nm, height 150 nm. (a) and (e) $\theta_l = 53°$, $\phi_l = 0°$, TE polarization; (b) and (f) $\theta_l = 11°$, $\phi_l = 0°$, TE polarization; (c) and (g) $\theta_l = 54°$, $\phi_l = 90°$, TM polarization; (d) and (h) $\theta_l = 10°$, $\phi_l = 90°$, TM polarization. 79
3.88 Modulus (first line) and phases (second line) of the data set in the Fourier space, obtained by PSI. Samples diameter 150 nm, height 150 nm. (a) and (e) $\theta_l = 53°$, $\phi_l = 0°$, TE polarization; (b) and (f) $\theta_l = 11°$, $\phi_l = 0°$, TE polarization; (c) and (g) $\theta_l = 54°$, $\phi_l = 90°$, TM polarization; (d) and (h) $\theta_l = 10°$, $\phi_l = 90°$, TM polarization. 80
3.89 Modulus (first line) and phases (second line) of the theoretical field in the Fourier space. Samples diameter 150 nm, height 150 nm. (a) and (e) $\theta_l = 53°$, $\phi_l = 0°$, TE polarization; (b) and (f) $\theta_l = 11°$, $\phi_l = 0°$, TE polarization; (c) and (g) $\theta_l = 54°$, $\phi_l = 90°$, TM polarization; (d) and (h) $\theta_l = 10°$, $\phi_l = 90°$, TM polarization. 80
3.90 Modulus and phases of the data set in the Fourier space, obtained by off-axis holography. Samples diameter 150 nm, height 150 nm. (a) and (e) $\theta_l = 54°$, $\phi_l = 0°$, TE polarization; (b) and (f) $\theta_l = 11°$, $\phi_l = 0°$, TE polarization; (c) and (g) $\theta_l = 54°$, $\phi_l = 90°$, TM polarization; (d) and (h) $\theta_l = 11°$, $\phi_l = 90°$, TM polarization. 81

3.91 Transverse cut image at $z = 100$ nm of the reconstruction obtained with the PSI data set (20 incidences). Sample diameter 150 nm, height 150 nm. 82
3.92 Longitudinal cut image at $y = 150$ nm of the reconstruction obtained with the PSI data set (20 incidences). Sample diameter 150 nm, height 150 nm. 82
3.93 Transverse cut image at $z = 100$ nm of the reconstruction obtained with the PSI data set (8 incidences). Sample diameter 150 nm, height 150 nm. 82
3.94 Longitudinal cut image at $y = 150$ nm of the reconstruction obtained with the PSI data set (8 incidences). Sample diameter 150 nm, height 150 nm. 82
3.95 Transverse cut image at $z = 100$ nm of the reconstruction obtained with the off-axis data set (20 incidences). Sample diameter 150 nm, height 150 nm. 83
3.96 Longitudinal cut image at $y = 150$ nm of the reconstruction obtained with the off-axis data set (20 incidences). Sample diameter 150 nm, height 150 nm. 83

4.1 Modulus of the scattered field computed by the CDM, in Fourier domain. Samples diameter $D = 150$ nm, height $h = 150$ nm. (a), (c) and (e) $\theta_l = 55°$, $\phi_l = 0°$, TE polarization; (a) presents the computed full vectorial scattered field, (c) the scattered field in the incident electric field direction, (e) the scattered field in the orthogonal direction of incident electric field (crossed polarization). (b), (d) and (f) $\theta_l = 54°$, $\phi_l = 270°$, TM polarization; (b) is the computed full vectorial scattered field, (d) the scattered field in the incident electric field direction, (f) the scattered field in the orthogonal direction of incident electric field (crossed polarization). . . 87
4.2 Sketch of the experimental setup, laser source emitting at 633 nm; M, adjustable mirror; PL, polarizer; HW, half-waveplate for changing the polarization. $L_{i=1,\cdots,6}$ lenses; f_i, $f_i^{'}$, object and image focal planes of lenses; B_1, B_2, B_3, beam splitters; BE_1, BE_2 beam expander; TM, pinhole; D_1, D_2, diaphragms. The red crosses correspond to the polarization bases, two cases are considered for the detection : $(\widehat{\boldsymbol{h}}, \widehat{\boldsymbol{v}})$ (a) and $(\widehat{\boldsymbol{d_1}}, \widehat{\boldsymbol{d_2}})$ (b) 89
4.3 Orientation of the directions for TM (or p) and TE (or s) polarizations compared to the vertical and horizontal $(\widehat{\boldsymbol{v}}, \widehat{\boldsymbol{h}})$ directions. 89
4.4 Transverse cut image at $z = 100$ nm of the reconstruction obtained with the off-axis data set (20 incidences), polarizers in $\widehat{\boldsymbol{h}}\widehat{\boldsymbol{h}}$ mode. Sample diameter $D = 200$ nm, height $h = 150$ nm. 91
4.5 Longitudinal cut image at $y = 200$ nm of the reconstruction obtained with the off-axis data set (20 incidences), polarizers in $\widehat{\boldsymbol{h}}\widehat{\boldsymbol{h}}$ mode. Sample diameter $D = 200$ nm, height $h = 150$ nm. 91
4.6 Transverse cut image at $z = 100$ nm of the reconstruction obtained with the off-axis data set (20 incidences), polarizers in $\widehat{\boldsymbol{v}}\widehat{\boldsymbol{v}}+ \widehat{\boldsymbol{h}}\widehat{\boldsymbol{h}}$ mode. Sample diameter $D = 200$ nm, height $h = 150$ nm. 91
4.7 Longitudinal cut image at $y = 200$ nm of the reconstruction obtained with the off-axis data set (20 incidences), polarizers in $\widehat{\boldsymbol{v}}\widehat{\boldsymbol{v}}+ \widehat{\boldsymbol{h}}\widehat{\boldsymbol{h}}$ mode. Sample diameter $D = 200$ nm, height $h = 150$ nm. 91
4.8 Transverse cut image at $z = 100$ nm, obtained by considering full polarization. Sample with diameter $D = 200$ nm and height $h = 150$ nm. 92
4.9 Longitudinal cut image at $y = 200$ nm, obtained by considering full polarization. Sample with diameter $D = 200$ nm and height $h = 150$ nm. 92
4.10 Transverse cut image at $z = 100$ nm, obtained by using scattered field obtained from only TM-polarization incidence. Sample with diameter $D = 200$ nm and height $h = 150$ nm. 92
4.11 Longitudinal cut image at $y = 200$ nm, obtained by using scattered field obtained from only TM incidence. Sample with diameter $D = 200$ nm and height $h = 150$ nm. 92
4.12 Same as Fig. 4.10 for TE polarization. 92
4.13 Same as Fig. 4.11 for TE polarization. 92

4.14 Transverse cut image at $z = 100$ nm of the reconstruction obtained with the off-axis data set (20 incidences), polarizers in $\widehat{\boldsymbol{h}}\widehat{\boldsymbol{h}}$ mode. Sample diameter $D = 150$ nm, height $h = 150$ nm. 93
4.15 Longitudinal cut image at $y = 150$ nm of the reconstruction obtained with the off-axis data set (20 incidences), polarizers in $\widehat{\boldsymbol{h}}\widehat{\boldsymbol{h}}$ mode. Sample diameter $D = 150$ nm, height $h = 150$ nm. 93
4.16 Transverse cut image at $z = 100$ nm of the reconstruction obtained with the off-axis data set (20 incidences), polarizers in $\widehat{\boldsymbol{v}}\widehat{\boldsymbol{v}}+\widehat{\boldsymbol{h}}\widehat{\boldsymbol{h}}$ mode. Sample diameter $D = 150$ nm, height $h = 150$ nm. 94
4.17 Longitudinal cut image at $y = 150$ nm of the reconstruction obtained with the off-axis data set (20 incidences), polarizers in $\widehat{\boldsymbol{v}}\widehat{\boldsymbol{v}}+\widehat{\boldsymbol{h}}\widehat{\boldsymbol{h}}$ mode. Sample diameter $D = 150$ nm, height $h = 150$ nm. 94
4.18 Transverse cut image at $z = 100$ nm, obtained by using total scattered field. Sample with diameter $D = 150$ nm and height $h = 150$ nm. 94
4.19 Longitudinal cut image at $y = 150$ nm, obtained by using total scattered field. Sample with diameter $D = 150$ nm and height $h = 150$ nm. 94
4.20 Transverse cut image at $z = 100$ nm, obtained by using scattered field obtained from only TM polarization incidence. Sample with diameter $D = 150$ nm and height $h = 150$ nm. 95
4.21 Longitudinal cut image at $y = 150$ nm, obtained by using scattered field obtained from only TM polarization incidence. Sample with diameter $D = 150$ nm and height $h = 150$ nm. 95
4.22 Same as in Fig. 4.20 with TE polarization. 95
4.23 Same as in Fig. 4.21 with TE polarization. 95

B.1 Diagram for illustrating of the approximation of scalar green function under Born approximation. 103

C.1 Modulus and phases of the data set in the Fourier space, obtained by off-axis holography, polarizers in $\widehat{\boldsymbol{h}}\widehat{\boldsymbol{h}}$ mode. Samples diameter 200 nm, height 150 nm. (a) and (e) $\theta_l = 55°$, $\phi_l = 0°$, TE polarization; (b) and (f) $\theta_l = 9°$, $\phi_l = 0°$, TE polarization; (c) and (g) $\theta_l = 54°$, $\phi_l = 90°$, TM polarization; (d) and (h) $\theta_l = 10°$, $\phi_l = 90°$, TM polarization. 105
C.2 Modulus (first line) and phases (second line) of the theoretical field in the Fourier space, polarizers in $\widehat{\boldsymbol{h}}\widehat{\boldsymbol{h}}$ mode. Samples diameter 200 nm, height 150 nm. (a) and (e) $\theta_l = 55°$, $\phi_l = 0°$, TE polarization; (b) and (f) $\theta_l = 9°$, $\phi_l = 0°$, TE polarization; (c) and (g) $\theta_l = 54°$, $\phi_l = 90°$, TM polarization; (d) and (h) $\theta_l = 10°$, $\phi_l = 90°$, TM polarization. 106
C.3 Modulus and phases of the data set in the Fourier space, obtained by off-axis holography, polarizers in $\widehat{\boldsymbol{h}}\widehat{\boldsymbol{h}}$ mode. Samples diameter 150 nm, height 150 nm. (a) and (e) $\theta_l = 55°$, $\phi_l = 0°$, TE polarization; (b) and (f) $\theta_l = 9°$, $\phi_l = 0°$, TE polarization; (c) and (g) $\theta_l = 54°$, $\phi_l = 90°$, TM polarization; (d) and (h) $\theta_l = 10°$, $\phi_l = 90°$, TM polarization. 106
C.4 Modulus (first line) and phases (second line) of the theoretical field in the Fourier space, polarizers in $\widehat{\boldsymbol{h}}\widehat{\boldsymbol{h}}$ mode. Samples diameter 150 nm, height 150 nm. (a) and (e) $\theta_l = 55°$, $\phi_l = 0°$, TE polarization; (b) and (f) $\theta_l = 9°$, $\phi_l = 0°$, TE polarization; (c) and (g) $\theta_l = 54°$, $\phi_l = 90°$, TM polarization; (d) and (h) $\theta_l = 10°$, $\phi_l = 90°$, TM polarization. 107

D.1 Modulus and phases of the data set measured by $\widehat{\boldsymbol{v}}\widehat{\boldsymbol{d}}_1$ mode, in Fourier domain, off-axis holography method, respectively. Samples diameter 200 nm, height 150 nm. (a) and (e) $\theta_l = 55°$, $\phi_l = 0°$, TM polarization; (b) and (f) $\theta_l = 9°$, $\phi_l = 0°$, TM polarization; (c) and (g) $\theta_l = 54°$, $\phi_l = 90°$, TE polarization; (d) and (h) $\theta_l = 9°$, $\phi_l = 90°$, TE polarization. 109

D.2 Modulus and phases of the data set measured by $\widehat{\boldsymbol{v}}\widehat{\boldsymbol{d}}_2$ mode, in Fourier domain, off-axis holography method, respectively. Samples diameter $200nm$, height $150nm$. (a) and (e) $\theta_l = 55°$, $\phi_l = 0°$, TM polarization; (b) and (f) $\theta_l = 9°$, $\phi_l = 0°$, TM polarization; (c) and (g) $\theta_l = 54°$, $\phi_l = 90°$, TE polarization; (d) and (h) $\theta_l = 9°$, $\phi_l = 90°$, TE polarization. 110
D.3 Modulus and phases of the data set measured by $\widehat{\boldsymbol{h}}\widehat{\boldsymbol{d}}1$ mode, in Fourier domain, off-axis holography method, respectively. Samples diameter 200 nm, height 150 nm. (a) and (e) $\theta_l = 55°$, $\phi_l = 0°$, TM polarization; (b) and (f) $\theta_l = 9°$, $\phi_l = 0°$, TM polarization; (c) and (g) $\theta_l = 54°$, $\phi_l = 90°$, TE polarization; (d) and (h) $\theta_l = 9°$, $\phi_l = 90°$, TE polarization. 110
D.4 Modulus and phases of the data set measured by $\widehat{\boldsymbol{h}}\widehat{\boldsymbol{d}}_2$ mode, in Fourier domain, off-axis holography method, respectively. Samples diameter 200 nm, height 150 nm. (a) and (e) $\theta_l = 55°$, $\phi_l = 0°$, TM polarization; (b) and (f) $\theta_l = 9°$, $\phi_l = 0°$, TM polarization; (c) and (g) $\theta_l = 54°$, $\phi_l = 90°$, TE polarization; (d) and (h) $\theta_l = 9°$, $\phi_l = 90°$, TE polarization. 111
D.5 Modulus and phases of the data set measured by $\widehat{\boldsymbol{v}}\widehat{\boldsymbol{d}}_1$ mode, in Fourier domain, off-axis holography method, respectively. Samples diameter 150 nm, height 150 nm. (a) and (e) $\theta_l = 55°$, $\phi_l = 0°$, TM polarization; (b) and (f) $\theta_l = 9°$, $\phi_l = 0°$, TM polarization; (c) and (g) $\theta_l = 54°$, $\phi_l = 90°$, TE polarization; (d) and (h) $\theta_l = 9°$, $\phi_l = 90°$, TE polarization. 111
D.6 Modulus and phases of the data set measured by $\widehat{\boldsymbol{v}}\widehat{\boldsymbol{d}}_2$ mode, in Fourier domain, off-axis holography method, respectively. Samples diameter 150 nm, height 150 nm. (a) and (e) $\theta_l = 55°$, $\phi_l = 0°$, TM polarization; (b) and (f) $\theta_l = 9°$, $\phi_l = 0°$, TM polarization; (c) and (g) $\theta_l = 54°$, $\phi_l = 90°$, TE polarization; (d) and (h) $\theta_l = 9°$, $\phi_l = 90°$, TE polarization. 112
D.7 Modulus and phases of the data set measured by $\widehat{\boldsymbol{h}}\widehat{\boldsymbol{d}}_1$ mode, in Fourier domain, off-axis holography method, respectively. Samples diameter 150 nm, height 150 nm. (a) and (e) $\theta_l = 55°$, $\phi_l = 0°$, TM polarization; (b) and (f) $\theta_l = 9°$, $\phi_l = 0°$, TM polarization; (c) and (g) $\theta_l = 54°$, $\phi_l = 90°$, TE polarization; (d) and (h) $\theta_l = 9°$, $\phi_l = 90°$, TE polarization. 112
D.8 Modulus and phases of the data set measured by $\widehat{\boldsymbol{h}}\widehat{\boldsymbol{d}}_2$ mode, in Fourier domain, off-axis holography method, respectively. Samples diameter 150 nm, height 150 nm. (a) and (e) $\theta_l = 55°$, $\phi_l = 0°$, TM polarization; (b) and (f) $\theta_l = 9°$, $\phi_l = 0°$, TM polarization; (c) and (g) $\theta_l = 54°$, $\phi_l = 90°$, TE polarization; (d) and (h) $\theta_l = 9°$, $\phi_l = 90°$, TE polarization. 113

Résumé en Français

Contents

1 Le mot du directeur de thèse xvii
2 Généralités xvii
3 Quelques mots sur la résolution xviii
4 Quelques mots sur la la sphère d'Ewald xix
5 La tomographie optique xix

1) Le mot du directeur de thèse

Une nouvelle règle a été établie par le conseil scientifique (CS) de l'université Aix-Marseille. Le CS exige que pour les thèses écrites en anglais, au moins 10% de la thèse soit rédigée en Français. M. Ruan étant chinois il était pour lui difficile de satisfaire cette lubie du CS (soit dit en passant j'aimerais bien voir les membres du CS écrire 10 pages en chinois!). J'ai donc pris mon plus beau clavier pour satisfaire les desiderata et délires schizo maniaco psychotiques du CS. Ce chapitre est donc un résumé succinct de la thèse de M. Ruan et présente quelques résultats choisis de son travail. Le lecteur a donc tout intérêt à passer ce chapitre très rapidement...

2) Généralités

Les progrès rapides de la science sur les structures de taille nanométrique, dans le domaine de la biologie, des matériaux, de la microélectronique, ont provoqué un intérêt croissant pour les techniques d'imagerie à haut pouvoir de résolution. La microscopie électronique, la microscopie à force atomique produisent des images dont la résolution est inférieure à une dizaine de nanomètres. Cependant, ce sont des techniques coûteuses, difficiles à mettre en œuvre et elles ne permettent pas de faire, sans intrusion, une cartographie tridimensionnelle de l'objet. Or, de plus en plus, les nano-structures manufacturées deviennent complexes selon les trois dimensions de l'espace. Le besoin en techniques d'imagerie tridimensionnelle non intrusives ayant un pouvoir de résolution inférieur à une centaine de nanomètres est donc patent, pour la caractérisation et le contrôle de ces nouveaux composants, mais aussi, de manière générale, pour l'analyse des structures internes d'objets semi-transparents. Les microscopes optiques traditionnels n'atteignent pas ce niveau de résolution et ne permettent pas de restituer la carte de permittivité relative de l'objet en trois dimensions.

Le travail développé durant cette thèse portait sur l'utilisation des ondes électromagnétiques dans le domaine optique pour détecter, localiser, caractériser des objets à distance. Les ondes sont ainsi utilisées comme des sondes qui interagissent avec les objets et les milieux étudiés. Les propriétés (répartition d'intensité, phase, polarisation, fréquence) des ondes renvoyées par les objets sont ensuite analysées, grâce à différents modèles, pour remonter aux paramètres caractéristiques tridimensionnelles décrivant les objets ou milieux étudiés.

Ce travail de thèse s'inscrivait donc dans une thématique majeure de l'équipe SEMO, celle-ci ayant l'avantage de développer aussi bien le coté expérimental que théorique. Le travail de thèse portait plus sur le développement expérimentale de la mesure des champs diffractés par l'objet étudié, mais a quand même demandé une implication importante sur la partie théorique.

La diffusion d'une onde électromagnétique par un objet de permittivité relative et de forme arbitraires est ce que nous définissons comme étant le problème direct, *i.e.*, l'objet étant connu, il faut calculer/mesurer en un ou plusieurs points d'observation donnés, le champ diffracté. Il est alors possible de définir le problème inverse : connaissant le champ diffracté en différents points d'observation, il s'agit de "trouver l'objet" qui a créé ce champ diffracté. Le terme "trouver l'objet" est mis entre guillemets, car il peut avoir différentes significations suivant la problématique posée:

- détection: repérer le nombre de diffuseurs.
- localisation: connaître la position des diffuseurs.
- contour: déterminer la forme des objets inconnus.
- caractérisation: accéder à la forme et à la permittivité relative des diffuseurs.

Ce travail de thèse s'intéresse à la caractérisation des objets et à la résolution atteignable par le montage expérimental.

3) Quelques mots sur la résolution

Avant d'aborder la microscopie optique à haute résolution, nous devons d'abord définir dans le domaine de la microscopie optique classique [i] ce qu'on entend par le terme de résolution (la résolution étant le pouvoir séparateur de l'instrument d'optique considéré). La définition la plus commune de la résolution se fait à travers le critère de Rayleigh: la résolution d'un instrument c'est l'écart angulaire minimal entre deux objets lumineux ponctuels incohérents, pour que l'observateur puisse les distinguer l'un de l'autre avec l'instrument considéré:[ii]

$$\Delta\theta = 1.22\frac{\lambda}{a}, \tag{1}$$

où λ est la longueur d'onde utilisée et a est le diamètre instrumental. L'Eq. (1), dans le cas d'un microscope travaillant dans l'air, donne:

$$d = \frac{1.22\lambda}{2\sin\alpha} \Rightarrow d_{\text{minimum}} = 0.61\lambda, \tag{2}$$

[i] Notons que l'invention du microscope optique remonte à 1595. Le hollandais Zacharias Janssen profite de ses compétences de fabriquant de lentilles pour inventer un système optique qui va bouleverser la biologie : le microscope. Il est alors équipé de deux lentilles convexes dans un ensemble de tubes coulissants. Grâce aux modifications apportées par Antoine van Leeuwenhoek et Robert Hooke, le microscope permettra notamment à ce dernier d'aboutir à la découverte de la cellule en 1665.

[ii] Cela correspond au moment où le maximum de la tache de diffraction de la première source coïncide au premier minimum de la tache de diffraction pour la seconde source

où d est la plus petite distance pour laquelle deux objets peuvent être séparés, et α l'angle de collection de la lentille objectif. Au mieux $\alpha = \pi/2$, soit un pouvoir de séparation de 0.61λ. Dans le domaine du visible pour des microscopes optiques en transmission la résolution est donc typiquement de 300 nm. Notons que dans le cadre d'un microscope en champ proche optique, type PSTM par exemple, il est de coutume de dire que son pouvoir de résolution est largement inférieur au critère de Rayleigh, vu que des objets séparés de quelques dizaines de nanomètres sont discernables. Mais nous étudions alors des objets qui n'ont plus un caractère ponctuel, et qui de plus sont fortement couplés de par la distance qui les sépare. Il est alors difficile dans ces conditions de définir un critère de résolution, celle-ci variant suivant la diffusion multiple entre les objets.

4) Quelques mots sur la sphère d'Ewald

Dans le cas où le diffuseur est petit vis-à-vis de la longueur d'onde, par exemple une sphère de diamètre $\lambda/10$, le champ diffracté par celle-ci peut s'écrire comme:

$$\boldsymbol{f}(\boldsymbol{r}) \propto \frac{e^{ik_\mathrm{d} r}}{r} \boldsymbol{E}_0^\perp \tilde{\chi}(\boldsymbol{k}_\mathrm{d} - \boldsymbol{k}_0). \tag{3}$$

Le champ diffracté par l'objet au point d'observation $\boldsymbol{r}$ est donc proportionnel à la transformée de Fourier de la susceptibilité linéaire χ prise en $\boldsymbol{k}_\mathrm{d} - \boldsymbol{k}_0$, $\boldsymbol{E}_0^\perp$ étant la composante du champ incident perpendiculaire à la direction d'observation. En faisant varier la direction du champ incident et la position d'observation, il est donc possible d'accéder à un certain domaine spectral de $\tilde{\chi}$. Par exemple, dans la configuration d'un microscope optique en transmission, quand l'angle d'incidence est tel que $\theta_0 \in [-90°; 90°]$ nous obtenons $k_{0,x} \in [-k_0; k_0]$ et $k_{0,z} \in [0; k_0]$. Quant au champ diffracté, si les points d'observations sont tels que $\theta_\mathrm{d} \in [-90°; 90°]$ nous obtenons $k_{d,x} \in [-k_0; k_0]$ et $k_{d,z} \in [0; k_0]$. Le support spectral accessible pour $\tilde{\chi}$ est alors de $[-2k_0; 2k_0]$ suivant la direction transversale et de $[-k_0; k_0]$ dans la direction longitudinale.[iii] Normalement avec un tel domaine de fréquence la résolution transverse est de 0.3λ, mais il convient de tempérer ce résultat. En effet, avoir accès à un large domaine spectral n'assure en rien l'existence des hautes fréquences, ou de leurs signatures plus élevées par rapport au bruit. Par exemple, pour un objet dipolaire déposé sur un substrat plan, il est toujours possible de mettre un point d'observation à $\theta_\mathrm{d} \approx 90°$, mais il n'y aura pas de champ diffracté...

5) La tomographie optique

a) Descriptif du montage

La technique d'imagerie que nous sommes en train de développer s'apparente à de la tomographie par diffraction : l'échantillon étudié est éclairé par un faisceau laser sous différentes incidences successives, et le champ diffracté est alors mesuré en différents points d'observation, c'est-à-dire qu'il nous faut mesurer le module **et** la phase du champ diffracté. Notons que si la mesure de la phase du champ diffracté dans le domaine des micro-ondes est chose facile à réaliser, dans le domaine du visible les fréquences sont telles ($\approx 10^{14}$ Hz) qu'un montage interférométrique est nécessaire pour l'obtention de la phase. Contrairement à un microscope conventionnel, où l'image de l'objet est construite analogiquement par l'action des lentilles sur le champ diffracté, nous utilisons des algorithmes de résolution du problème inverse afin de remonter à la carte de permittivité relative de l'objet. Figure 1 présente le schéma du montage utilisé pour mesurer les champs diffractés par l'échantillon. Le principe de ce montage repose sur l'interférence entre une voie de référence dont nous pouvons faire varier la phase de manière contrôlée et le champ diffracté par l'objet. Par une combinaison linéaire des intensités mesurées pour différentes valeurs de phase de la voie de référence nous pouvons en déduire le champ complexe (module et phase) diffracté par l'échantillon. D'autres

[iii] Si l'incident et la position d'observation tournent tout autour de l'objet alors le domaine spectral accessible est de $[-2k_0; 2k_0]$ dans toutes les directions de l'espace.

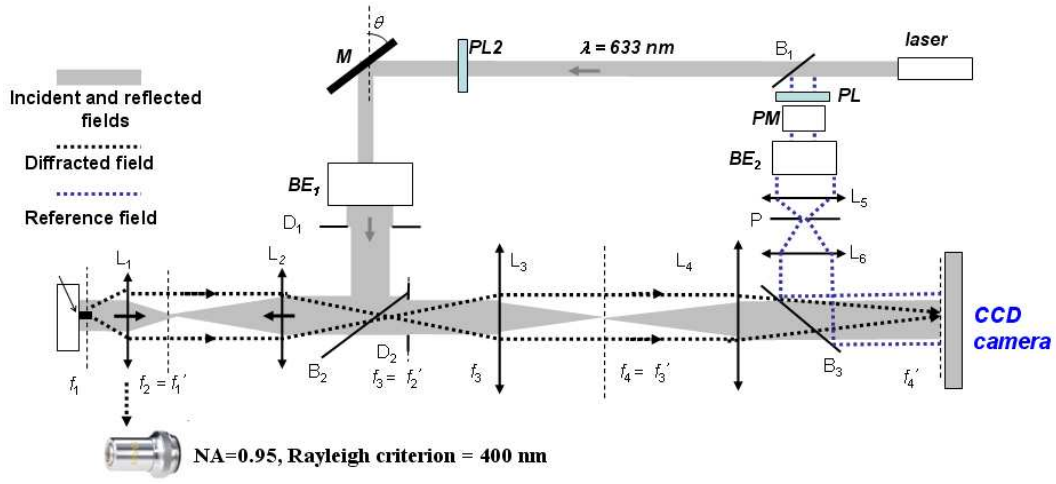

Figure 1 : *Schéma du montage utilisé. Le laser émet à 633 nm; M miroir ajustable; PL polariseur; L_1 lentille objectif du microscope; $L_{2,\cdots,6}$ lentilles; f_i, $f_i^{'}$ focales objet et image de la lentille L_i; B_1, B_2, B_3, séparateur de faisceaux; BE_1, BE_2 systèmes afocaux; TM, pinhole ; PM, modulateur de phase; D_1, D_2, diaphragmes.*

types de montages ont été réalisés durant cette thèse, comme l'holographie numérique hors-axe ou l'utilisation d'un analyseur de front d'onde. Une comparaison de ces trois méthodes a été réalisée au cours de cette thèse.

b) Les premiers résultats

Les premières mesures ont été réalisées en supposant que les objets étaient suffisamment gros (comparativement à la longueur d'onde) pour ne mesurer que la composante du vecteur champ diffracté parallèle à la direction du champ électrique incident. L'éclairement est réalisé dans deux plans d'incidence orthogonaux, (x, z) et (y, z), et cette configuration d'incidence sera valable pour tous les résultats expérimentaux présentés dans ce chapitre. Pour l'instant la direction de la polarisation du champ électrique incident est toujours la même, cela veut donc dire que pour un des plans d'incidence l'éclairement est en polarisation TE et que l'autre plan est en polarisation TM. Une fois le champ diffracté par l'échantillon mesuré, en utilisant un algorithme d'inversion itératif de type gradient conjugué nous pouvons donc retrouver la carte de permittivité relative tridimensionnelle de l'objet. [iv] Figures 2 et 3 présentent l'image des objets étudiés obtenues avec un microscope électronique. Les cylindres sont de diamètre D de hauteur h de permittivité relative $\varepsilon = 2$ déposés sur un substrat en silicium.

[iv] A noter quand dans l'algorithme d'inversion itératif nous rajouttons l'information *a priori* que le matériau cherché est non absorbant et que sa permittivité relative est plus grande que 1.

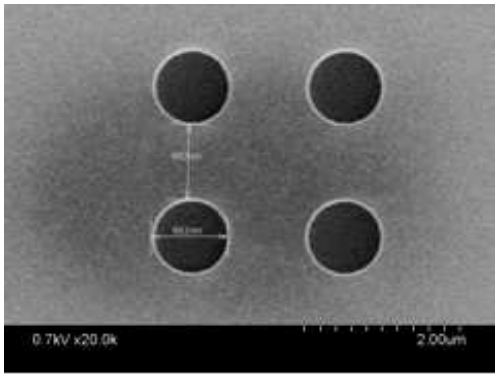

Figure 2 : *Vue de dessus de l'échantillon par un microscope électronique: les cylindres sont de diamètre D et séparés d'une distance D.*

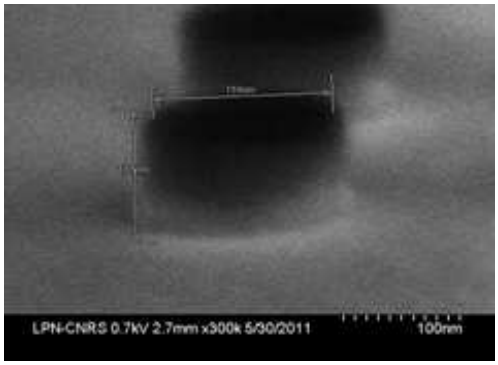

Figure 3 : *Profil de l'échantillon par un microscope électronique. Les cylindres sont de hauteur h.*

Figures 4(a) et 4(b) présentent la reconstruction obtenue itérativement d'après les champs mesurés pour les 4 plots cylindriques avec $D = 1$ μm et $h = 150$ nm. Nous pouvons noter une très bonne reconstruction obtenue quant à la hauteur et au diamètre des cylindres retrouvés mais aussi une bonne estimation quantitative pour la permittivité relative.

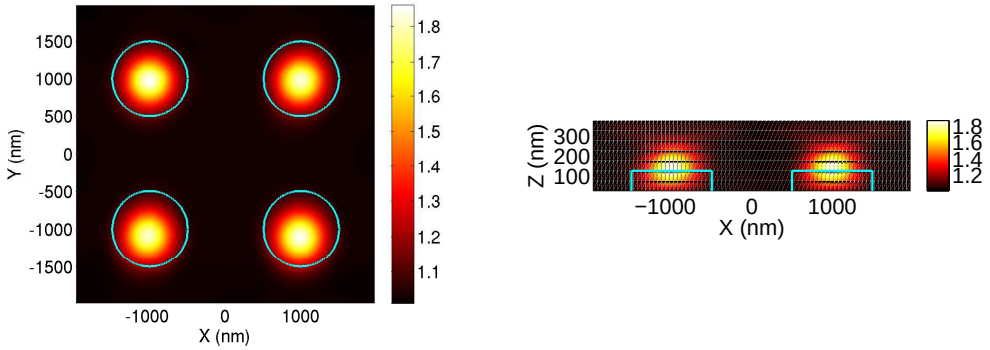

(a) (b)

Figure 4 : *Image de reconstruction obtenue avec la méthode itérative. Les plots ont les caractéristiques géométriques suivantes: $D = 1$ μm et $h = 150$ nm. (a) Carte dans le plan (x, y) pour $z = 125$ nm. (b) Carte dans le plan (x, z) pour $y = 1$ μm.*

A titre de comparaison, Figs. 5(a) et 5(b) présentent les résultats obtenus quand l'inversion utilisée est une simple transformée de Fourier inverse, voir Eq. (3). A noter que cette technique d'imagerie implique que l'échantillon est considéré comme suffisamment petit et peu contrasté pour que l'approximation de Born soit valide. Les images ainsi obtenues montrent une reconstruction bruité des 4 plots et ceci est particulièrement vrai suivant la direction z. Ceci est *a priori* dû à la présence du substrat réfléchissant interprété comme un objet miroir de l'objet initial. Les plots d'une hauteur de 150 nm apparaissent alors comme des objets de 1 μm de hauteur. A noter bien sûr que la carte obtenue par transformée de Fourier inverse ne peut pas nous donner une valeur quantitative de la valeur de la permittivité relative de l'objet.

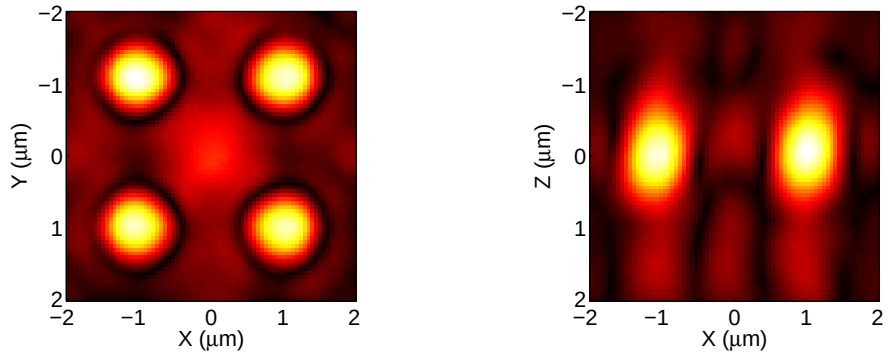

(a) (b)

Figure 5 : *Image de reconstruction obtenue avec la transformée de Fourier 3D inverse du champ diffracté mesuré. Les plots ont les caractéristiques géométriques suivantes: $D = 1$ μm et $h = 150$ nm. (a) Carte dans le plan (x, y) pour $z = 125$ nm. (b) Carte dans le plan (x, z) pour $y = 1$ μm.*

Figures 6(a) et 6(b) présentent la reconstruction obtenue d'après les champs mesurés pour les 4 plots cylindriques avec $D = 500$ nm et $h = 150$ nm. Nous pouvons encore noter une très bonne reconstruction obtenue quant à la hauteur et au diamètre des cylindres retrouvés et aussi une bonne estimation quantitative pour la permittivité relative.

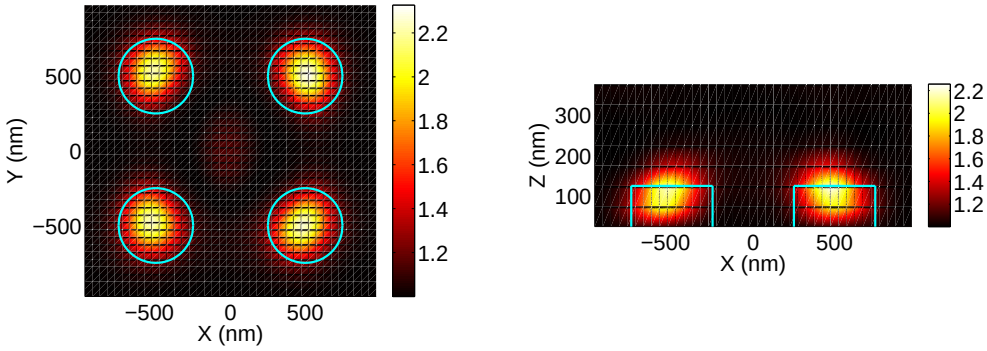

(a) (b)

Figure 6 : *Image de reconstruction obtenue avec la méthode itérative. Les plots ont les caractéristiques géométriques suivantes: $D = 1$ μm et $h = 150$ nm. (a) Carte dans le plan (x, y) pour $z = 125$ nm. (b) Carte dans le plan (x, z) pour $y = 500$ nm.*

Notons que pour les deux précédents cas étudiés les cylindres sont séparés centre à centre de 2 μm et 1 μm. Le critère de Rayleigh au vue de l'ouverture utilisée est d'environ 400 nm. Nous sommes donc pour l'instant largement au dessus de la résolution limite de notre instrument. A noter que la bonne reconstruction quantitative de la permittivité relative des objets n'a pu être obtenue que grâce à une procédure de normalisation rigoureuse (module et phase) au niveau des champs électromagnétiques mesurés. Cette procédure est bien sûr détaillée au sein de cette thèse.

c) Résolution sous le critère de Rayleigh

Dans le cas d'objets petits, *i.e.* des objets d'une taille inférieure à la longueur d'onde, nous avons décidé de mesurer toutes les composantes du vecteur champ électrique diffracté. Cette décision vient du fait que les hautes fréquences spatiales, déterminantes pour caractériser un objet de petite taille, seront sur les bords de l'ouverture numérique, cas où le vecteur champ électrique diffracté ne pourra plus être considéré comme parallèle au vecteur champ électrique incident. Cette mesure vectorielle du champ électrique a nécessité un changement au niveau du montage sur l'orientation des polariseurs un peu plus compliqué qu'il n'y paraît, plus une procédure de renormalisation fortement complexifiée. Ce nouveau montage permet d'accéder au champ diffracté vectoriel pour un éclairement incident en polarisation TE ou TM. A notre connaissance dans la littérature actuelle il n'existe pour l'instant pas de montage mesurant et utilisant dans les algorithmes d'inversion la nature vectorielle du champ électrique.

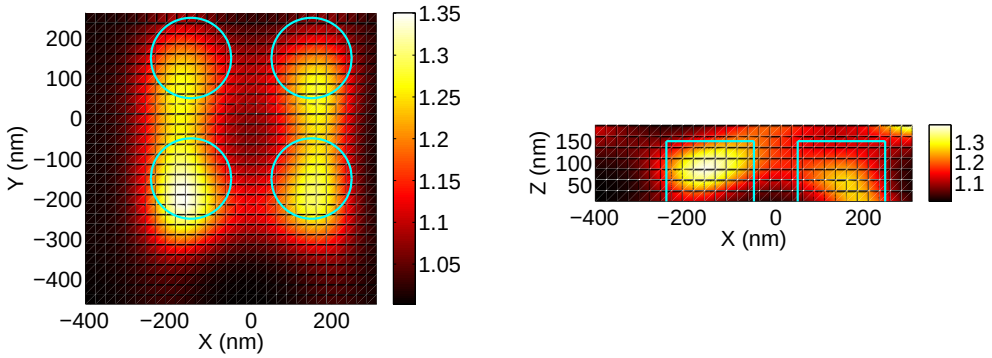

(a) (b)

Figure 7 : *Image de reconstruction obtenue avec la méthode itérative. Nous faisons l'hypothèse que le champ diffracté est parallèle au champ électrique incident et que le champ électrique incident est toujours suivant la même direction. Les plots ont les caractéristiques géométriques suivantes:* $D = 150$ *nm et* $h = 150$ *nm. (a) Carte dans le plan* (x, y) *pour* $z = 125$ *nm. (b) Carte dans le plan* (x, z)*.*

Pour étudier l'apport de la mesure vectorielle du champ diffracté nous commençons par présenter sur les Figs 7(a) et 7(b) les reconstructions obtenues quand les mesures sont effectuées comme précédemment, *i.e.* seul le champ diffracté parallèle à l'orientation du champ incident est mesuré, avec le champ incident toujours orienté selon la même direction quelque soit son angle d'incidence. Il est clair que la carte de permittivité relative reconstruite montre une anisotropie quant à la résolution obtenue car les plots ne sont pas séparés suivant la direction y. Ceci est dû au fait que le champ incident est toujours orienté suivant une seule direction. Quand la manipulation est dans une configuration purement scalaire il est clair que la résolution au dessous du critère de Rayleigh n'est pas atteinte.

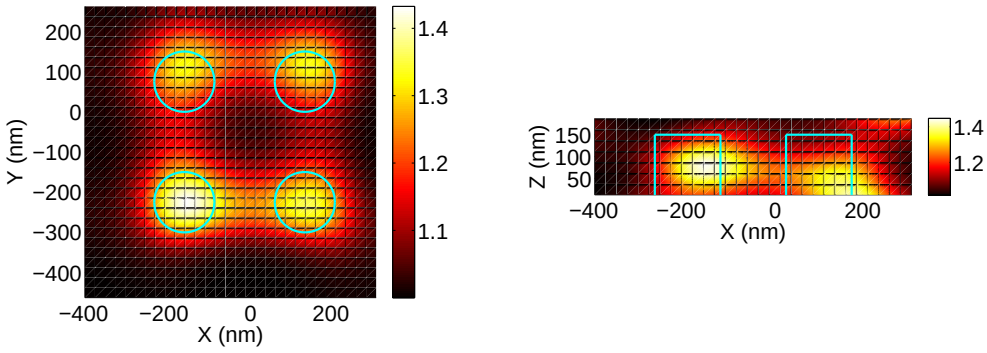

(a) (b)

Figure 8 : *Image de reconstruction obtenue avec la méthode itérative. Nous faisons l'hypothèse que le champ diffracté est parallèle au champ électrique incident par contre le champ électrique incident possède deux orientations orthogonales. Les plots ont les caractéristiques géométriques suivantes: $D = 150$ nm et $h = 150$ nm. (a) Carte dans le plan (x, y) pour $z = 125$ nm. (b) Carte dans le plan (x, z).*

Figures 8(a) et 8(b) montrent les reconstructions quand le vecteur champ électrique incident est orienté successivement suivant deux directions orthogonales avec toujours la mesure du champ diffracté parallèle à l'orientation du champ incident (le nombre de mesures dans ce cas est donc doublé). Dans cette configuration l'aspect vectoriel est introduit pour l'éclairement et le champ diffracté mesuré reste quant à lui suivant la direction utilisée pour cet éclairement. Dans ce cas les reconstructions obtenues sont isotropes et nous obtenons la séparation des 4 plots. Néanmoins la valeur de la permittivité relative reconstruite est très en dessous de sa valeur.

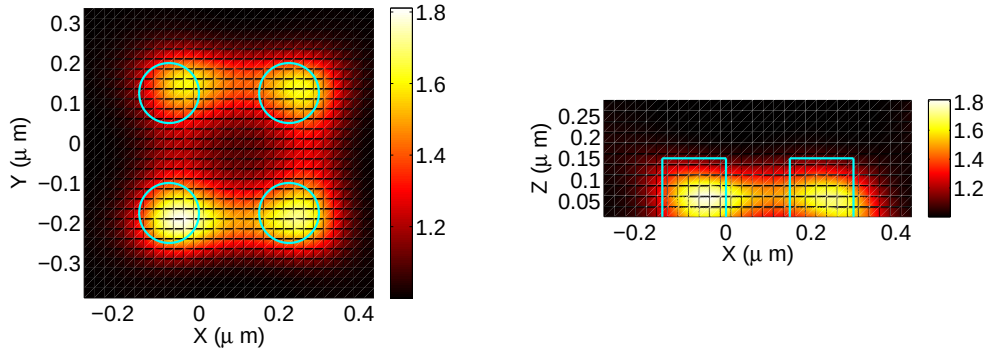

(a) (b)

Figure 9 : *Image de reconstruction obtenue avec la méthode itérative. Le champ électrique incident possède deux orientations orthogonales et le champ diffracté est mesuré vectoriellement. Les plots ont les caractéristiques géométriques suivantes: $D = 150$ nm et $h = 150$ nm. (a) Carte dans le plan (x, y) pour $z = 125$ nm. (b) Carte dans le plan (x, z).*

Figures 9(a) et 9(b) montrent les reconstructions quand le vecteur champ électrique incident est orienté successivement suivant deux directions orthogonales et que le champ diffracté est mesuré vectoriellement. Dans ce cas là nous observons une très bonne séparation des plots avec une

permittivité relative trouvée très proche de sa vraie valeur. L'apport d'un champ incident vectoriel (c'est à dire avec plusieurs orientations) et la mesure vectorielle du champ diffracté nous permet d'obtenir de la super résolution quantitative.

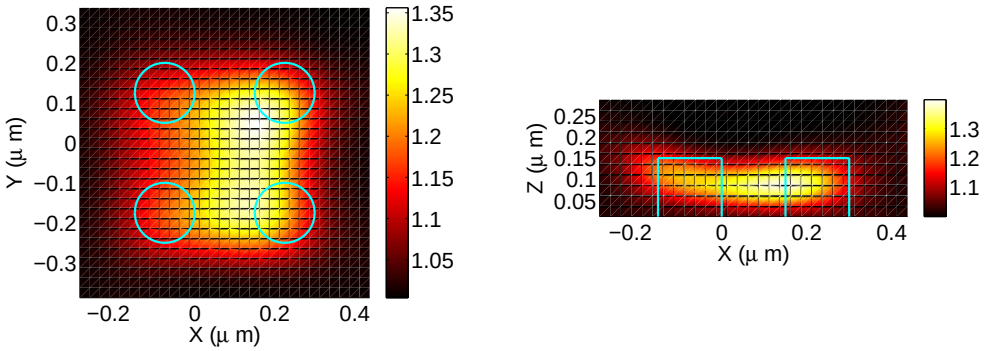

(a) (b)

Figure 10 : *Image de reconstruction obtenue avec la méthode itérative. Le champ électrique incident est en polarisation TE et le champ diffracté est mesuré vectoriellement. Les plots ont les caractéristiques géométriques suivantes: $D = 150$ nm et $h = 150$ nm. (a) Carte dans le plan (x, y) pour $z = 125$ nm. (b) Carte dans le plan (x, z).*

A noter que dans les cas précédents le champ incident comprend les deux polarisations TE et TM dans chacun des plans d'incidence (x, z) et (y, z). Figures 10(a) et 10(b) montrent les reconstructions obtenues quand seule l'illumination TE est utilisée avec une mesure du champ diffracté vectorielle. Il est clair que les reconstructions sont mauvaises car les 4 plots ne sont absolument pas retrouvés.

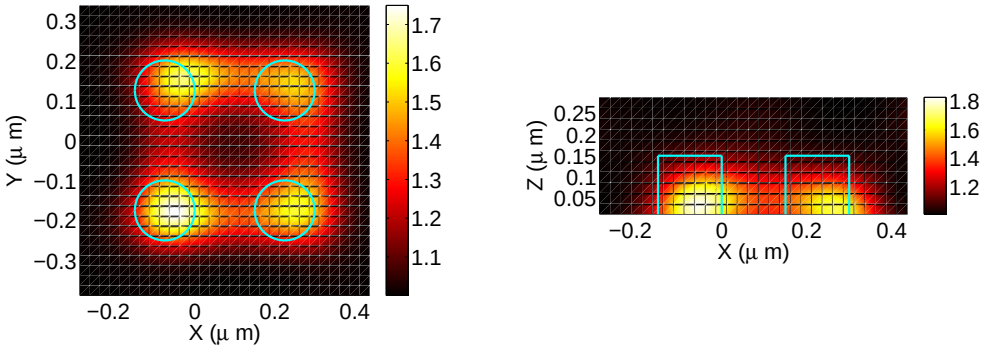

(a) (b)

Figure 11 : *Image de reconstruction obtenue avec la méthode itérative. Le champ électrique incident est en polarisation TM et le champ diffracté est mesuré vectoriellement. Les plots ont les caractéristiques géométriques suivantes: $D = 150$ nm et $h = 150$ nm. (a) Carte dans le plan (x, y) pour $z = 125$ nm. (b) Carte dans le plan (x, z).*

Les Figs 11(a) et 11(b) quant à elles présentent les reconstructions obtenues quand l'illumination est faite en polarisation TM. Il est clair que dans ce cas présent les 4 plots sont bien retrouvés et que le résultat est proche de la configuration complète même si le résultat est un chouïa moins bon.

Des différentes reconstructions données pour les 4 plots de diamètre D =150 nm et h =150 nm, nous pouvons déduire que si la résolution est bonne dans une direction donnée dans le cas scalaire c'est parce que une des direction est éclairée en TE et la direction orthogonale en TM. Une des pistes pour expliquer pourquoi la polarisation incidente polarisée TM est meilleure est que le substrat est très réfléchissant et donc pour les grands angles, ceux qui nous apportent la résolution, le champ juste au dessus du substrat est très faible en polarisation TE (donc images de champ diffracté plus bruitées et poids des angles grands affaibli par rapport aux faibles incidences) et fort en polarisation TM.

On peut se poser la question pourquoi la configuration complète donne une reconstruction un peu meilleure que la configuration en polarisation TM uniquement. *A priori*, même si les champs diffractés en polarisation TE sont très bruités aux grands angles d'incidence, la redondance d'information pour les faibles angles d'incidence apportée par la polarisation TE aide à stabiliser l'inversion itérative.

General introduction

This PhD thesis was carried out in the SEMO team (Sondage ElectroMagnétique et Optique) of the Institut Fresnel, and mainly concerns experimental work with a quite recent optical imaging technique : tomographic diffractive microscopy (TDM). It consists in illuminating the sample with coherent collimated light under different successive incidence angles, and detecting both in amplitude and phase its scattered field imaged through a microscope set-up. As a result, the three-dimensional permittivity map of the probed sample can be reconstructed with an increased resolution compared to conventional wide-field microscopy. TDM has until now been applied successfully to three-dimensional samples only in the case of weak refractive index contrasts (usually below 5.10^{-2}) where linear approximations to calculate the scattered field are valid. As a result, an important field of applications is still out of reach of this new imaging tool. To go beyond these limitations, we present in this manuscript the results obtained by coupling a TDM set-up to a sophisticated inversion algorithm based on a rigorous modelling of the wave-sample interaction.

The first chapter of this manuscript firstly describes what is the place of TDM compared to other microscopy modalities. It then details its principles in the case of linear approximations to calculate the scattered field, and presents the main results obtained so far in this framework.

The second chapter firstly describes the TDM set-up developed during this PhD, and more especially the three modalities that have used to perform amplitude and phase measurements : phase-shifting interferometry, off-axis holography and wavefront sensing by quadri-wave lateral shearing interferometry. Then, the principles of the rigorous non-linear inversion algorithm developed in the SEMO team to tackle the 3D case are presented.

The third chapter at first presents the data treatment procedure that has to be applied to the measurements so that they become compatible with the modelling hypotheses underlying the non-linear inversion algorithm. The 3D reconstructions obtained with this approach are then presented in the case of small resin objects deposited on a silicon substrate, with diameters ranging from 1 μm to 150 nm.

The fourth chapter presents an improved configuration of the set-up where both the polarization of the illuminating beam and that of the detected field are modified. The aim is to retrieve the full vectorial field scattered by the object, and not just a projection, for any polarization state of the illumination. It is shown that such an approach permits to improve the resolution of the reconstructions, what is illustrated for a case clearly beyond the Rayleigh limit.

Chapter 1

Principles of tomographic diffractive microscopy (TDM)

Contents

1.1 Introduction 3

1.2 Principles of conventional wide-field optical microscopy 4

1.3 Principles of TDM under the Born approximation . . . 6

1.3.1 Modelling of tomographic diffractive microscopy 6

1.3.2 Synthetic aperture 10

1.3.3 Linear inversion with an inverse Fourier transform 14

1.4 State-of-the-art results obtained by TDM under linear approximations 18

1.1 Introduction

The optical microscope and its associated technology have became more and more popular, due to the development of lasers and data acquisition technology. Indeed, although more sophisticated imaging tools, such as scanning tunneling microscopes [1–3], scanning near field optical microscopes [4–7], atomic force microscopes [8–11] or electronic microscopes exist, optical microscopes are still essential for many applications because of their readiness of utilization and their non-invasive properties. Because of their advanced modalities allowing to image specimens in three dimensions, they can be widely used as an invaluable tool for biology and nanotechnology or others industrial fields. Improving the resolution of optical microscopes has therefore been an important and urgent field of research recently.

In this aspect, a lot of a work has been performed to conceive and realize microscope objectives with high numerical apertures. However, the room for improvement is now very small and limited by the accessible refractive indices of media that are compatible with immersion objectives. In fluorescence microscopy, non linear interactions between the illumination and the sample are used to reach nanometric resolutions (for instance in PALM, STORM and STED microscopies) [12–17]. But these spectacular improvements are only possible if the sample can be tagged with specific fluorescent molecules, that is mainly for biological applications.

When photobleaching and phototoxicity play a limiting role in biology, or when other application fields are considered, such as the characterization of components in nanotechnology, a

label-free microscopy technique is preferable. In its conventional form, the optical microscope provides images where the contrast is due to the scattering of light by the permittivity distribution of the sample. However, this conventional wide-field microscopy does not permit to retrieve quantitatively the permittivity from the measured intensity images. Indeed, reconstructing a 3D permittivity distribution from measurements of scattered fields, *i.e.* solving the inverse scattering problem, requires that both the amplitude and phase of the field are known [18]. The scattered fields are uniquely related to the structure of the object, but a given intensity may be produced by many fields.

With the development of digital holographic microscopy [19,20], the phase measurement in optics became more and more reliable, and quite recently a technique called optical diffraction tomography, or tomographic diffractive microscopy (TDM), emerged to provide such 3D quantitative reconstructions of the object [21]. TDM generally consists in illuminating the sample from many different directions with coherent collimated light and collecting the complex diffracted field under many scattered angles [22]. TDM relies entirely on a numerical inversion procedure for reconstructing the map of permittivity of the sample from the scattered field. This technique can be useful to characterize a biological samples [23–25], the aberrations introduced by the optical index variations [23], or the different elements of a microelectronic components, etc. Although some reconstruction algorithms using intensity data only have been proposed [26], most inversion procedures require amplitude and phase measurements. Thus, different interferometric set-ups, such as phase-shifting holography, have been developed for measuring the phase and amplitude together. The hologram is obtained by the interference of a reference field with the field scattered by the observed object.

On the other hand, most inversion procedures used in TDM are based on a linear link between the diffracted field and the parameter of interest of the object, usually by assuming that the Born approximation is valid, *i.e.* the field inside the object under study is the incident field. Such a linear inversion permits to combine the information obtained with several successive illumination angles through a process known as synthetic aperture generation [22,27,43,53]. This ameliorates the resolution compared to conventional wide-field microscopy and enables a 3D reconstruction of the object. Although many experimental configurations have been proposed to implement this idea [21,28–30], such an approximation limits the field of application of TDM to a weak-scattering case, where the object permittivity contrast with the surrounding medium (air, water, oil ...) is low. For samples with high permittivity contrasts, the Born approximation is no longer valid, and it is necessary to consider a rigorous modelling of the scattering process. To deal with this general case, an original non-linear inversion algorithm has been developed at the Institut Fresnel [31–34].

In this first chapter, the principles of the conventional wide-field microscopy are firstly briefly presented, and also the resolution limits of this technique. Then, the TDM linear approach under the Born approximation is developed : the link between the object permittivity and the scattered field is detailed, as well as the synthetic aperture generation and the corresponding linear inversion procedure. At last, an overview of the main results obtained so far with this approach is presented.

1.2 Principles of conventional wide-field optical microscopy

The most commonly encountered optical microscopes are wide-field microscopes, where the illumination system is equivalent to illuminating the object simultaneously by a sum of plane waves spatially incoherent with each other. Each plane wave propagates with a different illumination angle, so that the object is globally illuminated simultaneously with all possible angles within a given numerical aperture noted $\mathrm{NA}_{\mathrm{inc}}$. More precisely, $\mathrm{NA}_{\mathrm{inc}}$ is the sine of the maximum illumination angle with respect to the optical axis of the microscope. Usually in wide-field microscopy the illumination is also temporally incoherent by using white light produced by conventional halogen bulbs.

For the detection, the presently most commonly used architecture consists in placing the object in the vicinity (usually just before) of the object focal plane of an objective lens, called hereafter

objective. A second lens, the tube lens, then forms a magnified real image in its image focal plane. This is an image of the field in the object focal plane of the objective, that is detected in intensity on a detector like a CCD camera, or transmitted through an ocular lens for direct vision by the user. The system diagram of WFM is shown in the Fig. 1.1,

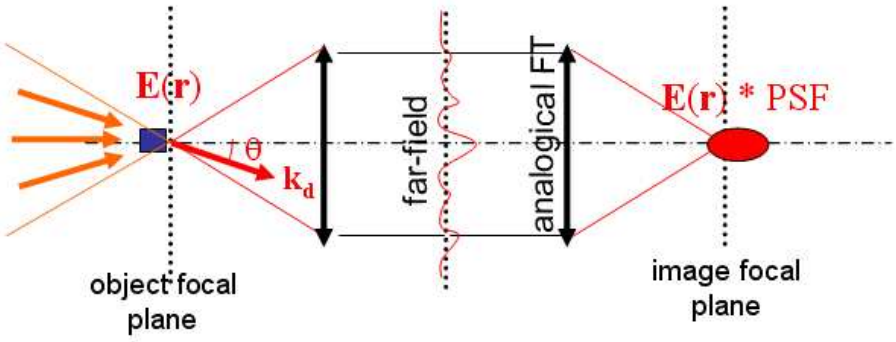

Figure 1.1 : *The schematic diagram of wide-field microscopy*

The intensity image provided by such a microscope cannot easily be related quantitatively to a physical parameter of the object like the permittivity, it gives merely an image of the intensity variations of the field after propagation through the object. The transverse resolution Δr within an image is generally defined by the Rayleigh criterion, which states that the smallest separation distance between two point sources that can be resolved is given by [35,36]:

$$\Delta r = 0.61 \frac{\lambda}{\mathrm{NA}}, \tag{1.1}$$

where λ is the illumination wavelength or the average one when a large spectrum is used, and NA is the numerical aperture of the objective, that is the sine of the maximum angle that can propagate through the microscope. This criterion originates from the truncation of the spatial frequencies of the field due to the numerical aperture : only the spatial frequencies below $\frac{2\pi}{\lambda}\mathrm{NA}$ are transmitted through the microscope. As a result, the intensity image of an ideal point source is an Airy disk consisting of a central bright spot surrounded by a succession of dark and more and more attenuated bright rings. The radial intensity profile of the Airy disk is proportional to $\left(\frac{J_1(r)}{r}\right)^2$, where J_1 is the first order Bessel function and r is the radial position. The central spot of the Airy disk contains 84 percents of the intensity. The Rayleigh criterion is obtained when the two point sources are separated by a distance equal to the radial position of the first zero of the Airy disk. When the point sources are closer to each other, it is considered that the sum of the two Airy disks does not allow to resolve their two maxima. Figure 1.2(a) illustrates a hypothetical Airy disk containing a central maximum (typically termed a zeroth order maximum) surrounded by concentric 1st, 2nd, 3rd, etc., order maxima of sequentially decreasing brightness that make up the intensity distribution. Figure 1.2(b) shows two Airy disks and their intensity distributions in a situation where the center-to-center distance between the zeroth order maxima is equal to the Rayleigh criterion. Notice that there is several closely related values for the diffraction limit, the Abbe, Rayleigh, Sparrow, ... criterion. The difference between them is based on the definition that the different authors used in their derivation for what is meant by two objects being resolvable from each other. In practical applications, this difference is small.

The axial resolution, *i.e.* along the optical axis, of wide-field microscopy can be defined in a similar manner. Taking a point source in the object focal plane of the objective, it produces in the image plane an Airy disk with a maximal intensity value in its center. If the point source is moved away little by little along the optical axis, the intensity value at this pixel will more and

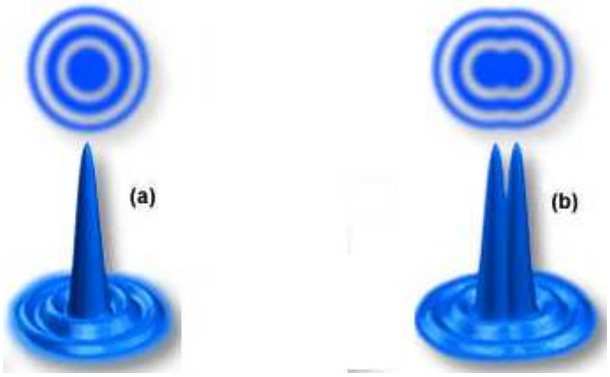

Figure 1.2 : *Intensity distributions of Airy disks. (a) is a hypothetical Airy disk, (b) shows two Airy disks and their intensity distributions.*

more decrease, until reaching zero when the point source has been displaced by a distance Δz that is considered as the axial resolution of the microscope. This distance is commonly given by [40] :

$$\Delta z = \frac{\lambda}{1 - \sqrt{1 - \mathrm{NA}^2}}. \tag{1.2}$$

It means in practice that if the object of interest is placed at a position within the range $\pm\Delta z/2$ with respect to the object focal plane of the objective, its image will be in focus on the detector. Beyond this range, the defocus will produce an image with strong blurring. That is why Δz can also be considered as the depth of field of the microscope.

1.3 Principles of tomographic diffractive microscopy under the Born approximation

1.3.1 Modelling of tomographic diffractive microscopy

1.3.1.1 Position of the problem

Tomographic diffractive microscopy (TDM) generally consists in illuminating the sample with coherent collimated light under different successive incidence angles, and detecting the amplitude and phase of the scattered field through a microscope with an interferometer set-up. The principle diagram of tomographic diffractive microscopy is shown in Fig. 1.3, and the system diagram of TDM is shown in the Fig. 1.4.

The TDM schematic diagram is very close to that the WFM in Figure.1.1, the main differences are :

1. The measurement data are the amplitude and phase (not only the intensity like in WFM)
2. The illumination of the sample by different plane waves is successive (not simultaneous like in WFM)

From this recorded scattered field for each illumination it is possible to reconstruct the unknown object. Hence the knowledge of the interaction between an object and an illumination is the cornerstone of tomographic diffractive microscopy.

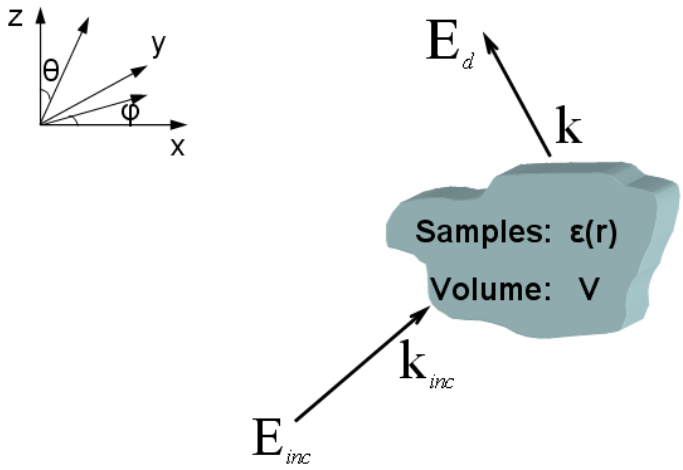

Figure 1.3 : *The principle diagram of tomographic diffractive microscopy.* $\boldsymbol{E}_{inc}$ *denotes the incident field in the direction* $\boldsymbol{k}_{inc}$, $\boldsymbol{E}_d$ *denotes the incident field in the direction* $\boldsymbol{k}_d$, x, y, z *is the orientation of the spatial coordinates.*

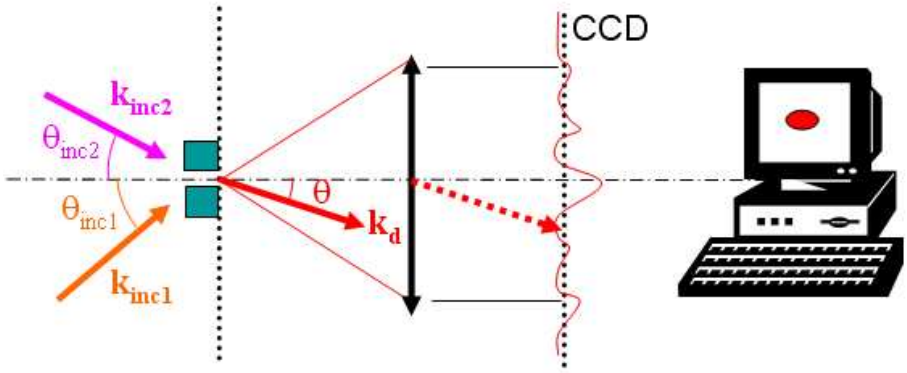

Figure 1.4 : *The schematic diagram of tomographic diffractive microscopy*

1.3.1.2 Electromagnetic scattering by an object of volume V and relative permittivity $\varepsilon(\boldsymbol{r})$

In this section we study the electromagnetic scattering problem. An incident electromagnetic wave $[\boldsymbol{E}_{\text{inc}}(\boldsymbol{r}),\boldsymbol{H}_{\text{inc}}(\boldsymbol{r})]$ interacts with an object that occupies a bounded region V in three dimensional space and a relative permittivity $\varepsilon(\boldsymbol{r})$ for $\boldsymbol{r} \in V$, hence $\varepsilon(\boldsymbol{r}) = 1$ for $\boldsymbol{r} \notin V$. Notice that both the shape and the permittivity are arbitrary.

In the particular case of the harmonic regime and without the temporal term (*i.e.* $e^{-i\omega t}$), the total electromagnetic field ($\boldsymbol{E}$,$\boldsymbol{H}$) at position $\boldsymbol{r}$ is given by the Maxwell equations as follows [i]:

$$\nabla \times \boldsymbol{H}(\boldsymbol{r}) = -i\omega \boldsymbol{D}(\boldsymbol{r}) + \boldsymbol{J}(\boldsymbol{r}) \tag{1.3}$$
$$\nabla \times \boldsymbol{E}(\boldsymbol{r}) = i\omega \boldsymbol{B}(\boldsymbol{r}) \tag{1.4}$$
$$\nabla \cdot \boldsymbol{D}(\boldsymbol{r}) = \boldsymbol{\rho}(\boldsymbol{r}) \tag{1.5}$$
$$\nabla \cdot \boldsymbol{B}(\boldsymbol{r}) = 0, \tag{1.6}$$

ω is the pulsation of the electromagnetic field, $\boldsymbol{J}(\boldsymbol{r})$ the electric current density and $\rho(\boldsymbol{r})$ the density of charge. We assume that the object is illuminated by a plane wave, such that the source $\boldsymbol{J}(\boldsymbol{r})$ is rejected at an infinite distance and therefore $\boldsymbol{J}(\boldsymbol{r})$ will be considered as equal to zero in the following calculations. Assuming that there is no free charge in space, that the particle is non-ferromagnetic, *i.e.* $\mu = 1$, and that we study isotropic linear materials we can write the constitutive relationship between the auxiliary fields $\boldsymbol{D}$ and $\boldsymbol{H}$ and $\boldsymbol{E}$ and $\boldsymbol{B}$ as :

$$\boldsymbol{H}(\boldsymbol{r}) = \boldsymbol{B}(\boldsymbol{r})/\mu_0 \tag{1.7}$$
$$\boldsymbol{D}(\boldsymbol{r}) = \varepsilon_0 \varepsilon(\boldsymbol{r}) \boldsymbol{E}(\boldsymbol{r}), \tag{1.8}$$

where ε_0 and μ_0 denote the permittivity and permeability of the vacuum, respectively. Then we can write the Maxwell's equation as:

$$\nabla \times \boldsymbol{H}(\boldsymbol{r}) = -i\omega\varepsilon_0 \varepsilon(\boldsymbol{r}) \boldsymbol{E}(\boldsymbol{r}) \tag{1.9}$$
$$\nabla \times \boldsymbol{E}(\boldsymbol{r}) = i\omega\mu_0 \boldsymbol{H}(\boldsymbol{r}) \tag{1.10}$$
$$\nabla \cdot \boldsymbol{D}(\boldsymbol{r}) = 0 \tag{1.11}$$
$$\nabla \cdot \boldsymbol{B}(\boldsymbol{r}) = 0. \tag{1.12}$$

By combining Eqs. (1.9) and (1.10) one obtains the following equation :

$$\boldsymbol{\nabla} \times \boldsymbol{\nabla} \times \boldsymbol{E}(\boldsymbol{r}) - \varepsilon(\boldsymbol{r}) k_0^2 \boldsymbol{E}(\boldsymbol{r}) = 0, \tag{1.13}$$

where $k_0 = \frac{\omega}{c} = \frac{2\pi}{\lambda}$ is the wave number, with λ the wavelength in vacuum. Thus we can transform Eq. (1.13) as:

$$\boldsymbol{\nabla} \times \boldsymbol{\nabla} \times \boldsymbol{E}(\boldsymbol{r}) - k_0^2 \boldsymbol{E}(\boldsymbol{r}) = k_0^2 [\varepsilon(\boldsymbol{r}) - 1] \boldsymbol{E}(\boldsymbol{r}). \tag{1.14}$$

Thus we get now an inhomogeneous differential equation with constant coefficients, which is easy to solve. Notice that the right side of this equation represents the electric linear polarization:

$$\boldsymbol{P}(\boldsymbol{r}) = 0 \quad \text{if} \quad \boldsymbol{r} \notin V \tag{1.15}$$
$$\boldsymbol{P} = \varepsilon_0 [\varepsilon(\boldsymbol{r}) - 1] \boldsymbol{E}(\boldsymbol{r}) = \varepsilon_0 \Delta\varepsilon(\boldsymbol{r}) \boldsymbol{E}(\boldsymbol{r}) \quad \text{if} \quad \boldsymbol{r} \in V, \tag{1.16}$$

A standard solution technique to solve Eq. (1.14) is to find the Green's function, *i.e.* the solution to the corresponding differential equation with a Dirac-delta-inhomogeneity:

$$\boldsymbol{\nabla} \times \boldsymbol{\nabla} \times \boldsymbol{G}(\boldsymbol{r}, \boldsymbol{r}') - k_0^2 \boldsymbol{G}(\boldsymbol{r}, \boldsymbol{r}') = \boldsymbol{I} \delta(\boldsymbol{r} - \boldsymbol{r}'), \tag{1.17}$$

where $\boldsymbol{I}$ is the identity matrix. The solution of Eq. (1.17) is known analytically and is given by (see Appendix A):

$$\boldsymbol{G}(\boldsymbol{r}, \boldsymbol{r}') = \left[\boldsymbol{I} + \frac{1}{k_0^2} \boldsymbol{\nabla}\boldsymbol{\nabla} \right] \frac{e^{ik_0 |\boldsymbol{r} - \boldsymbol{r}'|}}{4\pi |\boldsymbol{r} - \boldsymbol{r}'|}. \tag{1.18}$$

[i] $\nabla\cdot$ is the divergence operator and $\nabla\times$ the curl operator.

This Green's function is known as the free-space dyadic Green's function. With the free-space dyadic Green's function, the solution to Eq. (1.14) can be written as:

$$\boldsymbol{E}(\boldsymbol{r}) = \boldsymbol{E}_{\text{ref}}(\boldsymbol{r}) + k_0^2 \int_V \boldsymbol{G}(\boldsymbol{r}, \boldsymbol{r}')[\varepsilon(\boldsymbol{r}') - 1]\boldsymbol{E}(\boldsymbol{r}')\mathrm{d}V, \tag{1.19}$$

where the reference field $\boldsymbol{E}_{\text{ref}}$ is a special solution to the homogeneous equation obtained by setting $\varepsilon(\boldsymbol{r})$ to the homogeneous background *i.e.* $\varepsilon(\boldsymbol{r}) = 1$, it consists of the field in the absence of the object under study. Then we define the scattered field as the difference between the total field and the reference field:

$$\boldsymbol{E}_{\text{s}}(\boldsymbol{r}) = \boldsymbol{E}(\boldsymbol{r}) - \boldsymbol{E}_{\text{ref}}(\boldsymbol{r}) = k_0^2 \int_V \boldsymbol{G}(\boldsymbol{r}, \boldsymbol{r}')\Delta\varepsilon(\boldsymbol{r}')\boldsymbol{E}(\boldsymbol{r}')\mathrm{d}V. \tag{1.20}$$

Then one can notice that the integration defined in Eq. (1.20) is only performed over the volume V occupied by the object, where $\Delta\varepsilon$ is non zero. This equation means that once the total field $\boldsymbol{E}$ is known inside V, $\boldsymbol{E}_{\text{s}}(\boldsymbol{r})$ can be calculated at any location $\boldsymbol{r}$. All the computations presented is the paragraph are done without approximation. Equation (1.19) is a self consistent equation which can be solved numerically. This resolution can take a lot of time, and one can use some approximations, such as the Born approximation, to solve it quickly.

1.3.1.3 TDM in the case of the Born approximation

The conventional tomographic diffractive microscopy approach neglects the polarization effects induced by the object and the set-up, so that a scalar approximation is used for the field and Eq. (1.20) can be rewritten as a scalar propagation equation in an inhomogeneous medium :

$$E_{\text{s}}(\boldsymbol{r}) = k_0^2 \int_V G(\boldsymbol{r}, \boldsymbol{r}')\Delta\varepsilon(\boldsymbol{r}')E(\boldsymbol{r}')\mathrm{d}V. \tag{1.21}$$

The Born approximation is the most commonly encountered to calculate $E_{\text{s}}(\boldsymbol{r})$ in the frame of tomographic diffractive microscopy. It consists in stating that if the object is weakly scattering enough, the amplitude of the scattered field is very small compared to that of the reference field, so that E can be replaced by E_{ref}. This approximation is usually verified for object with small permittivity contrasts, typically below 0.1.

Thanks to it, the expression of $E_{\text{s}}(\boldsymbol{r})$ can be expressed in a very interesting way in the far field, that is for a position $\boldsymbol{r}$ sufficiently far away from the object. The scalar Green function can be approximated in far field in the direction given by the wave vector $\boldsymbol{k}$ as (see Appendix B):

$$G(\boldsymbol{r}, \boldsymbol{r}') = \frac{e^{ik_0 r}}{4\pi r} e^{-i\boldsymbol{k}\cdot\boldsymbol{r}'}, \tag{1.22}$$

where $\boldsymbol{k} = k_0 \frac{\boldsymbol{r}}{r}$ and $r = |\boldsymbol{r}|$. Taking for E_{ref} a plane wave with incident wave vector $\boldsymbol{k}_{\text{inc}}$, Eq. (1.21) then reads :

$$E_{\text{s}}(\boldsymbol{r}) = k_0^2 \frac{e^{ik_0 r}}{4\pi r} \int_V \Delta\varepsilon(\boldsymbol{r}')e^{-i(\boldsymbol{k}-\boldsymbol{k}_{\text{inc}})\cdot\boldsymbol{r}'}\mathrm{d}V. \tag{1.23}$$

It means that in far field and under the Born approximation, the field E_{s} scattered along the wave vector $\boldsymbol{k}$ for an illuminating wave vector $\boldsymbol{k}_{\text{inc}}$ is directly proportional to the 3D Fourier transform of $\Delta\varepsilon$ taken at $\boldsymbol{k} - \boldsymbol{k}_{\text{inc}}$:

$$E_{\text{s}}(\boldsymbol{k}, \boldsymbol{k}_{\text{inc}}) \propto \Delta\tilde{\varepsilon}(\boldsymbol{k} - \boldsymbol{k}_{\text{inc}}). \tag{1.24}$$

Therefore, the relative permittivity map of the object can be retrieved via a simple inverse Fourier transform of the scattered field detected in far field. The resolution of TDM under the Born approximation is then given by the accessible Fourier domain that depends on the configuration of illumination and detection.

1.3.2 Synthetic aperture

For a given angle of illumination with wave vector $\boldsymbol{k}_{\text{inc}}$, according to Eq. (1.24), TDM permits to detect the Fourier components of the object permittivity contrast on a cap of sphere of radius k_0, truncated by the numerical aperture (NA) of the objective used to collect the scattered field, and centered on the extremity of wave vector $-\boldsymbol{k}_{\text{inc}}$. This cap of sphere is represented on Fig. 1.5 for the case of NA = 1. To increase the amount of Fourier components that can be detected, and therefore ameliorate the resolution of the object reconstruction, various angles of illumination are used successively on the sample. Each of them provides different Fourier components, and the merging of all the components is a process known as synthetic aperture generation. Indeed, a synthetic aperture is built through the measurement, and permits to access spatial frequencies of the object that are beyond those confined in sole the detection NA. This synthetic aperture is described in the three-dimensional Fourier space by an Optical Transfer Function (OTF) that is equal to one for a Fourier component that can be detected, and zero elsewhere. The permittivity contrast of the object that is reconstructed through an inverse Fourier transform (FT^{-1}) of the detected field can thus be written as :

$$\Delta\varepsilon(\boldsymbol{r})_{\text{rec}} = \int_{-\infty}^{+\infty} (\Delta\tilde{\varepsilon}(\boldsymbol{K}) \times \text{OTF}) \text{e}^{\text{i}\boldsymbol{K}\cdot\boldsymbol{r}} \text{d}^3\boldsymbol{K} \tag{1.25}$$

$$= \Delta\varepsilon(\boldsymbol{r}) * \text{FT}^{-1}(\text{OTF}) = \Delta\varepsilon(\boldsymbol{r}) * \text{PSF}, \tag{1.26}$$

where * denotes the convolution product. The projections of $\boldsymbol{K}$ give the three-dimensional spatial frequencies of the object, and PSF is the point spread function which describes the response of the imaging system to a point source. The PSF is given by the inverse Fourier transform of the OTF. The reconstructed permittivity contrast of the object is therefore the actual one convoluted with the PSF. Depending on the configuration for illumination and detection, TDM has access

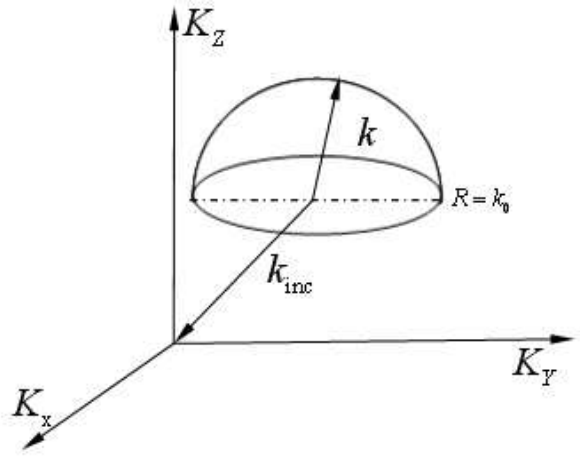

Figure 1.5 : *Accessible 3D Fourier domain for one incidence*

to different Fourier components of the object, what modifies the OTF and the PSF. Hereafter are presented the main configurations that can be used and the associated OTF and PSF. Note that, for the sake of simplicity, an ideal numerical aperture equal to one is considered both for the illumination and the detection.

1.3.2.1 One normal incidence working in transmission: $k_{\text{inc;z}} = k_0$ and $k_z > 0$

Here the object is only illuminated by one incidence at normal incidence, and the scattered field is detected in transmission with NA = 1. In this case, the OTF is equal to one at the surface of the

half sphere with radius k_0 represented on Figure 1.6. The corresponding PSF has been calculated

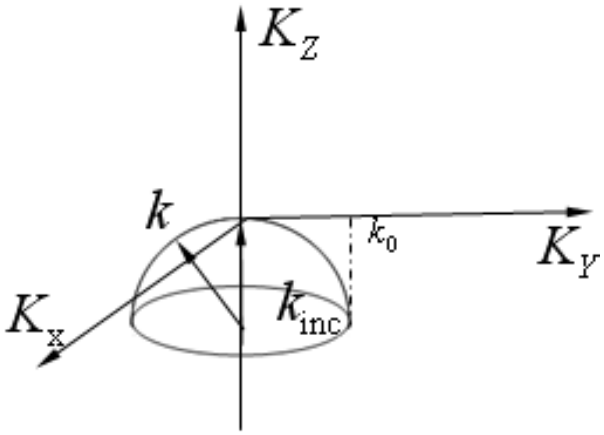

Figure 1.6 : *Optical transfer function (OTF) for one normal incidence in transmission*

and is presented on Figs. 1.7 and 1.8. Note that within this manuscript, the spatial coordinate z is the one along the optical axis of the microscope, and x and y are the transverse coordinates perpendicular to this axis. The PSF is shown inside a cubic domain centered on the spatial origin and with a side equal to twice the wavelength of illumination : a transverse cut on Fig. 1.7 and a longitudinal one on Fig. 1.8. Only the real part of the PSF is shown here.

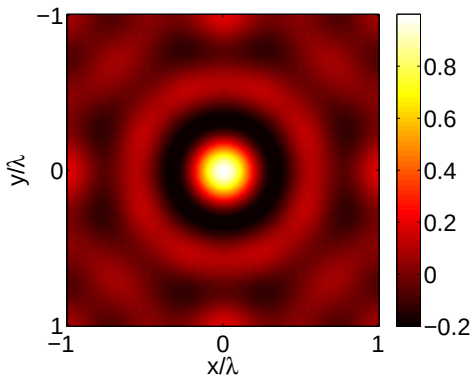

Figure 1.7 : *Transverse cut at $z = 0$ of the PSF for one normal incidence in transmission and scattered field detected in transmission with $NA = 1$.*

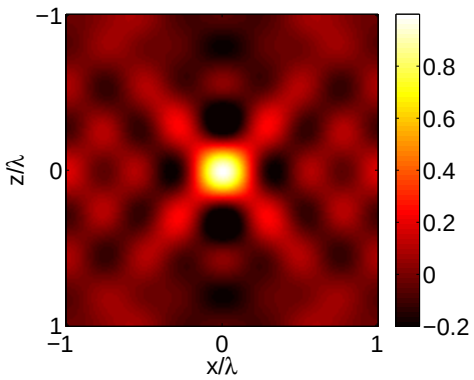

Figure 1.8 : *Longitudinal cut at $y = 0$ of the PSF for one normal incidence in transmission and scattered field detected in transmission with $NA = 1$.*

With such a configuration, it can be seen that the resolution of the reconstruction will be mostly deteriorated along the z axis, because of the strong negative rebounds present on the PSF along this axis.

1.3.2.2 The complete configuration

To obtain the biggest amount of Fourier components, the ideal case would consist in illuminating the object along all possible directions within 4π steradians, and performing the detection also for all these directions. Therefore for a given illumination direction, the accessible Fourier components lie on the surface of a sphere with radius k_0 (the smaller dotted sphere) in Figure 1.9. Then, varying the illumination angle permits to fill the volume of a sphere with radius $2k_0$, the larger solid sphere in Fig. 1.9.

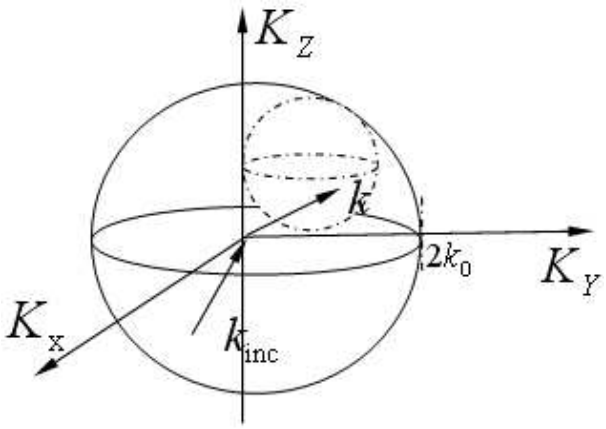

Figure 1.9 : *OTF for the complete configuration*

With this complete configuration, all the spatial frequencies given by $\boldsymbol{k} - \boldsymbol{k}_{\text{inc}}$ for any wave vectors $\boldsymbol{k}$ and $\boldsymbol{k}_{\text{inc}}$ are accessible. The corresponding PSF is presented with a transverse cut and a longitudinal one on Figures 1.10 and 1.11, respectively.

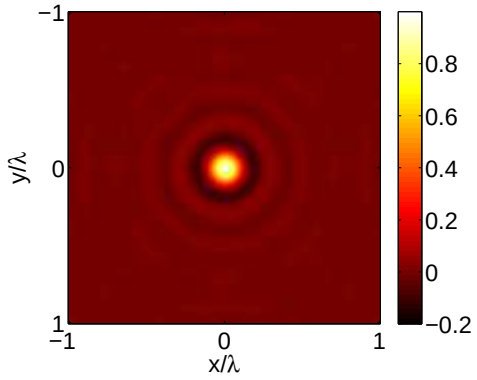

Figure 1.10 : *Transverse cut of the complete configuration PSF at $z = 0$*

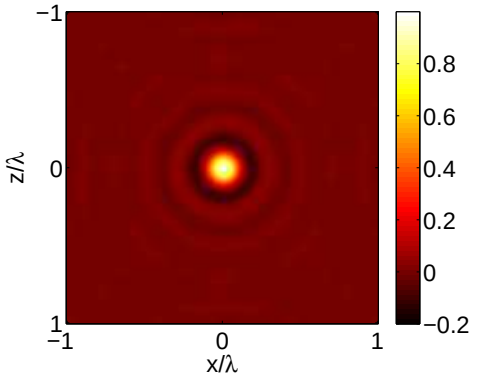

Figure 1.11 : *Longitudinal cut of the complete configuration PSF at $y = 0$*

Both cuts are identical, and such a PSF therefore permits to obtain an isotropic resolution. It can be evaluated by the position of the first zero of the PSF along any radial direction, and is close to 0.35λ. Such a resolution is nearly twice better than what is obtained in the transverse plane by a conventional wide field microscope with NA$= 1$, and three times better along the optical axis.

1.3.2.3 The transmission configuration: $k_{\mathrm{inc;z}} > 0$ and $k_z > 0$

In practice, the complete configuration is difficult to implement in a TDM set-up, as most of the microscopes work in a transmission or in a reflection configuration. In the transmission case, the illumination is performed on one side of the sample along the optical axis, and the detection on the other side. The OTF is then only a portion of the sphere of radius $2k_0$ of the complete configuration. It is a torus with the z axis as symmetrical axis, and its cross section in a longitudinal plane consists of two circles with radius k_0, as shown in Fig. 1.12.

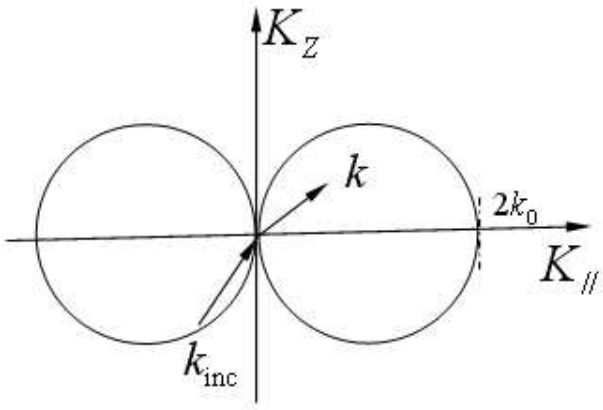

Figure 1.12 : *OTF for the transmission configuration*

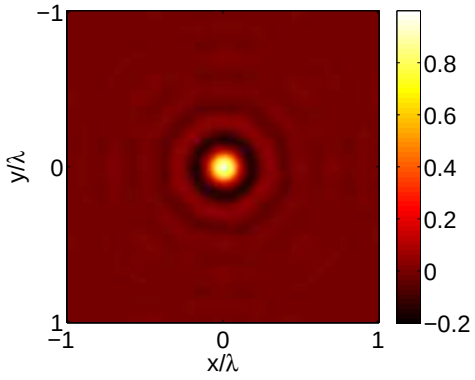

Figure 1.13 : *Transverse cut of the transmission PSF at $z = 0$*

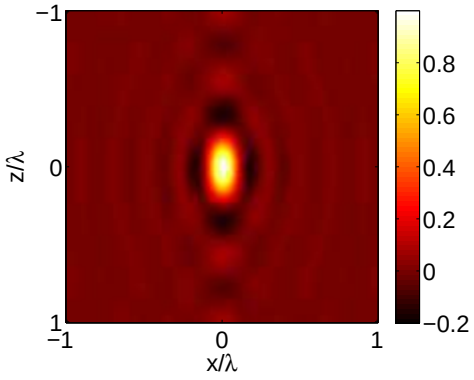

Figure 1.14 : *Longitudinal cut of the transmission PSF at $y = 0$*

Transverse and longitudinal cuts of the PSF are presented on Figs. 1.13 and 1.14, respectively. The PSF is elongated along the z axis, which strongly deteriorates the axial resolution compared to the complete configuration.

1.3.2.4 The reflection configuration: $k_{\mathrm{inc;z}} < 0$ and $k_z > 0$

For the case of the reflection configuration, where the illumination and the detection are performed on the same side of the sample, the OTF becomes the half of the complete sphere of radius $2k_0$, on one side of the transverse plane (x, y), as shown on Fig. 1.15. Contrarily to the complete and

transmission configurations, the PSF is this time a complex function since the OTF has no longer a center of symmetry. The real part of this PSF is equal to the PSF of the complete case.

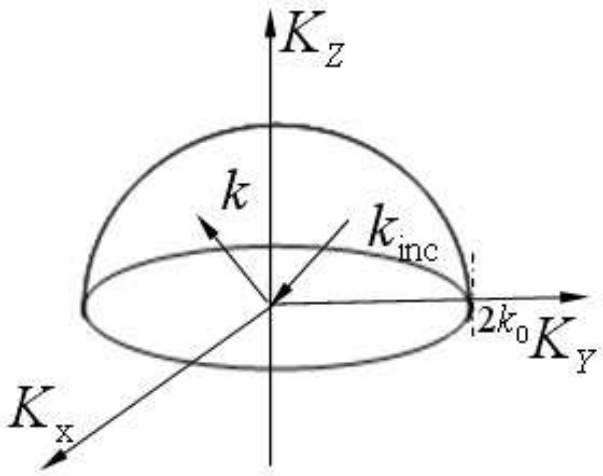

Figure 1.15 : *OTF for the reflection configuration*

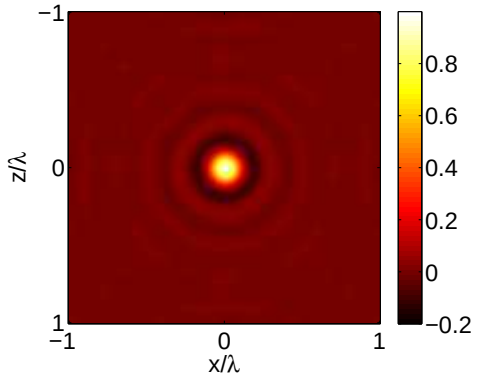

Figure 1.16 : *Longitudinal cut of the real part of the reflection PSF at* $y = 0$

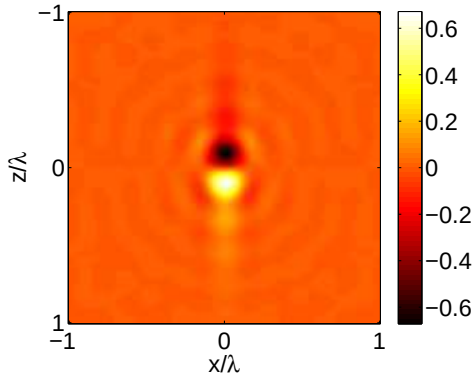

Figure 1.17 : *Longitudinal cut of the imaginary part of the reflection PSF at* $y = 0$

Figures 1.16 and 1.17 are longitudinal cuts of the real part and the imaginary part of the PSF, respectively. For objects with purely real permittivity contrast (phase objects), it means the resolution can be the same as in the complete configuration. But if the permittivity contrast is a complex number, that is for absorbing objects, Eq. (1.26) implies that the real and imaginary parts of the reconstructed permittivity contrast mingle in an unpredictable way. Note however that Mudry *et al.*[37] have introduced a mirror-assisted configuration for TDM to restore the isotropic resolution in the presence of absorption, by placing the sample in front of a perfect mirror.

1.3.3 Linear inversion with an inverse Fourier transform

Under the Born approximation, as described in the previous section with Eq. (1.26), the permittivity contrast of the sample is reconstructed by applying a 3D inverse Fourier transform to the

measured scattered field once the synthetic aperture has been generated. This quite simple approach has however several requirements to be successful. Firstly, when generating the synthetic aperture in the Fourier space, the Fourier components that are redundant between several illumination angles have to be averaged. Moreover, it is necessary to use a lot of different illuminations to fill the whole accessible Fourier domain with fine enough discretization steps for the FT^{-1} to be accurate. Every missing Fourier component is considered as zero in the FT^{-1} and therefore corrupts the PSF and the reconstruction. In practice several hundreds of illumination angles are used, and as they are set successively this is usually a limitation for the speed of the acquisition [22,52,53,55]. Lastly, the FT^{-1} is only valid if the illumination field can be considered as a plane wave and if the sample is placed in an homogeneous surrounding. Under these conditions, the reference field E_{ref} can be assimilated to a plane wave and the scattered field can be expressed as Eq. (1.24).

We present here the results of this linear inversion when some of the requirements are not fulfilled. We use as test samples cylindrical resin blocks deposited on a silicon substrate. They were fabricated by Anne Talneau in the Laboratoire de Photonique et Nanostructures in Marcoussis, with a resin provided by Dow Corning Corporation (XR 1541-6). The schematic of these samples is presented on Fig. 1.18, where h is the height of the cylinders and D their diameter and side to side distance. The orientation of the spatial coordinates x, y, z has also been indicated. The refractive index of the resin in the visible range remains close to 1.41 and the cylinders are considered as pure phase objects, neglecting the absorption of the resin.

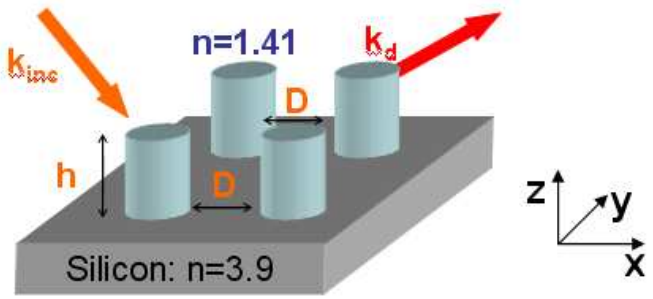

Figure 1.18 : *The sample geometry : resin blocks deposited on a silicon substrate. h is the height of the cylinders and D their diameter and side to side distance. The configuration used is the reflection configuration.*

For such samples, the relative permittivity contrast in the air is about 1, which is larger than the ones usually encountered under the Born approximation, generally below 0.1. Moreover, the objects are deposited on a reflective substrate, so that E_{ref} is the interference between the illumination field, that is a plane wave, and its specular reflection on the substrate. As a result, Eq. (1.24) is no longer valid in such a case, and the linear FT^{-1} inversion will in particular produce a mirror image of the object symmetrically to the reflective substrate. Lastly, to be able to decrease considerably the acquisition time, we will use a restricted amount of illumination angles and test the linear inversion in such a case.

The set-up used for measuring the field scattered by these objects will be presented in the first part of next chapter. Both the illumination and the detection take place above the substrate (reflection configuration). For the sample tested here, $D = 1\mu$m and $h = 120$nm. Figure 1.19 and 1.20 are electron microscope images of this sample.

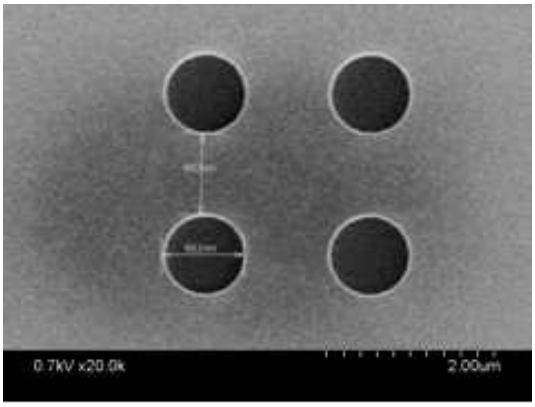

Figure 1.19 : *Overview of the sample imaged by electron microscopy*

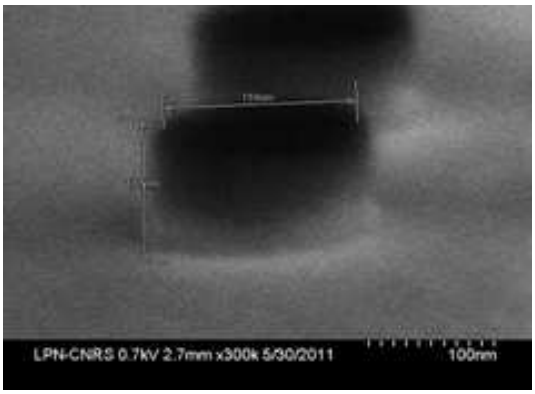

Figure 1.20 : *Profile of the sample imaged by electron microscopy*

12 illuminations angles have been chosen : 6 in the plane of incidence (x, z) with the electric field orthogonal to the plane of incidence (polarization TE), and 6 in the plane of incidence (y, z) with the electric field parallel to the plane of incidence (polarization TM). The incidence angles with respect to the normal to the substrate are 10°, 20° and 31° for the four cases of azimuthal angle $\phi = 0$, $\phi = 90°$, $\phi = 180°$ and $\phi = 270°$, as shown on Fig. 1.21.

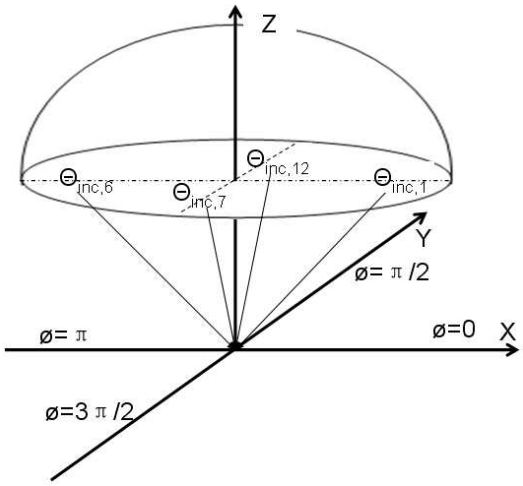

Figure 1.21 : *Diagram for the different illumination angles used with four azimuthal angles ϕ.*

Figure 1.22 shows the modulus of the scattered field for the four extreme illumination angles at 31°.

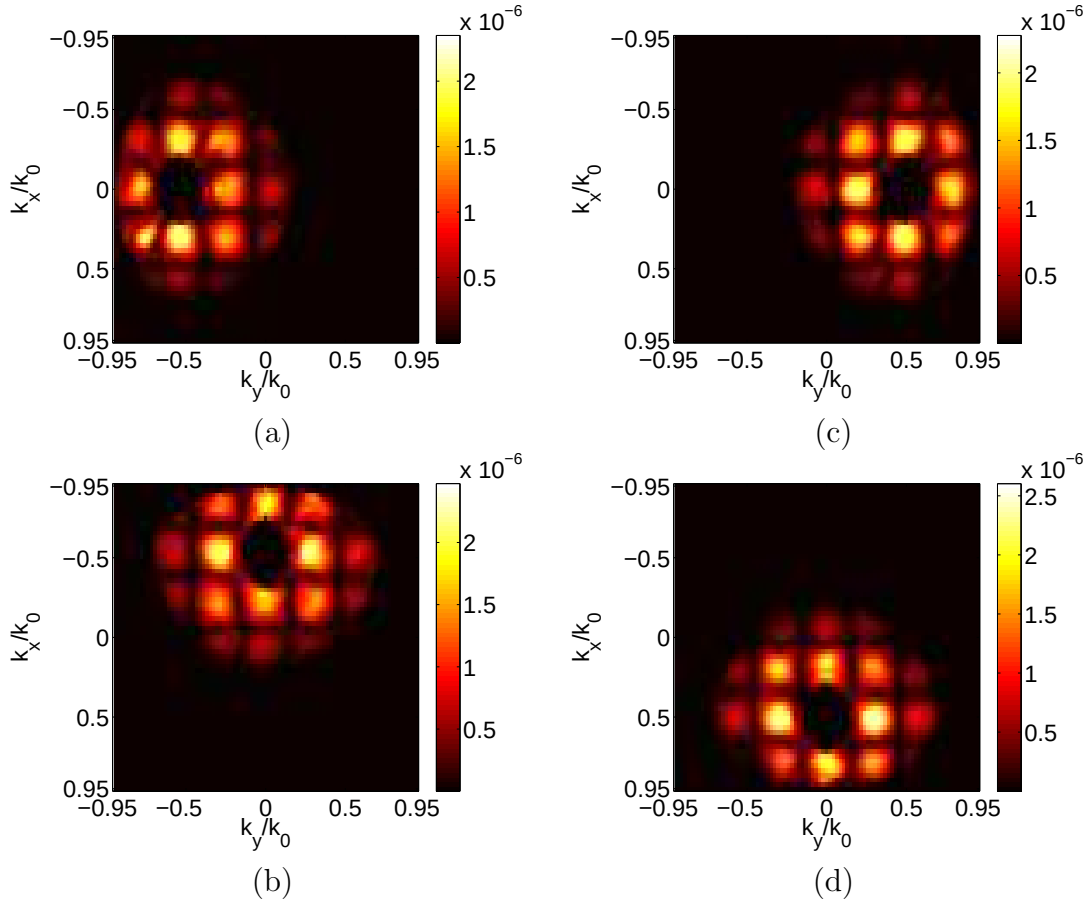

Figure 1.22 : *Modulus of the field scattered by the sample for an illumination angle of* 31° *and the four possible azimuthal angles: (a)*$\phi = 0°$*, (b)*$\phi = 90°$*, (c)*$\phi = 180°$*, (d)*$\phi = 270°$*; k_x and k_y are the spatial frequencies of the field.*

They are presented in the Fourier space, that is in the far field, with coordinates k_x and k_y that are the spatial frequencies of the field. The edges of the Fourier domain correspond to the spatial frequency $0.95k_0$, since the numerical aperture of the objective used for the measurement is NA=0.95. The missing circle appearing in black in each data image corresponds to the domain where the field scattered by the sample is masked by the specular reflection on the substrate, which is far stronger. Moreover, only about 2000 scattering angles centered on the specular reflection have been kept, as for the present object the modulus of the scattered field becomes negligible further away in the far-field.

Once the synthetic aperture has been generated, the linear FT^{-1} inversion has been applied to the data set and produces a reconstruction with a 53 nm meshing. Figure 1.23 is a transverse cut (x, y) of the reconstruction at a height $z = 53$ nm above the substrate and Fig. 1.24 is a longitudinal cut (y, z) in the middle of two of the cylinders. Note that on these figures the modulus of the 3D FT^{-1} of the data set has been displayed. It has indeed been found that the modulus is less disturbed than the real and imaginary parts when the Born approximation is not strictly valid[21], an this is also what was observed on the present samples.

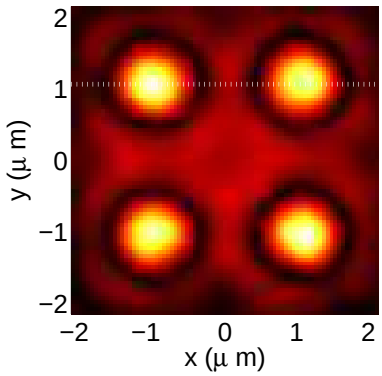

Figure 1.23 : *Transverse cut of the modulus of the reconstruction at a height $z = 53$ nm under Born approximation, the tested sample with diameter 1 μm.*

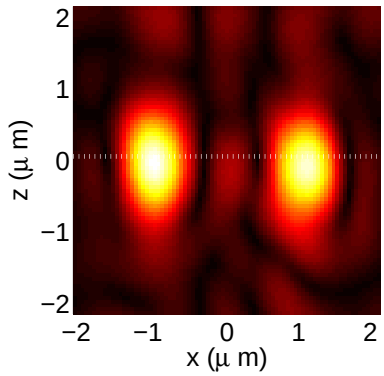

Figure 1.24 : *Longitudinal cut of the modulus of the reconstructions at $y = 1$ μm under Born approximation, the tested sample with diameter 1 μm.*

On the reconstruction, the dimensions of the cylinders are correctly retrieved in the transverse cut, since their diameter and side to side distance are equal to 1 μm and are thus well above the Rayleigh criterion of 400 nm (calculated with Eq. (1.1) and NA=0.95). However, some noise can be clearly seen around the cylinders. On the longitudinal cut, in addition to the noise, the cylinders are strongly distorted and the actual height of 120 nm cannot be retrieved. These features can be explained by the presence of the reflective substrate that in not taken into account in the linear inversion, and by the limited number of illumination angles, since the FT^{-1} is very sensitive to the missing points in the Fourier space.

With this quite simple sample, that is studied in a specific configuration (presence of the substrate, few illumination angles), the linear FT^{-1} inversion clearly shows some limitations. Therefore, an original non-linear inversion algorithm has been developed during this PhD and will be presented in the next chapter. It performs a rigorous modelling of the scattering process and can thus take into account the presence of the substrate as well as the possible multiple scattering phenomenon that occurs out of the validity domain of Born approximation. As will be shown in Chapter 3, it is also less sensitive to using a restricted amount of illumination angles to increase the acquisition speed.

1.4 State-of-the-art results obtained by TDM under linear approximations

Synthetic aperture techniques are particularly attractive to improve the resolution of microscopes on unstained samples, but not so many research teams have actually implemented it experimentally for the reconstruction of three-dimensional objects. The synthetic aperture is indeed more easily generated on bi-dimensional objects [28–30]. As tomography aims at reconstructing 3D objects from 2D data sets (usually obtained on a CCD camera), we therefore focus here on such achievements.

Most of the work has been done on samples with low permittivity contrasts, usually biological ones, with microscopes in transmission configuration. As a result the axial resolution is not as good as the transverse one. The first demonstration of 3D reconstruction with TDM and resolution improvement compared to wide-field microscopy was performed by V. Lauer [21]. An optimized set-up based on the same configuration was then developed in Olivier Haeberlé's research team in Mulhouse [27,43] and pushed forward the resolution performances close to the theoretical synthetic aperture limit [54]. This team has also shown that a reflection configuration set-up improves the

sectioning capabilities along the optical axis [52]. In all this work, the synthetic aperture is generated from multiple measurements where the illumination angle on the sample is changed thanks to a motorized mirror. This approach is the most encountered one [23,44–46], but another technique consists in using a fixed illumination at normal incidence and rotating the sample about an axis in the transverse plane [39,47,49]. It permits to enlarge the accessible domain of spatial frequencies, with only a reduced missing Fourier domain along the rotation axis of the specimen. The main drawback is that performing a precise rotation of the sample at the microscopic scale within an interferometric set-up is experimentally challenging, so that in practice keeping the specimen static is usually the preferred solution.

Most of the 3D experimental reconstructions are obtained with the 3D FT^{-1} inversion based on the Born approximation [21,27,43,45,46,50,51,54]. However a more crude approach has also been used, based on the Radon transform, that neglects diffraction and refraction [23,39,49]. Light is considered as propagating in straight lines through the specimen with a phase shift that varies from one illumination angle to another. This can be valid if the permittivity contrast is very low and if the specimen is not structured at the scale of the wavelength. Hence it provides reconstructions that have poorer resolution performances [47].

On the other hand, another linear approximation different from the Born approximation has also been used, namely the Rytov approximation [48]. In the case of the Born approximation, the field scattered by the object has to be sufficiently weak so that the total field inside of it can be assimilated to the reference field E_{ref}. This condition is generally interpreted as having a small enough refractive index contrast of the object. However this can be misleading, as even a very small refractive index contrast can produce a non negligible phase delay if the object is large enough. The Rytov approximation is on the contrary not sensitive to the size of the sample or to the total phase delay, but rather to the gradient of the refractive index. Its validity condition can be stated as :

$$[\nabla(\phi(\boldsymbol{r}) - \phi_{\mathrm{inc}}(\boldsymbol{r}))]^2 \ll k_0^2 \Delta n(\boldsymbol{r}), \tag{1.27}$$

where ϕ and ϕ_{inc} are the phase of the total field and of the illumination field, respectively, and Δn is the refractive index contrast of the object. As to a first approximation $\nabla(\phi(\boldsymbol{r}) - \phi_{\mathrm{inc}}(\boldsymbol{r})) \simeq k_0 \Delta n(\boldsymbol{r})$ for a weakly scattering object, the validity condition of the Rytov approximation simply becomes $\Delta n(\boldsymbol{r}) \ll 1$ and does not make any assumption on the object size. Similarly to the Born approximation, it can be shown that when the Rytov approximation is valid, the object permittivity contrast can be retrieved linearly by a 3D FT^{-1} applied this time in far field on $E_{\mathrm{inc}}(\boldsymbol{k}_{\mathrm{inc}}) \ln[E(\boldsymbol{k}, \boldsymbol{k}_{\mathrm{inc}})/E_{\mathrm{inc}}(\boldsymbol{k}_{\mathrm{inc}})]$. This approach has recently provided undistorted reconstructions on 10 μm large objects producing a total phase delay close to π, contrarily to the Born approximation [44].

One drawback of TDM in all the previous approaches is that the data acquisition time can be a limiting factor, as several hundreds of illumination angles are usually required to reconstruct accurately the object. A different set-up configuration has thus been recently proposed, where the sample is simultaneously illuminated by a sum of incoherent plane waves with the same polar angle but with all possible azimuthal angles [50,51]. This illumination cone technique necessitates to perform multiple measurements by scanning the sample along the optical axis so that 3D reconstructions are possible. The common path interferometer configuration of the set-up has also been optimized to limit the sensitivity to external perturbations. The 3D reconstruction capabilities of this technique have been validated, but so far no resolution improvement beyond the Rayleigh criterion has been shown.

Another limitation of TDM concerns the difficulty to obtain an isotropic resolution, as would be given by illuminating the object and detecting its scattered field along all possible angles in 4π steradians. New illumination schemes have been proposed to make it possible experimentally : placing the sample in the vicinity of a flat mirror and using a reflection scheme set-up [37], or combining the rotation of the sample about a transverse axis with the rotation of the illumination through a transmission scheme set-up [38].

Chapter 2

Tomographic diffractive microscopy with non-linear inversion procedures

Contents

2.1 Description of the tomographic diffractive microscopy set-up 21

2.2 The phase measurement techniques 23

2.2.1 Phase shifting interferometry 24

2.2.2 Off-axis holography 25

2.2.3 Phase measurement with a wavefront sensor 26

2.3 Rigorous nonlinear inversion procedures in 3D 30

2.3.1 The direct problem 30

2.3.2 The nonlinear inversion algorithm for 3D imaging 32

2.1 Description of the tomographic diffractive microscopy set-up

The TDM set-up has two main objectives : detecting the field scattered by the probed object both in phase and in amplitude, and illuminating this object with a collimated coherent beam with a controlled angle of incidence. As will be detailed hereafter, different modalities have been tested to detect the phase of the field. They are generally based on an interferometric arrangement. The TDM set-up has been developed horizontally on a stabilized optical table and is presented on Fig. 2.1.

The light is emitted at wavelength 633 nm by a 10 mW Helium-Neon laser and is linearly polarized. It is divided into two beams by beamsplitter B_1 : a reference beam and a beam directed towards the sample. A rotating mirror (M) mounted on two stepping motors (Newport NSA12) permits to control the deflection of this latter beam. Then a beam expander (BE_1) and diaphragm D_1 generate a wide collimated beam with near homogeneous power density. This beam illuminates the sample after transmission through the microscope objective (L_1) and the associated tube lens

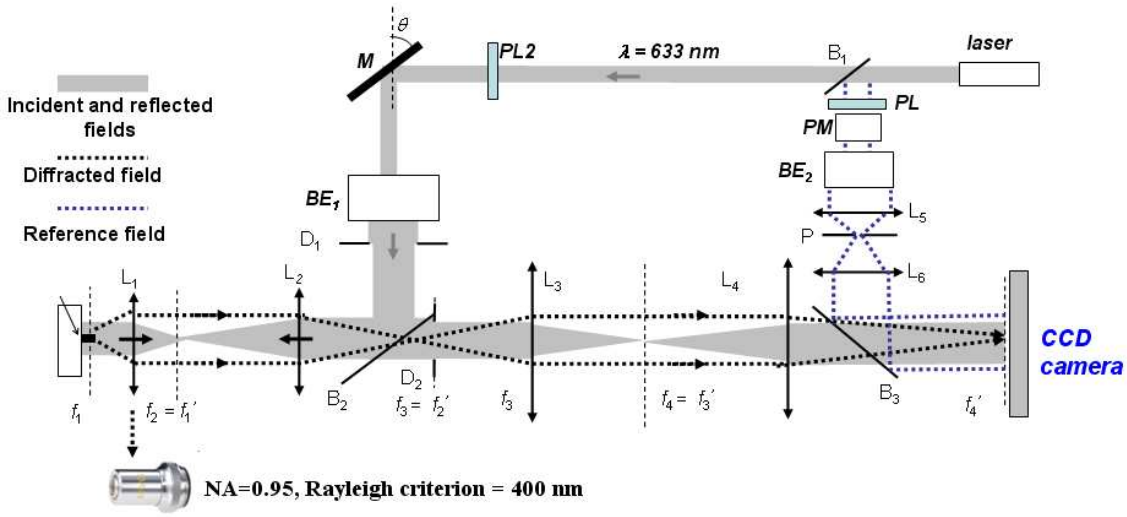

Figure 2.1 : *Sketch of the experimental TDM set-up, laser source emitting at 633 nm; M, adjustable mirror; PL, polarizer; L_1, microscope objective; $L_{2,\cdots,6}$, lenses; f_i, f_i', object and image focal planes of lens L_i; B_1, B_2, B_3, beam splitters; BE_1, BE_2 beam expanders; P, pinhole; PM, phase modulator; D_1, D_2, diaphragms.*

(L_2). It can be locally assimilated to a plane wave since the dimensions of the object are small compared to the width of the beam. The center of the mirror is conjugated through the beam expander with diaphragm D_1, which is itself conjugated with the center of the sample through the tube lens and the microscope objective. Thus, rotating the mirror varies the incidence angle without shifting laterally the illumination beam on the object and with an illumination field defined by D_1. The polar angle of the illumination can be varied over the whole NA of the objective.

The field scattered by the object is collected by the microscope objective (Zeiss Epiplan-Apochromat 50×, NA = 0.95) and imaged on a CCD camera (Kappa PS4-1020) after passing through relay lenses L_3 and L_4 to obtain a global magnification of about 290. This is therefore a reflection configuration microscope, where the same high NA objective is used both for the illumination and the detection. The diaphragm D_2 is placed in an intermediate conjugated plane of the object, and permits to adjust the field of view on the camera. The reference field extracted by B_1 firstly passes through an electro-optic phase modulator (PM), that is used to perform phase-shifting interferometry and detect the phase of the scattered field, as will be explained hereafter. The beam is then enlarged by beam expander BE_2, focused on pinhole P for spatial filtering and collimated by lens L_6. In the end, it is coherently superimposed on the imaged scattered field thanks to beam splitter B_3. Figures 2.2 and 2.3 show the images of diaphragm D_1 and diaphragm D_2 on the camera. They are good indicators that the set-up is optically well adjusted, since in this case they should be obtained simultaneously in focus on the camera. Indeed, if the object is correctly placed in the object focal plane of the objective and if it is deposited on a reflective substrate, the diaphragm D_1 will be optically conjugated with the plane of the camera after reflection on the substrate.

Note that the field scattered by the object is detected in the image space, that is in a plane conjugated with the object focal plane of the objective where the object is located. However, it was described in the previous chapter that the linear inversion with a 3D FT^{-1} under the Born approximation must be applied to the scattered field detected in far-field. It will also be the case for the non-linear inversion algorithm that has been developed during this PhD, and will be described in the last section of this chapter. In fact, the scattered field in far-field can be obtained

by applying a simple 2D FT^{-1} to the field in the image space. The Fourier space, *i.e.* the space of the spatial frequencies of the imaged field, can indeed be assimilated to the far-field space [56–61].

The interest of placing the camera in the image space rather than in the Fourier space is twofold. It firstly permits to adjust easily the position of the sample in the object focal plane of the objective, so that it appears in focus on the camera. Second, it is more adapted to the observation of small objects in terms of signal to noise ratio. Indeed, the flux scattered by a small object will spread over the whole NA of the objective in the Fourier space, while in the image space it will focus to form an image. Moreover the part of the illumination that has not been scattered by the object will focus in the Fourier space (that is usually the case for TDM in transmission configuration, and also in reflection configuration when the object is deposited on a reflective substrate). This signal is far stronger than the scattered field in the case of small objects. The dynamic range of the detector would therefore not be sufficient to detect both this strong focus and the scattered field in the Fourier space, whereas in the image space the non scattered field is a plane wave that produces a background illumination. Note that it is important to have access to the non scattered field in far-field, since its amplitude and phase are used to normalize the data detected for each illumination angle, and get rid of the amplitude and phase fluctuations of the illuminating field during the measurement. This normalization procedure will be detailed below in the Chapter 3.

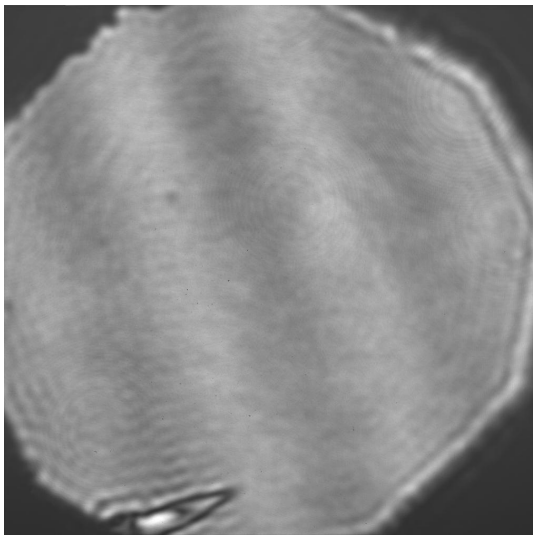

Figure 2.2 : *The image of diaphragm D_1 obtained on the CCD camera when a reflective substrate is placed in the vicinity of the object focal plane of L_1. This kind of setting is usually accurate enough.*

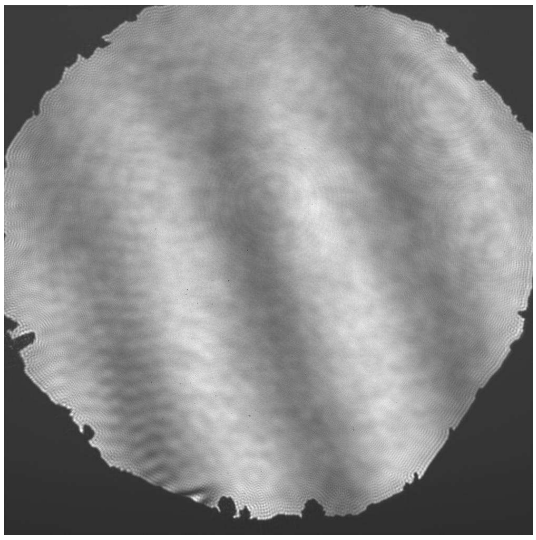

Figure 2.3 : *The image of diaphragm D_2, optically conjugated with the CCD camera.*

2.2 The phase measurement techniques

For each illumination angle on the sample, the field has to be detected both in phase and in amplitude. Three different techniques have been applied for this purpose and are presented hereafter. The two first ones rely on the interference of the field scattered by the object with a reference beam, and the last one aims at simplifying the set-up thanks to the use of a wavefront sensor.

2.2.1 Phase shifting interferometry

2.2.1.1 Principle of the method

Based on the experimental set-up illustrated in Fig. 2.1, phase shifting interferometry was described by Carre *et al.*[69] in 1966 and by Bruning *et al.*[70] in 1974, and was then further developed in the eighties and later on[19,58]. It is a highly efficient and accurate phase measuring method that has been applied to 3D[62], color[63,64], polarization[62], synthetic aperture[65], low-coherence[66], surface shape[67] and microscopic[68] imaging. It is based on the recording of several interference patterns between the field scattered by the object and the reference wave. The optical path of the reference wave can be controlled accurately, typically thanks to a mirror mounted on a piezoelectric support or a phase modulator where the refractive index of an electro-optic crystal can be varied by applying a voltage. Each interference pattern is obtained with a different additional phase shift inserted in the reference wave. In our set-up, four phase retardations are introduced by the phase modulator (New Focus 4002) to retrieve the complex scattered field : $-\frac{\pi}{2}$, 0, $\frac{\pi}{2}$, π. The corresponding intensity patterns detected on the camera are called S_1, S_2, S_3 and S_4, respectively, and can be written as :

$$S_1 = I_{\text{obj}} + I_{\text{ref}} + 2\sqrt{I_{\text{obj}} I_{\text{ref}}}\cos\left(\varphi + \frac{\pi}{2}\right) \tag{2.1}$$

$$S_2 = I_{\text{obj}} + I_{\text{ref}} + 2\sqrt{I_{\text{obj}} I_{\text{ref}}}\cos\varphi \tag{2.2}$$

$$S_3 = I_{\text{obj}} + I_{\text{ref}} + 2\sqrt{I_{\text{obj}} I_{\text{ref}}}\cos\left(\varphi - \frac{\pi}{2}\right) \tag{2.3}$$

$$S_4 = I_{\text{obj}} + I_{\text{ref}} + 2\sqrt{I_{\text{obj}} I_{\text{ref}}}\cos\left(\varphi - \pi\right), \tag{2.4}$$

where I_{obj} and I_{ref} are the intensities of the object field and of the reference field, respectively, and φ is the phase difference between the object field and the reference one. Note that the object field E_{obj} is the sum of the field scattered by the object E_{s} with the remaining non scattered illuminating field E_{ill} :

$$E_{\text{obj}} = E_{\text{s}} + E_{\text{ill}}. \tag{2.5}$$

E_{ill} is in our case due to the specular reflection of the illumination on the reflective substrate where the objects are deposited. The object field can then be obtained from the following calculation :

$$\frac{(S_2 - S_4) + i(S_3 - S_1)}{4\sqrt{I_{\text{ref}}}} = \sqrt{I_{\text{obj}}}\exp(i\varphi) = E_{\text{obj}}. \tag{2.6}$$

As can be seen from this equation, it is necessary to measure separately the intensity of the reference wave to retrieve the complex object field E_{obj}. Moreover, to assimilate the argument of this calculation to the phase of the object field, the reference wave must have a plane wavefront propagating along the optical axis of the microscope, and thus arriving at normal incidence on the camera. Such a configuration is usually called an on-axis (or inline) interferometric arrangement. Performing phase-shifting interferometry requires a very accurate phase shift between consecutive images, since the useful information are obtained by making image subtractions. In practice, to improve the signal to noise ratio of the result, several cycles of the four phase retardation are applied and the retrieved complex fields for each cycle are averaged.

2.2.1.2 Calibration of the phase-stepper

The phase shift introduced by the phase modulator can be considered with a good approximation as proportional to the voltage applied to the electro-optic crystal. The most common residual error to deal with in this case is when there is a slight discrepancy $\tau \ll 1$ between the desired phase shift and the actual one. With the linear link between the voltage and the phase shift, the four

intensity patterns are modified the following way :

$$S_1 = I_{\text{obj}} + I_{\text{ref}} + 2\sqrt{I_{\text{obj}} I_{\text{ref}}}\cos(\varphi + \frac{\pi}{2} + \tau) \tag{2.7}$$

$$S_2 = I_{\text{obj}} + I_{\text{ref}} + 2\sqrt{I_{\text{obj}} I_{\text{ref}}}\cos\varphi \tag{2.8}$$

$$S_3 = I_{\text{obj}} + I_{\text{ref}} + 2\sqrt{I_{\text{obj}} I_{\text{ref}}}\cos(\varphi - \frac{\pi}{2} - \tau) \tag{2.9}$$

$$S_4 = I_{\text{obj}} + I_{\text{ref}} + 2\sqrt{I_{\text{obj}} I_{\text{ref}}}\cos(\varphi - \pi - 2\tau). \tag{2.10}$$

Applying Eq. (2.6) to this data set produces a corrupted object field E'_{obj} that can be expressed, assuming that $\tau \ll 1$, as :

$$E'_{\text{obj}} = \sqrt{I_{\text{obj}}}(\cos\varphi + \tau\sin\varphi + i\sin\varphi) = \text{Re}(E_{\text{obj}}) + i(1 - i\tau)\text{Im}(E_{\text{obj}}), \tag{2.11}$$

where Re and Im denote the real and imaginary parts of the field, respectively. This equation can be reformulated as :

$$E'_{\text{obj}} = \left(1 - i\frac{\tau}{2}\right) E_{\text{obj}} + i\frac{\tau}{2} E^*_{\text{obj}}, \tag{2.12}$$

where E^*_{obj} is the complex conjugate of E_{obj}.

Therefore, when E'_{obj} is transferred to the Fourier space with a 2D FT^{-1}, E^*_{obj} produces what is called a ghost signal, whose modulus is symmetrical with respect to the spatial frequency origin to that produced by E_{obj}. It can therefore considerably corrupt the measurement. Several methods are possible to correct the residual phase shift error τ. For instance, it is possible to compare the modulus of the signal in the Fourier space due to the two contributions E_{obj} and E^*_{obj}. This can be done more easily at the focus of the non scattered fields E_{ill} and E^*_{ill}, and an estimation of τ can be extracted from the ratio of these two signals.

2.2.1.3 Limitations of phase-shifting interferometry

If the phase steps are carefully set, phase-shifting interferometry produces a highly accurate phase signal. However, even with perfect phase steps, the measurement can be disturbed by phase fluctuations due to thermal and/or mechanical drifts during the acquisition. The interferometric detection is indeed very sensitive to external perturbations between the reference optical path and the one for illumination and detection. That is why a cycle of phase steps has to be run as quickly as possible, and an average on several cycles can also be done. Common path interferometer geometries[50,71] have been recently proposed to lower the sensitivity to external phase fluctuations, but the necessity to perform several phase steps remains time consuming, especially if a large number of illumination angles have to be applied successively.

To diminish the constraints imposed by external perturbations and accelerate the acquisition time, another phase measurement technique has been tested during this PhD : off-axis holography.

2.2.2 Off-axis holography

Off-axis holography[81] is the oldest and the simplest configuration adapted to digital holography[82–86]. The main difference compared to phase-shifting interferometry is that the reference wave propagates with a carefully chosen angle with respect to the set-up optical axis, and therefore illuminates the camera with a phase ramp. The phase modulator is in this case no longer necessary : the phase and the amplitude of the object field can be obtained with a single-shot measurement. Off-axis holography has been applied recently to particle[87] , polarization[88], phase contrast[89], synthetic aperture[90] and microscopic imaging[91,92]. If the reference wave can be assimilated to a plane wave, its field on the camera can be written as $E_{\text{ref}} = e^{i(\alpha x + \beta y)}$, with x and y the transverse coordinates with respect to the optical axis along coordinate z. To simplify the explanation, we consider $\beta = 0$. The intensity I detected on the camera is :

$$I = I_{\text{ref}} + I_{\text{obj}} + e^{-i\alpha x} E_{\text{obj}} + e^{i\alpha x} E^*_{\text{obj}}. \tag{2.13}$$

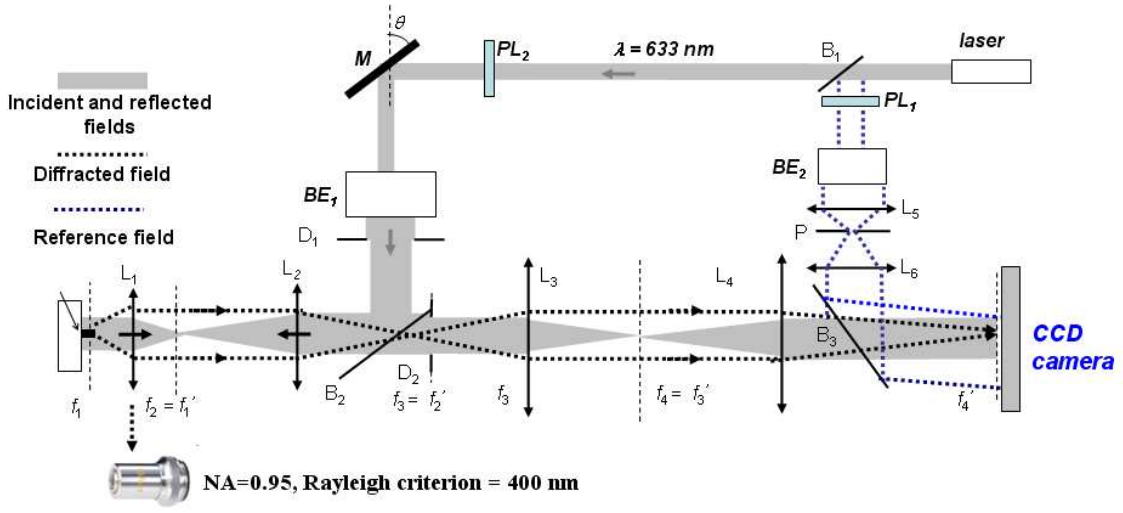

Figure 2.4 : *Sketch of the TDM set-up in off-axis configuration. The phase modulator has been suppressed and the reference wave propagates with an angle with respect to the optical axis.*

By performing the 2D FT^{-1} of I, one obtains the Fourier space intensity $\tilde{I}$:

$$\tilde{I} = \tilde{I}_{\text{ref}} + \tilde{I}_{\text{obj}} + \delta_{-\alpha} * \tilde{E}_{\text{obj}} + \delta_{\alpha} * \tilde{E}^{*}_{\text{obj}}, \tag{2.14}$$

where δ_α is the Dirac function placed at the spatial frequency coordinates $(\alpha, 0)$. In this equation, $\tilde{I}_{\text{ref}}$ and $\tilde{I}_{\text{obj}}$ are centered at the spatial frequency origin and have a cut-off frequency that is twice that of the NA of the objective, whereas $\tilde{E}_{\text{obj}}$ and $\tilde{E}^{*}_{\text{obj}}$ are both confined within this NA. Thanks to the convolution with the Dirac function, these two terms are shifted in the Fourier space and become centered on spatial frequencies $(\alpha, 0)$ and $(-\alpha, 0)$, respectively. If the off-axis angle of the reference wave is large enough, they will not overlap with the intensity terms $\tilde{I}_{\text{ref}}$ and $\tilde{I}_{\text{obj}}$. It is then possible to filter $\tilde{E}_{\text{obj}}$ and have a direct access to the complex field E_{obj} in the Fourier space. Note that in practice the modulus of the reference wave is not equal to unity, so it is necessary to measure I_{ref} separately and divide Eq. (2.13) by $\sqrt{I_{\text{ref}}}$ prior to performing the 2D FT^{-1}. In this way both the modulus and the phase of $\tilde{E}_{\text{ref}}$ can be extracted through the procedure.

The single shot nature of the measurement dramatically decreases the sensitivity to external fluctuations, but this is done at the expense of the available number of pixels of the camera : only a fraction of the total number can be used with the constraint of separating the different interference terms in the Fourier space. Additionally, another discretization constraint is imposed by the fact that it is necessary to resolve on the camera the interference fringes between the reference wave and any propagating plane wave transmitted by the microscope objective. For a plane wave at the edge of the objective NA and propagating with an angle of opposite sign compared to that of the reference wave, the period of the fringes will be particularly small. There is therefore a minimal off-axis angle to separate the terms in the Fourier space, but also a maximal one to discretize successfully the interference fringes.

2.2.3 Phase measurement with a wavefront sensor

2.2.3.1 Choice of the wavefront sensor

In contrast to the two previous methods based on an interferometric microscope, it is possible to suppress the reference wave and detect the phase by replacing the CCD camera with a wavefront sensor. This permits to greatly simplify the set-up architecture and gives the opportunity to use

light sources with lower temporal coherence, such as laser diodes. Interferometric microscopy indeed usually requires light sources with high temporal coherence, and is therefore plagued by the speckle noise stemming from the parasitic reflections and diffraction along the light path. As wavefront sensors perform the measurement of the amplitude and the phase of the field in a single shot manner, they moreover offer the advantages of rapidity and insensitivity to external perturbations.

Wavefront sensors (WFS) are generally used to estimate relatively slow phase variations like those produced by lenses aberrations or weakly scattering biological samples, or in the field of adaptive optics. For the study of the aberrations of light beams, only the lower-order aberrations (like spherical aberration or coma) are usually considered, because they are sufficient to considerably improve the beam quality [18,74]. Thus, a few thousands of phase measurement points are sufficient to analyze the beam wavefront and subsequently compensate low order aberrations, and this is easily performed by Shack-Hartmann wavefront sensors (SHWFS) [75,76]. However, for high resolution microscopy applications, more pixels are necessary. We have therefore used another type of wavefront sensor, based on quadri-wave lateral shearing interferometry (QWLSI) [75,78]. This type of sensor is based on lateral shearing interferometry, that permits to measure the phase gradient of a wavefront along one direction of the image. It consists in replicating the incident wavefront into two identical but tilted wavefronts, and recording after propagation their mutual interference pattern on a CCD camera. Primot and Sogno [73] have extended this principle to more than one gradient direction with multiwave interferometry (typically, QWLSI) to recover a full two dimensional phase-field. It has the potential to sample intensity and phase images with a higher lateral resolution compared to Shack-Hartmann WFS [77]. Four replicas are created by a specific 2D diffraction grating (a modified Hartmann mask, see Fig. 2.5), and two gradients along two perpendicular directions are measured and then integrated to determine the field intensity and phase [78].

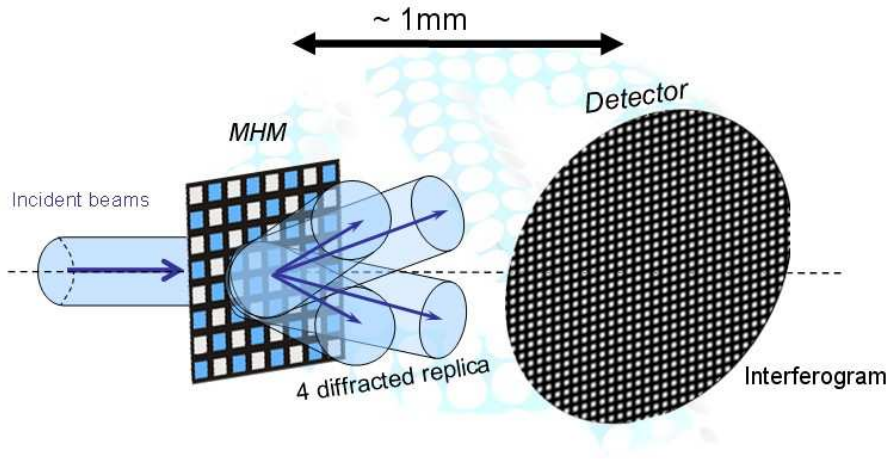

Figure 2.5 : *Principle of quadri-wave lateral shearing interferometry.*

The wavefront sensor based on this technique that we use is the SID4-HR model of the Phasics company, that samples the imaged field on a 300x400 matrix, with a pixel size of about 30 μm. Integrated in the set-up, it replaces the CCD camera and the reference beam is completely suppressed, as shown on in Fig. 2.6.

2.2.3.2 Principle of lateral shearing interferometry

To better illustrate the working modalities of the wavefront sensor, lateral shearing interferometry is detailed in this section. For this one dimensional case, the x coordinate is the direction along which the phase gradient will be retrieved, and the z coordinate is along the optical axis, that is

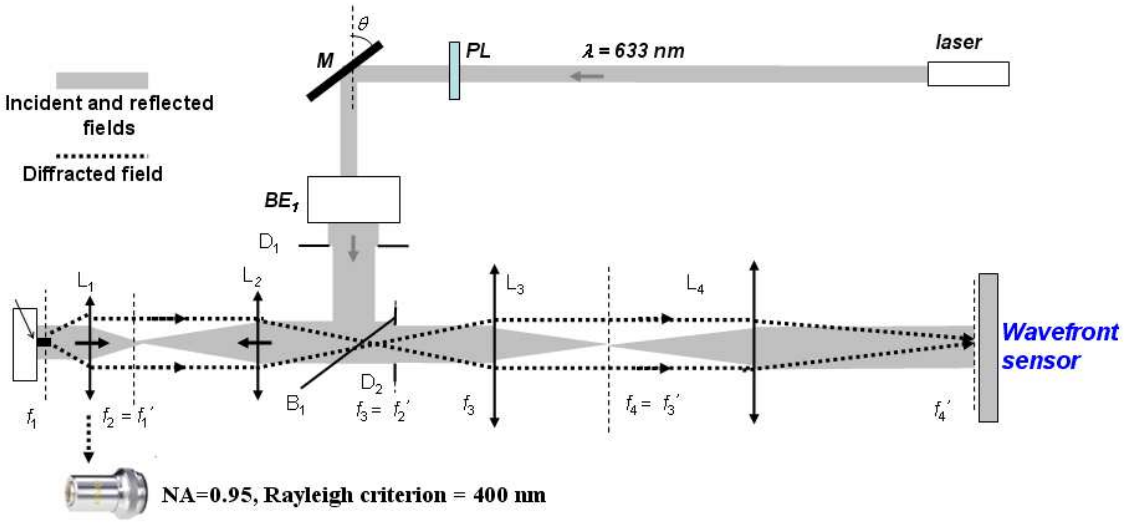

Figure 2.6 : *Sketch of the experimental setup using wavefront sensor SID4-HR. M, adjustable mirror; PL, polarizer; L_1, L_2, L_3, L_4, lenses; f_i, $f_i^{'}$, object and image focal planes of lenses; B_1, beam splitters; BE_1, beam expander; D_1, diaphragms.*

perpendicular to the wavefront sensor and the modified Hartmann mask (MHM). In this case, the transmission coefficient in amplitude $t(x)$ of a perfect modified Hartmann mask is:

$$t(x) = \cos\left(\frac{\pi x}{p}\right), \tag{2.15}$$

where $2p$ is the period of the MHM. In the following equations, proportionality factors are omitted as a matter of clarity, and the origin of the z coordinate is taken on the plane of the MHM. If $E_{\text{obj}}(x, z = 0)$ is the object field incident on the MHM of the wavefront sensor, it can be written as :

$$E_{\text{obj}}(x, z = 0) \propto \int \tilde{E}_{\text{obj}}(\alpha) e^{i\alpha x} \mathrm{d}\alpha, \tag{2.16}$$

where $\tilde{E}_{\text{obj}}(\alpha)$ is its one dimensional Fourier transform. The field $E_t(x, z = 0)$ that is transmitted by the MHM can also be written as a Fourier expansion :

$$E_t(x, z = 0) = \cos\left(\frac{\pi x}{p}\right) E_{\text{obj}}(x, z = 0) \propto \int \left[\tilde{E}_{\text{obj}}\left(\alpha - \frac{\pi}{p}\right) + \tilde{E}_{\text{obj}}\left(\alpha + \frac{\pi}{p}\right)\right] e^{i\alpha x} \mathrm{d}\alpha. \tag{2.17}$$

When the transmitted field propagates from the MHM to the sensor plane, its plane wave decomposition can thus be written as :

$$E_t(x, z) \propto \int \left[\tilde{E}_{\text{obj}}\left(\alpha - \frac{\pi}{p}\right) + \tilde{E}_{\text{obj}}\left(\alpha + \frac{\pi}{p}\right)\right] e^{i\alpha x + i\gamma(\alpha) z} \mathrm{d}\alpha, \tag{2.18}$$

where $\gamma(\alpha) = \sqrt{k_0^2 - \alpha^2}$ is the axial component of the wave vector. The diffraction orders -1 and +1 created by the MHM are visible in this equation. If we focus on the diffraction order +1 $E_{t,+1}(x, z)$, it can be reformulated with a change of variable as :

$$E_{t,+1}(x, z) \propto \int \tilde{E}_{\text{obj}}(\alpha') e^{i(\alpha' + \frac{\pi}{p})x + i\gamma(\alpha' + \frac{\pi}{p})z} \mathrm{d}\alpha'. \tag{2.19}$$

Lateral shearing interferometry is then based on the fact that the spatial frequencies of the object field are very small compared to that of the MHM : $\alpha' \ll \frac{\pi}{p}$. In this case, as described on Fig. 2.7, the following approximation can be done :

$$\gamma\left(\alpha' + \frac{\pi}{p}\right) \simeq \gamma\left(\frac{\pi}{p}\right) - \alpha' \tan\theta_1, \tag{2.20}$$

where $\theta_1 = \sin^{-1}\left(\frac{\pi}{pk_0}\right)$ is the propagation angle of the first diffraction angle with respect to the optical axis. In the end $E_{t,+1}(x,z)$ can be approximated as :

$$\begin{aligned} E_{t,+1}(x,z) &\propto e^{i\left[\frac{\pi}{p}x + \gamma\left(\frac{\pi}{p}\right)z\right]} \int \tilde{E}_{\text{obj}}(\alpha') e^{-i\alpha' z \tan\theta_1} e^{i\alpha' x} \mathrm{d}\alpha' \\ &= E_{\text{obj}}(x - z\tan\theta_1) e^{i\left[\frac{\pi}{p}x + \gamma\left(\frac{\pi}{p}\right)z\right]}. \end{aligned} \tag{2.21}$$

The object field can be expressed as $E_{\text{obj}}(x, z=0) = A_{\text{obj}}(x) e^{i\phi_{\text{obj}}(x)}$ and $E_t(x,z) = E_{t,+1}(x,z) +$

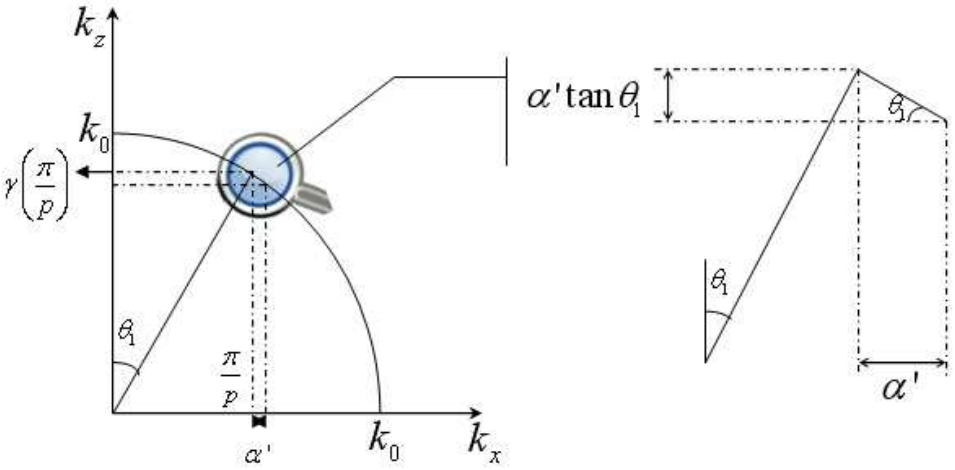

Figure 2.7 : *Schematic used to evaluate the axial component of a wave vector for a small perturbation α' of its transverse wave vector around $\frac{\pi}{p}$.*

$E_{t,-1}(x,z)$ then reads :

$$\begin{aligned} E_t(x,z) \propto\ & A_{\text{obj}}(x - z\tan\theta_1) e^{i\left[\frac{\pi}{p}x + \gamma\left(\frac{\pi}{p}\right)z + \phi_{\text{obj}}(x - z\tan\theta_1)\right]} \\ & + A_{\text{obj}}(x + z\tan\theta_1) e^{i\left[-\frac{\pi}{p}x + \gamma\left(-\frac{\pi}{p}\right)z + \phi_{\text{obj}}(x + z\tan\theta_1)\right]}. \end{aligned} \tag{2.22}$$

The intensity $I_t(x,z) \propto \|E_t(x,z)\|^2$ detected by the CCD camera of the wavefront sensor is then :

$$\begin{aligned} I_t(x,z) \propto\ & A_{\text{obj}}^2(x - z\tan\theta_1) + A_{\text{obj}}^2(x + z\tan\theta_1) \\ & + 2A_{\text{obj}}(x - z\tan\theta_1) A_{\text{obj}}(x + z\tan\theta_1) \cos\left(\frac{2\pi}{p}x - 2\frac{\partial\phi_{\text{obj}}(x)}{\partial x}\tan\theta_1 z\right), \end{aligned} \tag{2.23}$$

with $z = 1.5$ mm in practice. One can see that $I_t(x,z)$ is an interferogram that gives access to the phase gradient component along the x direction. This interferogram is interpreted as a non-uniform phase gradient function, frequency-modulating a perfect sinusoidal pattern of period p. The phase is recovered by applying a Fourier transform to the interferogram, that is then demodulated around its specific carrier frequency to extract the phase gradient, before performing an integration. Because

the phase information is coded in the interferogram by a frequency modulation, the phase and the intensity are independently determined. The intensity image is recovered by applying a low pass filter on the interferogram to just keep the first two terms of Eq. (2.23).

Note that the CCD camera has a pixel pitch of $p/4$ to sample the interferogram, and the final image of the phase and the intensity of the field has a pitch of p once the Fourier analysis has been performed. The wavefront sensor is calibrated so that $z \tan\theta_1$ is small compared to p, and therefore the shift of the intensity image in the first two terms of Eq. (2.23) is negligible. Moreover, in the TDM set-up, the condition $\alpha' \ll \frac{\pi}{p}$ is verified thanks to the high magnification (about 290) of the field imaged on the wavefront sensor. The highest spatial frequency $\alpha'_{\max}$ of this field is given through the Abbe relation by $\alpha'_{\max} = k_0 \mathrm{NA}/290 = 32.5\ \mathrm{nm}^{-1}$, to be compared to $\frac{\pi}{p} = 106\ \mathrm{nm}^{-1}$, with $p = 29.6\ \mu\mathrm{m}$.

2.3 Rigorous nonlinear inversion procedures in 3D

The nonlinear numerical inversion procedures reconstruct the sample permittivity map according to the diffracted field for many scattered angles and under illuminating the sample with different directions. This algorithm has already been applied with success to the imaging of highly contrasted two-dimensional sample[32,79,80].

2.3.1 The direct problem

The scattering of an electromagnetic wave by an arbitrary, three dimensional scatterer is a complex problem of central importance in optics and photonics. Aside from a few particular systems, the interaction of electromagnetic waves with an arbitrary object induces an analytical representation and numerical methods are needed. Many such methods have been developed[93], in this thesis, we have considered a volume integral method named the coupled dipole method (CDM). This approach was introduced by Purcell and Pennypacker in 1973[94] to study the scattering light by non-spherical dielectric grains in free space. The theoretical foundation of the CDM depends on the fact that when an object interacts with an electromagnetic field, it develops a polarization and gives rise to a system of linear equations. If one considers a small enough volume inside the object, the induced polarization is uniform within this volume, and hence any object can be discretized as a collection of dipolar subunits[34].

2.3.1.1 Computation of the scattered field: the coupled dipole method

To compute the scattered field by an arbitrary object with a volume integral method, one needs to solve Eq. (1.19) established in chapter 1:

$$\boldsymbol{E}(\boldsymbol{r}) = \boldsymbol{E}_{\mathrm{ref}}(\boldsymbol{r}) + k_0^2 \int_V \boldsymbol{G}(\boldsymbol{r},\boldsymbol{r}')[\varepsilon(\boldsymbol{r}') - 1]\boldsymbol{E}(\boldsymbol{r}')\mathrm{d}V, \tag{2.24}$$

where $\boldsymbol{E}_{\mathrm{ref}}(\boldsymbol{r})$ is the electromagnetic field in the absence of the object under study: it could be the incident field in homogeneous space or the incident field plus its reflected field if the object is in presence of a substrate. A straightforward method for numerically solving Eq. (2.24) is the coupled dipole method or equivalently the method of moments (MoM) which is based on replacing the volume integral by a discrete sum over finite volume elements. We show the case of a cubical grid in Fig. 2.8. If the volume elements are sufficiently small compared to the wavelength of illumination or the variation of the field inside the object, we can assume that $\varepsilon(\boldsymbol{r})$ and $\boldsymbol{E}(\boldsymbol{r})$ are uniform in each cell.

In using the cubic discretization Eq. (2.24) can be rewritten as:

$$\boldsymbol{E}(\boldsymbol{r}) = \boldsymbol{E}_{\mathrm{ref}}(\boldsymbol{r}) + k_0^2 \sum_{j=1}^{N} \int_{V_j} \boldsymbol{G}(\boldsymbol{r},\boldsymbol{r}')[\varepsilon(\boldsymbol{r}') - 1]\boldsymbol{E}(\boldsymbol{r}')\mathrm{d}V. \tag{2.25}$$

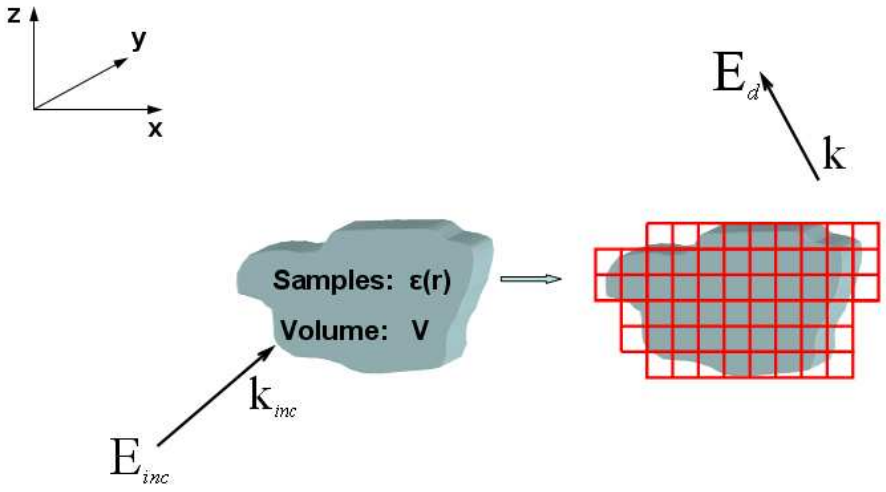

Figure 2.8 : *Discretization diagram for direct problem. The permittivity of sample is $\varepsilon(\boldsymbol{r})$ and volume V, the object under study is discretized into small cubic units.*

where N denotes the number of cubic subunits to represent the object and V_j the volume of the j-th element of discretization with $V_j = V = d^3$ where d is the mesh size of the lattice. Then we use the hypothesis that the field and the permittivity are uniform and equal to their value at the center of the subunit:

$$\boldsymbol{E}(\boldsymbol{r}) = \boldsymbol{E}_{\mathrm{ref}}(\boldsymbol{r}) + k_0^2 \sum_{j=1}^{N} \left[\int_{V_j} \boldsymbol{G}(\boldsymbol{r}, \boldsymbol{r}') \mathrm{d}V \right] [\varepsilon(\boldsymbol{r}_j) - 1] \boldsymbol{E}(\boldsymbol{r}_j). \tag{2.26}$$

Afterwards, Eq. (2.26) can be transformed into a system of linear equations if the total field is evaluated inside the object under study at the position of a subunit:

$$\boldsymbol{E}(\boldsymbol{r}_i) = \boldsymbol{E}_{\mathrm{ref}}(\boldsymbol{r}_i) + k_0^2 \sum_{j=1}^{N} \left[\int_{V_j} \boldsymbol{G}(\boldsymbol{r}_i, \boldsymbol{r}') \mathrm{d}V \right] [\varepsilon(\boldsymbol{r}_j) - 1] \boldsymbol{E}(\boldsymbol{r}_j). \tag{2.27}$$

with $i = 1, \cdots, N$.

At this stage one can notice that the free-space dyadic Green's function has a singularity when we need to evaluate $\int_{V_i} \boldsymbol{G}(\boldsymbol{r}_i, \boldsymbol{r}')$ with $\boldsymbol{r}' \in V_i$. We have in the literature different approximations of this self term. The most cruder approximation consists in computing the self term assuming that the volume V_i approaches zero, *i.e.* as V_i shrinks down around the point $\boldsymbol{r}_i$ [95,96]:

$$\int_{V_i} \boldsymbol{G}(\boldsymbol{r}_i, \boldsymbol{r}') \mathrm{d}V = -\frac{\boldsymbol{I}}{3k_0^2}. \tag{2.28}$$

The problem with this formulation is that if one computes the cross section or optical forces one gets an incorrect result. This is due to the fact that the optical theorem is not satisfied. This is due to the approximation to assume that the volume V_i approaches zero. The evaluation of this integral can be accomplished numerically for regions of different shape, but it is difficult and time consuming to perform the integration without any approximation on the cubic cell. Hence the region V_i is often assumed to be a spherical cell with a radius a such that $\frac{4\pi}{3}a^3 = d^3$, *i.e.* the same volume between the spherical cell and cubic cell [97–100]. Then in that case we get

$$\int_{V_i} \boldsymbol{G}(\boldsymbol{r}_i, \boldsymbol{r}') \mathrm{d}V \approx -\frac{\boldsymbol{I}}{3k_0^2} + i\frac{2}{3}\boldsymbol{I}\frac{d^3}{4\pi}k_0 := d^3 \boldsymbol{G}(\boldsymbol{r}_i, \boldsymbol{r}_i). \tag{2.29}$$

Notice that when we evaluate $\int_{V_j} \boldsymbol{G}(\boldsymbol{r}_i, \boldsymbol{r}')$ with $i \neq j$ we also assume the Green's function to be constant versus $\boldsymbol{r}'$ so that we get:

$$\int_{V_j} \boldsymbol{G}(\boldsymbol{r}_i, \boldsymbol{r}')\mathrm{d}V \simeq d^3 \boldsymbol{G}(\boldsymbol{r}_i, \boldsymbol{r}_j). \tag{2.30}$$

Then the linear system can be written as:

$$\boldsymbol{E}(\boldsymbol{r}_i) = \boldsymbol{E}_{\mathrm{ref}}(\boldsymbol{r}_i) + k_0^2 d^3 \sum_{j=1}^{N} \boldsymbol{G}(\boldsymbol{r}_i, \boldsymbol{r}_j)[\varepsilon(\boldsymbol{r}_j) - 1]\boldsymbol{E}(\boldsymbol{r}_j). \tag{2.31}$$

with $i = 1, \cdots, N$. Once the linear system represented by Eq. (2.31) is solved, the total field inside the object is perfectly known and the scattered field in the far-field zone, $\boldsymbol{E}_{\mathrm{s}}(\boldsymbol{r})$ can be computed at an arbitrary position $\boldsymbol{r}$ with

$$\boldsymbol{E}_{\mathrm{s}}(\boldsymbol{r}) = k_0^2 d^3 \sum_{j=1}^{N} \boldsymbol{G}(\boldsymbol{r}, \boldsymbol{r}_j)[\varepsilon(\boldsymbol{r}_j) - 1]\boldsymbol{E}(\boldsymbol{r}_j). \tag{2.32}$$

The self-consistent Eq. (2.31) and the far-field Eq. (2.32) assuming that the scattered field is computed at M points of observation, can be rewritten in a more condensed form as:

$$\boldsymbol{E} = \boldsymbol{E}_{\mathrm{ref}} + \boldsymbol{A}\chi\boldsymbol{E} \tag{2.33}$$

$$\boldsymbol{E}_{\mathrm{s}} = \boldsymbol{B}\chi\boldsymbol{E}, \tag{2.34}$$

where $\boldsymbol{A}$ is a square matrix of size $(3N \times 3N)$ and contains all the tensors $\boldsymbol{G}(\boldsymbol{r}_i, \boldsymbol{r}_j)$. We have

$$\boldsymbol{E} = [E_x(\boldsymbol{r}_1), E_y(\boldsymbol{r}_1), E_z(\boldsymbol{r}_1), \cdots, E_z(\boldsymbol{r}_N)] \tag{2.35}$$

$$\boldsymbol{E}_{\mathrm{ref}} = [E_{x,\mathrm{ref}}(\boldsymbol{r}_1), E_{y,\mathrm{ref}}(\boldsymbol{r}_1), E_{z,\mathrm{ref}}(\boldsymbol{r}_1), \cdots, E_{z,\mathrm{ref}}(\boldsymbol{r}_N)], \tag{2.36}$$

$\boldsymbol{B}$ is a matrix of size $(3M \times 3N)$. The matrix $\boldsymbol{B}$ contains the tensors, $\boldsymbol{G}(\boldsymbol{r}_k, \boldsymbol{r}_j)$, where $\boldsymbol{r}_j$ denotes a point in the discretized object, $j = 1, \cdots, N$, while $\boldsymbol{r}_k$ is an observation point, $k = 1, \cdots, M$. Note that $\boldsymbol{B}$ and $\boldsymbol{A}$ do not depend on the angle of incidence. χ is a diagonal matrix of size $(3N \times 3N)$ which contains the contrast of permittivity. As the material is isotropic the diagonal of the matrix can be written as $\mathrm{Diag}(\chi) = [\Delta\varepsilon(\boldsymbol{r}_1), \Delta\varepsilon(\boldsymbol{r}_1), \Delta\varepsilon(\boldsymbol{r}_1), \cdots, \Delta\varepsilon(\boldsymbol{r}_N)]$.

2.3.1.2 Strengths and drawbacks of the coupled dipole method

Volume-integral equation methods have several advantages. They are applicable to arbitrarily shaped, inhomogeneous and anisotropic particles. The radiation condition is automatically satisfied through the dyadic Green's function. The computation is confined to the volume of the scatterer, which results in fewer unknowns as in many finite-difference methods. Notice that if the particle under study is in presence of a substrate or multilayer or grating one needs only to compute the new Green's function to take into account the new complex environment [101–104].

A disadvantage is that the computational accuracy is only improved slowly as the number of cells is increased. In the configuration presented in this manuscript the spacing lattice used is typically around $d = \lambda/10$. In fact, the main problem is the time of computation needed to solve the large linear system represented by Eq. (2.31). Generally to perform this resolution quickly, we use a conjugate gradient method with fast Fourier transform [105–107]

2.3.2 The nonlinear inversion algorithm for 3D imaging

The aim of inverse algorithm is stated as finding the relative permittivity ε of the object under study from its measured scattered field . A numbers of accurate iterative techniques have been developed to solve this inverse problem, for example, the linearized methods are developed based on

Born type approximation by W. Chew, A. G. Tijhuis, K. Belkebir, etc[108–111], a modified gradient method is presented by R. E. Kleinman and P. M. Van Den Berg[112,113] to find the permittivity by a minimization procedure, under the condition of a unknown test domain Ω. However, almost all these methods deal with two dimensional inverse problems, especially, in three dimensions, most techniques use a linear inversion based on Born approximation or Rytov approximation[44,50] and are restricted to the scalar case. Therefore, a hybrid method with an iterative nonlinear inversion algorithm based on a rigorous vectorial modeling of the wave-sample interaction, combing the two main methods mentioned above, is developed to solve the 3D reconstruction problem[105,114,115] in our team. This algorithm has already been applied with success to the imaging of highly contrasted two dimensional objects[32,79,80,116].

In our TDM measurement the scattered electromagnetic field is detected in far field in M observation points that are located on a surface Γ by L successive illuminations. This measured field is noted $\boldsymbol{f}_l$ with $l = 1, \cdots, L$. Note that we assume that the unknown object is confined in a known bounded box Ω (test domain or an investigation domain,see Fig. 2.9). Notice that in

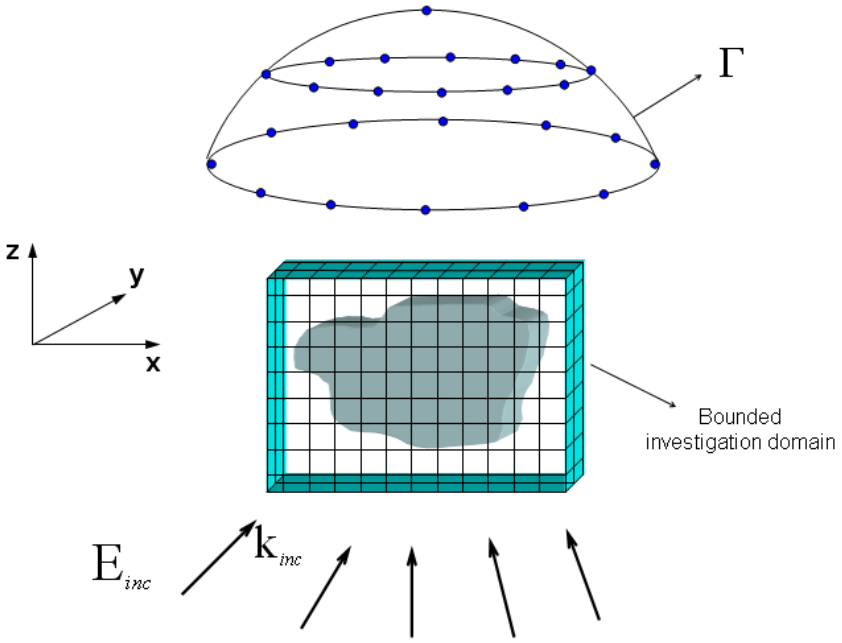

Figure 2.9 : *Sketch of the illumination and detection configuration of TDM, the large discretized box is the investigation domain for the inverse problem, the blue points are the observation points in far-field.*

practice, as the dimensions of the object are *a priori* not known, it is necessary to find at a first step a size for the domain that is large enough to contain the object. The transverse dimensions of the domain can easily be determined from the image field of the object illuminated under normal incidence. The axial dimension can be evaluated by observing this image field for different positions of the object along the optical axis, or from the 3D reconstruction obtained with the conventional 3D inverse Fourier transform inversion. This point will be discussed in more details in chapter 3.

The Hybrid Method (HM) combines the advantage of conjugate gradient method and contrast source inversion: χ and the internal field $\boldsymbol{E}_l$ are determined iteratively. The minimized cost function of HM is the one used in the Modified Gradient Method[112]:

$$\mathcal{F}_n(\chi_n, \boldsymbol{E}_{l,n}) = W_\Gamma \sum_{l=1}^{L} \|\boldsymbol{h}_{l,n}^{(1)}\|_\Gamma^2 + W_\Omega \sum_{l=1}^{L} \|\boldsymbol{h}_{l,n}^{(2)}\|_\Omega^2, \tag{2.37}$$

The subscripts Ω and Γ are included in the norm $\|.\|$ to indicate the domain of integration. $\boldsymbol{h}^{(1)}$ and W_Γ are the residual error in the observation equation and a weighting coefficient, respectively.

$$\boldsymbol{h}_{l,n}^{(1)} = \boldsymbol{f}_l - \boldsymbol{B}\chi\boldsymbol{E}_l \quad \text{and} \quad W_\Gamma = \left(\sum_{l=1}^{L} \|\boldsymbol{f}_l\|_\Gamma^2\right)^{-1}, \tag{2.38}$$

Physically, $\sum_{l=1}^{L} \|\boldsymbol{h}_{l,n}^{(1)}\|_\Gamma^2$ describes the discrepancy between the measured scattered far-field and the simulated one associated to the best available estimate of the relative permittivity. $\boldsymbol{h}^{(2)}$ and W_Ω are the residual error in the near field equation and a weighting coefficient, respectively:

$$\boldsymbol{h}_{l,n}^{(2)} = \boldsymbol{E}_{l,\text{ref}} - \boldsymbol{E}_{l,n} + \boldsymbol{A}\chi_n\boldsymbol{E}_{l,n} \quad \text{and} \quad W_\Omega = \left(\sum_{l=1}^{L} \|\chi_{n-1}\boldsymbol{E}_{l,\text{ref}}.\|_\Omega^2\right)^{-1}, \tag{2.39}$$

where $\sum_{l=1}^{L} \|\boldsymbol{h}_{l,n}^{(2)}\|_\Omega^2$ represents the discrepancy between the estimate $\mathbf{E}_{l,n}$ and its calculation following Maxwell's equations using the estimated χ_n and $\mathbf{E}_{\text{ref}}$.

Two sequences related to the contrast χ and to the field $\boldsymbol{E}_l$ inside the investigating domain Ω are built up according to the following recursive relations

$$\chi_n = \chi_{n-1} + b_n d_n \tag{2.40}$$

$$\boldsymbol{E}_{l,n} = \boldsymbol{E}_{l,n-1} + a_{l,n}^v \boldsymbol{v}_{l,n} + a_{l,n}^w \boldsymbol{w}_{l,n}, \tag{2.41}$$

where $\boldsymbol{v}_{l,n}$, $\boldsymbol{w}_{l,n}$ and d_n are updating directions with respect to the total field $\boldsymbol{E}_l$ and to the contrast χ, respectively. The scalar coefficients $a_{l,n}^v$, $a_{l,n}^w$ and $b_{l,n}$ are weights that are determined at each iteration step n such that they minimize the normalized cost functional given in Eq. (2.37). The minimization is accomplished using the Polak-Ribière conjugate gradient procedure [119]. The originality of HM lays in the introduction of two search directions for the total field, $\boldsymbol{w}_{l,n}$, and $\boldsymbol{v}_{l,n}$ which stem from the conjugate gradient method and contrast source inversion, respectively. Basically, $\boldsymbol{w}_{l,n}$ fastens the retrieval of the internal field (especially if the data are not too noisy and the target is not too contrasted) as in conjugate gradient method while $\boldsymbol{v}_{l,n}$ brings the robustness to noise and the stability when handling strongly diffracting targets as in contrast source inversion. They are written as[i],

$$\boldsymbol{v}_{l,n} = \boldsymbol{g}_{l,n;\boldsymbol{E}} + \gamma_{l,n;\boldsymbol{E}} \boldsymbol{v}_{l,n-1} \quad \text{with} \quad \gamma_{l,n;\boldsymbol{E}} = \frac{\langle \boldsymbol{g}_{l,n;\boldsymbol{E}}, \boldsymbol{g}_{l,n;\boldsymbol{E}} - \boldsymbol{g}_{l,n-1;\boldsymbol{E}} \rangle_\Omega}{\|\boldsymbol{g}_{l,n-1;\boldsymbol{E}}\|_\Omega^2} \tag{2.42}$$

$$\boldsymbol{w}_{l,n} = \tilde{\boldsymbol{E}}_l - \boldsymbol{E}_{l,n-1} \quad \text{with} \quad \tilde{\boldsymbol{E}}_l = (\boldsymbol{I} - \boldsymbol{A}\chi_{n-1})^{-1} \boldsymbol{E}_{l,\text{ref}}, \tag{2.43}$$

where $\boldsymbol{g}_{l,n;\boldsymbol{E}}$ is the gradient of the cost functional $\mathcal{F}_n(\chi_n, \boldsymbol{E}_{l,n})$ with respect to $\boldsymbol{E}_l$, assuming $\xi = \xi_{n-1}$ and $\eta = \eta_{n-1}$. Note that, similarly to conjugate gradient method, one forward problem has to be solved at each iteration.

To ameliorate the reconstruction, we incorporate *a priori* information stating that both real and imaginary parts of the electrical susceptibility χ are non negative. Instead of retrieving a complex valued function χ_n, two real auxiliary functions ξ_n and η_n are reconstructed such that $\chi_n = 1 + \xi_n^2 + i\eta_n^2 - \varepsilon_b$, with ε_b the relative permittivity of the background. The real and the imaginary parts of the relative complex permittivity distribution are, herein, forced to be greater than unity and non-negative, respectively. The recursive relation with respect to the complex contrast function χ_n is refined as

$$\xi_n = \xi_{n-1} + b_{n;\xi} d_{n;\xi} \quad \text{and} \quad \eta_n = \eta_{n-1} + b_{n;\eta} d_{n;\eta}. \tag{2.44}$$

The updating directions $d_{n;\xi}$ and $d_{n;\eta}$ are taken to be the standard Polak-Ribière conjugate gradient direction

$$d_{n;\xi} = g_{n;\xi} + \gamma_{n;\xi} d_{n-1;\xi} \quad \text{with} \quad \gamma_{n;\xi} = \frac{\langle g_{n;\xi}, g_{n;\xi} - g_{n-1;\xi} \rangle_\Omega}{\|g_{n-1;\xi}\|_\Omega^2} \tag{2.45}$$

$$d_{n;\eta} = g_{n;\eta} + \gamma_{n;\eta} d_{n-1;\eta} \quad \text{with} \quad \gamma_{n;\eta} = \frac{\langle g_{n;\eta}, g_{n;\eta} - g_{n-1;\eta} \rangle_\Omega}{\|g_{n-1;\eta}\|_\Omega^2}, \tag{2.46}$$

[i] We use the following notation: $\langle \boldsymbol{u} | \boldsymbol{v} \rangle_\Omega = \sum_\Omega \boldsymbol{u}^*.\boldsymbol{v}$ where * denotes the complex conjugate

where $g_{n;\xi}$ and $g_{n;\eta}$ are the gradients of the cost functional $\mathcal{F}_n(\chi_n, \boldsymbol{E}_{l,n})$ with respect to ξ (respectively η), evaluated at the n-th step assuming that the total field inside the test domain does not change.

The gradients used in the HM are the gradients of the functional:

$$\begin{aligned}\mathcal{F}_n(\xi_n, \eta_n, \boldsymbol{E}_{l,n}) = W_\Gamma \sum_{l=1}^{L} \|\boldsymbol{f}_l - \boldsymbol{B}(1 + \xi_n^2 + i\eta_n^2 - \varepsilon_b)\boldsymbol{E}_{l,n}\|_\Gamma^2 \\ + W_\Omega \sum_{l=1}^{L} \|\boldsymbol{E}_{l,\mathrm{ref}} - \boldsymbol{E}_{l,n} + \boldsymbol{A}(1 + \xi_n^2 + i\eta_n^2 - \varepsilon_b)\boldsymbol{E}_{l,n}\|_\Omega^2. \end{aligned} \tag{2.47}$$

Notice that to define the gradient of a functional, one needs first the definition of the directional derivative. If x is the unknown we call $D_x\mathcal{F}(u)$ the directional derivative of $\mathcal{F}$ along the direction u and write it as:

$$D_x\mathcal{F}(u) = \lim_{t\to 0} \frac{\mathcal{F}(x + tu) - \mathcal{F}(x)}{t}. \tag{2.48}$$

Then the gradient of $\mathcal{F}$ is defined as the direction where the directional derivative is the highest. Notice that, as shown in Eqs. (2.40) and (2.41), since the gradient is always multiplied by a constant that is optimised we do not care of the norm of the gradient, only of its direction. Then the gradients according to ξ_n and η_n are given by:

$$g_{n;\xi} = 2\xi_{n-1}\mathrm{Re}\left[W_\Omega \sum_{l=1}^{L} \boldsymbol{E}_{l,n-1}^*.\boldsymbol{A}^\dagger \boldsymbol{h}_{l,n-1}^{(2)} - W_\Gamma \sum_{l=1}^{L} \boldsymbol{E}_{l,n-1}^*.\boldsymbol{B}^\dagger \boldsymbol{h}_{l,n-1}^{(1)}\right], \tag{2.49}$$

$$g_{n;\eta} = 2\eta_{n-1}\mathrm{Im}\left[W_\Omega \sum_{l=1}^{L} \boldsymbol{E}_{l,n-1}^*.\boldsymbol{A}^\dagger \boldsymbol{h}_{l,n-1}^{(2)} - W_\Gamma \sum_{l=1}^{L} \boldsymbol{E}_{l,n-1}^*.\boldsymbol{B}^\dagger \boldsymbol{h}_{l,n-1}^{(1)}\right]. \tag{2.50}$$

The gradient according to $\boldsymbol{E}_{l,n}$ is given by:

$$g_{l,n;\boldsymbol{E}} = W_\Omega \left[\chi_{n-1}^* \boldsymbol{A}^\dagger \boldsymbol{h}_{l,n-1}^{(2)} - \boldsymbol{h}_{l,n-1}^{(2)}\right] - W_\Gamma \chi_{n-1}^* \boldsymbol{B}^\dagger \boldsymbol{h}_{l,n-1}^{(1)}. \tag{2.51}$$

In these three equations, the symbol * denotes the complex conjugate, and $\boldsymbol{M}^\dagger$ is the adjoint operator of the operator $\boldsymbol{M}$. With the values of the gradient then one needs to minimize the cost function with respect to the coefficient b_n, $+a_{l,n}^v$ and $a_{l,n}^w$. This minimization is done numerically.

Chapter 3

3D experimental reconstructions with non-linear inversion procedures

Contents

3.1 Data treatment procedures 37
3.1.1 Angular calibration 37
3.1.2 Normalization procedure of the measurements 38
3.1.3 Determination of the phase origin mismatch 42
3.2 Experimental results 43
3.2.1 Resin cylinders with diameter 1 μm. 44
3.2.2 Resin cylinders with diameter 500 nm 56
3.2.3 Resin cylinders with diameter 200 nm 72
3.2.4 Resin cylinders with diameter 150 nm 79

3.1 Data treatment procedures to apply before performing the numerical inversion

In order to obtain a quantitative reconstruction of the optogeometrical parameters of the sample, a normalization procedure has to be applied to the experimental data before applying the inversion procedure to the diffracted fields obtained for the different illumination incidences.

3.1.1 Angular calibration

The inversion of experimental data necessitates a precise knowledge of the illumination angles involved during the measurement and also of the scattering angles within the numerical aperture of the objective. The angular calibration is done with a reference object of known dimensions. As the measurements are performed in the image space, it is possible to determine precisely the discretization pitch of the image of this object. Then the discrete FT^{-1} used to transfer the data to the Fourier space gives the discretization pitch in the Fourier space. This pitch permits to address

a scattering angle to every pixel inside the objective NA, knowing that scattering angle zero is at the center of the Fourier space. Every illumination angle can thus also be evaluated thanks to the position of the pixel corresponding to the focus of the specular reflection, as the objects are deposited on a reflective substrate.

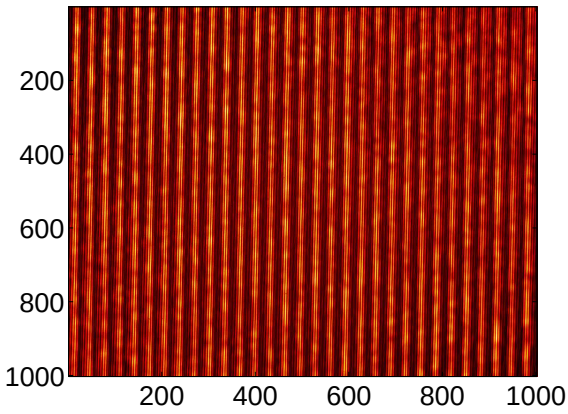

Figure 3.1 : *Intensity image of a grating (1200 grooves per mm) used as reference object*

The reference object used is a diffraction grating with 1200 grooves/mm, its intensity image is shown on Fig. 3.1. We found that on this image 933 pixels correspond to 29 periods of the grating, what gives a pitch Δx of 25.9 nm per pixel. The pitch Δk_x in the Fourier space is related to Δx thanks to the discrete FT through the equation :

$$N\Delta x\Delta k_x = 2\pi, \tag{3.1}$$

where $N = 1004$ is the number of pixels along the x direction on the CCD camera. The same equation is valid along the y direction since the CCD sensor is a square. The distance of any pixel in the Fourier space with respect to the origin can be written as $\sqrt{k_x^2 + k_y^2} = k_0 \sin\theta$, where θ is the polar scattering angle in spherical coordinates. Thus, knowing the pitch Δk_x permits to retrieve θ at any position in the Fourier space.

3.1.2 Normalization procedure of the measurements

To retrieve a quantitative 3D permittivity map of the sample, it is necessary to apply a normalization procedure to the amplitude and the phase of the measured scattered field prior to performing the non-linear inversion. Such a normalization aims at adapting the measurements to the modelling hypotheses underlying the inversion algorithm. It uses as reference the measured specular reflection on the substrate, ensuring that it matches both in amplitude and phase the specular reflection as calculated by the forward scattering model. This implies that the specular reflection has to be far stronger than the field scattered in the same direction by the sample, what is verified for small objects.

Note that the scattered field measured in the image space for illumination number l is called $\tilde{\boldsymbol{f}}_l$, to distinguish with the data $\boldsymbol{f}_l$ once transferred in the Fourier space and used by the non-linear inversion algorithm.

3.1.2.1 Amplitude normalization

The non-linear inversion assumes that the object is illuminated for each angle of incidence by a plane wave with a unity amplitude. The measured amplitudes $\|\tilde{\boldsymbol{f}}_l\|$ have therefore to be normalized

according to this hypothesis so that a correct estimation of the permittivity can be retrieved. The amplitude normalization is moreover useful to correct the intensity fluctuations of the illuminating beam that can occur from one illumination angle to another. It is performed for each illumination l by multiplying $\tilde{\boldsymbol{f}}_l$ by the factor M_l :

$$M_l = \frac{|\gamma_l||r_l|S}{2\pi\langle\|\tilde{\boldsymbol{f}}_l\|\rangle_S}, \tag{3.2}$$

where $\gamma_l = -k_0 \cos\theta_l$ is the projection of the illumination wave vector on the optical axis of the microscope (the minus sign is due to the reflection configuration), r_l is the Fresnel amplitude reflection coefficient on the substrate, and S the surface of the field of view that can be imaged on the CCD sensor. $\langle\|\tilde{\boldsymbol{f}}_l\|\rangle_S$ is the mean field modulus averaged over the field of view: as the object is small on the CCD image, it can be considered as the mean field modulus reflected by the substrate. The multiplication by M_l ensures that the maximal value of $\|\boldsymbol{f}_l\|$ in far field, which corresponds to the specular reflection, is equal to that scattered by a portion of substrate of surface S when illuminated by a plane wave with unity amplitude, as calculated by the forward scattering model.

★ **Fresnel reflection coefficient** r_l

The Fresnel amplitude reflection coefficient r_l on the substrate depends on the polarization of the illumination. If the illumination is a TE-polarized plane wave, which means its electric field is in the plane of the interface, r_l is given by :

$$r_l = \frac{(k_0^2 - \alpha_l^2)^{1/2} - (n_s^2 k_0^2 - \alpha_l^2)^{1/2}}{(k_0^2 - \alpha_l^2)^{1/2} + (n_s^2 k_0^2 - \alpha_l^2)^{1/2}}, \tag{3.3}$$

where $\alpha_l = k_0 \sin\theta_l$ is the projection of the illumination wave vector on the interface and $n_s = 3.882 + 0.019i$ is the refractive index of the silicon substrate. Note that the imaginary part of n_s is neglected to calculate r_l. For the case of a TM-polarized plane wave, where the elecric field is in the plane of incidence, r_l becomes :

$$r_l = \frac{-n_s^2(k_0^2 - \alpha_l^2)^{1/2} - (n_s^2 k_0^2 - \alpha_l^2)^{1/2}}{n_s^2(k_0^2 - \alpha_l^2)^{1/2} + (n_s^2 k_0^2 - \alpha_l^2)^{1/2}}. \tag{3.4}$$

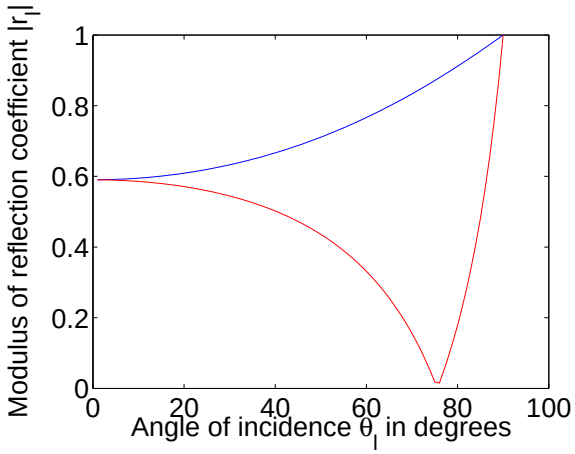

Figure 3.2 : *Fresnel amplitude reflection coefficient as a function of the illumination angle : TE case in blue and TM case in red.*

The modulus of r_l is shown as a function of the illumination angle θ_l on Fig. 3.2 for the TE and TM cases. While it increases with θ_l in the TE case, it decreases to reach zero at the Brewster

angle in the TM case, before increasing towards 1. Note however that the objective NA cut all angles above 72°, and therefore the Brewster incidence of 78° cannot be reached experimentally.

★ **Validation of the amplitude normalization**

The multiplication of the measured field by factor M_l aims at normalizing to one the maximal value of $\|\boldsymbol{f}_l\|$, and then multiply it by the maximal value of the modulus of the field scattered by a portion of substrate that has the size of the field of view imaged on the camera. This value is the specular reflection peak as calculated by the forward scattering model. To verify that it is given by $|\gamma_l||r_l|S/(2\pi)$, as stated in the expression of factor M_l, a reference object with a simple geometry has been used to calculate the scattered field with the Coupled Dipole Method (CDM).

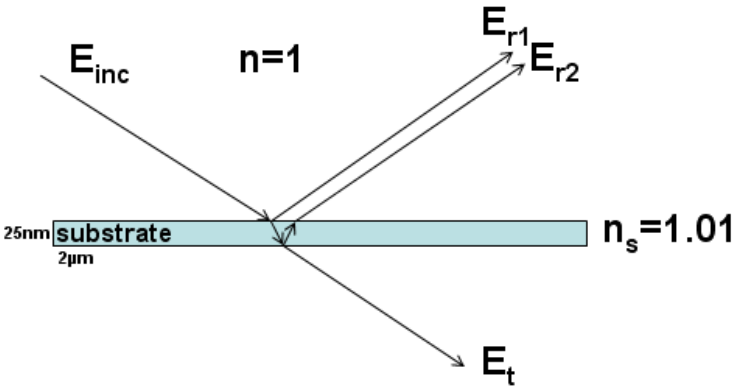

Figure 3.3 : *Sketch of the reference object used to test the validity of the amplitude normalization factor : a transparent parallelepiped of refractive index $n_s = 1.01$ and dimensions 2 μm × 2 μm × 25 nm.*

This object has been chosen as a very thin parallelepiped made of two squares of sides 2 μm, separated by $e = 25$ nm, with the inside filled with a material of very low refractive index $n_s = 1.01$ (see Fig. 3.3). When a plane wave illuminates one of the square faces with an angle of incidence θ_l, two reflections will be produced from each square face, neglecting multiple reflections due to the very low refractive index contrast with air. These two reflections will interfere in far-field, with a phase shift $\Delta\varphi = \pi + 2n_s e\cos(\theta_l^r)$, where θ_l^r is the refraction angle inside the parallelepiped. Thus, the specular reflection peak in far-field can be calculated by $|\gamma_l||r_l|S(1 + e^{i\Delta\varphi})/(2\pi)$, where S is the surface of the square.

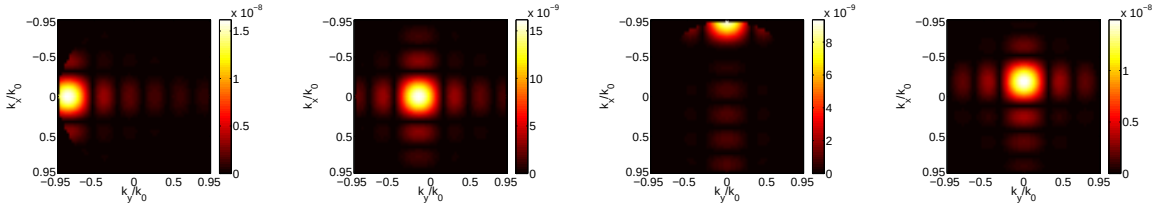

(a) (b) (c) (d)

Figure 3.4 : *Modulus of the far field scattered by the reference object depicted on Figure 3.3 for different polar and azimuthal illumination angles θ_l and ϕ_l, respectively. (a) $\theta_l = 55°$, $\phi_l = 0°$; (b) $\theta = 9°$, $\phi_l = 0°$; (c) $\theta_l = 57°$, $\phi_l = 90°$; (d) $\theta_l = 9°$, $\phi_l = 90°$*

The far field scattered by this object is calculated by the CDM with a meshing of 25 nm for different polar and azimuthal illumination angles θ_l and ϕ_l, respectively. The modulus of the

scattered field inside of the objective NA is shown on Fig. 3.4 for : (a) $\theta_l = 55°$, $\phi_l = 0°$, TE polarization; (b) $\theta = 9°$, $\phi_l = 0°$, TE polarization; (c) $\theta_l = 55°$, $\phi_l = 90°$, TM polarization; (d) $\theta_l = 9°$, $\phi_l = 90°$, TM polarization. The peak values computed with the CDM are respectively of 0.1618×10^{-7}, 0.1617×10^{-7}, 0.0741×10^{-7} and 0.1537×10^{-7}, whereas the ones calculated with the aforementioned expression are 0.1570×10^{-7}, 0.1560×10^{-7}, 0.0562×10^{-7} and 0.1483×10^{-7}. Such a good agreement was also found for other couples of values for θ_l and ϕ_l. It shows that the factor M_l can effectively normalize the amplitude of the measured field so that the specular reflection peak reaches the value that would have been calculated by the CDM. The scattered field has then the adapted signal level for the inversion procedure to retrieve the right value for the sample permittivity.

3.1.2.2 Phase normalization

The nonlinear inversion is usually set so that the spatial origin for the phase is placed on the substrate and in the middle of the transverse dimensions of the investigation domain Ω. It implies that whatever the illumination l, the phase of the illuminating plane wave is zero at this location. Experimentally however, the phase of the illuminating beam is never exactly the same when reaching the sample, since thermal and/or mechanical drifts can occur or simply because the optical path of the beam can vary from one illumination angle to another. Moreover, the experimental spatial origin for the phase is usually different from the one assumed in the model, what modifies the measured phase compared to that calculated with the forward model.

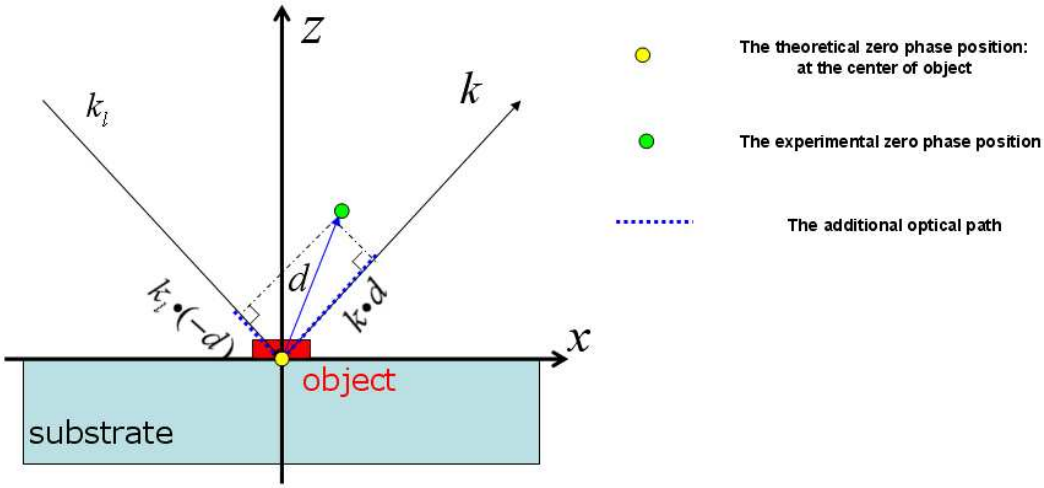

Figure 3.5 : *Positions of the theoretical and experimental phase origins with respect to the object, and indication of the additional phase shifts due to the shift of the phase origin from the theoretical position to the experimental one.*

Calling $\boldsymbol{d}$ the position of the experimental phase origin with respect to the theoretical one, the experimental phase φ_d of the scattered far-field is linked to the theoretical one φ_0 by the following equation :

$$\varphi_\mathrm{d}(\boldsymbol{k}, \boldsymbol{k}_l) = \varphi_0(\boldsymbol{k}, \boldsymbol{k}_l) + (\boldsymbol{k} - \boldsymbol{k}_l) \cdot \boldsymbol{d}, \tag{3.5}$$

where $\boldsymbol{k}_l$ is the illumination wave vector and $\boldsymbol{k}$ the one along which the field is scattered. Figure 3.5 shows the positions of the theoretical and experimental phase origins with respect to the position of the sample, and the additional phase shifts due to the shift of the phase origin at position $\boldsymbol{d}$. A first additional phase shift $(-\boldsymbol{k}_l \cdot \boldsymbol{d})$ is due to the propagation of the illumination field from the experimental phase origin to the theoretical one, where the sample has to be located for the

inversion. A second one ($\boldsymbol{k}\cdot\boldsymbol{d}$) stems from the propagation of the scattered field along direction $\boldsymbol{k}$ from the theoretical phase origin to the experimental one, before propagating to the far field.

As the scattered field $\tilde{\boldsymbol{f}}_l$ is measured in a plane conjugated with the object, the phase origin can be chosen visually at the object center in this plane when performing the 2D FT^{-1} to generate the far-field data $\boldsymbol{f}_l$. The transverse components of the phase origin mismatch $\boldsymbol{d}$ can then be neglected and the object reconstructed at the center of the transverse extent of Ω. However the imaging plane is never perfectly conjugated with the substrate plane, so that an axial component is remaining for $\boldsymbol{d}$. Dedicated methods have been developed to retrieve this component d_z, they are presented in the following section. Once d_z is determined, it is corrected on the data set using Eq. (3.5). Then, the phase for each illumination is shifted so that the phase at the specular reflection is equal to the argument of the theoretical Fresnel reflection coefficient on the substrate, for a phase origin taken on the substrate. In this way, the data set is normalized to the case where the illumination beam has a phase equal to zero at the spatial origin for each incidence angle.

3.1.3 Determination of the phase origin mismatch

A first method to retrieve the remaining axial component d_z of the phase origin mismatch consists in applying a 3D FT^{-1} to the data set $\boldsymbol{f}_l$, as if the Born approximation was valid. It generates an approximate reconstruction of the object, that is sufficient to locate accurately the axial position of the object center with respect to the center of the reconstruction domain, which is actually the d_z value we are looking for. Indeed, within the Born approximation and using Eqs. (1.24) and (3.5), the inverse Fourier transform of the data set corrupted by a mismatch $\boldsymbol{d}$ reads :

$$\int \Delta\tilde{\varepsilon}(\boldsymbol{k}-\boldsymbol{k}_l)e^{i(\boldsymbol{k}-\boldsymbol{k}_l)\cdot(\boldsymbol{r}-\boldsymbol{d})}\mathrm{d}^3(\boldsymbol{k}-\boldsymbol{k}_l) \propto \Delta\varepsilon(\boldsymbol{r}-\boldsymbol{d}). \tag{3.6}$$

The reconstruction is thus shifted by $\boldsymbol{d}$ compared to the one obtained without phase origin mismatch. Note that the inverse Fourier transform is performed with a normalized data set as described in the previous section. However the phase normalization is not perfectly achieved, since when the phase origin is not located on the substrate the term $2|\gamma_l|d_z$ has to be added to the argument of the Fresnel reflection coefficient, as will be mentioned hereafter. As d_z has not yet been determined, it is considered as equal to zero for the phase normalization. This approximation can at worst distort the object reconstruction, but not change its localisation within the reconstruction domain, so it does not compromise the method. Moreover, d_z can be set below 500 nm experimentally (it is the remaining defocus of the image on the camera), and such low values were not seen to deteriorate the coarse reconstruction given by the FT^{-1}.

A second method is derived from the one already implemented in 2D in previous work of the team[32]. Calling $\boldsymbol{f}'_l$ the data set where d_z has been corrected, it is given by :

$$\boldsymbol{f}'_l = \boldsymbol{f}_l \exp(-i[\gamma-\gamma_l]d_z), \tag{3.7}$$

where γ is the projection of $\boldsymbol{k}$ on the optical axis. The problem is stated as finding d_z so that the backpropagation[118] of the associated scattered field $\boldsymbol{f}'_l$ provides the best initial guess for the inversion scheme. This is accomplished by minimizing the following cost function $\mathcal{G}$:

$$\mathcal{G} = \sum_{l=1}^{L} \|\boldsymbol{f}'_l - \beta\boldsymbol{B}\boldsymbol{B}^\dagger\boldsymbol{f}'_l\|^2_\Gamma, \tag{3.8}$$

where β is a complex scalar weight and $\boldsymbol{B}^\dagger$ the complex conjugate transpose of matrix $\boldsymbol{B}$. The minimization of the cost function $\mathcal{G}$ depends on three unknowns *i.e.* d_z and the complex β. But there is an analytical relation between d_z and β. If d_z is given then to find β one needs to minimize $\mathcal{G}$ which can be written as:

$$\mathcal{G} = \sum_{l=1}^{L}\left[\|\boldsymbol{f}'_l\|^2_\Gamma - 2\beta_r\mathrm{Re}\left\langle\boldsymbol{f}'_l|\boldsymbol{B}\boldsymbol{B}^\dagger\boldsymbol{f}'_l\right\rangle_\Gamma - 2\beta_i\mathrm{Im}\left\langle\boldsymbol{f}'_l|\boldsymbol{B}\boldsymbol{B}^\dagger\boldsymbol{f}'_l\right\rangle_\Gamma + (\beta_r^2+\beta_i^2)\|\boldsymbol{B}\boldsymbol{B}^\dagger\boldsymbol{f}'_l\|_\Gamma\right] \tag{3.9}$$

where $\beta = \beta_r + i\beta_i$. Then with d_z given we derive $\mathcal{G}$ with respect to β_r and β_i as:

$$\frac{\partial \mathcal{G}}{\partial \beta_r} = \sum_{l=1}^{L} \left[-2\mathrm{Re}\left\langle \boldsymbol{f}'_l | \boldsymbol{B}\boldsymbol{B}^\dagger \boldsymbol{f}'_l \right\rangle_\Gamma + 2\beta_r \|\boldsymbol{B}\boldsymbol{B}^\dagger \boldsymbol{f}'_l\|_\Gamma^2 \right] \tag{3.10}$$

$$\frac{\partial \mathcal{G}}{\partial \beta_i} = \sum_{l=1}^{L} \left[-2\mathrm{Im}\left\langle \boldsymbol{f}'_l | \boldsymbol{B}\boldsymbol{B}^\dagger \boldsymbol{f}'_l \right\rangle_\Gamma + 2\beta_i \|\boldsymbol{B}\boldsymbol{B}^\dagger \boldsymbol{f}'_l\|_\Gamma^2 \right]. \tag{3.11}$$

Th value of β is found with $\frac{\partial \mathcal{G}}{\partial \beta_r} = \frac{\partial \mathcal{G}}{\partial \beta_i} = 0$, then:

$$\beta = \frac{\sum_{l=1}^{L} \mathrm{Re}\left\langle \boldsymbol{f}'_l | \boldsymbol{B}\boldsymbol{B}^\dagger \boldsymbol{f}'_l \right\rangle_\Gamma}{\sum_{l=1}^{L} \|\boldsymbol{B}\boldsymbol{B}^\dagger \boldsymbol{f}'_l\|_\Gamma^2} + i\frac{\sum_{l=1}^{L} \mathrm{Im}\left\langle \boldsymbol{f}'_l | \boldsymbol{B}\boldsymbol{B}^\dagger \boldsymbol{f}'_l \right\rangle_\Gamma}{\sum_{l=1}^{L} \|\boldsymbol{B}\boldsymbol{B}^\dagger \boldsymbol{f}'_l\|_\Gamma^2} = \frac{\sum_{l=1}^{L} \mathrm{Re}\left\langle \boldsymbol{f}'_l | \boldsymbol{B}\boldsymbol{B}^\dagger \boldsymbol{f}'_l \right\rangle_\Gamma}{\sum_{l=1}^{L} \|\boldsymbol{B}\boldsymbol{B}^\dagger \boldsymbol{f}'_l\|_\Gamma^2} \tag{3.12}$$

as $\left\langle \boldsymbol{f}'_l | \boldsymbol{B}\boldsymbol{B}^\dagger \boldsymbol{f}'_l \right\rangle_\Gamma = \left\langle \boldsymbol{B}^\dagger \boldsymbol{f}'_l | \boldsymbol{B}^\dagger \boldsymbol{f}'_l \right\rangle_\Gamma \in \mathbb{R}$. Then one needs to find one unknown d_z thanks to a simplex method. This second approach is more precise than the first one to estimate d_z, but it is more time consuming, especially for large investigation domains due to the product $\boldsymbol{B}\boldsymbol{B}^\dagger \boldsymbol{f}'_l$.

When the configuration used is the reflection case we get

$$\boldsymbol{f}'_l = \boldsymbol{f}_l \exp(-ik_0[\cos\theta + \cos\theta_l]d_z). \tag{3.13}$$

This equation corrects the phase origin mismatch, but one has also to correct the phase fluctuations of the incident field from one illumination angle to another. This is done by replacing the phase of the specular reflection measured in the Fourier space, φ_{spec}, by the argument of the Fresnel reflection coefficient. Note that this argument has to take into account the fact that the phase origin is shifted from the substrate by d_z when the measurements are performed. It provides an additional phase shift $2|\gamma_l|d_z = 2k_0 \cos\theta_l d_z$ to the reflection coefficient, compared to r_l as given by Eq. (3.3) and Eq. (3.4), that are valid when the phase origin is by default taken on the substrate. By taking into account all this, $\mathcal{G}$ should then be minimized with :

$$\boldsymbol{f}'_l = \boldsymbol{f}_l \exp(-ik_0[\cos\theta - \cos\theta_l]d_z) e^{-i\varphi_{\mathrm{spec}}} \frac{r_l}{|r_l|}. \tag{3.14}$$

Notice that this expression holds in the case where the incident field is in p or s polarization.

3.2 Experimental results

In this section, we present the experimental 3D reconstructions obtained with the non-linear inversion procedure on the type of objects that were described in section 1.1.3 of chapter 1. They consist in resin cylinders deposited on a silicon substrate, and were all fabricated by Anne Talneau at the Laboratoire de Photonique et Nanostructures de Marcoussis. Different heights were realized for the cylinders : 100 nm, 125 nm or 150 nm. They are deposited so that their axes are at the corners of a square. The diameter of the cylinders and the side by side distance of two neighbouring cylinders are equal in a given square. Squares with different cylinder diameters were realized: 1 μm, 500 nm, 200 nm, 150 nm and 100 nm. Such structures are well adapted for testing the resolution of our TDM approach.

As mentioned at the beginning of this chapter, the sample is imaged on the CCD camera so that one pixel corresponds to 25.9 nm thanks to a strong magnification. As a result, when the data are transferred to the Fourier space with a 2D discrete FT^{-1}, since the accessible range of spatial frequencies is given by Eq. (3.1), it is very large and the domain occupied by the numerical aperture of the objective is only a small fraction of it. The width of the NA is typically of 80 pixels. The discretization in far-field of this NA is shown on Figure 3.6. The color level indicates the polar angle in degrees inside of the NA. Such a quite low discretization is not detrimental to the non-linear inversion algorithm, and it is moreover particularly adapted to perform off-axis holography, as will be shown hereafter.

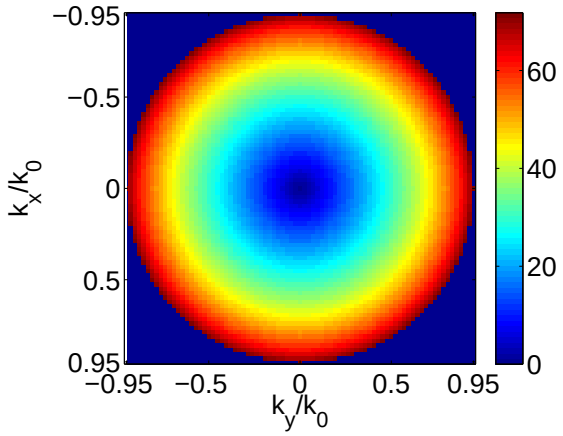

Figure 3.6 : *Polar angle distribution within the discretized numerical aperture in the Fourier space.*

3.2.1 Resin cylinders with diameter 1 μm.

For this sample, 6 illumination angles are used in the plane (x, z) with the electric field orthogonal to the plane of incidence (TE polarization), and other 6 incidences in the plane (y, z) with the electric field parallel to the plane of incidence (TM polarization), with polar angles varying in the $[-30, 30]$ degrees range.

3.2.1.1 Comparison of the measurement by phase-shifting interferometry and the simulated scattered field

The scattered fields obtained by phase shifting interferometry (PSI) in the image space are presented in Fig. 3.7 for certain illumination angles. The upper line is the modulus of the fields and the second one the corresponding phase. For each illumination angle, the measured field is averaged over 30 phase shifting cycles to increase the signal to noise ratio, since PSI can be very sensitive to external perturbations.

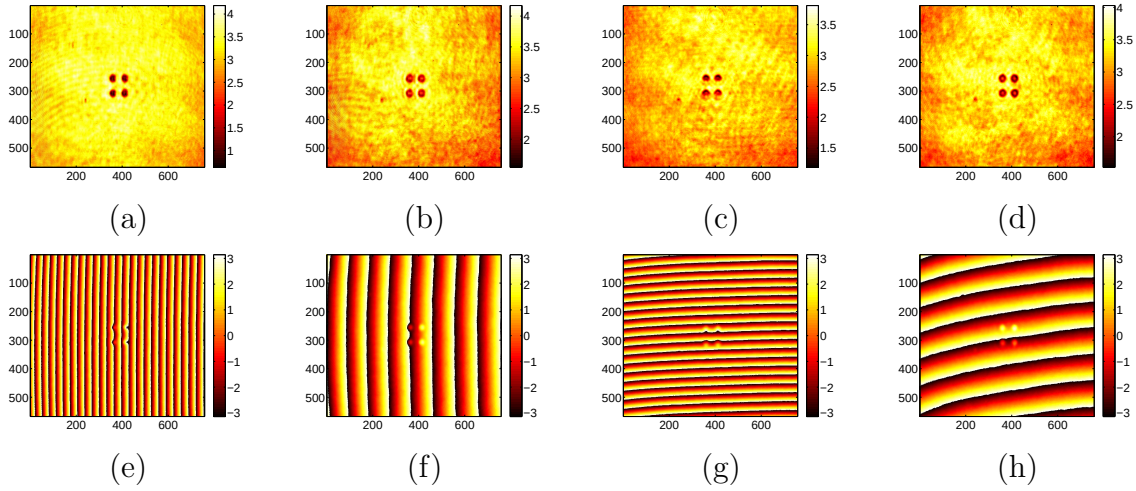

Figure 3.7 : *Modulus (first line) and phases (second line) of the field in the image space obtained by PSI on resin cylinders with diameter 1 µm and height 125 nm. (a) and (e) $\theta_l = 32°$, $\phi_l = 0°$, TE polarization; (b) and (f) $\theta_l = 10°$, $\phi_l = 0°$, TE polarization; (c) and (g) $\theta_l = 31°$, $\phi_l = 90°$, TM polarization; (d) and (h) $\theta_l = 10°$, $\phi_l = 90°$, TM polarization.*

This data set transferred in the Fourier space (in far field) is shown on Fig. 3.9. Notice that the amplitude and phase normalization described in the previous section has been applied to the data. Prior to the transfer in Fourier space, the data set has to be multiplied by a mask function in the image space. Indeed, strong artefacts are created by the discrete 2D FT^{-1} if it is applied to a domain where the signal is non zero on the edges. This mask function is equal to one in the region where the sample is located, and zero elsewhere. A smooth transition in squared cosine between these two values is implemented so that only low spatial frequencies in the vicinity of the specular reflection are generated by this mask in the Fourier space. Figure 3.8 presents a typical mask function. Thanks to it, the signal to noise ratio of the field scattered by the sample is also improved, suppressing possible unwanted scatterers, like dust, placed around the sample.

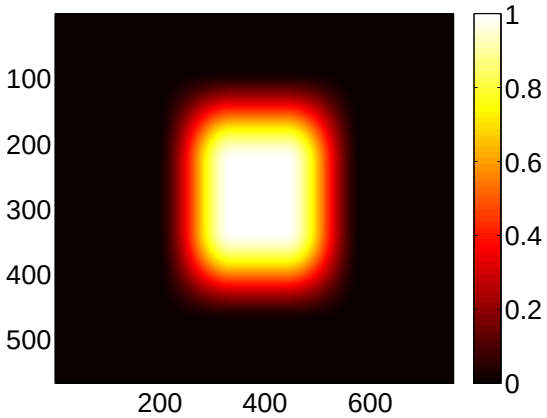

Figure 3.8 : *Mask function applied to the data in the image space to isolate the sample region and suppress artefacts created by the discrete 2D* FT^{-1} *for the transfer to Fourier space.*

This data has been restricted to about two thousands scattering angles centered on the specular reflection on the substrate. The missing circle in the data corresponds to the domain where the field scattered by the sample is masked by this reflection. Indeed, the specular reflection is only used as reference for the data normalization procedure, but it is suppressed for performing the inversion since it does not correspond to the field scattered by the object.

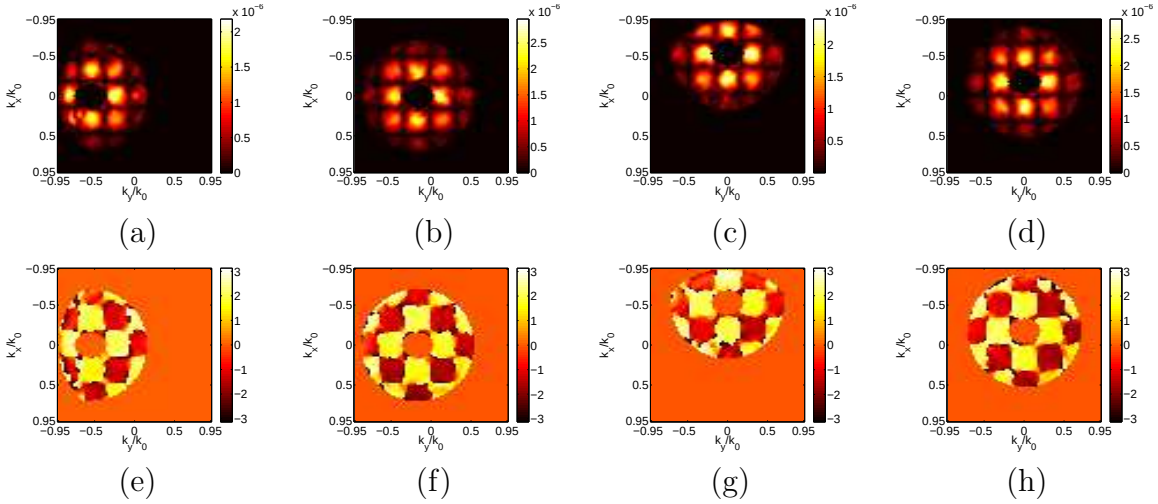

Figure 3.9 : *Modulus (first line) and phases (second line) of the field in the Fourier space obtained by PSI on resin cylinders with diameter 1 µm and height 125 nm. (a) and (e) $\theta_l = 32°$, $\phi_l = 0°$, TE polarization; (b) and (f) $\theta_l = 10°$, $\phi_l = 0°$, TE polarization; (c) and (g) $\theta_l = 31°$, $\phi_l = 90°$, TM polarization; (d) and (h) $\theta_l = 10°$, $\phi_l = 90°$, TM polarization.*

To verify that this normalized data set in far field is able to recover a quantitative 3D reconstruction of the object, we compare it with the theoretical scattered far field, computed with the CDM for the same illumination angles and polarizations. It is shown on Fig. 3.10.

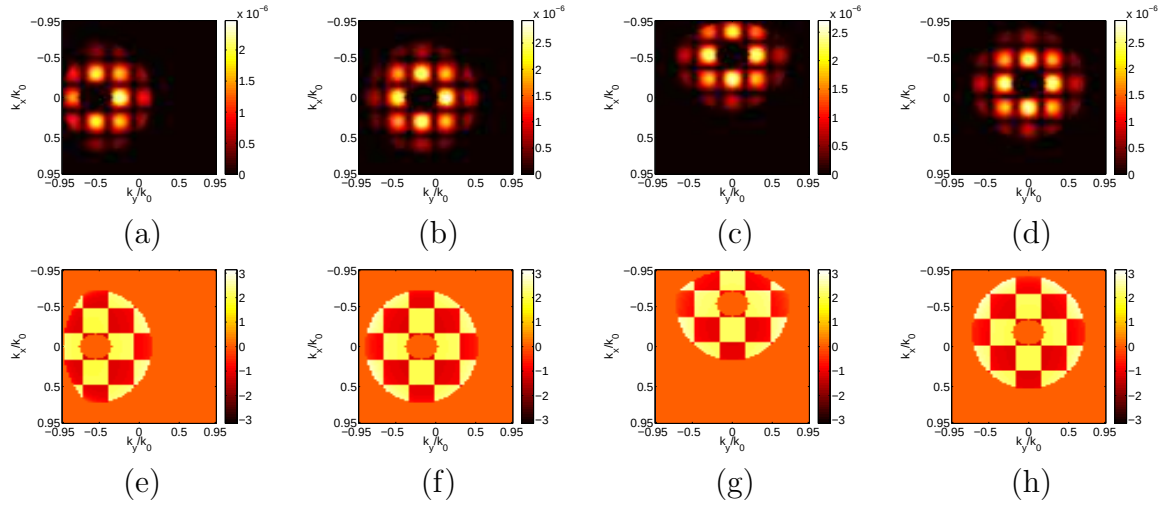

Figure 3.10 : *Modulus (first line) and phases (second line) of the theoretical far field (Fourier space) scattered by resin cylinders with diameter 1 μm and height 125 nm. (a) and (e) $\theta_l = 32°$, $\phi_l = 0°$, TE polarization; (b) and (f) $\theta_l = 10°$, $\phi_l = 0°$, TE polarization; (c) and (g) $\theta_l = 31°$, $\phi_l = 90°$, TM polarization; (d) and (h) $\theta_l = 10°$, $\phi_l = 90°$, TM polarization.*

A very good agreement has been obtained between the measured and the computed fields. As the non-linear inversion procedure has permitted to reconstruct successfully the object with the computed data set, the next step is to apply the inversion procedure to the measured data set.

3.2.1.2 Comparison of the data set measured by PSI and with a wavefront sensor (WFS)

The PSI measurement technique suffers from a high sensitivity to external perturbations, which is compensated in our set-up by averaging the data over several phase shift cycles, but it also increases the duration of the measurement. A long acquisition time can be problematic since the stability of the positioning of the object, particularly the axial one, cannot be guaranteed over periods typically longer than 10 minutes due to mechanical drifts. To speed up the measurement and increase its robustness, we have also performed the data acquisition with a wavefront sensor (WFS) based on quadriwave lateral shearing interferometry, as described in section 2.2.3 of chapter 2. This approach also permits to simplify the set-up by suppressing the need for a reference wave, and makes possible the use of cheaper and smaller light sources with lower temporal coherence, such as laser diodes or spatially filtered LEDs. Such light sources would diminish the speckle noise due to parasitic reflections and scattering along the light path.

The wavefront sensor used is the Phasics SID4-HR model. It measures the amplitude and the phase of the incoming field on 400 $\times$ 300 matrix with a pixel size of 29.6 μm. With the magnification of the set-up about 290 the discretization of the image is close to 100 nm per pixel. The resolution of the set-up is therefore still limited by the Rayleigh criterion of 400 nm imposed by the objective NA, and the inner spot of the point spread function is thus sampled with a sufficient number of pixels : about 8. The wavefront sensor is able to detect a phase difference between two adjacent pixels from 0.01 to 2.9 radians. The lower bound is essentially imposed by the sensitivity of the camera, whereas the upper one originates from the interferograms of Eq. (3.15) that are treated to retrieve the complex scattered fields. This equation is recalled hereafter for the sake of

clarity :

$$I_t(x,z) \propto A^2_{\mathrm{obj}}(x - z\tan\theta_1) + A^2_{\mathrm{obj}}(x + z\tan\theta_1) + 2A_{\mathrm{obj}}(x - z\tan\theta_1)A_{\mathrm{obj}}(x + z\tan\theta_1)\cos\left(\frac{2\pi}{p}x - 2\tan\theta_1 z\frac{\partial\phi_{obj}(x)}{\partial x}\right). \quad (3.15)$$

The upper bound corresponds to a phase gradient that gives $2\tan\theta_1 z\frac{\partial\phi_{\mathrm{obj}}(x)}{\partial x} = \pi$, which cannot be distinguished between a negative or a positive phase gradient in the interferogram. The constraint imposed by this upper bound is greatly relaxed by sampling the point spread function with about 8 pixels.

Figure 3.11 presents the scattered fields in the image space measured by the WFS for the same illumination angles as for the PSI technique. The data acquisition treatment of the WFS automatically suppresses the tilt of the incoming wavefront, thus no phase ramp appears on the phase images. Note that a phase reference is measured on the bare substrate for each illumination prior to imaging the sample to diminish the speckle noise. All the measurements are performed in a single shot manner.

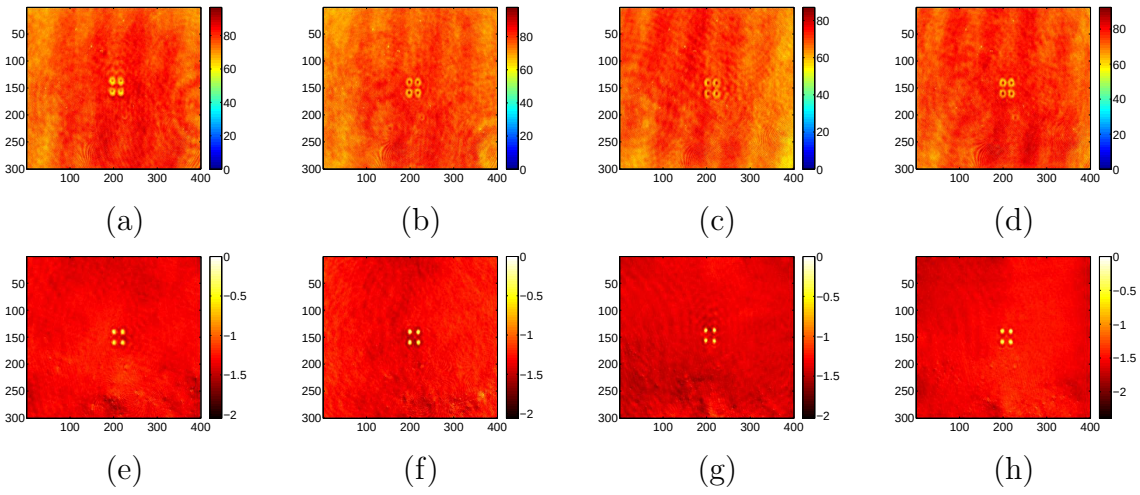

Figure 3.11 : *Modulus (first line) and phases (second line) of the field in the image space measured with a WFS on resin cylinders with diameter 1 µm and height 125 nm. (a) and (e) $\theta_l = 32°$, $\phi_l = 0°$, TE polarization; (b) and (f) $\theta_l = 10°$, $\phi_l = 0°$, TE polarization; (c) and (g) $\theta_l = 31°$, $\phi_l = 90°$, TM polarization; (d) and (h) $\theta_l = 10°$, $\phi_l = 90°$, TM polarization.*

The data set transferred in the Fourier space is shown on Fig. 3.12. The discretization in the Fourier space is quite similar as in the PSI case, since the lower number of pixels of the WFS is compensated by their larger extent, compared to the CCD camera. The two measurement techniques provide very similar data sets, which proves the feasibility of employing a WFS to simplify and improve the robustness of TDM.

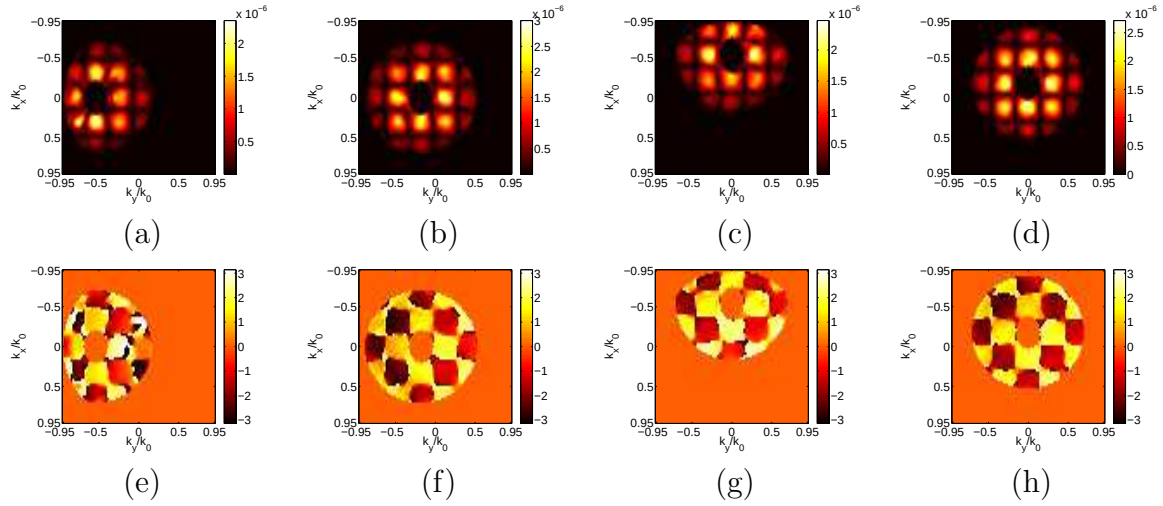

Figure 3.12 : *Modulus (first line) and phases (second line) of the field in the Fourier space measured with a WFS on resin cylinders with diameter 1 μm and height 125 nm. (a) and (e) $\theta_l = 32°$, $\phi_l = 0°$, TE polarization; (b) and (f) $\theta_l = 10°$, $\phi_l = 0°$, TE polarization; (c) and (g) $\theta_l = 31°$, $\phi_l = 90°$, TM polarization; (d) and (h) $\theta_l = 10°$, $\phi_l = 90°$, TM polarization.*

3.2.1.3 Application of the non-linear inversion algorithm to the experimental data for different sizes of investigation domain

The non-linear inversion algorithm is here applied to the WFS dataset. As stated in chapter 2, the *a priori* information that the real part of the permittivity of the sample is positive is used. Moreover the imaginary part of the permittivity of the resin is neglected, considering the samples as pure phase objects. Our inversion procedure necessitates to choose a size for the investigation domain Ω where the sample will be reconstructed. The usual approach is to choose a quite large size for Ω with a coarse meshing at a first step, and then diminishing the size and refining the meshing once the object dimensions have been evaluated. As the measurements are done in the image space, it is easy to calibrate the transverse extent of Ω from the image of the object. The axial dimension of the object can be estimated from the defocus of its image on the camera while it is translated along the optical axis and from the knowledge of the depth of field of the objective (below 1 μm for NA = 0.95). It can also be evaluated more precisely from the approximated reconstruction obtained by applying a 3D TF^{-1} to the data set.

A first large investigation domain of $8 \times 8 \times 3.2$ μm^3 with a 200 nm meshing is used on Figs. 3.13 and 3.14. They show a transverse cut and a longitudinal cut of the resin cylinders, respectively. The four resin pads can be located accurately, and Ω is then downsized to a box of $4 \times 4 \times 1.6$ μm^3 on Figs. 3.15 and 3.16.

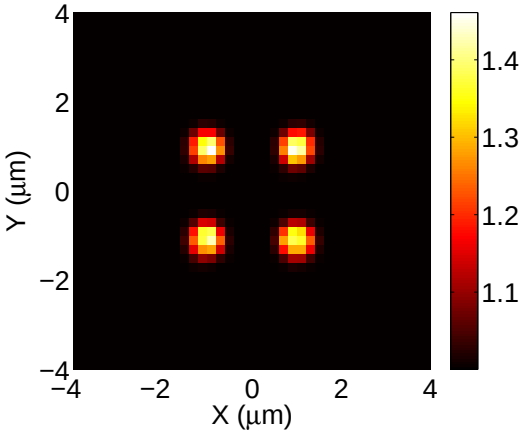

Figure 3.13 : *Transverse cut at $z = 100$ nm of the reconstruction with 200 nm meshing of 1 µm large resin cylinders with 125 nm height (WFS data set)*

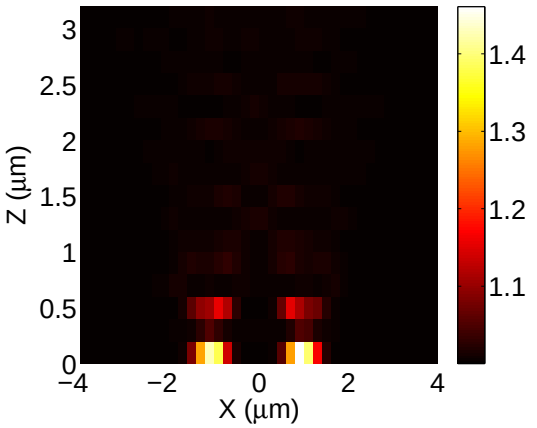

Figure 3.14 : *Longitudinal cut at $y = 1\mu m$ of the reconstruction with 200 nm meshing of 1 µm large resin cylinders with 125 nm height (WFS data set)*

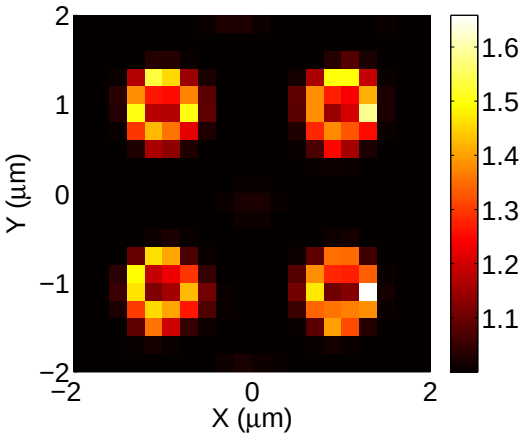

Figure 3.15 : *Transverse cut at $z = 100$ nm of the reconstruction with 200 nm meshing of 1 µm large resin cylinders with 125 nm height (WFS data set)*

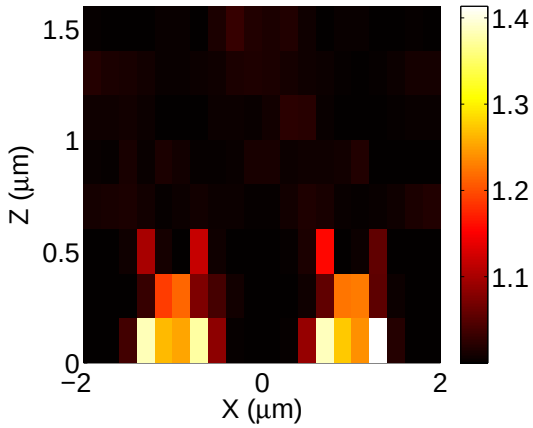

Figure 3.16 : *Longitudinal cut at $y = 1\mu m$ of the reconstruction with 200 nm meshing of 1 µm large resin cylinders with 125 nm height (WFS data set)*

We noticed that the spatial extent of the sample along the optical axis did not exceed 0.8 μm. To ameliorate further the accuracy of the reconstruction, we downsized the box to $4 \times 4 \times 0.8$ μm^3 and tightened the mesh size to 100 nm : Figs. 3.17 and 3.18.

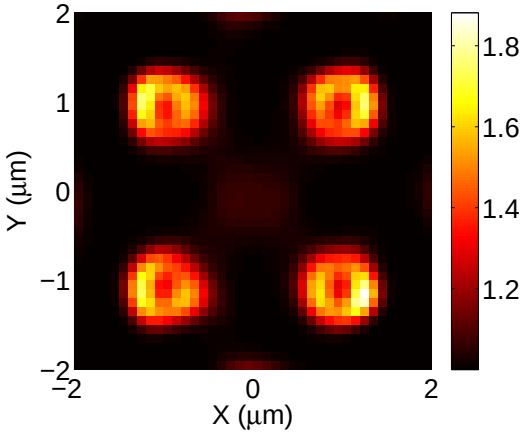

Figure 3.17 : *Transverse cut at $z = 150$ nm of the reconstruction with 100 nm meshing of 1 µm large resin cylinders with 125 nm height (WFS data set)*

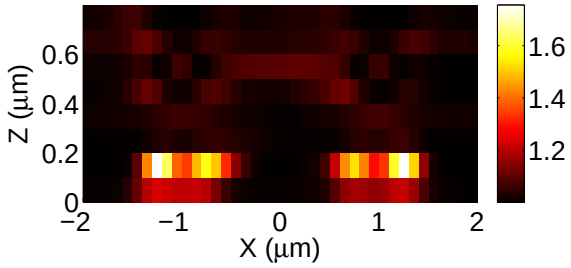

Figure 3.18 : *Longitudinal cut at $y = 1\mu m$ of the reconstruction with 100 nm meshing of 1 µm large resin cylinders with 125 nm height (WFS data set)*

We then estimated that the height of the sample was below 400 nm. We thus finally diminished the height of the domain to 400 nm and the mesh size to 50 nm : Figs. 3.19 and 3.20. The iterative inversion procedure has therefore been applied successfully on the WFS data set to reconstruct the sample. Only four iterations were needed for the convergence of the iterative process. To our knowledge, this is the first time that such an approach is validated on 3D experimental data in optics. The reconstructions obtained for the intermediate iterations will also be shown hereafter as illustration.

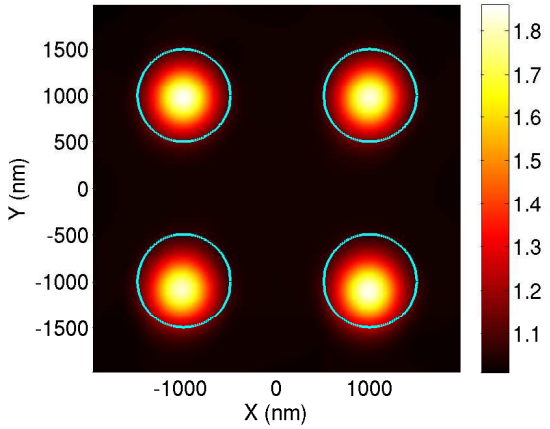

Figure 3.19 : *Transverse cut at $z = 125$ nm of the reconstruction with 50 nm meshing of 1 µm large resin cylinders with 125 nm height (WFS data set)*

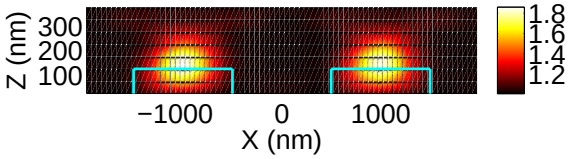

Figure 3.20 : *Longitudinal cut at $y = 1\mu m$ of the reconstruction with 50 nm meshing of 1 µm large resin cylinders with 125 nm height (WFS data set)*

3.2.1.4 Comparison of the non-linear inversions obtained with the WFS and the PSI data sets

As expected from the high similarity of the WFS and the PSI data sets in the Fourier space, the reconstructions obtained with the non-linear inversion procedure are in good agreement for the two measurement techniques. For illustration, Figs. 3.21 and 3.22 show the final iteration obtained with the PSI data set.

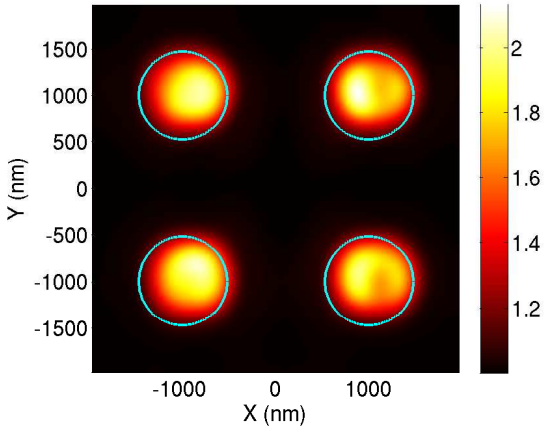

Figure 3.21 : *Transverse cut at $z = 125$ nm of the reconstruction with 50 nm meshing of 1 μm large resin cylinders with 125 nm height (PSI data set)*

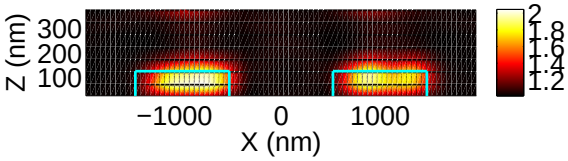

Figure 3.22 : *Longitudinal cut at $y = 1\mu m$ of the reconstruction with 50 nm meshing of 1 μm large resin cylinders with 125 nm height (PSI data set)*

As a result, it shows that TDM is compatible with the use of a wavefront sensor, which gives a simpler set-up architecture, close to that of a standard wide-field microscope, with possible use of low-cost weakly coherent sources. These results were recently published [116].

3.2.1.5 Comparison of the reconstructions obtained with the non-linear inversion procedure and the linear inversion valid for the Born approximation

Figure 3.23 shows a comparison of the reconstructions obtained with the non-linear inversion procedure and the 3D FT^{-1} valid under the Born approximation, for the case of the WFS data set. The Fourier transform technique provides a noisy reconstruction particularly distorted along the z axis, since the presence of the reflective surface is interpreted as a mirror object symmetrically placed along this axis. Such a behaviour is also observed in the case of the PSI data set, shown on Fig. 3.24.

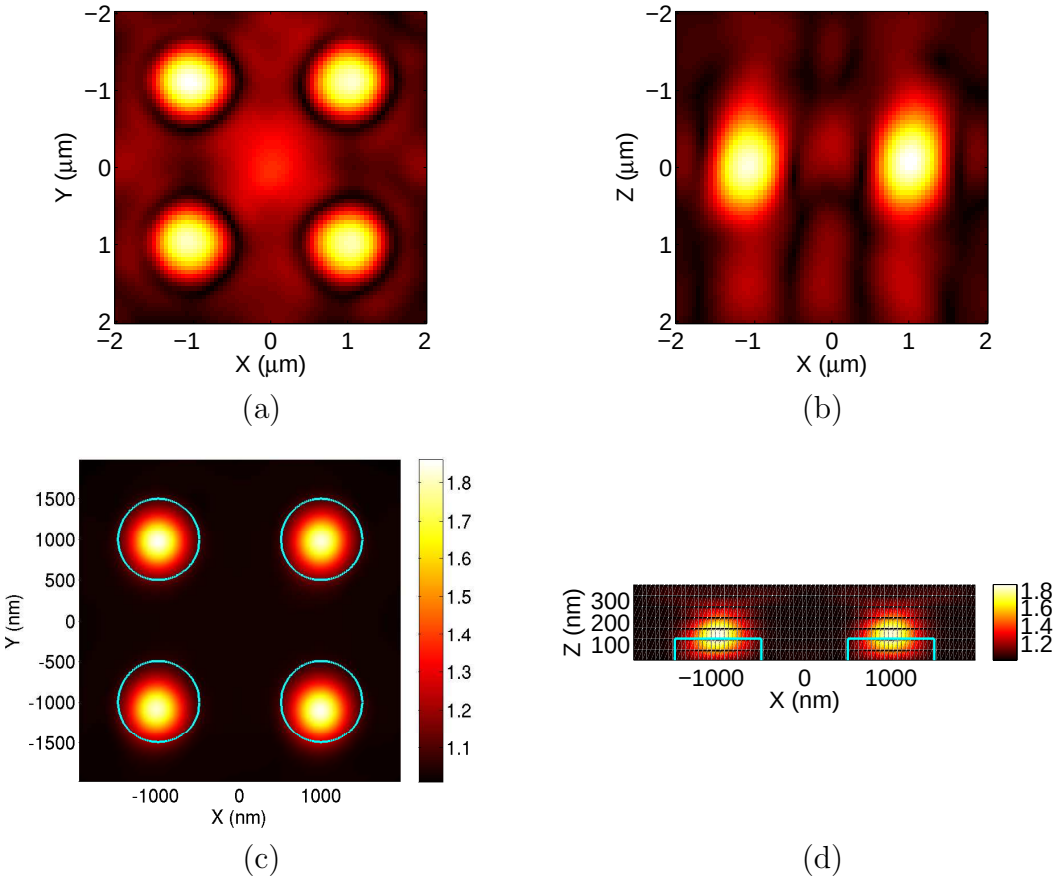

Figure 3.23 : *Comparison of the reconstructions of the 1 µm large resin cylinders with the non-linear inversion procedure and the 3D* FT^{-1}*, applied on the WFS data set.*

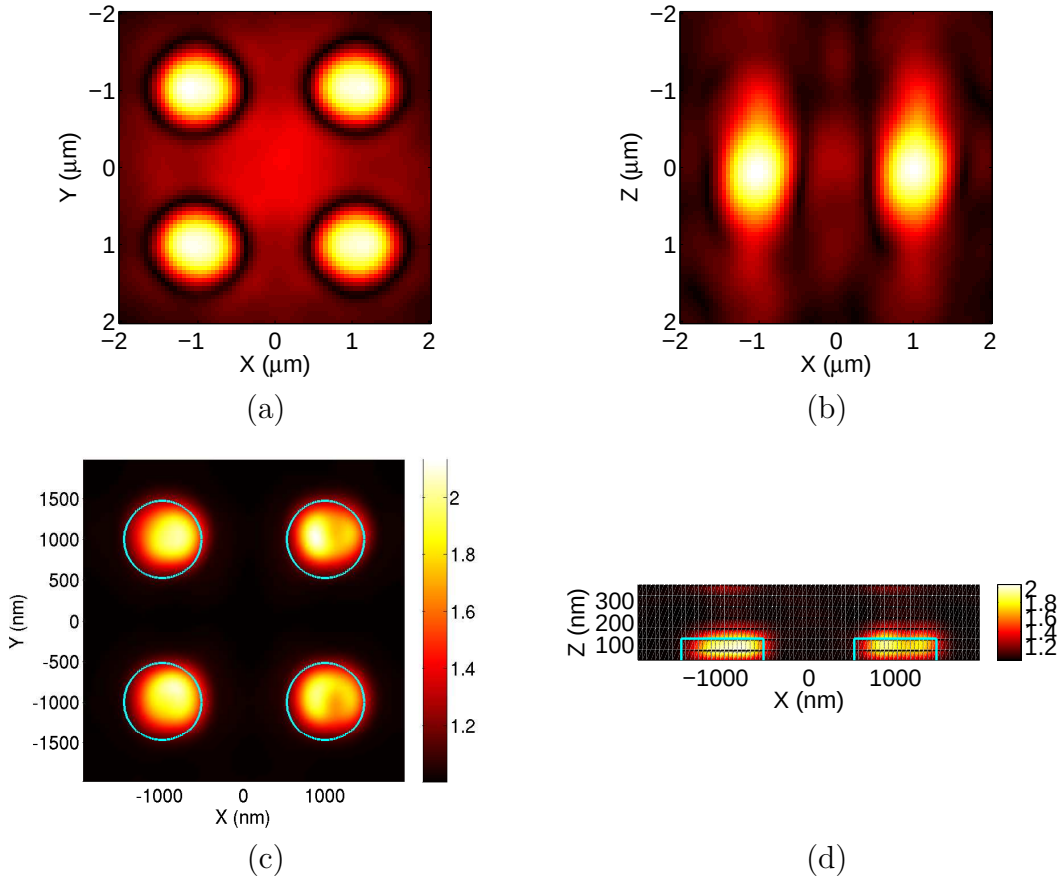

Figure 3.24 : *Comparison of the reconstructions of the 1 µm large resin cylinders with the non-linear inversion procedure and the 3D* FT^{-1}*, applied on the PSI data set.*

The Fourier transform technique is in fact very sensitive to the missing points in the Fourier space, due to the restricted amount of data with only 12 different illumination angles for the data set. Usually, to have a good reconstruction with this technique, several hundreds of incidences are required to fill the Fourier space adequately. As on the contrary, our non-linear inversion procedure estimates accurately the sample dimensions, even with the coarse meshing in Figs. 3.15 and 3.16. As a result, it seems particularly attractive to diminish the number of necessary illuminations : an acquisition time gain of at least ten can therefore be expected. Note also that no quantitative result on the permittivity can be obtained here with the 3D FT^{-1} because of the missing points in the Fourier space. However with such an inversion, the permittivity is usually estimated thanks to a reference object of known permittivity [27].

3.2.1.6 Iterative process of the inversion algorithm applied on the WFS data set

As written above, the non-linear inversion procedure has necessitated four iterations before converging to the final reconstruction of the sample. They are shown on Figs. 3.25 and 3.26, 3.27 and 3.28, 3.29 and 3.30, 3.19 and 3.20, respectively.

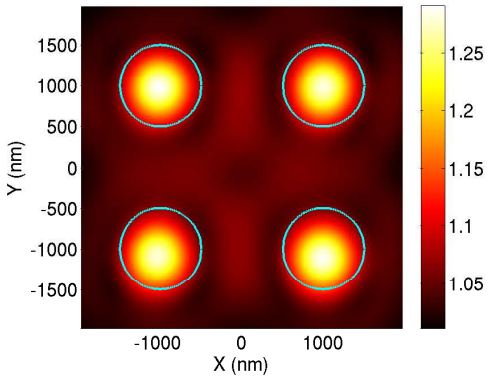

Figure 3.25 : *The 1st iteration, transverse cut at $z = 125$ nm of the reconstruction with 50 nm meshing of 1 μm large resin cylinders with 125 nm height (WFS data set)*

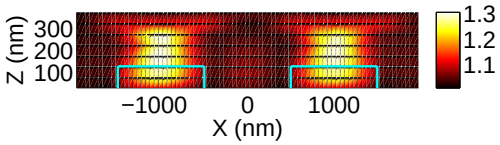

Figure 3.26 : *The 1st iteration, longitudinal cut at $y = 1$ μm of the reconstruction with 50 nm meshing of 1 μm large resin cylinders with 125 nm height (WFS data set)*

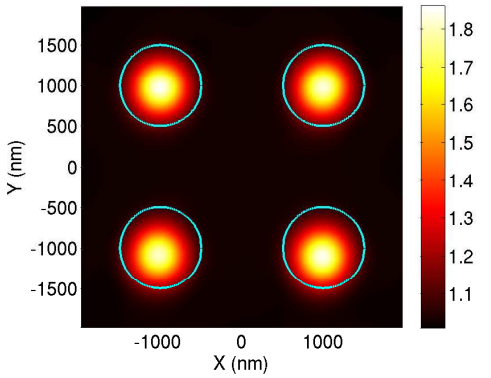

Figure 3.27 : *The 2nd iteration, transverse cut at $z = 125$ nm of the reconstruction with 50 nm meshing of 1 μm large resin cylinders with 125 nm height (WFS data set)*

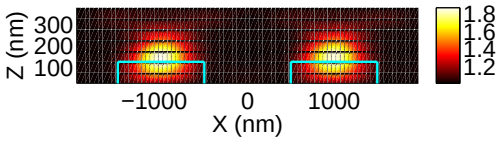

Figure 3.28 : *The 2nd iteration, longitudinal cut at $y = 1\mu$m of the reconstruction with 50 nm meshing of 1 μm large resin cylinders with 125 nm height (WFS data set)*

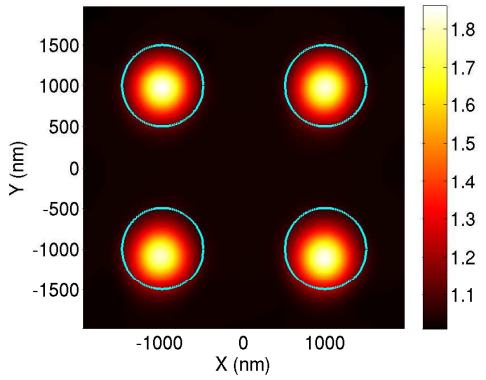

Figure 3.29 : *The 3^{rd} iteration, transverse cut at $z = 125$ nm of the reconstruction with 50 nm meshing of 1 μm large resin cylinders with 125 nm height (WFS data set)*

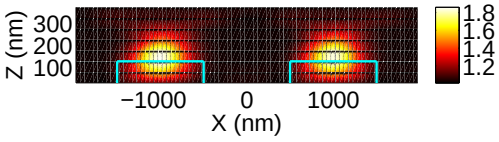

Figure 3.30 : *The 3^{rd} iteration, longitudinal cut at $y = 1\mu m$ of the reconstruction with 50 nm meshing of 1 μm large resin cylinders with 125 nm height (WFS data set)*

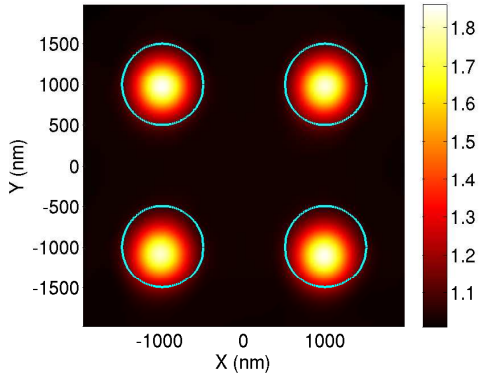

Figure 3.31 : *The final iteration, transverse cut at $z = 125$ nm of the reconstruction with 50 nm meshing of 1 μm large resin cylinders with 125 nm height (WFS data set)*

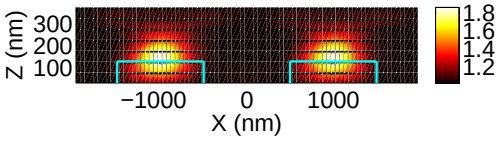

Figure 3.32 : *The final iteration, longitudinal cut at $y = 1\mu m$ of the reconstruction with 50 nm meshing of 1 μm large resin cylinders with 125 nm height (WFS data set)*

Note that compared to the Fourier transform technique, the computational time is significantly increased as Eq. (2.37) has to be solved rigorously at each iteration. Yet this rigorous calculation of the total field inside of Ω is necessary only if the sample supports multiple scattering. If the Born approximation is valid, the total field can be replaced by the reference field, and the computation time then remains comparable to that of the inverse Fourier transform.

3.2.2 Resin cylinders with diameter 500 nm

Measurements have been performed on resin cylinders with a smaller diameter of 500 nm : their axes are placed at the corners of a square with 1 μm side. Different heights have been fabricated : 150 nm, 125 nm and 98 nm. The robustness of the non-linear inversion procedure can thus be tested on such objects with smaller features. Note that to speed up the measurement acquisition time, namely the movement of the motors to change the illumination angle and the cycles of phase steps

for PSI measurements, the computer controlling the set-up has been changed and the operating system has moved from Windows to Linux. As the acquisition software for the WFS is not directly compatible with Linux, the WFS technique has been let aside temporarily for these measurements. It has been replaced by another single shot technique presented in chapter 2 : off-axis holography. With this technique, the measurement time is about four times shorter compared to PSI : for a data set with 20 illumination angles, 15 minutes are required for PSI while less than five minutes are needed for the off-axis case.

3.2.2.1 Comparison of the PSI data set with the theory

The used sample has a height of 125 nm, and as the diameter of the resin cylinders has diminished the number of illumination angles has been increased compared to the previous sample to add larger angles : 10 incidences are used in the plane (x, z) with the electric field orthogonal to the plane of incidence (TE polarization), and 10 incidences in the plane (y, z) with the electric field parallel to the plane of incidence (TM polarization), with polar angles varying in the $[-60, 60]$ degrees range. The fields in the image space are presented on Fig. 3.33 for different illumination angles and polarizations.

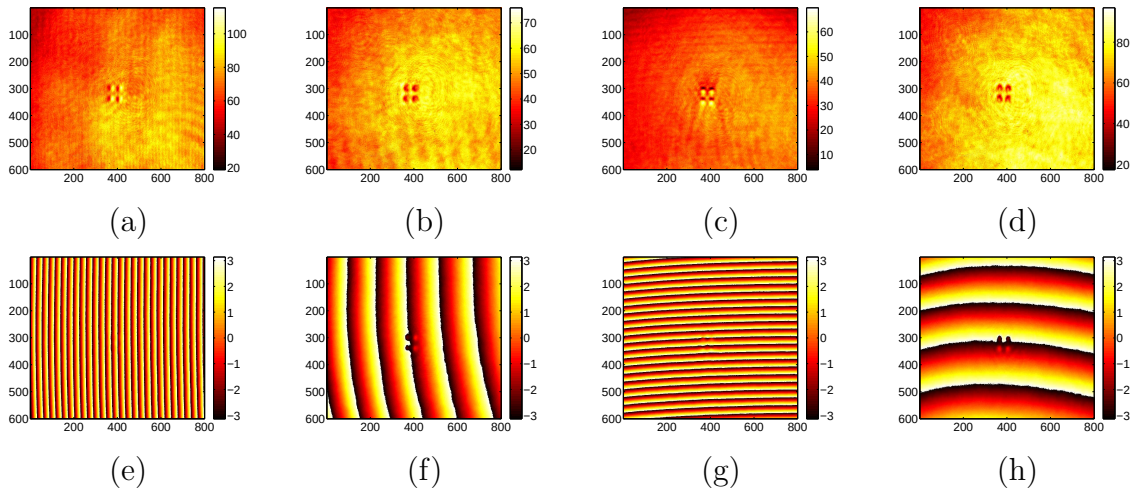

Figure 3.33 : *Modulus (first line) and phases (second line) of the field in the image space measured by PSI on resin cylinders with diameter 500 µm and height 125 nm. (a) and (e) $\theta_l = 55°$, $\phi_l = 0°$, TE polarization; (b) and (f) $\theta_l = 8.8°$, $\phi_l = 0°$, TE polarization; (c) and (g) $\theta_l = 55°$, $\phi_l = 90°$, TM polarization; (d) and (h) $\theta_l = 9°$, $\phi_l = 90°$, TM polarization.*

After application of the normalization procedure, the data set is transferred in the Fourier space and can be seen on Fig. 3.34. For comparison, the theoretical far field is presented on Fig. 3.35. The agreement is globally good. As for the previous sample, the data has been restricted to about two thousands scattering angles centered on the specular reflection on the substrate. The missing circle in the data corresponds to the domain where the field scattered by the sample is masked by this reflection.

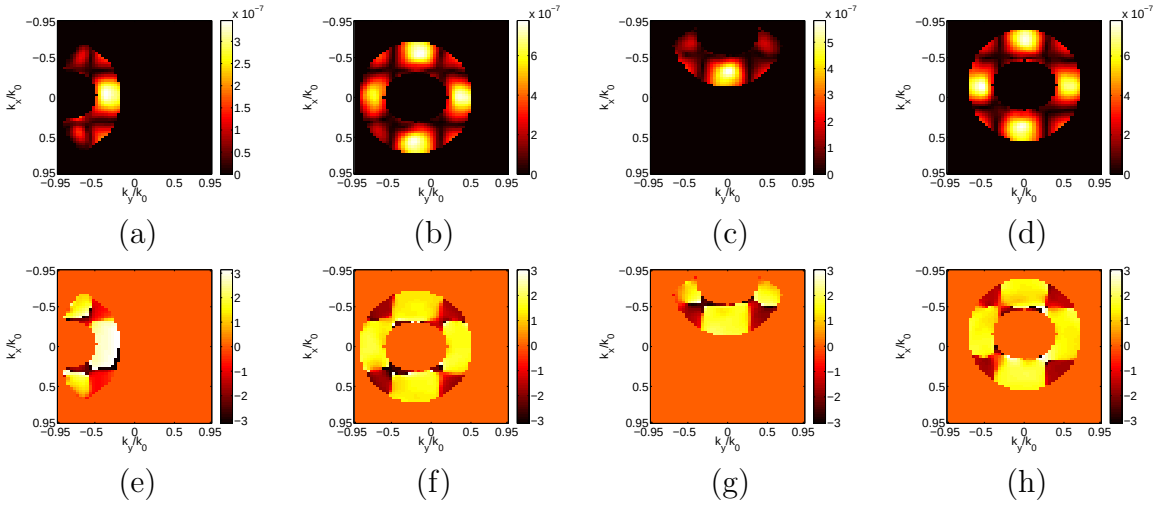

Figure 3.34 : *Modulus (first line) and phases (second line) of the field in the Fourier space measured by PSI on resin cylinders with diameter 500 µm and height 125 nm. (a) and (e) $\theta_l = 55°$, $\phi_l = 0°$, TE polarization; (b) and (f) $\theta_l = 8.8°$, $\phi_l = 0°$, TE polarization; (c) and (g) $\theta_l = 55°$, $\phi_l = 90°$, TM polarization; (d) and (h) $\theta_l = 9°$, $\phi_l = 90°$, TM polarization.*

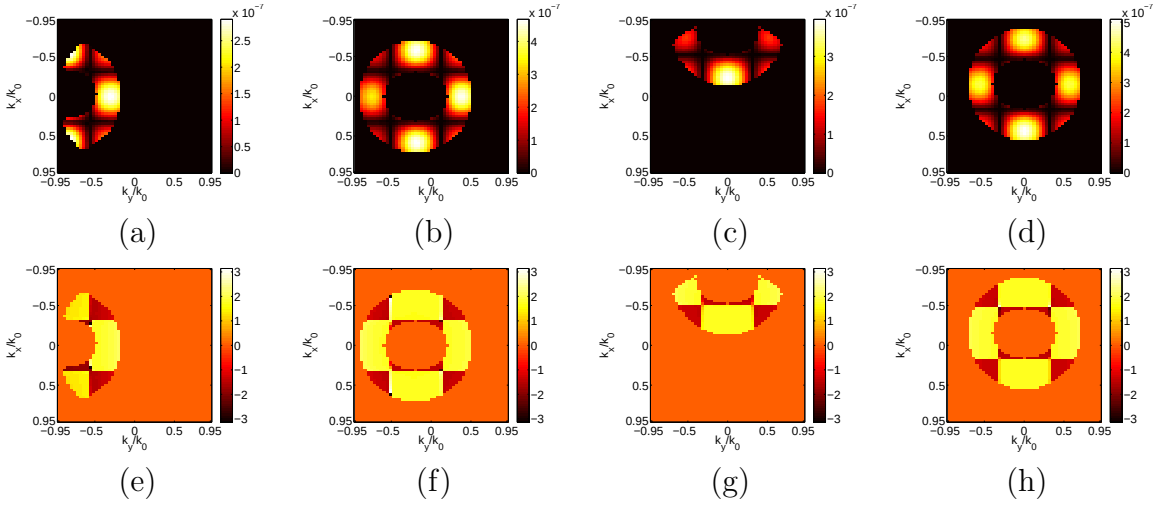

Figure 3.35 : *Modulus (first line) and phases (second line) of the theoretical field in the Fourier space scattered by resin cylinders with diameter 500 µm and height 125 nm. (a) and (e) $\theta_l = 55°$, $\phi_l = 0°$, TE polarization; (b) and (f) $\theta_l = 8.8°$, $\phi_l = 0°$, TE polarization; (c) and (g) $\theta_l = 55°$, $\phi_l = 90°$, TM polarization; (d) and (h) $\theta_l = 10°$, $\phi_l = 90°$, TM polarization.*

3.2.2.2 Measurement of the field by off-axis holography

Off-axis holography is an interesting method to measure the phase and the amplitude of the field in a single shot manner, therefore diminishing the acquisition time and the sensitivity to experimental perturbations. The main drawback is that only a fraction of the pixels of the detector can be used to obtain the useful signal, as stated in section 2 of chapter 2. This is however not a limiting factor in our procedure since the inversion algorithm does not necessitate a very high number of

scattering angles : they are limited to about 2000. This technique is applied here on resin cylinders with 500 nm diameter and 98 nm height. Approximately the same 20 illumination angles as those for the previous PSI measurement are used. For each angle, 30 intensity patterns are averaged to improve the signal to noise ratio. The resulting intensity measurements obtained in the image space for some of these angles are presented on Fig. 3.36. The interference fringes between the off-axis reference wave and the specular reflection on the substrate are visible on these images.

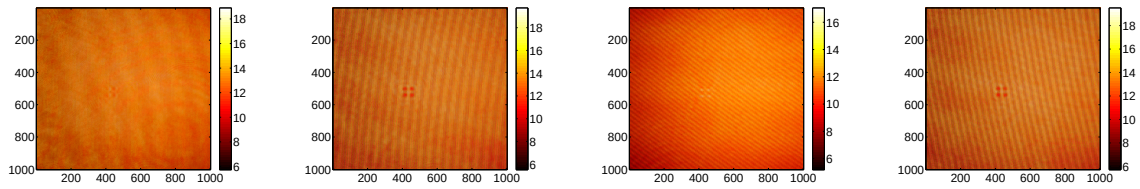

(a) (b) (c) (d)

Figure 3.36 : *Intensity of the field in the image space measured by off-axis holography on resin cylinders with diameter 500 µm and height 98 nm. (a)* $\theta_l = 58°$, $\phi_l = 0°$, *TE polarization; (b)* $\theta_l = 10°$, $\phi_l = 0°$, *TE polarization; (c)* $\theta_l = 57°$, $\phi_l = 90°$, *TM polarization; (d)* $\theta_l = 9°$, $\phi_l = 90°$, *TM polarization.*

By applying a 2D FT^{-1} to this data, the scattered field in phase and amplitude can be retrieved in the Fourier space. It is shown on Fig. 3.37. The three interference terms are clearly separated, the one due to the intensity of the scattered field in the middle, and the ones due to the scattered field and its complex conjugate on the two sides.

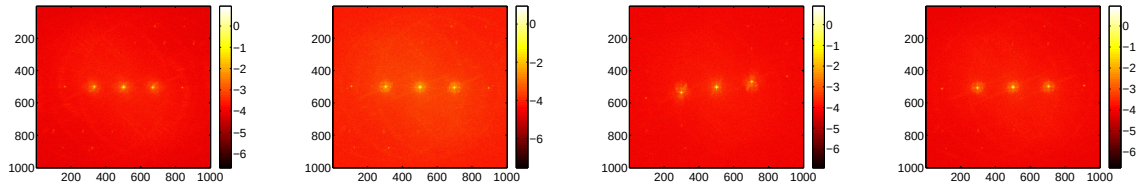

Figure 3.37 : *Modulus of the far field propagation of the intensity images measured by off-axis holography on resin cylinders with diameter 500 µm and height 98 nm. (a)* $\theta_l = 58°$, $\phi_l = 0°$, *TE polarization; (b)* $\theta_l = 9°$, $\phi_l = 0°$, *TE polarization; (c)* $\theta_l = 58°$, $\phi_l = 90°$, *TM polarization; (d)* $\theta_l = 10°$, $\phi_l = 90°$, *TM polarization.*

It is possible to retrieve the modulus and the phase of the field in the image space from the data in the Fourier space, and thus obtain the same kind of measurements as PSI. For this only one interference term on the side is kept, as shown on Fig. 3.38.

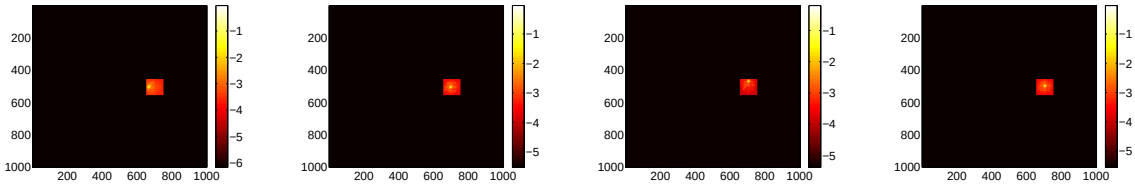

Figure 3.38 : *The kept term modulus of the far field propagation of the intensity images measured by off-axis holography on resin cylinders with diameter 500 µm and height 98 nm. (a) $\theta_l = 58°$, $\phi_l = 0°$, TE polarization; (b) $\theta_l = 9°$, $\phi_l = 0°$, TE polarization; (c) $\theta_l = 58°$, $\phi_l = 90°$, TM polarization; (d) $\theta_l = 10°$, $\phi_l = 90°$, TM polarization.*

A 2D FT generates these field into the image space. The modulus and the phase of this retrieved field are presented on Fig. 3.39. The attenuation on the edges of the modulus image is due to the mask function initially applied to the data set before transfer to the Fourier space. The image space data can then be used to locate the spatial origin for the phase at the center of the object, as it cannot always be clearly seen on the raw off-axis intensity measurement because of the interference fringes. Moreover the factor $\langle \|\tilde{\boldsymbol{f}}_l\| \rangle_S$ in Eq. (3.2) can be calculated inside of the mask for the amplitude normalization.

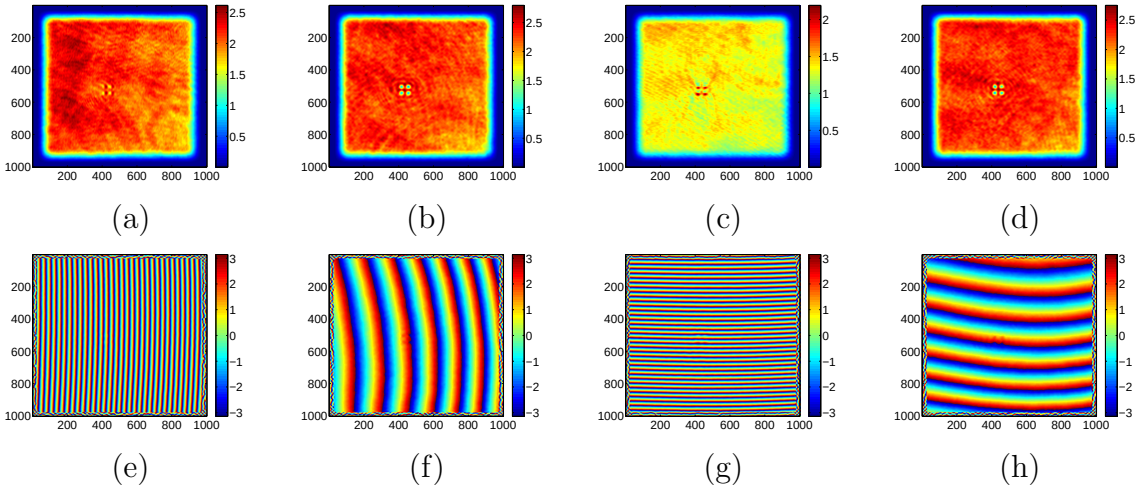

Figure 3.39 : *Modulus and phase of the field in the image space retrieved from the off-axis data set on resin cylinders with diameter 500 µm and height 98 nm. (a) and (e) $\theta_l = 58°$, $\phi_l = 0°$, TE polarization; (b) and (f) $\theta_l = 9°$, $\phi_l = 0°$, TE polarization; (c) and (g) $\theta_l = 58°$, $\phi_l = 90°$, TM polarization; (d) and (h) $\theta_l = 10°$, $\phi_l = 90°$, TM polarization.*

The modulus and the phase of the data set transferred to the Fourier space are shown on Fig. 3.40. They present a similar far field profile compared to that of the PSI measurement and the theory, which validate the use of off-axis holography for our set-up.

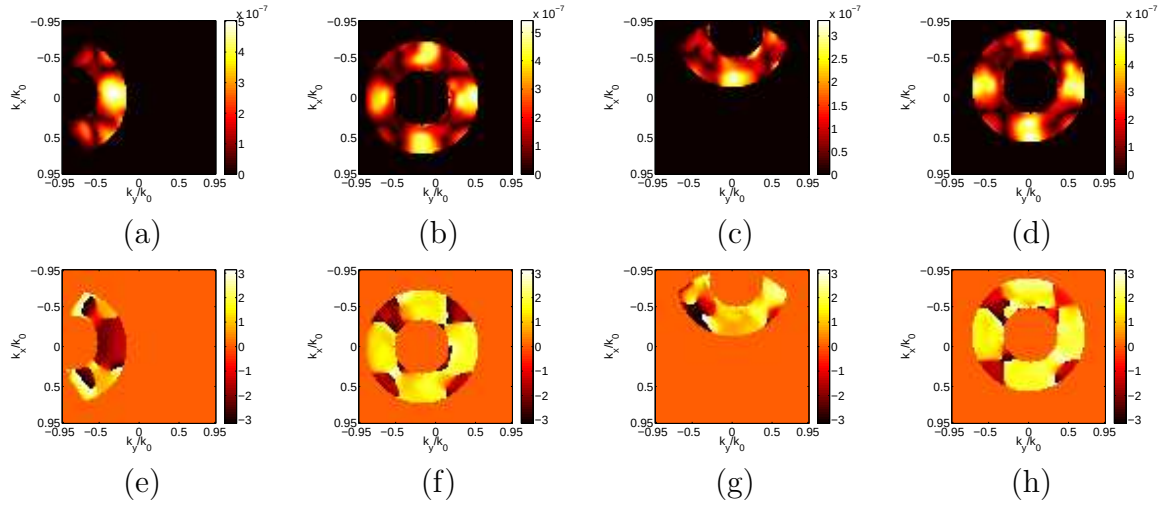

Figure 3.40 : *Modulus (first line) and phases (second line) of the field in the Fourier space measured by off-axis holography on resin cylinders with diameter 500 μm and height 98 nm. (a) and (e) $\theta_l = 58°$, $\phi_l = 0°$, TE polarization; (b) and (f) $\theta_l = 9°$, $\phi_l = 0°$, TE polarization; (c) and (g) $\theta_l = 58°$, $\phi_l = 90°$, TM polarization; (d) and (h) $\theta_l = 10°$, $\phi_l = 90°$, TM polarization.*

3.2.2.3 Application of the non-linear inversion algorithm to the PSI data set for different sizes of investigation domain

The normalized PSI data set is injected in the inversion procedure for different sizes of investigation domain, with the same approach as what was presented above for the resin cylinders with 1 μm diameter. At first, the investigation domain is a rectangular box with dimensions $2 \times 2 \times 1.6$ μm^3 and a mesh size of 200 nm. The sample permittivity contrast has again been considered as a real number, neglecting the absorption of the resin. The permittivity map reconstructed with our iterative inversion procedure is displayed in Figs. 3.41 and 3.42. They show a transverse cut (x, y) at a height of 200 nm above the substrate and a longitudinal cut (x, z) in the middle of two of the cylinders, respectively.

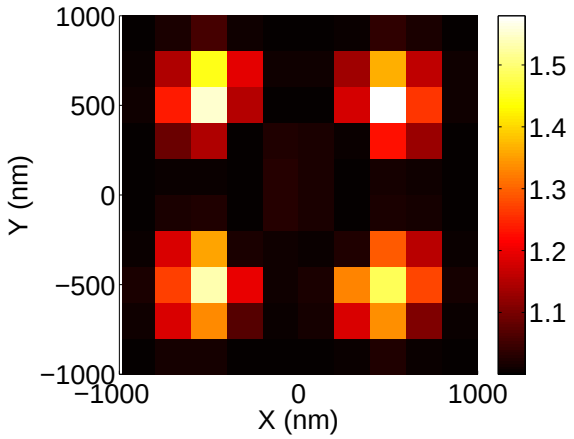

Figure 3.41 : *Transverse cut at $z = 200$ nm of the reconstruction with 200 nm meshing of 500 nm large resin cylinders with 125 nm height (PSI data set)*

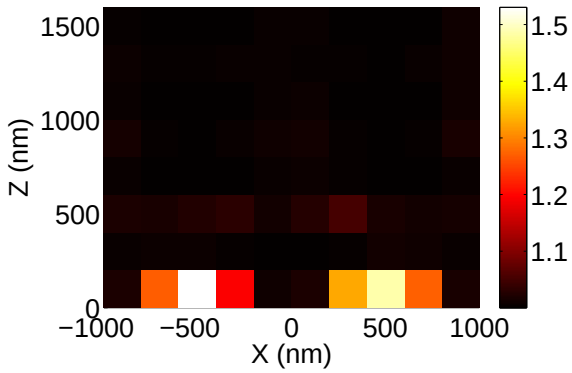

Figure 3.42 : *Longitudinal cut at $y = 500$ nm of the reconstruction with 200 nm meshing of 500 nm large resin cylinders with 125 nm height (PSI data set)*

The domain is then reduced to a rectangular box with dimensions $2 \times 2 \times 0.8$ μm^3 and a mesh size of 100 nm. The results are shown on Figs. 3.43 and 3.44. Lastly, a rectangular box with dimensions $2 \times 2 \times 0.4$ μm^3 is chosen and a mesh size of 50 nm is adopted to have a better discretization. The object is successfully reconstructed as can be seen on Figs. 3.45 and 3.46. The convergence of the iterative process was obtained after seven iterations.

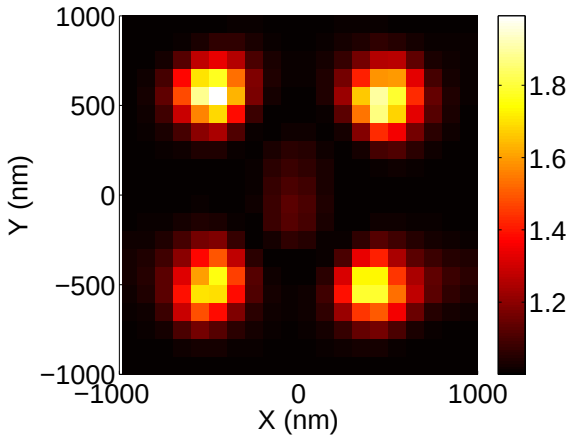

Figure 3.43 : *Transverse cut at $z = 100$ nm of the reconstruction with 100 nm meshing of 500 nm large resin cylinders with 125 nm height (PSI data set)*

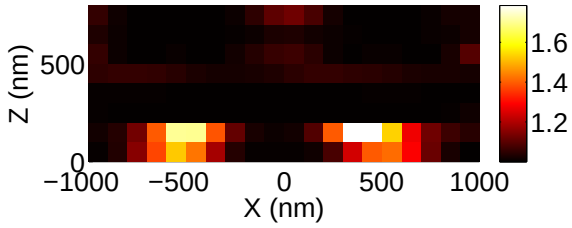

Figure 3.44 : *Longitudinal cut at $y = 500$ nm of the reconstruction with 100 nm meshing of 500 nm large resin cylinders with 125 nm height (PSI data set)*

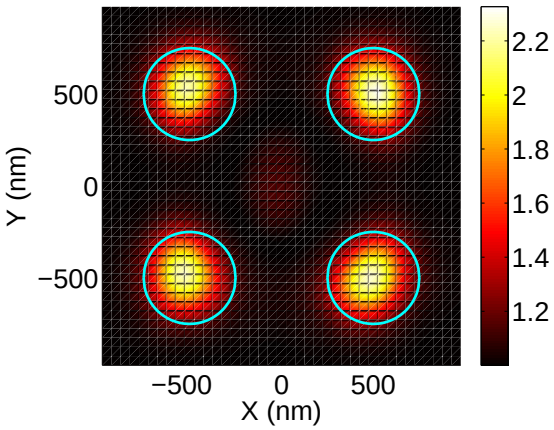

Figure 3.45 : *Transverse cut at $z = 125$ nm of the reconstruction with 50 nm meshing of 500 nm large resin cylinders with 125 nm height (PSI data set)*

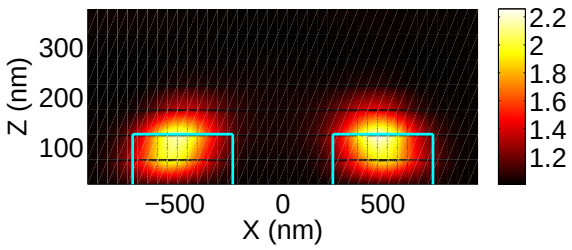

Figure 3.46 : *Longitudinal cut at $y = 500$ nm of the reconstruction with 50 nm meshing of 500 nm large resin cylinders with 125 nm height (PSI data set)*

3.2.2.4 Application of the non-linear inversion algorithm to the off-axis data set

The data set recorded with off-axis holography has roughly the same illumination angles as the PSI one, but it is obtained on samples with a height of 98 nm instead of 125 nm. After the same size adjustment steps for the investigation domain, the reconstruction obtained with an investigation box of $2 \times 2 \times 0.4$ μm^3 and a mesh size of 50 nm is presented on Figs. 3.47 and 3.48.

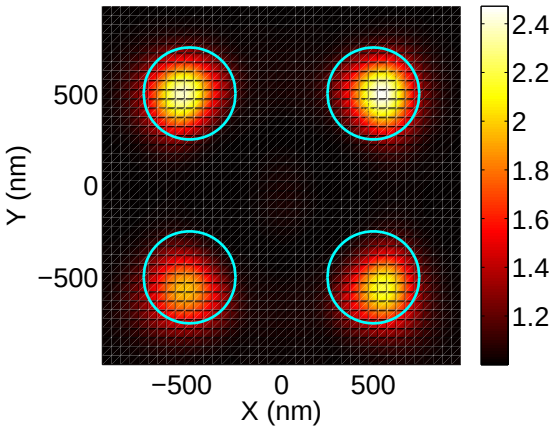

Figure 3.47 : *Transverse cut at $z = 75$ nm of the reconstruction with 50 nm meshing of 500 nm large resin cylinders with 98 nm height (Off-axis data set)*

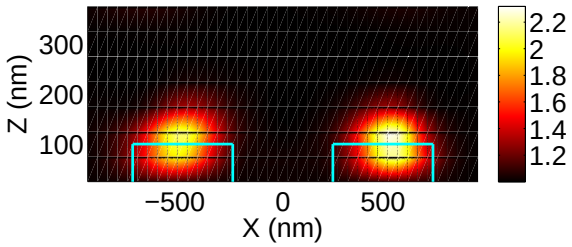

Figure 3.48 : *Longitudinal cut at $y = 500$ nm of the reconstruction with 50 nm meshing of 500 nm large resin cylinders with 98 nm height (Off-axis data set)*

The result is again satisfactory, which validates the use of off-axis holography to speed up the acquisition time. There is however no clear evidence that the inversion procedure is sensitive to the

27 nm height difference of the samples between the PSI and the off-axis data sets. The question of the axial sensitivity of our approach will be studied in more details hereafter.

3.2.2.5 Reconstructions obtained with the linear inversion valid under the Born approximation

Here, the 3D FT^{-1} linear inversion valid under the Born approximation is applied on the PSI and off-axis data sets. Both data sets use 20 illumination angles and the meshing of the reconstruction is about 53 nm. Figures 3.49 and 3.50 show the case of the PSI data set, whereas Figs. 3.51 and 3.52 present the off-axis holography case.

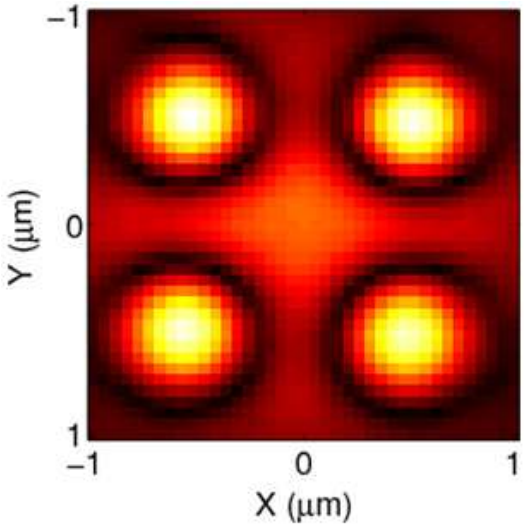

Figure 3.49 : *Transverse cut at $z = 53$ nm of the reconstruction under Born approximation with 53 nm meshing of 500 nm large resin cylinders with 125 nm height (PSI data set)*

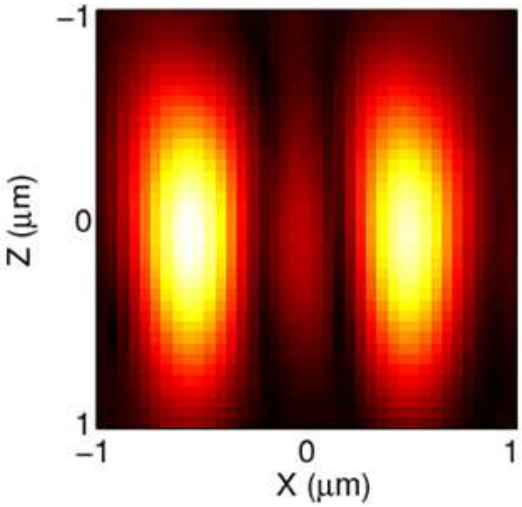

Figure 3.50 : *Longitudinal cut at $y = 500$ nm of the reconstruction under Born approximation with 53 nm meshing of 500 nm large resin cylinders with 125 nm height (PSI data set)*

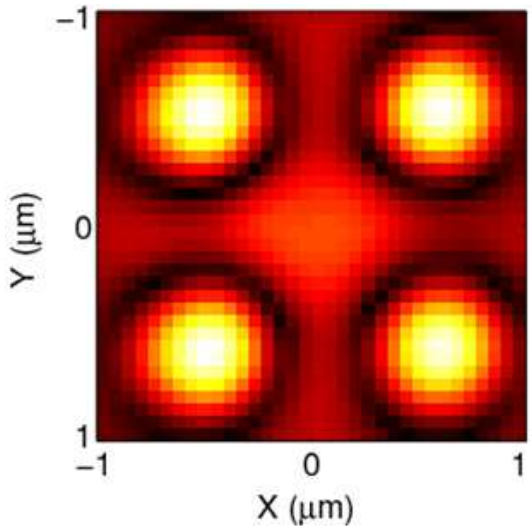

Figure 3.51 : *Transverse cut at $z = 53$ nm of the reconstruction under Born approximation with 53 nm meshing of 500 nm large resin cylinders with 98 nm height (Off-axis data set)*

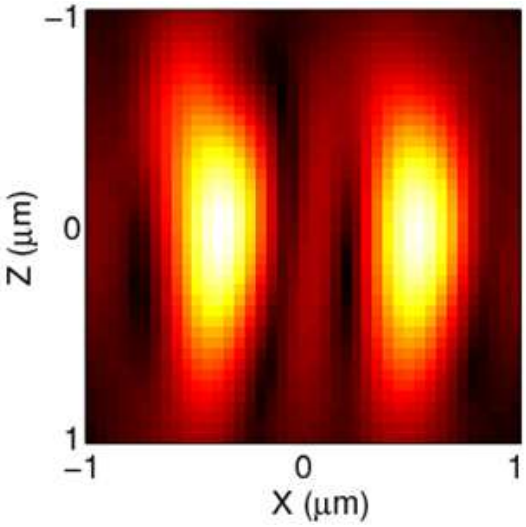

Figure 3.52 : *Longitudinal cut at $y = 500$ nm of the reconstruction under Born approximation with 53 nm meshing of 500 nm large resin cylinders with 98 nm height (Off-axis data set)*

Again, these reconstructions with the conventional linear inversion scheme present more noise than the ones with the non-linear procedure, and remain particularly distorted along the optical axis, due to the presence of the reflective substrate and the limited amount of data in the Fourier space. The four resin pads can be however clearly resolved in the transverse plane, but this is due to the fact that the center to center distance of 1 μm between two cylinders remains well above the Rayleigh criterion, which is of 400 nm in our set-up.

3.2.2.6 Influence of the number of illumination angles on the reconstructions

As we known, the classic Born approximation is very sensitive to the number of incidences, more accessible Fourier domain means better resolution. To clarify the dependence of our non-linear inversion procedure on the number of illumination angles, a measurement with 40 incidences has been carried out with the PSI technique on a sample with 150 nm height. This sample height change will also be used hereafter for the study of the axial sensitivity. To obtain the 40 angles, we keep the same 20 angles as previously and add a new one in the middle of the range between each two successive angles.

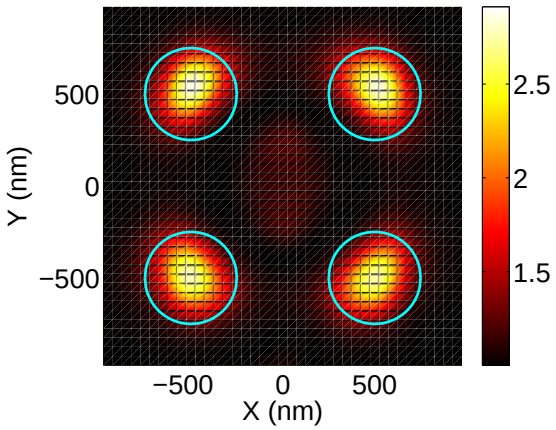

Figure 3.53 : *Transverse cut at $z =$ 125 nm of the reconstruction with 50 nm meshing of 500 nm large resin cylinders with 150 nm height (Off-axis data set, double incidences)*

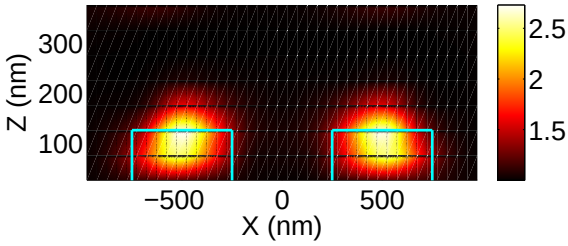

Figure 3.54 : *Longitudinal cut at $y =$500 nm of the reconstruction with 50 nm meshing of 500 nm large resin cylinders with 150 nm height (PSI data set, 40 incidences)*

Figures 3.53 and 3.54 show the reconstruction obtained with the 40 illumination angles in a $2 \times 2 \times 0.4$ μm^3 investigation box with 50 nm meshing. On the other hand, Figs. 3.55 and 3.56 depict a reconstruction obtained with only 10 incidences in TE polarization, whereas Figs. 3.57 and 3.58 is the case for 10 incidences in TM polarization. It is shown that even with a lower number of incidences the geometry of the reconstruction remains satisfactory. It thus confirms the ability of our approach to diminish the number of necessary illumination angles to reconstruct in 3D a sample, compared to the conventional linear inversions. It can therefore be used to increase the speed of the data acquisition.

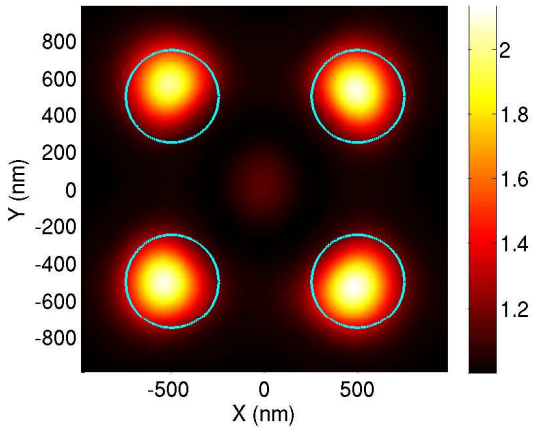

Figure 3.55 : *Transverse cut at $z =$ 125 nm of the reconstruction with 50 nm meshing of 500 nm large resin cylinders with 150 nm height (PSI data set, 10 incidences in TE polarization)*

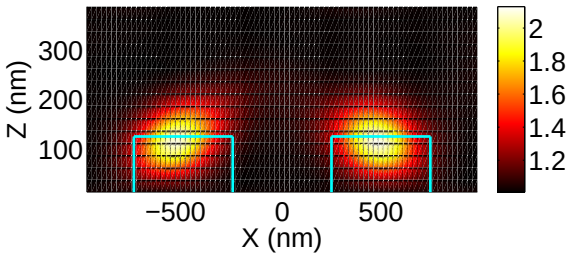

Figure 3.56 : *Longitudinal cut at $y =$500 nm of the reconstruction with 50 nm meshing of 500 nm large resin cylinders with 150 nm height (PSI data set, 10 incidences in TE polarization)*

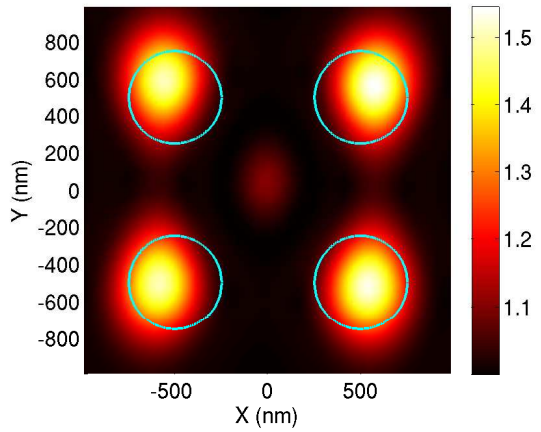

Figure 3.57 : *Transverse cut at $z = 125$ nm of the reconstruction with 50 nm meshing of 500 nm large resin cylinders with 150 nm height (PSI data set, 10 incidences in TM polarization)*

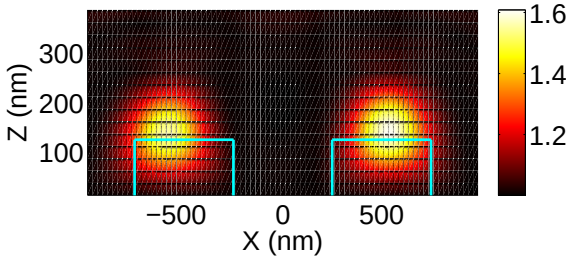

Figure 3.58 : *Longitudinal cut at $y = 500$ nm of the reconstruction with 50 nm meshing of 500 nm large resin cylinders with 150 nm height (PSI data set, 10 incidences in TM polarization)*

3.2.2.7 Spatial filtering of the scattered field for the selective reconstruction of objects

Thanks to the detection in the image space of the field scattered by the object, it is possible to select the part of the image that is of interest to reconstruct only a fraction of the objects imaged on the sensor. When filtering the scattered field in the image space that produces the object of interest, its transfer to the Fourier space also provides the far field scattered by this very object, without interferences with the other parts of the sample. Here we want to show that it is possible to reconstruct only a part of the four cylinders that form a square. In this way, if we are able to reconstruct only one of the cylinders, the investigation domain can become smaller to be adapted to one single cylinder, and the meshing can get denser without requiring a too large memory performance of the computer. In this way a meshing smaller than 50 nm could be used to see if the inversion procedure is sensitive enough to distinguish a resin cylinder with height 98 nm or 150 nm. Note that the spatial filtering in the image space is only possible if the different objects can be resolved and thus spaced by distances above the Rayleigh criterion.

To test if the cylinders can be reconstructed selectively, the PSI data set with 40 illumination angles of the cylinders with diameter 500 nm and height 150 nm is used, but only 20 incidences are conserved. The filtering of the cylinders of interest is performed the following way. The field in the image space is multiplied by a mask function that is equal to one inside of squares where the cylinders of interest are located, and zero outside. These squares are taken large enough so that their edges lie on the substrate where the intensity is almost uniform. Outside of these squares, a uniform complex value is then set. Its modulus and phase are the average modulus and phase along the edges of the squares, respectively. To obtain the average phase, it is at first necessary to correct for the phase ramp due to the tilted illumination so that the phase is uniform on the substrate. Once the complex value has been inserted into the mask, the initial illumination tilt is reintroduced. As a result, the initial scattered field is conserved inside of the squares, and outside has been created an equivalent uniform field reflected by the sample. To decrease the sharpness of the transition between the inside and outside of the square, a convolution by a gaussian function is performed on this global equivalent field, by paying attention to let unchanged the scattered field inside of the squares. The resulting global field can then be multiplied by the same kind of mask function as previously to be transferred in the Fourier space.

For the case of selecting just one cylinder among the four, the filtered scattered field amplitude and phase after processing is presented in Fig. 3.59 for different illumination angles. (a) to (d) and (e) to (h) show the modulus and the phases in the image space, respectively, whereas (i) to (l) and (m) to (p) the modulus and the phases in the Fourier space, respectively.

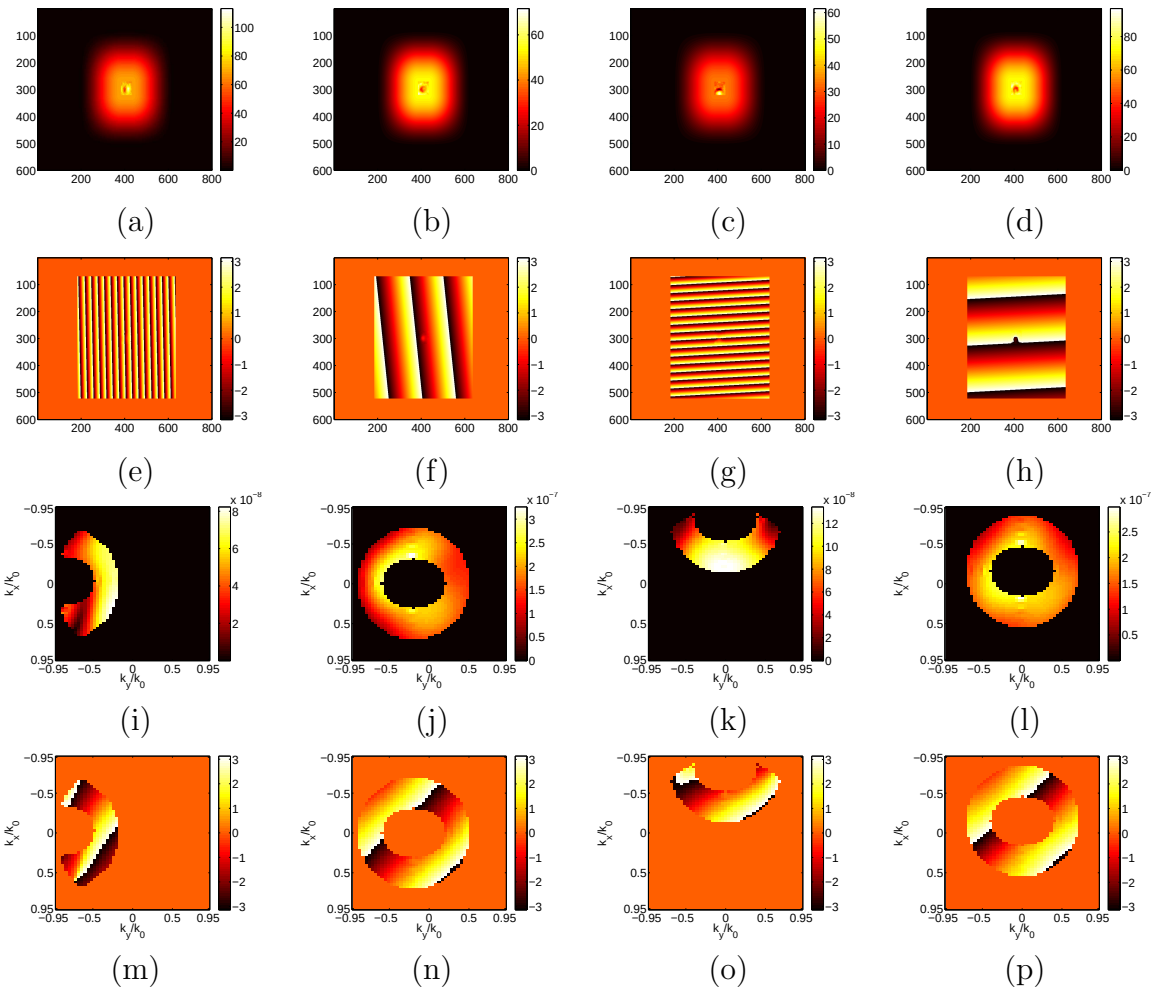

Figure 3.59 : *The upper two rows are the modulus and phases of the field scattered by one cylinder detected on the CCD camera, the lowers are the modulus and phases of the field scattered by one cylinder in Fourier domain, respectively. Data set obtained by PSI. (a, e, i, m)* $\theta_l = 55°$, $\phi_l = 0°$, *TE polarization; (b, f, j, n)* $\theta_l = 8.8°$, $\phi_l = 0°$, *TE polarization; (c, g, k, o)* $\theta_l = 55°$, $\phi_l = 90°$, *TM polarization; (d, h, l, p)* $\theta_l = 9°$, $\phi_l = 90°$, *TM polarization.*

The same treatment steps could be applied for selecting the field scattered by two diagonal cylinders. Similarly to Fig. 3.59, Fig. 3.60 displays for this case the resulting field in the image space and in the Fourier space.

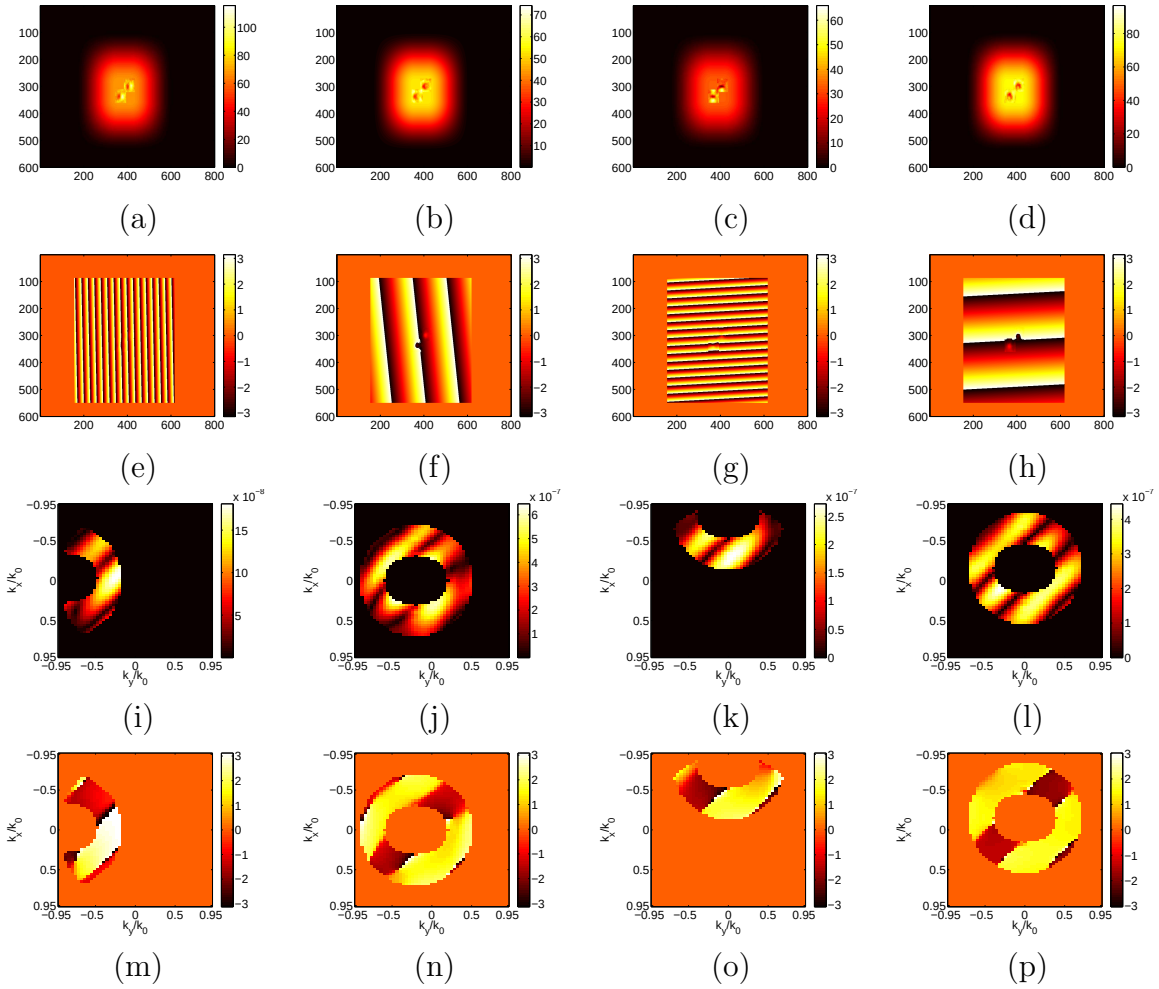

Figure 3.60 : *The upper two rows are the modulus and phases of the field scattered by two diagonal cylinders detected on the CCD camera, the lowers are the modulus and phases of the field scattered by two diagonal cylinders in Fourier domain, respectively. Data set obtained by PSI. (a, e, i, m)* $\theta_l = 55°$, $\phi_l = 0°$, *TE polarization; (b, f, j, n)* $\theta_l = 8.8°$, $\phi_l = 0°$, *TE polarization; (c, g, k, o)* $\theta_l = 55°$, $\phi_l = 90°$, *TM polarization; (d, h, l, p)* $\theta_l = 9°$, $\phi_l = 90°$, *TM polarization.*

To obtain the reconstructions through the non-linear inversion, note that the data in the Fourier space has been again restricted to about two thousands scattering angles centered on the specular reflection on the substrate. The case of the single cylinder is presented on Figs. 3.61 and 3.62, in a 2 μm×2 μm×400 nm investigation domain with 50 nm meshing. The reconstruction for the two diagonal cylinders is displayed on Figs. 3.63 and 3.64.

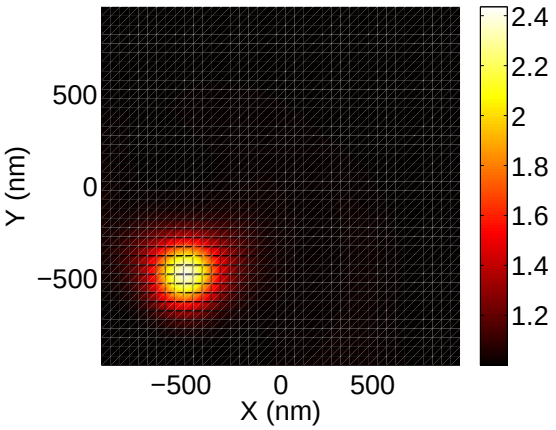

Figure 3.61 : *Transverse cut at z = 125 nm of the reconstruction with 50 nm meshing of one 500 nm large resin cylinders with 150 nm height (PSI data set)*

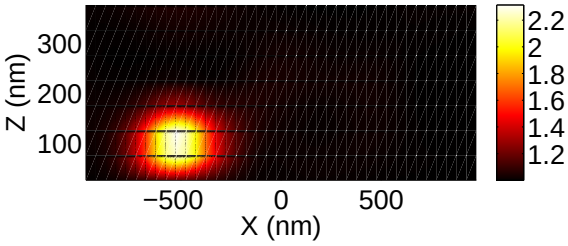

Figure 3.62 : *Longitudinal cut at y =-500 nm of the reconstruction with 50 nm meshing of one 500 nm large resin cylinders with 150 nm height (PSI data set)*

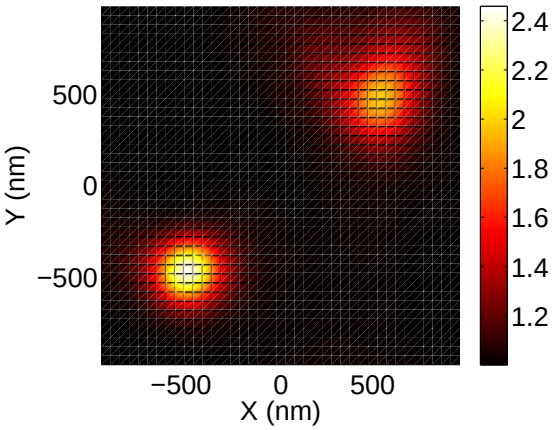

Figure 3.63 : *Transverse cut at z = 125 nm of the reconstruction with 50 nm meshing of two 500 nm large resin cylinders with 150 nm height (PSI data set)*

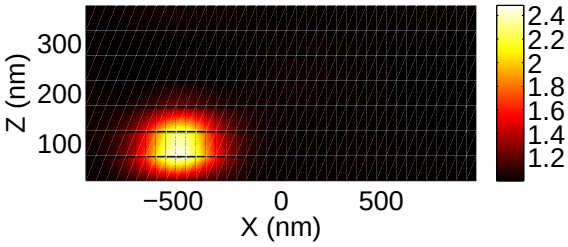

Figure 3.64 : *Longitudinal cut at y =-500 nm of the reconstruction with 50 nm meshing of two 500 nm large resin cylinders with 150 nm height (PSI data set)*

From these figures, it can be seen that the selective reconstruction of objects can be obtained successfully. It will be used in the next section to focus on the height of one cylinder in a smaller investigation domain.

3.2.2.8 Comparison of different sample heights

To figure out if the non-linear inversion procedure is able to detect a height difference of 52 nm between the cylinders with heights of 98 nm and 150 nm, reconstructions are generated here selectively on a single resin cylinder for both height cases. The chosen investigation domain size

to contain one cylinder is 750×750× 300 nm^3. This smaller volume can be discretized with a tight meshing of 10 nm without requiring too much memory and computation time for the calculations.

The reconstruction obtained for the 150 nm height case is presented on Figs. 3.65 and 3.66, whereas the 98 nm height case is displayed on Figs. 3.67 and 3.68.

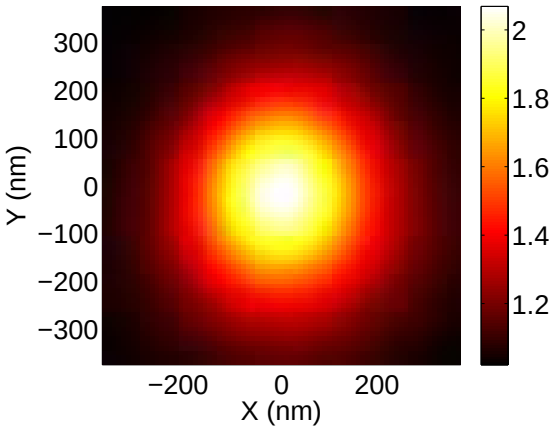

Figure 3.65 : *Transverse cut at z = 120 nm of the reconstruction with 10 nm meshing of 500 nm large resin cylinders with 150 nm height (PSI data set)*

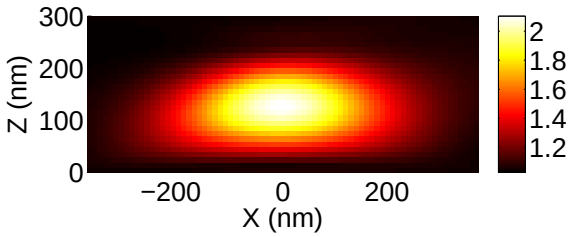

Figure 3.66 : *Longitudinal cut at y =0 nm of the reconstruction with 10 nm meshing of one 500 nm large resin cylinders with 150 nm height (PSI data set)*

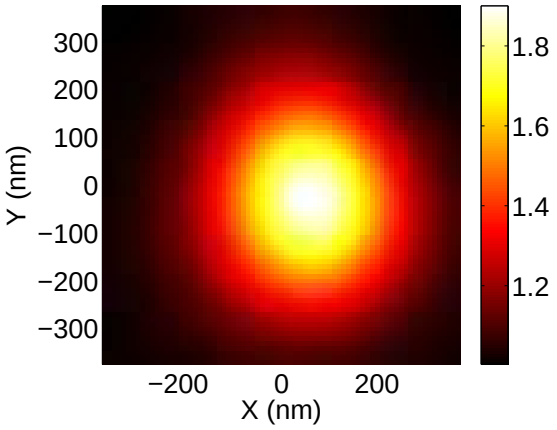

Figure 3.67 : *Transverse cut at z = 80 nm of the reconstruction with 10 nm meshing of 500 nm large resin cylinders with 98 nm height (Off-axis data set)*

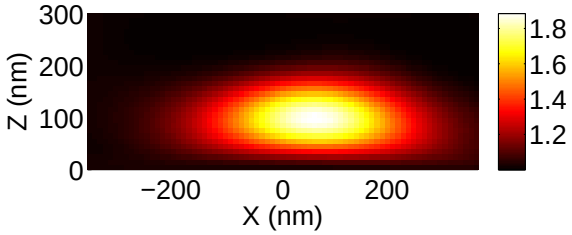

Figure 3.68 : *Longitudinal cut at y =-30 nm of the reconstruction with 10 nm meshing of one 500 nm large resin cylinders with 98 nm height (Off-axis data set)*

To better estimate if a height difference can be detected on the reconstructions, the permittivity profile along the z direction in the middle of the cylinder is presented for the height cases of 98 nm and 150 nm on Figs. 3.70 and 3.69, respectively. The full width at half maximum on these profiles are 116 nm and 139 nm, respectively. A higher value is clearly retrieved for the higher

height case, but the height difference of 52 nm is not quantitatively determined. The non-linear inversion procedure has therefore a high axial sensitivity but more *a priori* information on the object, like a lower and a higher boundaries for the permittivity, would be certainly necessary to improve quantitatively the height estimation in the nanometric range.

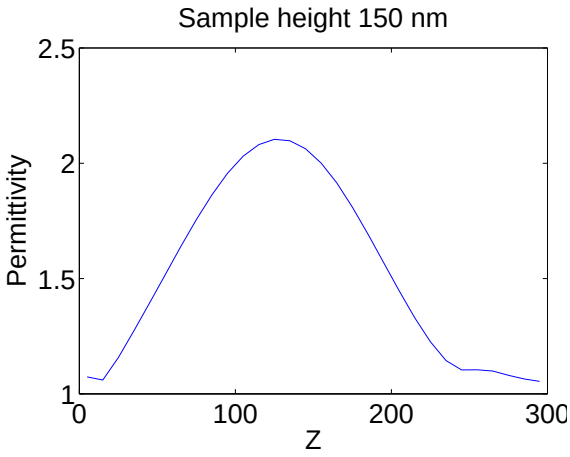

Figure 3.69 : *A line cut map along z with* 150*nm height sample at* $x = 0nm$

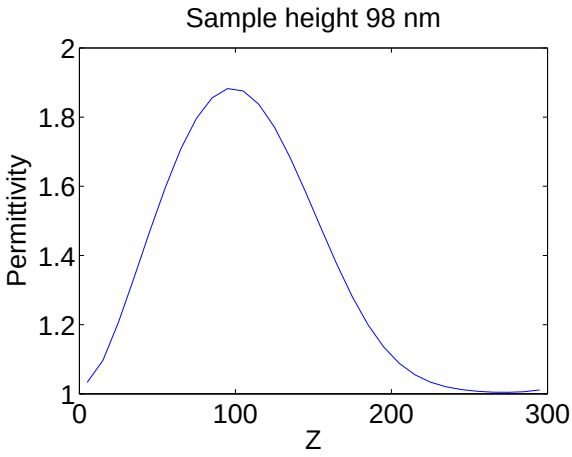

Figure 3.70 : *A line cut map along z with* 98*nm height sample at* $x = 50nm$

3.2.3 Resin cylinders with diameter 200 nm

Until now, successful reconstructions have been obtained on samples with transverse features above the Rayleigh criterion of 400 nm of our set-up. Here, we deal with resin cylinders of diameter 200 nm and height 150 nm that have a center to center distance that is equal to the Rayleigh criterion.

3.2.3.1 Comparison of the data set measured by PSI with the theory

20 illuminations angles are used in the measurement similarly to the case of the samples with 500 nm diameter. Figure 3.71 shows the detected image field in the vicinity of the object for different angles. It can be seen that the spatial frequencies contained in the modulus of the field vary a lot with respect to the illumination angle : higher spatial frequencies are present in the case of a large illumination angle. Of course as the object is at the limit of the Rayleigh criterion the four cylinders cannot be distinguished when illuminated by a single plane wave.

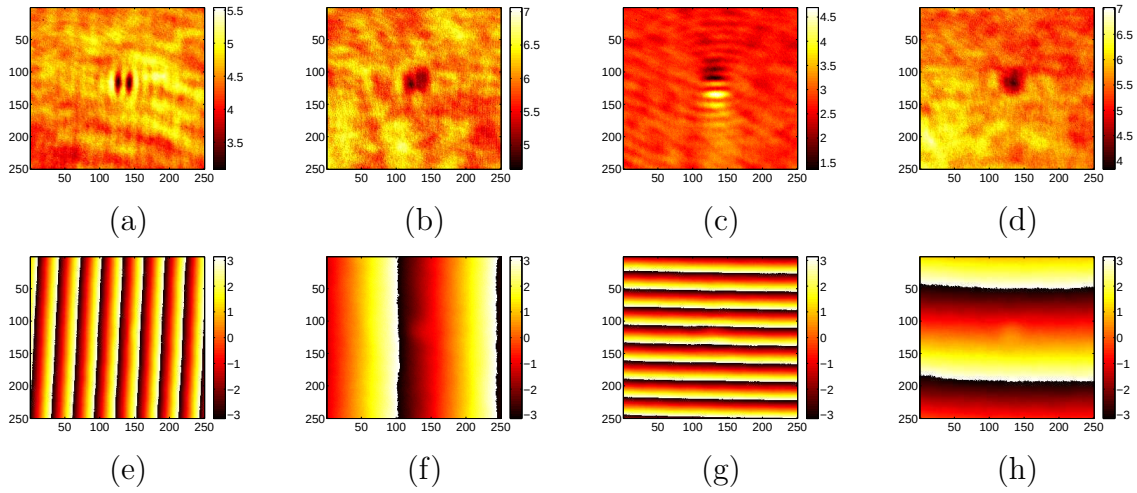

Figure 3.71 : *Modulus [(a)-(d)] and phases [(e)-(h)] of the data set obtained by PSI, respectively. Samples diameter* 200*nm, height* 150*nm. (a) and (e)* $\theta_l = 53°$, $\phi_l = 0°$, *TE polarization; (b) and (f)* $\theta_l = 11°$, $\phi_l = 0°$, *TE polarization; (c) and (g)* $\theta_l = 54°$, $\phi_l = 90°$, *TM polarization; (d) and (h)* $\theta_l = 9°$, $\phi_l = 90°$, *TM polarization.*

Figure 3.72 presents the data for the same illumination angles in the Fourier space. The theoretical field calculated by the CDM is also shown on Fig. 3.73 for comparison. In both cases it can be seen that a larger illumination angle permits to detect inside of the objective NA a diffraction lobe at higher spatial frequencies, which is beneficial to determine the center to center distance of the cylinders.

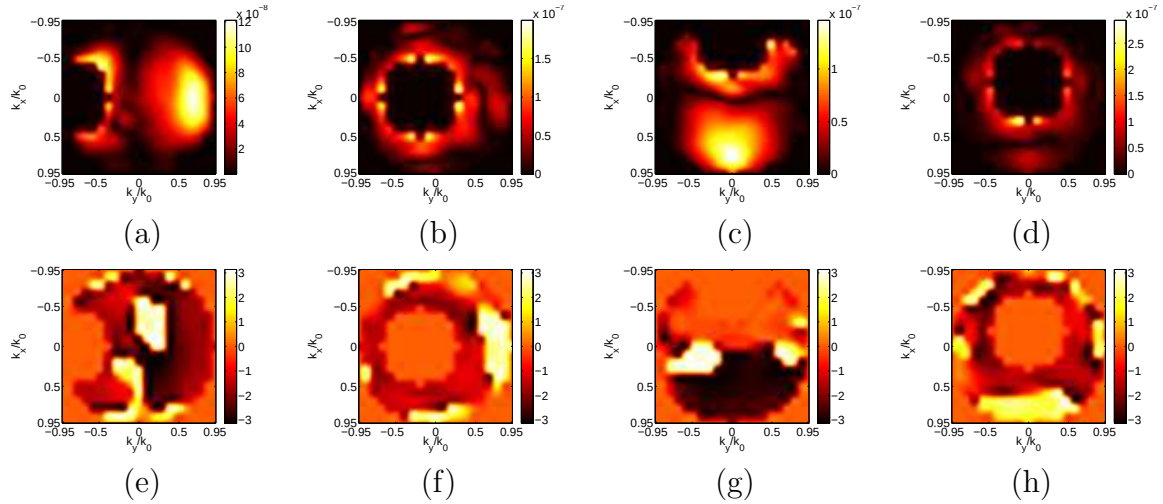

Figure 3.72 : *Modulus (first line) and phases (second line) of the far field (Fourier space) scattered by resin cylinders with diameter 200 nm and height 150 nm, obtained by PSI. (a) and (e)* $\theta_l = 53°$, $\phi_l = 0°$, *TE polarization; (b) and (f)* $\theta_l = 11°$, $\phi_l = 0°$, *TE polarization; (c) and (g)* $\theta_l = 54°$, $\phi_l = 90°$, *TM polarization; (d) and (h)* $\theta_l = 9°$, $\phi_l = 90°$, *TM polarization.*

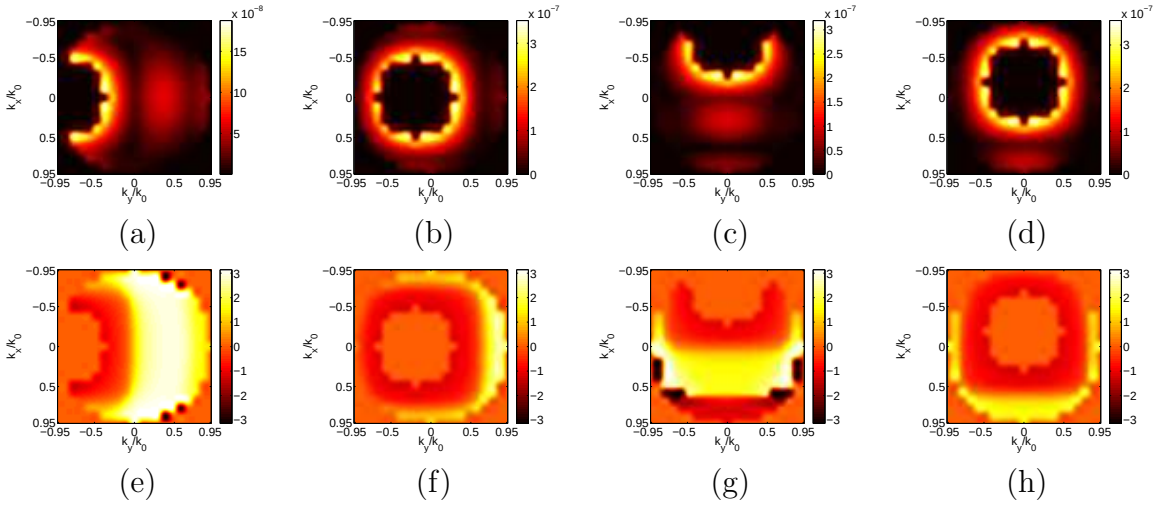

Figure 3.73 : *Modulus (first line) and phases (second line) of the theoretical far field (Fourier space) scattered by resin cylinders with diameter 200 nm and height 150 nm. (a) and (e) $\theta_l = 53°$, $\phi_l = 0°$, TE polarization; (b) and (f) $\theta_l = 11°$, $\phi_l = 0°$, TE polarization; (c) and (g) $\theta_l = 54°$, $\phi_l = 90°$, TM polarization; (d) and (h) $\theta_l = 9°$, $\phi_l = 90°$, TM polarization.*

3.2.3.2 Data set obtained by off-axis holography

With smaller object sizes, the sensibility to external perturbations of the PSI method can become more critical. Therefore the measurement has also been carried out by off-axis holography. For each illumination angle the scattered field can be retrieved by a single shot measurement, but 30 repetitions are here averaged for each angle to increase the signal to noise ratio. The acquisition time is thus reduced to about one quarter of the time necessary for the PSI technique. The intensity measured in the image space is presented on Fig. 3.74 for several illumination angles. As the object is small, it can barely be seen as it is hidden by the interference fringes between the off-axis reference wave and the specular reflection.

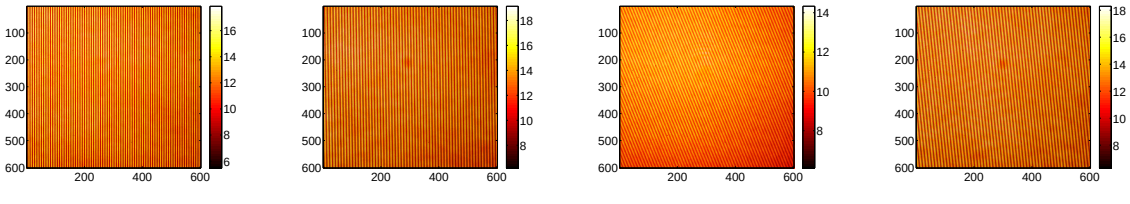

Figure 3.74 : *Intensity in the image space measured by off-axis holography on samples with diameter 200 nm and height 150 nm. (a) $\theta_l = 52°$, $\phi_l = 0°$, TE polarization; (b) $\theta_l = 10°$, $\phi_l = 0°$, TE polarization; (c) $\theta_l = 54°$, $\phi_l = 90°$, TM polarization; (d) $\theta_l = 10°$, $\phi_l = 90°$, TM polarization.*

Once divided by the reference wave modulus, that is measured independently, these intensities are transferred to the Fourier space. Figure 3.74 displays the modulus of the signal in the Fourier space for the same illumination angles as previously. The three interference orders can clearly be seen. Only one of them on the side is filtered to retrieve the field scattered by the object, as shown on Fig. 3.75.

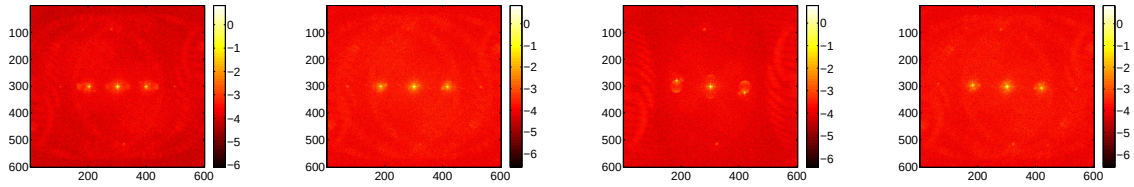

(a) (b) (c) (d)

Figure 3.75 : *Modulus of the far field (Fourier space) scattered by resin cylinders with diameter 200 nm and height 150 nm, obtained by off-axis method. (a)* $\theta_l = 52°$, $\phi_l = 0°$, *TE polarization; (b)* $\theta_l = 10°$, $\phi_l = 0°$, *TE polarization; (c)* $\theta_l = 54°$, $\phi_l = 90°$, *TM polarization; (d)* $\theta_l = 10°$, $\phi_l = 90°$, *TM polarization.*

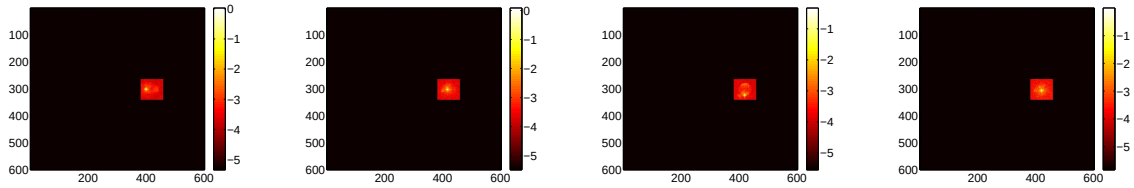

(a) (b) (c) (d)

Figure 3.76 : *Modulus of the selected interference order of the far field (Fourier space) scattered by resin cylinders with diameter 200 nm and height 150 nm, obtained by off-axis method. (a)* $\theta_l = 52°$, $\phi_l = 0°$, *TE polarization; (b)* $\theta_l = 10°$, $\phi_l = 0°$, *TE polarization; (c)* $\theta_l = 54°$, $\phi_l = 90°$, *TM polarization; (d)* $\theta_l = 10°$, $\phi_l = 90°$, *TM polarization.*

As previously explained for the case of the 500 nm large resin cylinders, a 2D FT is then applied to this filtered field to obtain the complex scattered field in the image space, as would have been obtained by the PSI technique. The modulus of this field is presented on Fig. 3.77 for the same illumination angles. For small angles the scattering spot due to the object can be easily detected. Thus the phase origin can be placed on the object position before transfer to the Fourier space, what was impossible to perform accurately on the raw intensity measurement in the image space. Note that the modulus attenuation on the sides of the image is due to the mask function introduced on the intensity measurement to limit the artefacts of the discrete 2D FT^{-1} for the Fourier space transfer. Finally, the modulus and phase of the scattered field in the Fourier space inside of the objective NA are displayed on Fig. 3.78. As in the PSI and theoretical cases, the diffraction lobe appearing at high illumination angles is clearly resolved. However, the data appears more noisy in the off-axis case compared to PSI.

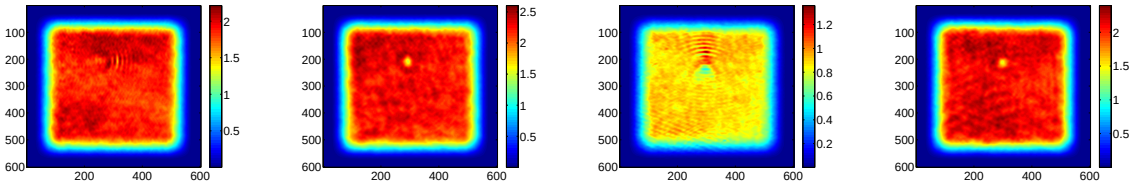

(a) (b) (c) (d)

Figure 3.77 : *Modulus of the field in the image space retrieved from the off-axis holography data set on samples with diameter 200 nm and height 150 nm. (a) $\theta_l = 52°$, $\phi_l = 0°$, TE polarization; (b) $\theta_l = 10°$, $\phi_l = 0°$, TE polarization; (c) $\theta_l = 54°$, $\phi_l = 90°$, TM polarization; (d) $\theta_l = 10°$, $\phi_l = 90°$, TM polarization.*

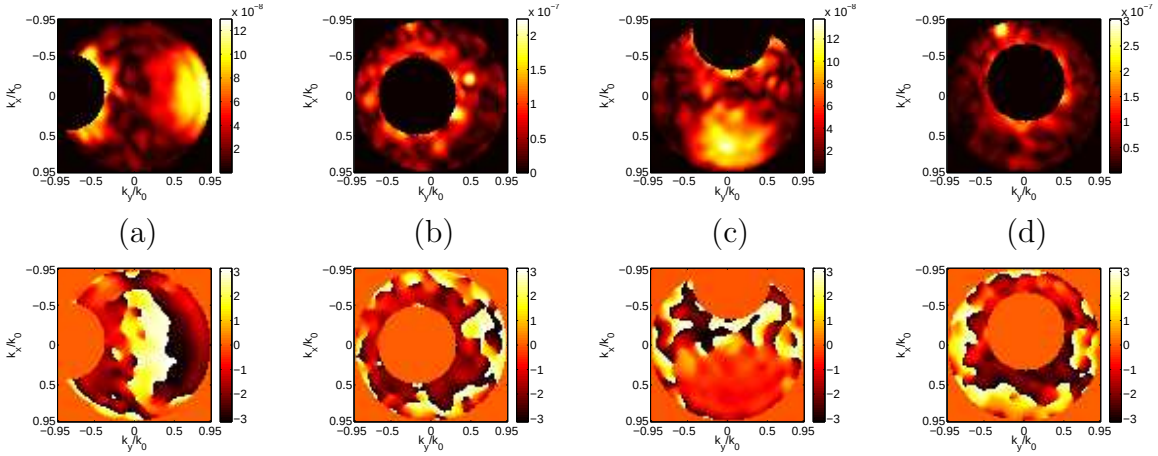

(a) (b) (c) (d)

(e) (f) (g) (h)

Figure 3.78 : *Modulus (first line) and phase (second line) of the field in the Fourier space retrieved from the off-axis holography data set on samples with diameter 200 nm and height 150 nm. (a) and (e) $\theta_l = 53°$, $\phi_l = 0°$, TE polarization; (b) and (f) $\theta_l = 11°$, $\phi_l = 0°$, TE polarization; (c) and (g) $\theta_l = 54°$, $\phi_l = 90°$, TM polarization; (d) and (h) $\theta_l = 9°$, $\phi_l = 90°$, TM polarization.*

3.2.3.3 Reconstructions obtained with the non-linear inversion procedure on the PSI and off-axis data sets

The non-linear inversion algorithm is applied on the PSI and off-axis data sets presented in the previous section. Once again, the linear 3D FT^{-1} inversion is used to estimate the initial investigation domain size for the iterative algorithm. The application of the 3D FT^{-1} to the PSI data set is shown on Figs. 3.79 and 3.80, whereas the off-axis case is presented on Figs. 3.81 and 3.82. In both cases, the reconstruction is not only axially distorted as previously, but also in the transverse plane where the four cylinders cannot be resolved. The reconstruction is moreover much more distorted in the off-axis case, due to a more noisy data set. Note that for such distorted reconstructions, it is preferable to use the iterative method based on the backpropagation to correct the phase origin mismatch d_z. As the investigation domain is reduced with smaller objects, the computation time requirements are no longer an issue.

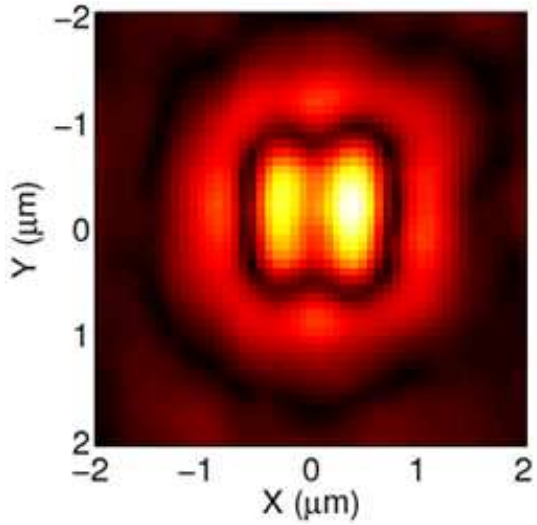

Figure 3.79 : *Transverse cut at $z = 53$ nm of the reconstruction under Born approximation with 53 nm meshing of 200 nm large resin cylinders with 150 nm height (PSI data set)*

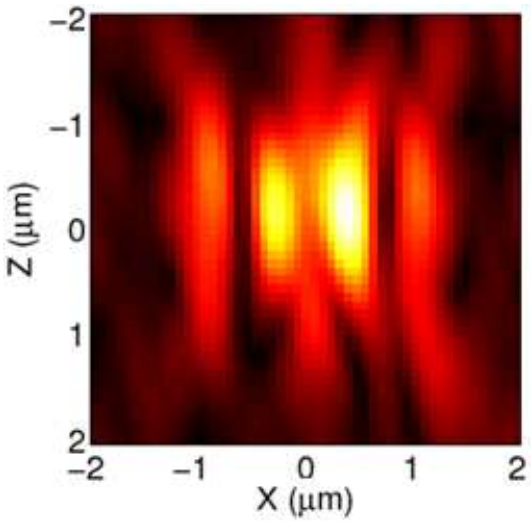

Figure 3.80 : *Longitudinal cut at $y = 0$ nm of the reconstruction under Born approximation with 53 nm meshing of 200 nm large resin cylinders with 150 nm height (PSI data set)*

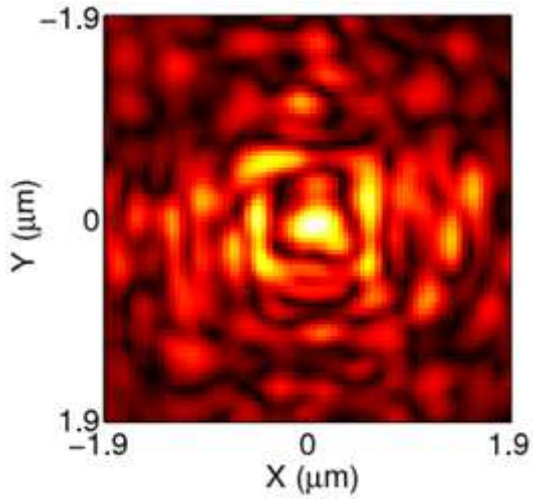

Figure 3.81 : *Transverse cut at $z = 53$ nm of the reconstruction under Born approximation with 53 nm meshing of 200 nm large resin cylinders with 150 nm height (Off-axis data set)*

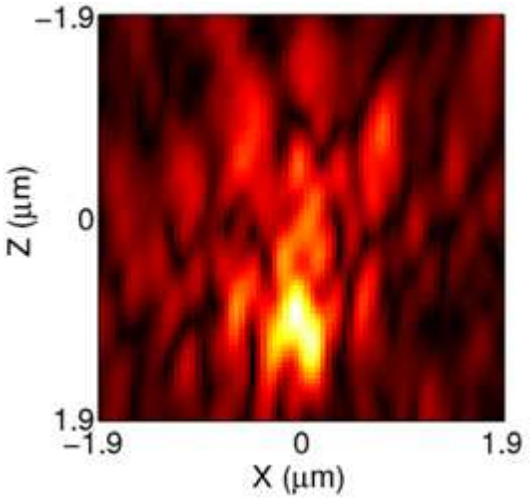

Figure 3.82 : *Longitudinal cut at $y = 0$ nm of the reconstruction under Born approximation with 53 nm meshing of 200 nm large resin cylinders with 150 nm height (Off-axis data set)*

The reconstruction obtained with our algorithm and the PSI data set for a 1 μm×1 μm ×400 nm domain with a 50 nm meshing is displayed on Figs. 3.83 and 3.84. The off-axis case is presented on Figs. 3.85 and 3.86. In both cases the four resin cylinders are resolved, but the PSI reconstruction has a better homogeneity on the four cylinders than the off-axis one.

The interest of off-axis holography to improve the robustness of the set-up is therefore not proved on this example. It has on the contrary given rise to a more noisy data set than PSI. The required measurement time for 20 illumination angles with the PSI technique seems therefore compatible with a sample position that is not altered too much by mechanical drifts. The stabilization of the optical table seems also sufficient to limit the impact of external perturbations on the applied phase shifts. The signal to noise ratio can in this case be better with the PSI technique compared to off-axis holography. In PSI, as described in chapter 2, the useful signal is retrieved by performing a differential detection between several interference patterns. It therefore eliminates any additive noise level in the signal and increases by a factor 2 its useful part, which contains the two interference terms involving the scattered field. On the other hand in off-axis holography only one interference term is kept, so the useful signal is four times weaker than in PSI, and no correction of the additive noise level is performed. On this small object with weak scattering signal it can be an important factor.

The main result here is however that to our knowledge, this is the first time that such an iterative non linear inversion procedure successfully reaches the Rayleigh limit with 3D experimental data in optics.

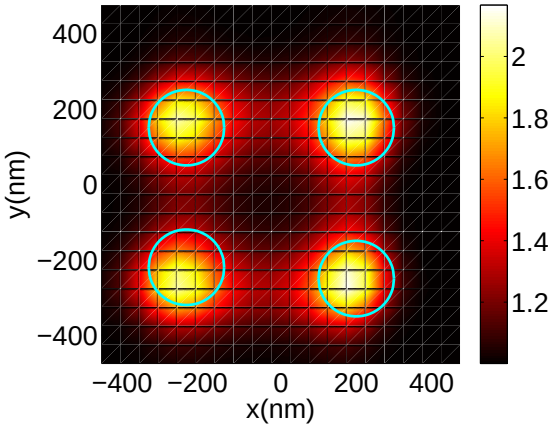

Figure 3.83 : *Transverse cut at $z = 125$ nm of the reconstruction with 50 nm meshing of 200 nm large resin cylinders with 150 nm height (PSI data set)*

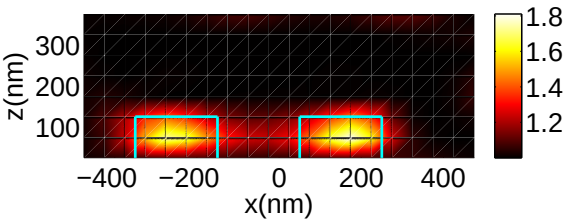

Figure 3.84 : *Longitudinal cut at $y = 200$ nm of the reconstruction with 50 nm meshing of 200 nm large resin cylinders with 150 nm height (PSI data set)*

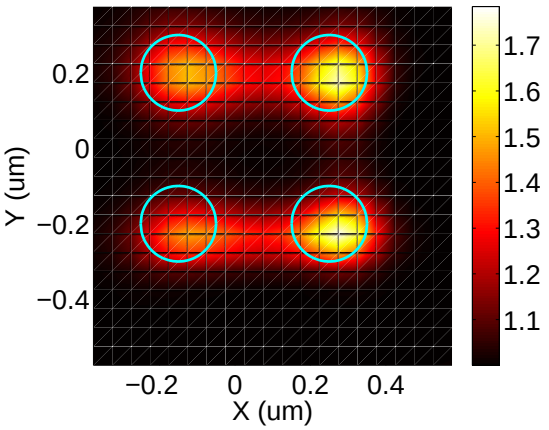

Figure 3.85 : *Transverse cut at $z =$ 125 nm of the reconstruction with 50 nm meshing of 200 nm large resin cylinders with 150 nm height (Off-axis data set)*

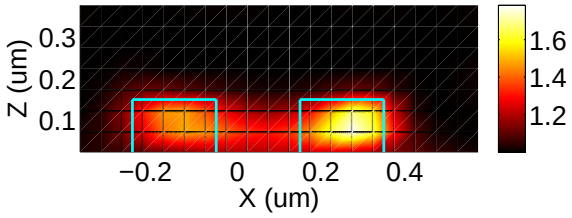

Figure 3.86 : *Longitudinal cut at $y =$300 nm of the reconstruction with 50 nm meshing of 200 nm large resin cylinders with 150 nm height (Off-axis data set)*

3.2.4 Resin cylinders with diameter 150 nm

3.2.4.1 Comparison of the data set measured by PSI with the theory

The resin cylinders have here a diameter and a height of 150 nm, their center to center distance of 300 nm is thus clearly below the Rayleigh criterion. The measurement is carried out with the same 20 illumination angles as for the previous sample. The first detection method used here is the PSI technique. Figure 3.87 presents the measured fields in the image space for several illumination angles. The signal is as expected still weaker than for the 200 nm diameter case.

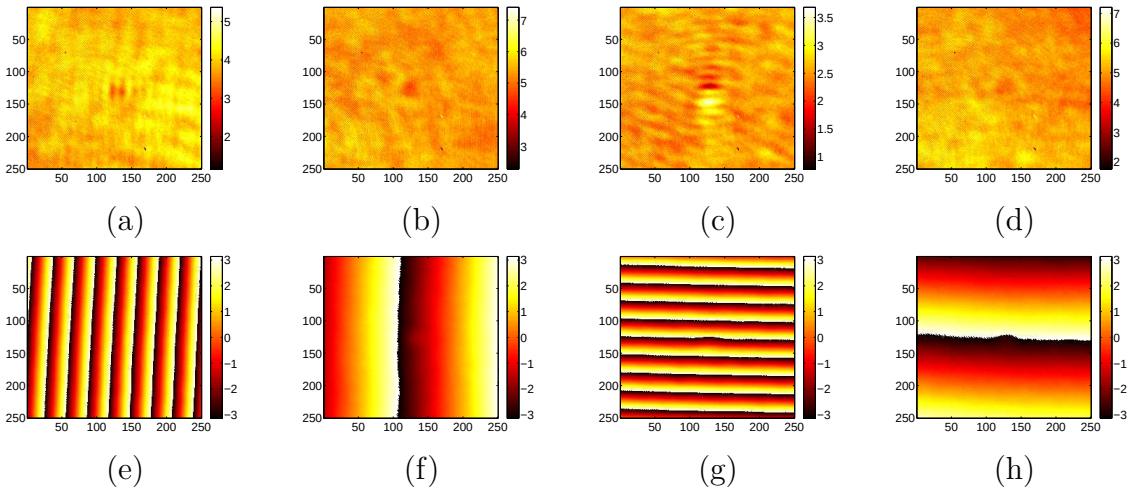

Figure 3.87 : *Modulus (first line) and phases (second line) of the data set obtained by PSI. Samples diameter* 150 *nm, height* 150 *nm. (a) and (e) $\theta_l = 53°$, $\phi_l = 0°$, TE polarization; (b) and (f) $\theta_l = 11°$, $\phi_l = 0°$, TE polarization; (c) and (g) $\theta_l = 54°$, $\phi_l = 90°$, TM polarization; (d) and (h) $\theta_l = 10°$, $\phi_l = 90°$, TM polarization.*

The data for the same angles is shown in the Fourier space on Fig. 3.88, and for comparison Fig. 3.89 displays the theoretical field calculated with the CDM. As expected, the diffraction lobe appearing at high spatial frequencies for large angles is more reduced than in the 200 nm diameter case.

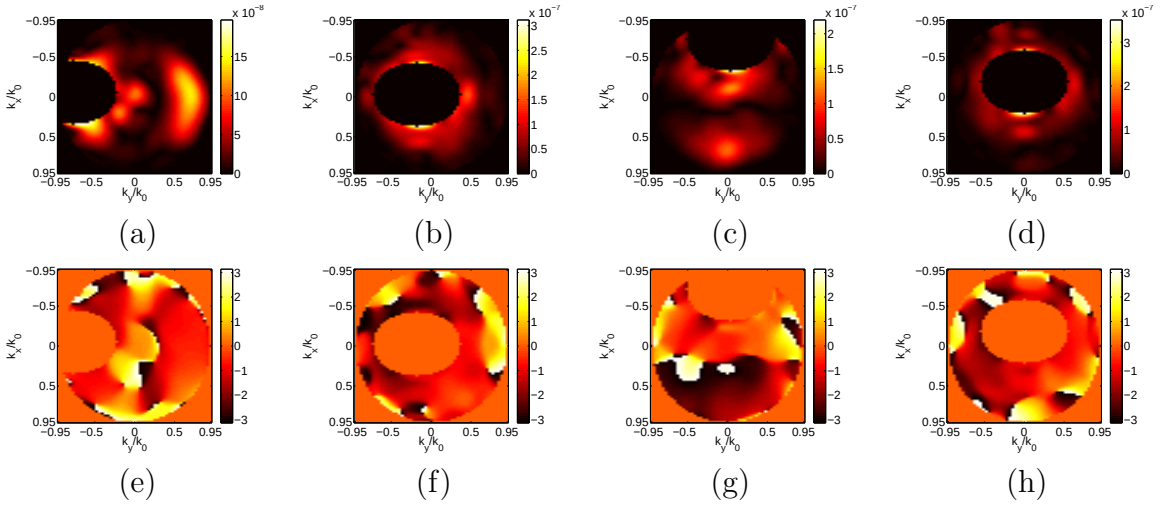

Figure 3.88 : *Modulus (first line) and phases (second line) of the data set in the Fourier space, obtained by PSI. Samples diameter* 150 *nm, height* 150 *nm. (a) and (e)* $\theta_l = 53°$, $\phi_l = 0°$, *TE polarization; (b) and (f)* $\theta_l = 11°$, $\phi_l = 0°$, *TE polarization; (c) and (g)* $\theta_l = 54°$, $\phi_l = 90°$, *TM polarization; (d) and (h)* $\theta_l = 10°$, $\phi_l = 90°$, *TM polarization.*

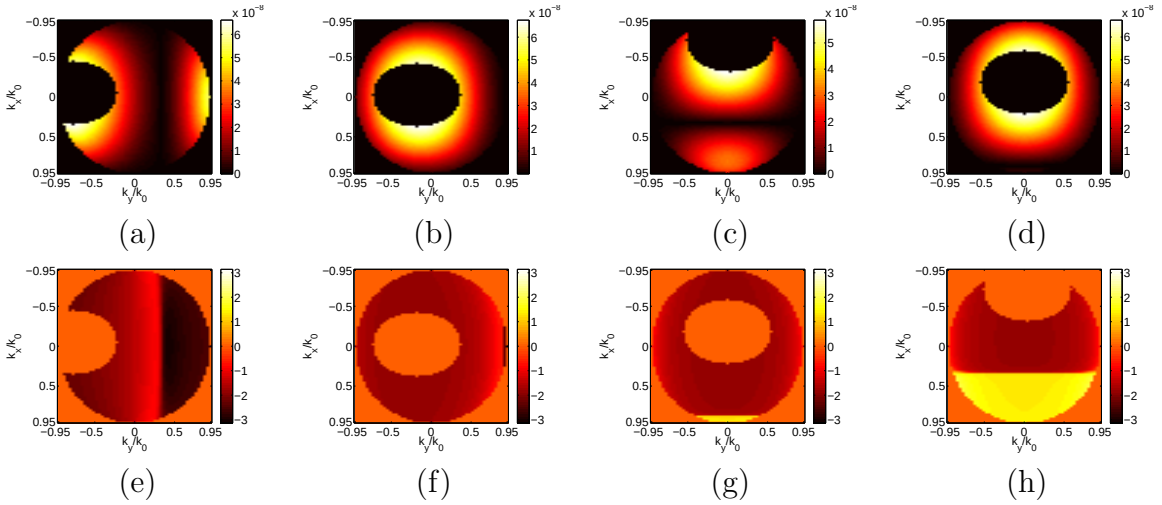

Figure 3.89 : *Modulus (first line) and phases (second line) of the theoretical field in the Fourier space. Samples diameter* 150 *nm, height* 150 *nm. (a) and (e)* $\theta_l = 53°$, $\phi_l = 0°$, *TE polarization; (b) and (f)* $\theta_l = 11°$, $\phi_l = 0°$, *TE polarization; (c) and (g)* $\theta_l = 54°$, $\phi_l = 90°$, *TM polarization; (d) and (h)* $\theta_l = 10°$, $\phi_l = 90°$, *TM polarization.*

3.2.4.2 Data set measured by off-axis holography

For comparison with the PSI technique, the same measurement is performed by off-axis holography and presented on Fig. 3.90. The acquisition time is about four times quicker, but again it appears that the data is more noisy in the case of off-axis holography compared to PSI.

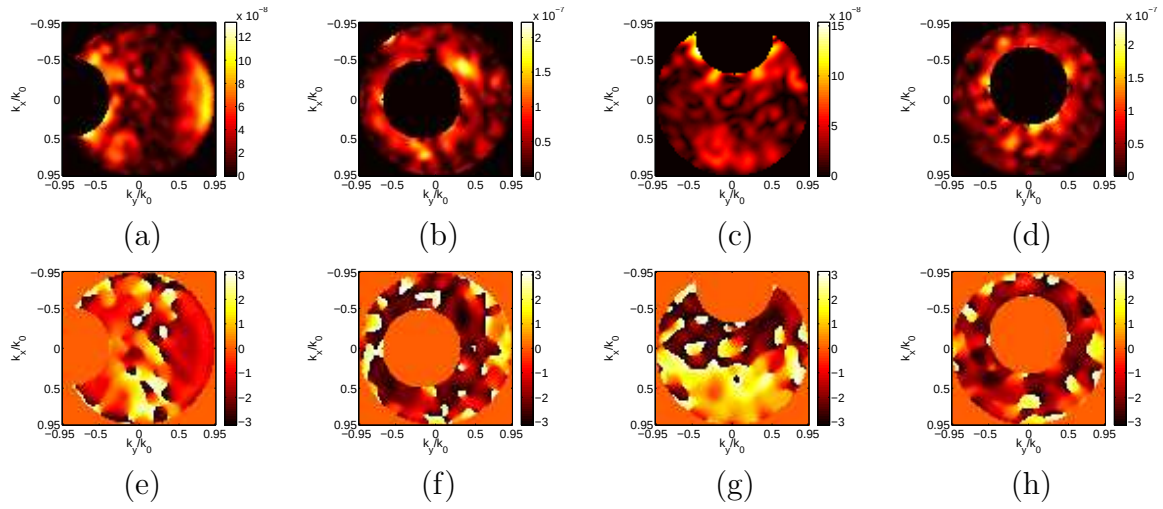

Figure 3.90 : *Modulus and phases of the data set in the Fourier space, obtained by off-axis holography. Samples diameter 150 nm, height 150 nm. (a) and (e) $\theta_l = 54°$, $\phi_l = 0°$, TE polarization; (b) and (f) $\theta_l = 11°$, $\phi_l = 0°$, TE polarization; (c) and (g) $\theta_l = 54°$, $\phi_l = 90°$, TM polarization; (d) and (h) $\theta_l = 11°$, $\phi_l = 90°$, TM polarization.*

3.2.4.3 Comparison of the reconstructions obtained with the non-linear inversion procedure on the PSI and off-axis data sets

The non-linear inversion procedure is applied on the PSI and the off-axis data sets. Figs. 3.91 and 3.92 show the reconstruction obtained with the PSI data set in a 1 μm $\times$1 μm $\times$400 nm investigation domain with 50 nm meshing. Four cylinders are reconstructed but their separation distance is wrong. As the information on this distance is mainly present in the large angle measurements, the data set is restricted to its eight larger illumination angles and the corresponding reconstruction is shown on Figs. 3.93 and 3.94. No real improvement can be seen, the separation distance is still wrong, so even if the lower angle measurements do not carry much information on the object, they do not seem to be detrimental to the reconstruction process.

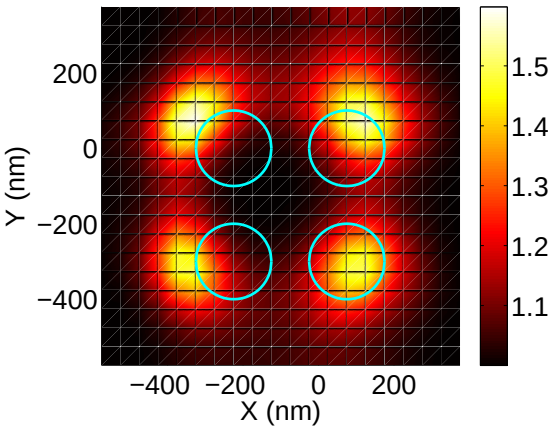

Figure 3.91 : *Transverse cut image at $z = 100$ nm of the reconstruction obtained with the PSI data set (20 incidences). Sample diameter* 150 *nm, height* 150 *nm.*

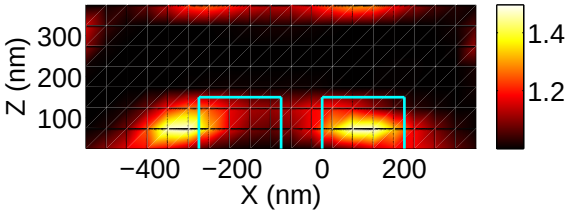

Figure 3.92 : *Longitudinal cut image at $y = 150$ nm of the reconstruction obtained with the PSI data set (20 incidences). Sample diameter* 150 *nm, height* 150 *nm.*

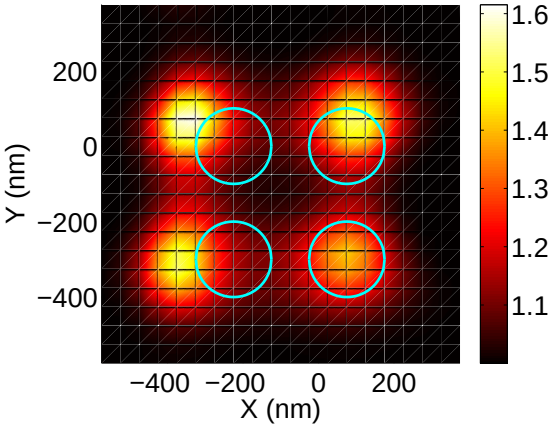

Figure 3.93 : *Transverse cut image at $z = 100$ nm of the reconstruction obtained with the PSI data set (8 incidences). Sample diameter* 150 *nm, height* 150 *nm.*

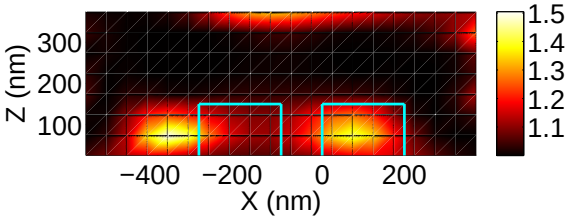

Figure 3.94 : *Longitudinal cut image at $y = 150$ nm of the reconstruction obtained with the PSI data set (8 incidences). Sample diameter* 150 *nm, height* 150 *nm.*

The reconstruction obtained with the off-axis data set and the 20 illumination angles is presented on Figs. 3.95 and 3.96, this time in a $750\times750\times200$ nm^3 investigation domain with 25 nm meshing. The result is as expected more noisy than in the PSI case, and the cylinders cannot be resolved any more.

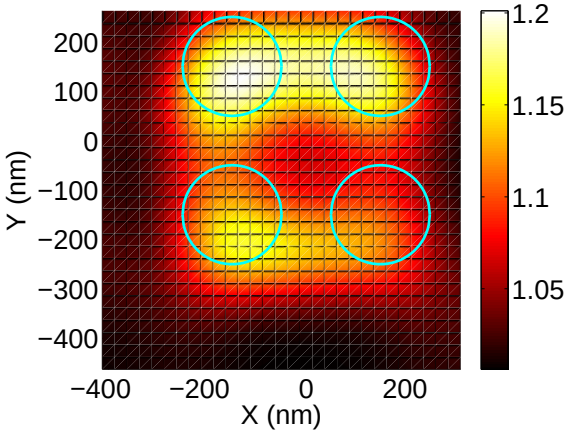

Figure 3.95 : *Transverse cut image at $z = 100$ nm of the reconstruction obtained with the off-axis data set (20 incidences). Sample diameter* 150 *nm, height* 150 *nm.*

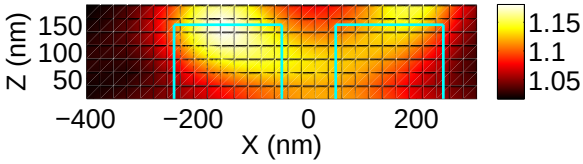

Figure 3.96 : *Longitudinal cut image at $y = 150$ nm of the reconstruction obtained with the off-axis data set (20 incidences). Sample diameter* 150 *nm, height* 150 *nm.*

In conclusion, the non-linear inversion procedure is able to reconstruct small 3D objects successfully until the Rayleigh limit with very few illumination angles compared to the classical linear inversion performed under the Born approximation. However, our approach is not straightforward to go beyond the Rayleigh criterion, and in the next chapter we will show that such a resolution improvement is possible by taking into account polarization effects.

Chapter 4

Polarization resolved measurements for tomographic diffractive microscopy

Contents

4.1 Introduction 85

4.2 Measurement of the vectorial scattered field with the experimental set-up 88

4.3 Amplitude and phase normalization 89

4.3.1 Correction on the measured field 89

4.3.2 Decomposition in TM and TE polarizations 89

4.4 Experimental results with polarization resolved measurements 90

4.4.1 Samples with diameter 200 nm 90

4.4.2 Samples with diameter 150 nm 93

4.5 Some final remarks on the reconstructions 96

4.1 Introduction

In the previous chapters, the TDM set-up has been used with a laser beam that was polarized vertically for both the illumination and the reference wave. To our knowledge, such a configuration where the polarization state is the same for both the illumination and the detection is the only one that has been used so far in tomographic diffractive microscopy. With our test objects, the far field diffraction pattern is made of various lobes separated by intensity minima. These minima carry useful information on the separation distance between the resin cylinders. When the object becomes smaller and smaller, the minima shift towards the edge of the numerical aperture and their number decreases inside of the objective NA, as can be seen when comparing Fig. 3.10 ($D = 1$ μm), Fig. 3.35 ($D = 500$ nm) and Fig. 3.73 ($D = 200$ nm). For a resolution beyond the Rayleigh criterion, a minimum can only be seen for large illumination angles close to the edge of the NA opposite to the specular reflection. The problem is that close to the edge of the NA (and

far from the specular) the scattered field is no longer parallel to the polarization of the incident field.

Hence, we have improved the set-up so that both polarizations of the illuminating beam and that of the detected field can be modified. The aim is to retrieve the full vectorial field scattered by the object, and not just a projection, for any polarization state of the illumination, and see if the resolution can be improved by this way.

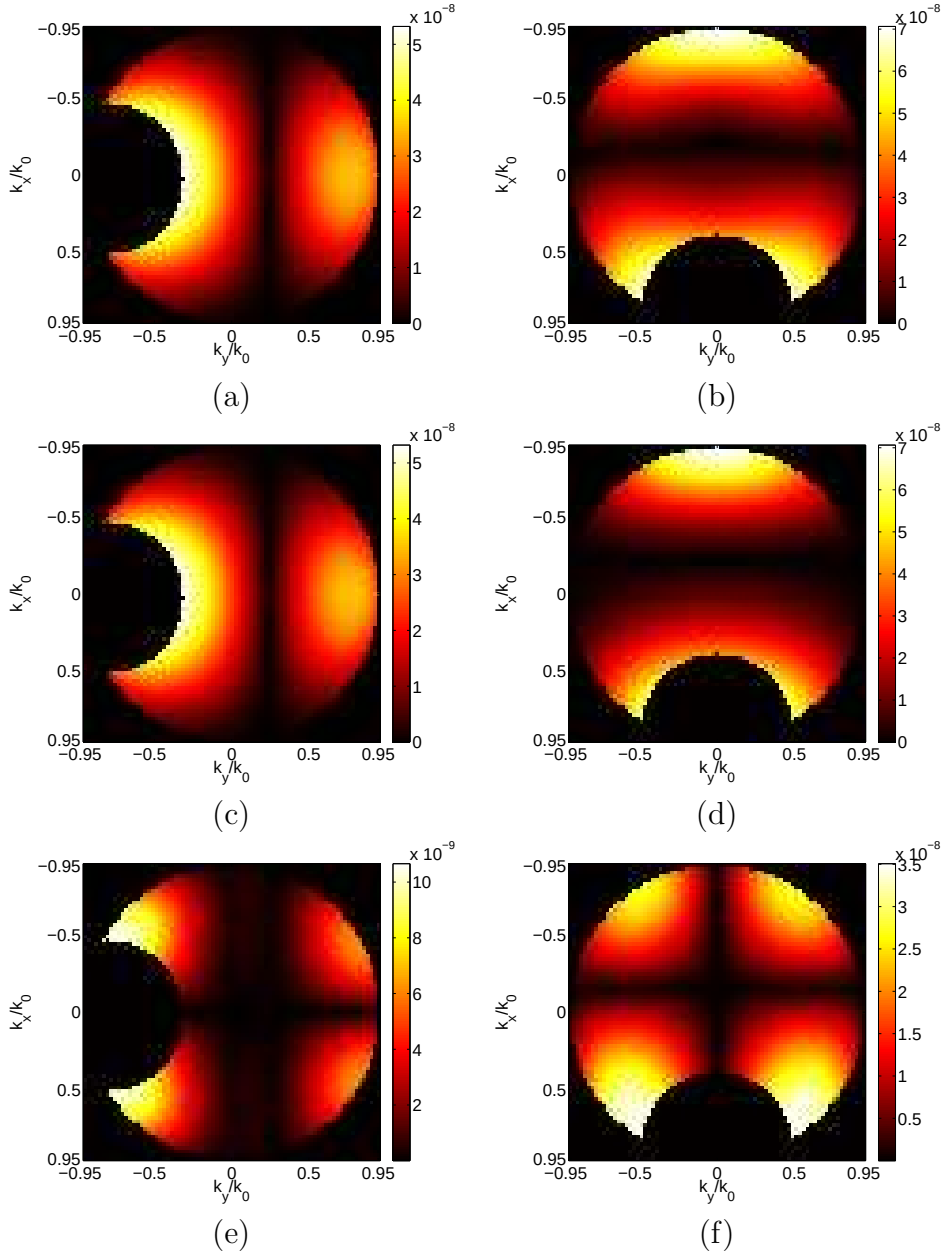

Figure 4.1 : *Modulus of the scattered field computed by the CDM, in Fourier domain. Samples diameter $D = 150$ nm, height $h = 150$ nm. (a), (c) and (e) $\theta_l = 55°$, $\phi_l = 0°$, TE polarization; (a) presents the computed full vectorial scattered field, (c) the scattered field in the incident electric field direction, (e) the scattered field in the orthogonal direction of incident electric field (crossed polarization). (b), (d) and (f) $\theta_l = 54°$, $\phi_l = 270°$, TM polarization; (b) is the computed full vectorial scattered field, (d) the scattered field in the incident electric field direction, (f) the scattered field in the orthogonal direction of incident electric field (crossed polarization).*

For the sake of clarity, a computation is done with different polarization conditions for both the illumination and the detection of the scattered field, for a sample with $D = 150$ nm and $h = 150$ nm. The results are presented in Fig. 4.1. One can notice that in TE polarization, the

crossed polarization gives a scattered field one order of magnitude lower than the scattered field in the incident electric field direction. Hence in that case it is not crucial to take into account the crossed polarization. This is no longer the case for the TM polarization, where the crossed polarization gives a scattered field with the same magnitude as the scattered field in the incident electric field direction.

4.2 Measurement of the vectorial scattered field with the experimental set-up

To retrieve the full vectorial field scattered by the object for any polarization state of the illumination, it is necessary to choose two bases to describe the polarization state of the illumination wave and that of the detected scattered field, respectively. Then, for each given illumination angle, four measurements are performed, that associate all the possible combinations between two independent polarization states in the illumination base and two independent polarization states in the detection base. As a result, it is possible by simple linear combinations of the measurements to obtain the vectorial scattered field for a any chosen polarization direction of the illumination.

To put in practice this approach, two half wave plates have been inserted in the set-up to modify at will the polarization state of both the illumination beam and the reference wave (see Fig. 4.2). A straightforward choice for the bases is the association of the vertical and horizontal directions $\widehat{\boldsymbol{v}}$ and $\widehat{\boldsymbol{h}}$, respectively, as shown for the case (a) on Fig. 4.2. In the previous chapters, all the measurements were done with both the illumination and detection polarization states along $\widehat{\boldsymbol{v}}$ (called $\widehat{\boldsymbol{v}}\widehat{\boldsymbol{v}}$ configuration, first letter indicating the direction for the illumination and second one that for detection). Retrieving the vectorial scattered field for any illumination polarization state requires to carry out the four measurements $\widehat{\boldsymbol{v}}\widehat{\boldsymbol{v}}$, $\widehat{\boldsymbol{h}}\widehat{\boldsymbol{h}}$, $\widehat{\boldsymbol{v}}\widehat{\boldsymbol{h}}$ and $\widehat{\boldsymbol{h}}\widehat{\boldsymbol{v}}$.

However, these four measurements have to be normalized both in phase and in amplitude as specified in chapter 3. Since this normalization is based on the detection of the specular reflection, the choice of the base $(\widehat{\boldsymbol{h}}, \widehat{\boldsymbol{v}})$ for the detection appears unsuitable since the specular reflection is killed for pure TE or TM illuminations in the measurements $\widehat{\boldsymbol{v}}\widehat{\boldsymbol{h}}$ and $\widehat{\boldsymbol{h}}\widehat{\boldsymbol{v}}$. As a result another detection base has been chosen with two orthogonal diagonal polarization states $\widehat{\boldsymbol{d_1}}$ and $\widehat{\boldsymbol{d_2}}$, as shown on Fig. 4.2, case (b). Four groups of scalar data for the scattered field are therefore measured on the CCD camera, we define them as: $E^{\widehat{\boldsymbol{v}}\widehat{\boldsymbol{d}}_1}_{\mathrm{s;exp}}$, $E^{\widehat{\boldsymbol{v}}\widehat{\boldsymbol{d}}_2}_{\mathrm{s;exp}}$, $E^{\widehat{\boldsymbol{h}}\widehat{\boldsymbol{d}}_1}_{\mathrm{s;exp}}$ and $E^{\widehat{\boldsymbol{h}}\widehat{\boldsymbol{d}}_2}_{\mathrm{s;exp}}$, where the subscript, for example, $\widehat{\boldsymbol{v}}\widehat{\boldsymbol{d}}_1$ means the incident electric field direction is vertical and the reference wave is polarized along the direction $\widehat{\boldsymbol{d}}_1$.

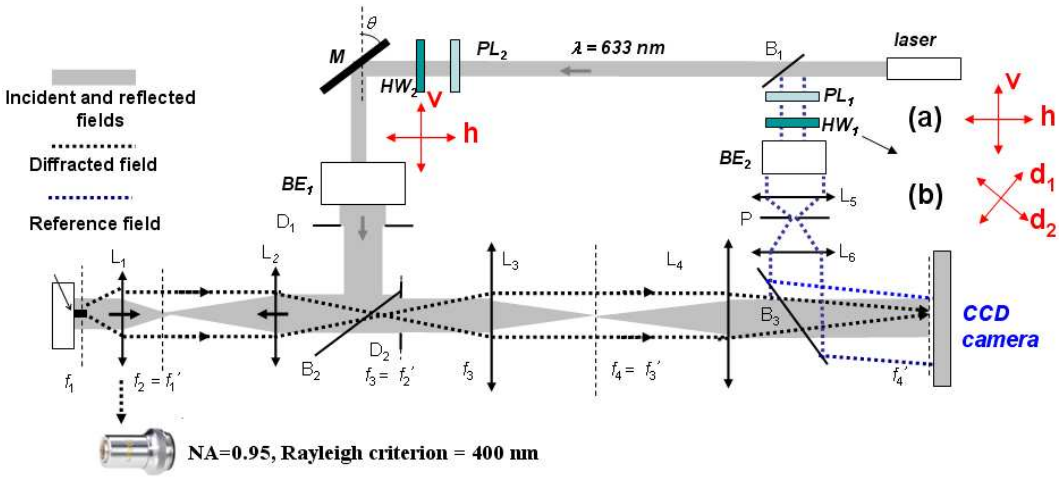

Figure 4.2 : *Sketch of the experimental setup, laser source emitting at 633 nm; M, adjustable mirror; PL, polarizer; HW, half-waveplate for changing the polarization. $L_{i=1,\cdots,6}$ lenses; f_i, f_i', object and image focal planes of lenses; B_1, B_2, B_3, beam splitters; BE_1, BE_2 beam expander; TM, pinhole; D_1, D_2, diaphragms. The red crosses correspond to the polarization bases, two cases are considered for the detection : $(\widehat{\boldsymbol{h}}, \widehat{\boldsymbol{v}})$ (a) and $(\widehat{\boldsymbol{d_1}}, \widehat{\boldsymbol{d_2}})$ (b)*

4.3 Amplitude and phase normalization

4.3.1 Correction on the measured field

As the electric polarization of the incident field, in this chapter, is always in TE or TM polarization the renormalization defined in chapter 3 still holds. Notice if one wants an illumination with a mixed of TE and TM polarizations for the electric incident field, the principle of the renormalization will be completely changed and more complex.

4.3.2 Decomposition in TM and TE polarizations

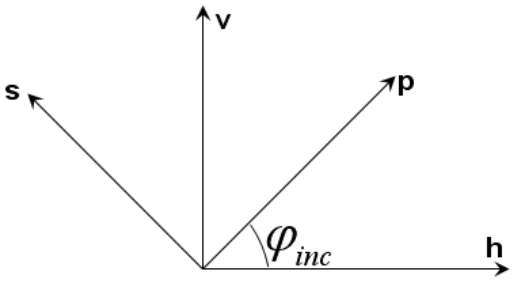

Figure 4.3 : *Orientation of the directions for TM (or p) and TE (or s) polarizations compared to the vertical and horizontal $(\widehat{\boldsymbol{v}}, \widehat{\boldsymbol{h}})$ directions.*

Once we get the scattered electric field by the incident field in the base $(\widehat{\boldsymbol{v}}, \widehat{\boldsymbol{h}})$, one can easily obtain the scattered field by the incident field in TM (or p) and TE (or s) polarisations. We decompose

the electric incident field as follows (see Fig. 4.3):

$$\begin{pmatrix} E^p_{\text{inc}} \\ E^s_{\text{inc}} \end{pmatrix} = \begin{pmatrix} \cos\varphi_{\text{inc}} & \sin\varphi_{\text{inc}} \\ -\sin\varphi_{\text{inc}} & \cos\varphi_{\text{inc}} \end{pmatrix} \begin{pmatrix} E^{\widehat{\boldsymbol{h}}}_{\text{inc}} \\ E^{\widehat{\boldsymbol{v}}}_{\text{inc}} \end{pmatrix} = \boldsymbol{A} \begin{pmatrix} E^{\widehat{\boldsymbol{h}}}_{\text{inc}} \\ E^{\widehat{\boldsymbol{v}}}_{\text{inc}} \end{pmatrix} \tag{4.1}$$

where E^p_{inc} and E^s_{inc} are the incident field in TM and TE polarization, respectively. The relationship Eq. (4.1), between the incident field in the bases $(\widehat{\boldsymbol{v}}, \widehat{\boldsymbol{h}})$ and (p, s), is the same for each component of the scattered field, hence the scattered field for an illumination in TM or TE polarization can be deduced by:

$$\begin{pmatrix} \boldsymbol{E}^{\text{cor};p}_{\text{d;exp}} \\ \boldsymbol{E}^{\text{cor};s}_{\text{d;exp}} \end{pmatrix} = \boldsymbol{A} \begin{pmatrix} \boldsymbol{E}^{\text{cor};\widehat{\boldsymbol{h}}}_{\text{d;exp}} \\ \boldsymbol{E}^{\text{cor};\widehat{\boldsymbol{v}}}_{\text{d;exp}} \end{pmatrix}. \tag{4.2}$$

Up to now, for any illumination angle and for two measurements with the incident polarization in the $(\widehat{\boldsymbol{h}}, \widehat{\boldsymbol{v}})$ base, we can separate the measured scattered field into two parts, corresponding to the incident field in TM polarization and TE polarization, respectively. And the measured scattered field can be normalized before the separation in TM and TE polarizations, for matching with the amplitude and the phase of the theoretical scattered field.

4.4 Experimental results with polarization resolved measurements

In chapter 3 we have presented experimental reconstructions for our resin test objects with different diameters $D = 1$ μm, 500 nm, 200 nm and 150 nm. We have seen that without taking into account polarization effects, which means with only $\widehat{\boldsymbol{v}}\widehat{\boldsymbol{v}}$ configuration measurements, the data set is sufficient to retrieve successfully the objects with $D = 1$ μm and 500 nm. However, when the resolution requirement reaches the Rayleigh criterion, which corresponds to the samples with diameter 200 nm, the useful signal gets closer to the edges of the NA in the Fourier space, where polarization changes can occur. In this section we present new reconstructions for the objects with D =200 nm and 150 nm using different polarization configurations for the measurements :

- $\widehat{\boldsymbol{h}}\widehat{\boldsymbol{h}}$
- combining $\widehat{\boldsymbol{v}}\widehat{\boldsymbol{v}}$ and $\widehat{\boldsymbol{h}}\widehat{\boldsymbol{h}}$
- combining $\widehat{\boldsymbol{v}}\widehat{\boldsymbol{d_1}}$, $\widehat{\boldsymbol{h}}\widehat{\boldsymbol{d_1}}$, $\widehat{\boldsymbol{v}}\widehat{\boldsymbol{d_2}}$ and $\widehat{\boldsymbol{h}}\widehat{\boldsymbol{d_2}}$ to retrieve the full vectorial field for both TE and TM illuminations
- combining $\widehat{\boldsymbol{v}}\widehat{\boldsymbol{d_1}}$, $\widehat{\boldsymbol{h}}\widehat{\boldsymbol{d_1}}$, $\widehat{\boldsymbol{v}}\widehat{\boldsymbol{d_2}}$ and $\widehat{\boldsymbol{h}}\widehat{\boldsymbol{d_2}}$ to retrieve the full vectorial field for TM illuminations only
- combining $\widehat{\boldsymbol{v}}\widehat{\boldsymbol{d_1}}$, $\widehat{\boldsymbol{h}}\widehat{\boldsymbol{d_1}}$, $\widehat{\boldsymbol{v}}\widehat{\boldsymbol{d_2}}$ and $\widehat{\boldsymbol{h}}\widehat{\boldsymbol{d_2}}$ to retrieve the full vectorial field for TE illuminations only.

The same 20 illuminations as in chapter 3 have been used and the set-up has been run in its off-axis holography configuration. For the sake of clarity, only the final reconstructions are presented in this chapter, and the scattered fields in the Fourier space are shown in Appendix C for $\widehat{\boldsymbol{h}}\widehat{\boldsymbol{h}}$ polarization and in Appendix D for $\widehat{\boldsymbol{v}}\widehat{\boldsymbol{d_1}}$, $\widehat{\boldsymbol{h}}\widehat{\boldsymbol{d_1}}$, $\widehat{\boldsymbol{v}}\widehat{\boldsymbol{d_2}}$ and $\widehat{\boldsymbol{h}}\widehat{\boldsymbol{d_2}}$ polarization.

4.4.1 Samples with diameter 200 nm

The non linear inversion procedure has been firstly applied to the $\widehat{\boldsymbol{h}}\widehat{\boldsymbol{h}}$ measurement using an investigation domain of 1 μm×1 μm×400 nm and a mesh size of 50 nm. The corresponding reconstructions are shown on Figs. 4.4 and 4.5. The case of the combination of the $\widehat{\boldsymbol{h}}\widehat{\boldsymbol{h}}$ and $\widehat{\boldsymbol{v}}\widehat{\boldsymbol{v}}$ measurements is displayed on Figures 4.6 and 4.7. Compared to the results with the $\widehat{\boldsymbol{v}}\widehat{\boldsymbol{v}}$

measurement presented in chapter 3 the $\widehat{\boldsymbol{h}}\widehat{\boldsymbol{h}}$ reconstruction is very similar, and few improvement can be seen by combining both polarization cases.

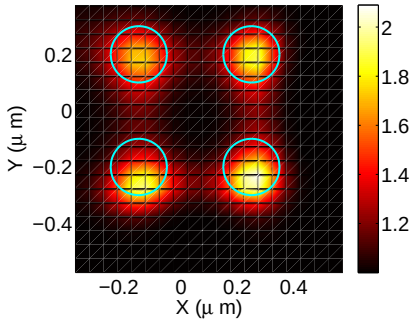

Figure 4.4 : *Transverse cut image at $z = 100$ nm of the reconstruction obtained with the off-axis data set (20 incidences), polarizers in $\widehat{\boldsymbol{h}}\widehat{\boldsymbol{h}}$ mode. Sample diameter $D = 200$ nm, height $h = 150$ nm.*

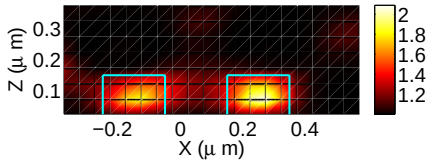

Figure 4.5 : *Longitudinal cut image at $y = 200$ nm of the reconstruction obtained with the off-axis data set (20 incidences), polarizers in $\widehat{\boldsymbol{h}}\widehat{\boldsymbol{h}}$ mode. Sample diameter $D = 200$ nm, height $h = 150$ nm.*

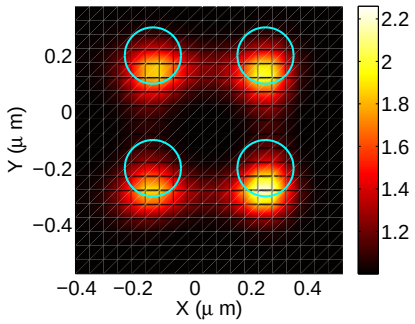

Figure 4.6 : *Transverse cut image at $z = 100$ nm of the reconstruction obtained with the off-axis data set (20 incidences), polarizers in $\widehat{\boldsymbol{v}}\widehat{\boldsymbol{v}}+\widehat{\boldsymbol{h}}\widehat{\boldsymbol{h}}$ mode. Sample diameter $D = 200$ nm, height $h = 150$ nm.*

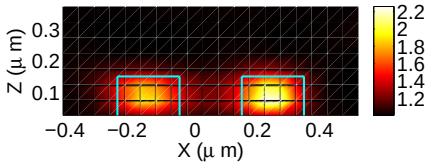

Figure 4.7 : *Longitudinal cut image at $y = 200$ nm of the reconstruction obtained with the off-axis data set (20 incidences), polarizers in $\widehat{\boldsymbol{v}}\widehat{\boldsymbol{v}}+\widehat{\boldsymbol{h}}\widehat{\boldsymbol{h}}$ mode. Sample diameter $D = 200$ nm, height $h = 150$ nm.*

The combination of the four measurements with the bases $(\widehat{\boldsymbol{v}}, \widehat{\boldsymbol{h}})$ and $(\widehat{\boldsymbol{d_1}}, \widehat{\boldsymbol{d_2}})$ is then tested to use the vectorial field as input data in the inversion. The corresponding reconstructions are shown on Figs. 4.8 and 4.9 when all the illuminations are kept, on Figs. 4.10 and 4.11 with only the TM illuminations, and on Figs. 4.12 and 4.13 with only the TE illuminations.

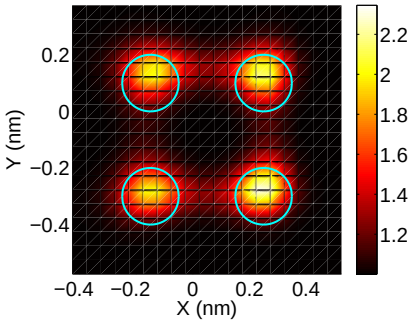

Figure 4.8 : *Transverse cut image at $z = 100$ nm, obtained by considering full polarization. Sample with diameter $D = 200$ nm and height $h = 150$ nm.*

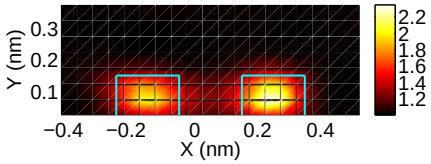

Figure 4.9 : *Longitudinal cut image at $y = 200$ nm, obtained by considering full polarization. Sample with diameter $D = 200$ nm and height $h = 150$ nm.*

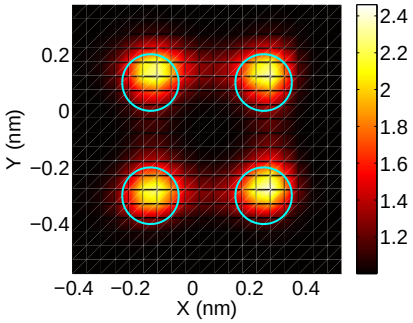

Figure 4.10 : *Transverse cut image at $z = 100$ nm, obtained by using scattered field obtained from only TM-polarization incidence. Sample with diameter $D = 200$ nm and height $h = 150$ nm.*

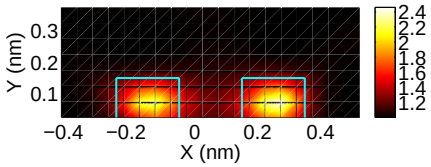

Figure 4.11 : *Longitudinal cut image at $y = 200$ nm, obtained by using scattered field obtained from only TM incidence. Sample with diameter $D = 200$ nm and height $h = 150$ nm.*

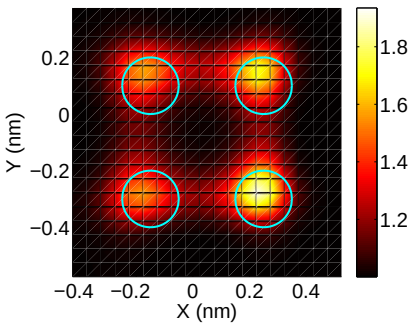

Figure 4.12 : *Same as Fig. 4.10 for TE polarization.*

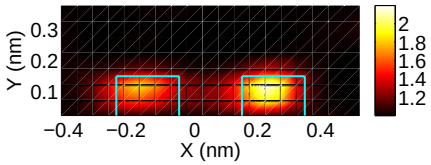

Figure 4.13 : *Same as Fig. 4.11 for TE polarization.*

The improvement is globally small using the vectorial field as input data, except that the four resin cylinders are reconstructed in a more homogeneous way. However, the reconstruction is degraded when only the TE illuminations are conserved.

4.4.2 Samples with diameter 150 nm

We therefore continue to work with smaller objects, samples with diameter 150 nm. Here the center to center distance of 300 nm is smaller than the Rayleigh limit of 400 nm. In chapter 3, the inversions with $\widehat{\boldsymbol{v}}\widehat{\boldsymbol{v}}$ data sets were unable to reconstruct correctly the four cylinders in this case. We first test here a data set in $\widehat{\boldsymbol{h}}\widehat{\boldsymbol{h}}$ configuration, the reconstructions are shown on Figs. 4.14 and 4.15 with an investigation domain 1 μm×1 μm ×400 nm and mesh size 50 nm. As for the off-axis data set in $\widehat{\boldsymbol{v}}\widehat{\boldsymbol{v}}$ configuration on the same sample, at the end of chapter 3 (Figs. 3.95 and 3.96), the four cylinders cannot be resolved. One can however notice here a vertical separation between the left and right cylinders on the transverse cut, whereas the separation was horizontal between the top and bottom cylinders in chapter 3. As will be confirmed hereafter, TM polarized illuminations seem therefore to have a better resolution power than TE polarized ones.

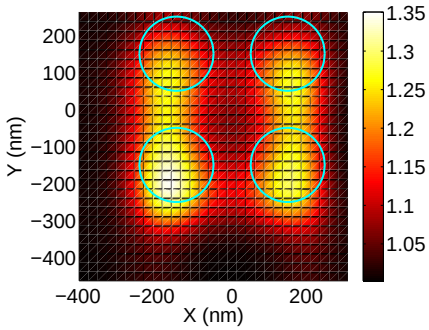

Figure 4.14 : *Transverse cut image at $z = 100$ nm of the reconstruction obtained with the off-axis data set (20 incidences), polarizers in $\widehat{\boldsymbol{h}}\widehat{\boldsymbol{h}}$ mode. Sample diameter $D = 150$ nm, height $h = 150$ nm.*

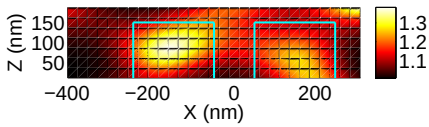

Figure 4.15 : *Longitudinal cut image at $y = 150$ nm of the reconstruction obtained with the off-axis data set (20 incidences), polarizers in $\widehat{\boldsymbol{h}}\widehat{\boldsymbol{h}}$ mode. Sample diameter $D = 150$ nm, height $h = 150$ nm.*

When combining $\widehat{\boldsymbol{v}}\widehat{\boldsymbol{v}}$ and $\widehat{\boldsymbol{h}}\widehat{\boldsymbol{h}}$ measurements the four cylinders are this time all resolved, as can be seen on Figs. 4.16 and 4.17.

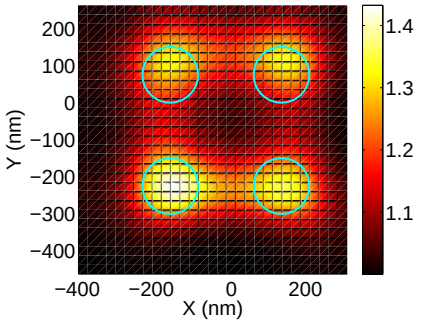

Figure 4.16 : *Transverse cut image at $z = 100$ nm of the reconstruction obtained with the off-axis data set (20 incidences), polarizers in $\widehat{\boldsymbol{v}}\widehat{\boldsymbol{v}}+\widehat{\boldsymbol{h}}\widehat{\boldsymbol{h}}$ mode. Sample diameter $D = 150$ nm, height $h = 150$ nm.*

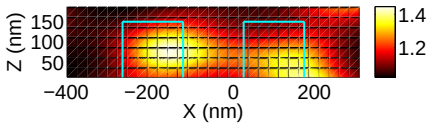

Figure 4.17 : *Longitudinal cut image at $y = 150$ nm of the reconstruction obtained with the off-axis data set (20 incidences), polarizers in $\widehat{\boldsymbol{v}}\widehat{\boldsymbol{v}}+\widehat{\boldsymbol{h}}\widehat{\boldsymbol{h}}$ mode. Sample diameter $D = 150$ nm, height $h = 150$ nm.*

We at last consider the bases $(\widehat{\boldsymbol{v}}, \widehat{\boldsymbol{h}})$ and $(\widehat{\boldsymbol{d_1}}, \widehat{\boldsymbol{d_2}})$ to use the vectorial field as input data in the inversion. The corresponding reconstructions are shown on Figs. 4.18 and 4.19 when all the illuminations are kept, on Figs. 4.20 and 4.21 with only the TM illuminations, and on Figs. 4.22 and 4.23 with only the TE illuminations.

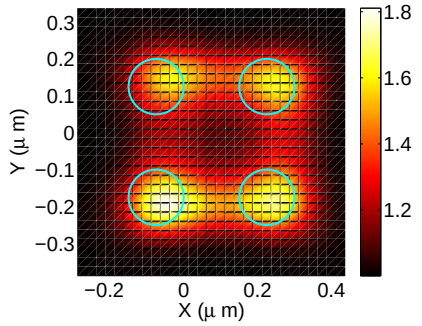

Figure 4.18 : *Transverse cut image at $z = 100$ nm, obtained by using total scattered field. Sample with diameter $D = 150$ nm and height $h = 150$ nm.*

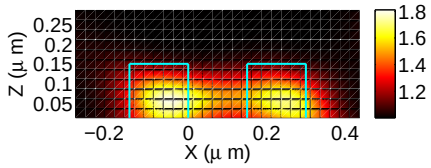

Figure 4.19 : *Longitudinal cut image at $y = 150$ nm, obtained by using total scattered field. Sample with diameter $D = 150$ nm and height $h = 150$ nm.*

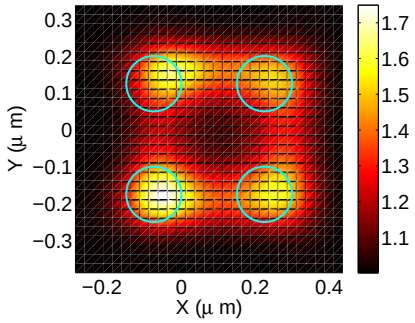

Figure 4.20 : *Transverse cut image at $z = 100$ nm, obtained by using scattered field obtained from only TM polarization incidence. Sample with diameter $D = 150$ nm and height $h = 150$ nm.*

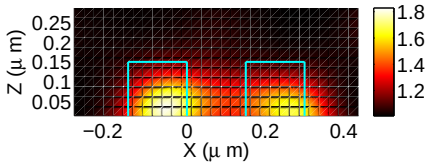

Figure 4.21 : *Longitudinal cut image at $y = 150$ nm, obtained by using scattered field obtained from only TM polarization incidence. Sample with diameter $D = 150$ nm and height $h = 150$ nm.*

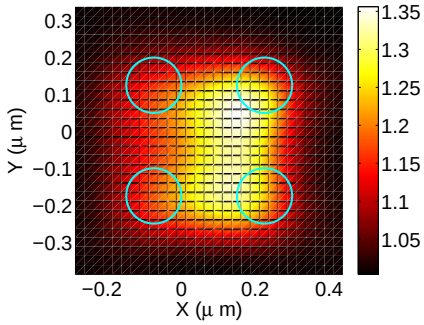

Figure 4.22 : *Same as in Fig. 4.20 with TE polarization.*

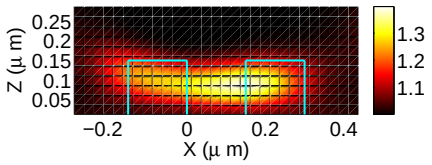

Figure 4.23 : *Same as in Fig. 4.21 with TE polarization.*

The vectorial field permits to improve further the retrieved geometry of the cylinders, and also to give a better estimation of their permittivity. Keeping only the TM illuminations does not change much the reconstructions, whereas keeping only the TE ones dramatically deteriorates the result.

To assess in a more quantitative manner the quality of the reconstructions obtained with the full vectorial case compared to the other cases, we define the error function :

$$\mathrm{Err}_\chi = \frac{\sum_\Omega \|\chi_{\mathrm{actual}} - \chi_{\mathrm{rec}}\|^2}{\sum_\Omega \|\chi_{\mathrm{actual}}\|^2}, \tag{4.3}$$

where χ_{actual} and χ_{rec} are the actual and the reconstructed permittivity contrasts, respectively, and the sum is done over all the subunits of the investigation domain. We get for the sample with $D = 150$ nm:

- $\mathrm{Err}_\chi = 76\%$ for $\widehat{\boldsymbol{h}}\widehat{\boldsymbol{h}}$ mode.
- $\mathrm{Err}_\chi = 63\%$ for $\widehat{\boldsymbol{h}}\widehat{\boldsymbol{h}}+\widehat{\boldsymbol{v}}\widehat{\boldsymbol{v}}$ mode.
- $\mathrm{Err}_\chi = 56\%$ for full vectorial configuration.
- $\mathrm{Err}_\chi = 59\%$ for TM illuminations only.

- $\mathrm{Err}_\chi = 78\%$ for TE illuminations only.

We can formally conclude that the reconstruction with full polarization gives the best map of relative permittivity.

4.5 Some final remarks on the reconstructions

1. If the separation between the cylinders is larger or equal to the Rayleigh criterion one can work with the $\widehat{\boldsymbol{vv}}+\widehat{\boldsymbol{hh}}$ mode without any loss compared to the full vectorial case.
2. The illuminations with TM polarization for the incident field always give reconstructions clearly better than illuminations with TE polarization (it is particular true for the sample with $D = 150$ nm where Err_χ gives the higher value). One way to explain this behaviour is that the intensity of the field above the substrate for large angles of incidence (the angles that give the resolution) is larger in TM polarization than in TE polarization. Hence, the signal to noise ratio decreases for TE polarization.
3. If the separation between the cylinders is smaller than the Rayleigh criterion, then the use of the full vectorial configuration increases the resolution and the quantitative value of the retrieved relative permittivity. This is particularly true for the TM polarization where the crossed polarization is not negligible, as seen in Fig. 4.1, and then clearly brings additional information.
4. We have studied objects with a separation below the Rayleigh criterion but still above the resolution limit given by the synthetic aperture in TDM.

General conclusion and perspectives

The work presented in this thesis aims at exploring new modalities for tomographic diffractive microscopy (TDM) and the 3D quantitative reconstruction of scattering objects, both at the experimental set-up level and for the numerical inversion procedure applied to the data. This work has firstly used different techniques to perform the phase measurement : classical ones like phase shifting interferometry and off-axis holography, but also wavefront sensing by quadri-wave lateral shearing interferometry. This is the first time that a wavefront sensor is used for TDM, as until now the number of pixels available on wavefront sensors was usually too low, an issue that is considerably relaxed thanks to quadri-wave lateral shearing interferometry. As a result the TDM set-up can be considerably simplified by suppressing the need for a reference wave, which also greatly improves its robustness regarding the sensitivity to external perturbations. Moreover, the use of low cost light sources with lower temporal coherence such as laser diodes or spatially filtered LEDs becomes possible, what diminishes the speckle noise stemming from the parasitic reflections and scattering along the light path. This improvement can therefore make TDM compatible with standard set-ups like the ones used for classical wide-field microscopy.

Another main specificity of the present work is the coupling of the TDM set-up to a non-linear inversion algorithm to retrieve the 3D permittivity map of the probed objects from the measurement of their scattered fields. The usual approach makes use of inversion procedures based on a 3D Fourier transform, which is valid only when the link between the scattered field and the permittivity contrast is linear. This restricts the application of TDM mainly to samples with low permittivity contrasts. Additionally, such an approach imposes that the object is coherently illuminated by a single plane wave. Here, the inversion algorithm performs a rigorous modelling of the wave sample interaction based on the Coupled Dipole Method, and relies on an iterative minimization of a cost function describing the discrepancy between the measurements and the field scattered by the estimated object. This approach is validated for resin objects deposited on a silicon reflective substrate, where the permittivity contrast is far higher than those usually encountered with linear approximations, and where the illumination is given by the interference between an incident plane wave and its specular reflection on the substrate. It also has the great advantage to be less sensitive to missing data for certain illumination and scattering angles, contrarily to the Fourier transform based technique. As a result, it has been carried out with a number of angles that is at least 10 times smaller for both the illuminations and the scattering directions. The speed of the data acquisition can therefore be greatly increased, and the necessity for a high number of pixels on the detector is considerably relaxed. The superiority of our non-linear inversion algorithm in these conditions has been clearly shown to retrieve both the geometry and the permittivity of the scattering objects.

Lastly, the set-up and the inversion algorithm have been improved to perform polarization resolved reconstructions. TDM usually relies on measurements where both the illumination and the reference wave are polarized linearly in the same direction. It means that when the object is illuminated at normal incidence, the incident electric field and the reference electric field are parallel. However, for other illumination angles the two fields cannot be considered as parallel, and in this case there are some scattering angles for which the electric field is not parallel to that of the reference wave, even if the object does not induce any depolarization effect. As a result only a projection of the total scattered field is measured. To take into account this effect, the measurements have been done with two polarization states for the illumination combined with two polarization states for the detection. This permits to retrieve the vectorial scattered field for any polarization state of the illumination by a simple linear combination of these measurements. We have shown on our test objects that such an approach ameliorates the resolution beyond the Rayleigh criterion and improves the quantitative estimation of the permittivity.

This work opens the way to 3D high resolution quantitative reconstructions of permittivity maps by TDM. The transverse resolution can still be improved to reach the limit predicted by a synthetic aperture analysis and even go beyond thanks to the insertion of additional *a priori* knowledge in the algorithm. The axial resolution, which is usually the weak point of microscopy set-ups, can compete with the transverse one if the object is placed in the vicinity of a perfect mirror [37], and such a configuration has been shown to be compatible with the inversion algorithm with these first results on resin objects deposited on a reflective substrate. New samples are being prepared to test more specifically the axial resolution in a near future. More advanced illumination schemes will also be studied, such as structured illumination patterns combining several plane waves to further diminish the required number of illuminations, or random speckle patterns to dramatically simplify the set-up illumination path [120]. Besides, more complex sample configurations will be considered : samples with different permittivity domains, and samples giving rise to a strong multiple scattering regime (for instance through plasmonic resonance), where a strong resolution enhancement can occur [80].

Appendix A

The dyadic Green's functions

Contents

A.1 Wave equation 99

A.2 The scalar Green's function 100

A.3 The dyadic Green's function 100

A.1 Wave equation

An important concept in field theory are Green's functions: the fields due to a point source. In electromagnetic theory, the dyadic Green's function $\boldsymbol{G}$ is is essentially defined by the electric field $\boldsymbol{E}$ at the field point $\boldsymbol{r}$ generated by a radiating electric dipole $\boldsymbol{p}$ located at the source point $\boldsymbol{r}'$.

The derivation of the Green's function for the electric field is most conveniently accomplished by considering the time-harmonic vector potential $\boldsymbol{A}$ and the scalar potential ϕ in an infinite and homogeneous space which is characterized by the constant ε_0 and μ_0. In this case, $\boldsymbol{A}$ and ϕ are defined by the relationships,

$$\boldsymbol{E}(\boldsymbol{r}) = i\omega\boldsymbol{A}(\boldsymbol{r}) - \boldsymbol{\nabla}\phi(\boldsymbol{r}) \tag{A.1}$$

$$\boldsymbol{H}(\boldsymbol{r}) = \frac{1}{\mu_0}\boldsymbol{\nabla}\times\boldsymbol{A}(\boldsymbol{r}). \tag{A.2}$$

We can insert these equations into Maxwell's second equation Eqs. (1.9) and (1.10), then obtain

$$\boldsymbol{\nabla}\times\boldsymbol{\nabla}\times\boldsymbol{A}(\boldsymbol{r}) = \mu_0\boldsymbol{J}(\boldsymbol{r}) - i\omega\varepsilon_0\mu_0[i\omega\boldsymbol{A}(\boldsymbol{r}) - \boldsymbol{\nabla}\phi(\boldsymbol{r})], \tag{A.3}$$

where we used $\boldsymbol{D}(\boldsymbol{r}) = \varepsilon_0\boldsymbol{E}(\boldsymbol{r})$. The potentials $\boldsymbol{A}$ and ϕ is not only uniquely defined by Eqs. (A.1) and (A.2), we are still free to define the value of $\boldsymbol{\nabla}\cdot\boldsymbol{A}$ which we choose as,

$$\boldsymbol{\nabla}\cdot\boldsymbol{A}(\boldsymbol{r}) = i\omega\varepsilon_0\mu_0\phi(\boldsymbol{r}). \tag{A.4}$$

A condition which fixes the redundancy of Eqs (A.1) and (A.2) is called a gauge condition. The gauge chosen through Eq. (A.4) is the so-called Lorentz gauge. Using the mathematical identity $\boldsymbol{\nabla}\times\boldsymbol{\nabla}\times\boldsymbol{A} = -\boldsymbol{\nabla}^2\boldsymbol{A} + \boldsymbol{\nabla}(\boldsymbol{\nabla}\cdot\boldsymbol{A})$ together with the Lorentz gauge we can rewrite Eq. (A.3) as

$$[\boldsymbol{\nabla}^2 + k_0^2]\boldsymbol{A}(\boldsymbol{r}) = -\mu_0\boldsymbol{J}(\boldsymbol{r}), \tag{A.5}$$

which is the inhomogeneous Helmholtz equation. It holds independently for each component A_i for $\boldsymbol{A}$. A similar equation can be derived for the scalar potential ϕ

$$[\boldsymbol{\nabla}^2 + k_0^2]\phi(\boldsymbol{r}) = \frac{-\rho(\boldsymbol{r})}{\varepsilon_0}, \tag{A.6}$$

thus, we could obtain four scalar Helmholtz equations of the form

$$[\boldsymbol{\nabla}^2 + k_0^2] f(\boldsymbol{r}) = -g(\boldsymbol{r}). \tag{A.7}$$

A.2 The scalar Green's function

To derive the *scalar* Green's function $G_0(\boldsymbol{r}, \boldsymbol{r}')$, for the Helmholtz operator we replace the source term $g(\boldsymbol{r})$ by a single point source $\delta(\boldsymbol{r} - \boldsymbol{r}')$ and obtain

$$[\boldsymbol{\nabla}^2 + k_0^2] G_0(\boldsymbol{r}, \boldsymbol{r}') = -\delta(\boldsymbol{r} - \boldsymbol{r}'). \tag{A.8}$$

The coordinate $\boldsymbol{r}$ denotes the location of the field point, for example, the point in which the fields are to be evaluated, whereas the coordinate $\boldsymbol{r}'$ designates the location of the point source. In free space without boundaries, the scalar Green function depends only of $\boldsymbol{r} - \boldsymbol{r}'$ due to a spherical symmetry must be a function only of $\boldsymbol{r} - \boldsymbol{r}'$ and must possess spherical symmetry about the source point. Thus in spherical coordinates, we can write Eq. (A.8) as:

$$\frac{1}{R}\frac{d^2}{dR^2}[RG_0(\boldsymbol{R})] + k_0^2 G_0(\boldsymbol{R}) = -\delta(\boldsymbol{R}), \tag{A.9}$$

with $\boldsymbol{R} = \boldsymbol{r} - \boldsymbol{r}'$ and $R = |\boldsymbol{R}|$. The homogeneous equation can be written as

$$\frac{d^2}{dR^2}[RG_0(\boldsymbol{R})] + k_0^2 RG_0(\boldsymbol{R}) = 0, \tag{A.10}$$

with the following solution

$$RG_0(\boldsymbol{R}) = Ae^{ik_0R} + Be^{-ik_0R} \tag{A.11}$$

$$G_0(\boldsymbol{R}) = \frac{1}{R}\left(Ae^{ik_0R} + Be^{-ik_0R}\right), \tag{A.12}$$

where A and B are constants. Near the origin, we can use the static approximation $k_0 \approx 0$ and Eqs. (A.8) and (A.12) become:

$$\nabla^2 G_0(\boldsymbol{R}) = \frac{1}{R}\frac{d^2}{dR^2}[RG_0(\boldsymbol{R})] = -\delta(\boldsymbol{R}) \tag{A.13}$$

$$G_0(\boldsymbol{R}) = \frac{1}{R}(A + B). \tag{A.14}$$

Equation (A.13) is the well known static case and has the solution $\frac{1}{4\pi R}$. This provides that $A + B = 1/(4\pi)$. The solution with the plus sign denotes a spherical wave that propagates out of the origin whereas the solution with the minus sign is a wave that converges towards the origin. In the following we only retain the outwards propagating wave. Then the scalar Green function can be written as :

$$G_0(\boldsymbol{R}) = \frac{e^{ik_0R}}{4\pi R}. \tag{A.15}$$

A.3 The dyadic Green's function

So far we reduced the treatment of Green's functions to the potentials $\boldsymbol{A}$ and ϕ because it allows us to work with scalar equations. The formalism becomes more involved when we consider the electric and magnetic fields. The reason for this is that a source current in x-direction leads to an electric and magnetic fields with x, y, and z-components. This is different for the vector potential: a source current in x gives only rise to a vector potential with a x component. Thus, in the case of the electric and magnetic fields we need a Green's function which relates all components of the

source with all components of the fields, or, in other words, the Green's function must be a tensor. This type of Green's function is denoted as *dyadic Green's function.* To determine the dyadic Green's function we start with Eq. (1.17) established in Chap. 1

$$\boldsymbol{\nabla}\times\boldsymbol{\nabla}\times\boldsymbol{G}(\boldsymbol{r},\boldsymbol{r}')-k_0^2\boldsymbol{G}(\boldsymbol{r},\boldsymbol{r}')=\boldsymbol{I}\delta(\boldsymbol{r}-\boldsymbol{r}'), \tag{A.16}$$

$\boldsymbol{I}$ being the unit dyad (unit tensor). The first column of the tensor $\boldsymbol{G}$ corresponds to the field due to a point source in x-direction, the second column to the field due to a point source in y-direction, and the third column is the field due to a point source in z-direction. Thus a dyadic Green's function is just a compact notation for three vectorial Green's functions. Using that $\boldsymbol{\nabla}.(\boldsymbol{\nabla}\times)=0$ the divergence of Eq. (A.16) gives :

$$-k_0^2\boldsymbol{\nabla}\boldsymbol{G}(\boldsymbol{r},\boldsymbol{r}')=\boldsymbol{\nabla}\boldsymbol{I}\delta(\boldsymbol{r}-\boldsymbol{r}'). \tag{A.17}$$

then using $\boldsymbol{\nabla}\times\boldsymbol{\nabla}\times\boldsymbol{G}=-\boldsymbol{\nabla}^2\boldsymbol{G}+\boldsymbol{\nabla}(\boldsymbol{\nabla}\boldsymbol{G})$ Eqs. (A.16) and (A.17) we get:

$$-\boldsymbol{\nabla}^2\boldsymbol{G}+\boldsymbol{\nabla}(\boldsymbol{\nabla}\boldsymbol{G})-k_0^2\boldsymbol{G}(\boldsymbol{r},\boldsymbol{r}')=\boldsymbol{I}\delta(\boldsymbol{r}-\boldsymbol{r}') \tag{A.18}$$

$$(\boldsymbol{\nabla}^2+k_0^2)\boldsymbol{G}(\boldsymbol{r},\boldsymbol{r}')=-\left(\boldsymbol{\nabla}\boldsymbol{\nabla}+\frac{1}{k_0^2}\right)\boldsymbol{I}\delta(\boldsymbol{r}-\boldsymbol{r}'), \tag{A.19}$$

using Eq. (A.8) we replace the δ function in Eq. (A.19) and write

$$(\boldsymbol{\nabla}^2+k_0^2)\boldsymbol{G}(\boldsymbol{r},\boldsymbol{r}')=\left(\boldsymbol{\nabla}\boldsymbol{\nabla}+\frac{1}{k_0^2}\right)\boldsymbol{I}[\boldsymbol{\nabla}^2+k_0^2]G_0(\boldsymbol{r},\boldsymbol{r}') \tag{A.20}$$

$$(\boldsymbol{\nabla}^2+k_0^2)\left[\boldsymbol{G}(\boldsymbol{r},\boldsymbol{r}')-\left(\boldsymbol{\nabla}\boldsymbol{\nabla}+\frac{1}{k_0^2}\right)\boldsymbol{I}G_0(\boldsymbol{r},\boldsymbol{r}')\right]=0, \tag{A.21}$$

hence a possible expression for the dyadic Green function is

$$\boldsymbol{G}(\boldsymbol{r},\boldsymbol{r}')=\left[\boldsymbol{I}+\frac{1}{k_0^2}\boldsymbol{\nabla}\boldsymbol{\nabla}\right]G_0(\boldsymbol{r},\boldsymbol{r}') \tag{A.22}$$

at last, the expansion formula of $\boldsymbol{G}(\boldsymbol{r},\boldsymbol{r}')$ could be obtained by derivation follows, we rewrite the component $\boldsymbol{\nabla}\boldsymbol{\nabla}$,

$$\boldsymbol{\nabla}\boldsymbol{\nabla}=\begin{vmatrix}\frac{\partial}{\partial x}\frac{\partial}{\partial x} & \frac{\partial}{\partial x}\frac{\partial}{\partial y} & \frac{\partial}{\partial x}\frac{\partial}{\partial z}\\ \frac{\partial}{\partial y}\frac{\partial}{\partial x} & \frac{\partial}{\partial y}\frac{\partial}{\partial y} & \frac{\partial}{\partial y}\frac{\partial}{\partial z}\\ \frac{\partial}{\partial z}\frac{\partial}{\partial x} & \frac{\partial}{\partial z}\frac{\partial}{\partial y} & \frac{\partial}{\partial z}\frac{\partial}{\partial z}\end{vmatrix}. \tag{A.23}$$

for the sake of computation simplicity, we replace x,y,z components two variables α,β, where $\alpha=x-x',y-y',z-z'$, $\beta=x-x',y-y',z-z'$, $R=\sqrt{(x-x')^2+(y-y')^2+(z-z')^2}$, we obtain,

$$\frac{\partial R}{\partial\alpha}=\frac{\alpha}{R} \tag{A.24}$$

$$\frac{\partial(\frac{\alpha}{R})}{\partial\beta}=-\frac{\alpha\beta}{R^3}+\frac{\delta_{\alpha\beta}}{R}, \tag{A.25}$$

substituting Eqs. (A.24) and (A.25) into Eq. (A.22), we yield a final resolution,

$$\boldsymbol{G}(\boldsymbol{r},\boldsymbol{r}')=\frac{e^{ik_0R}}{4\pi k_0^2}\left[(3\widehat{\boldsymbol{R}}\otimes\widehat{\boldsymbol{R}}-\boldsymbol{I})\left(\frac{1}{R^3}-\frac{ik_0}{R^2}\right)+(\boldsymbol{I}-\widehat{\boldsymbol{R}}\otimes\widehat{\boldsymbol{R}})\frac{k_0^2}{R}\right], \tag{A.26}$$

where $\widehat{\boldsymbol{R}}=\boldsymbol{R}/R$.

Appendix B

The approximation of scalar Green's function in far field

Let Q be a typical point in the scattering volume V and P a point far away from it, see in Fig. B.1. Let O be the origin. Moreover, let $\boldsymbol{r}'$ be the position vector of Q and $\boldsymbol{r} = r\boldsymbol{s}$, where $\boldsymbol{s}^2 = 1$, be

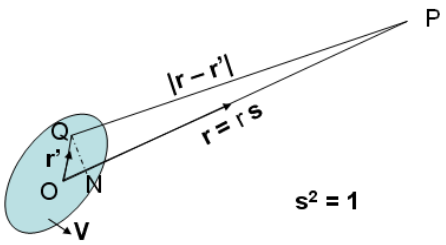

Figure B.1 : *Diagram for illustrating of the approximation of scalar green function under Born approximation.*

the position vector of P and let N be the foot of the perpendicular dropped from Q onto the OP. Then evidently, when r is large enough,

$$\mid \boldsymbol{r} - \boldsymbol{r}' \mid \approx r - \boldsymbol{s} \cdot \boldsymbol{r}' \tag{B.1}$$

and Eq. (A.15) becomes,

$$\frac{e^{ik_0|\boldsymbol{r}-\boldsymbol{r}'|}}{4\pi \mid \boldsymbol{r} - \boldsymbol{r}' \mid} \approx \frac{e^{ik_0 r}}{4\pi r} e^{-ik_0 \boldsymbol{s}\cdot\boldsymbol{r}'} = \frac{e^{ik_0 r}}{4\pi r} e^{-i\boldsymbol{k}\cdot\boldsymbol{r}'}, \tag{B.2}$$

where $\boldsymbol{k}$ is the wavevector of the diffracted field in the direction OP.

Appendix C

The measured scattered fields under $\widehat{h}\widehat{h}$ polarization

C.1 Samples with diameter 200 nm

The $\widehat{\boldsymbol{h}}\widehat{\boldsymbol{h}}$ data set of sample with diameter 200 nm is presented as follows in Fig. C.1.

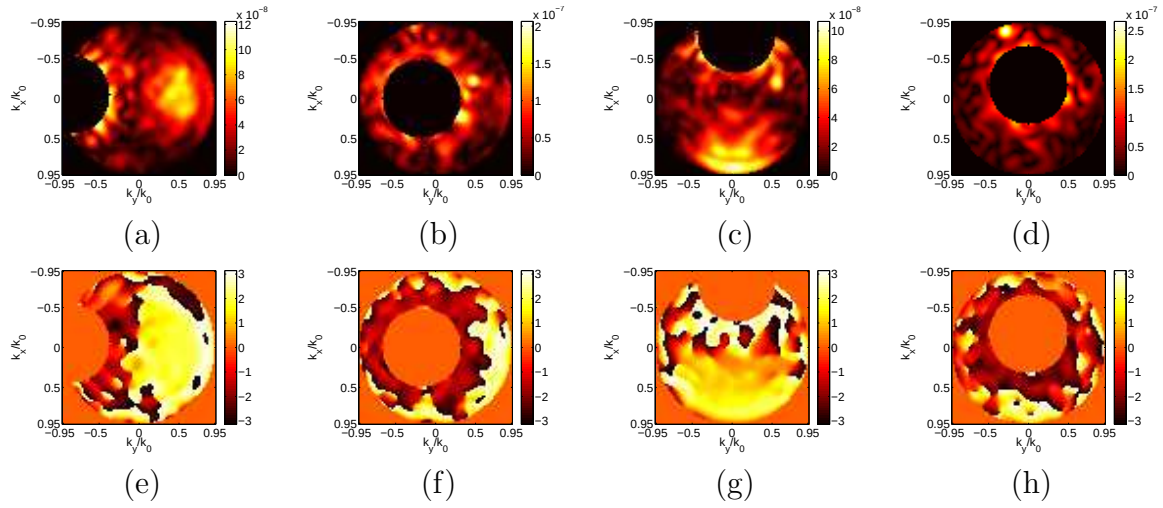

Figure C.1 : *Modulus and phases of the data set in the Fourier space, obtained by off-axis holography, polarizers in* $\widehat{\boldsymbol{h}}\widehat{\boldsymbol{h}}$ *mode. Samples diameter* 200 *nm, height* 150 *nm. (a) and (e)* $\theta_l = 55°$, $\phi_l = 0°$, *TE polarization; (b) and (f)* $\theta_l = 9°$, $\phi_l = 0°$, *TE polarization; (c) and (g)* $\theta_l = 54°$, $\phi_l = 90°$, *TM polarization; (d) and (h)* $\theta_l = 10°$, $\phi_l = 90°$, *TM polarization.*

Although we make an orthogonal polarization change for each incidence, if we overall research the $\widehat{\boldsymbol{v}}\widehat{\boldsymbol{v}}$ and $\widehat{\boldsymbol{h}}\widehat{\boldsymbol{h}}$ measurement, respectively, neglecting the polarizability of objects, these are two identical experiments. As usual, the theoretical diffracted field under such incident conditions computed by CDM are presented in Fig. C.2 for a nice comparison.

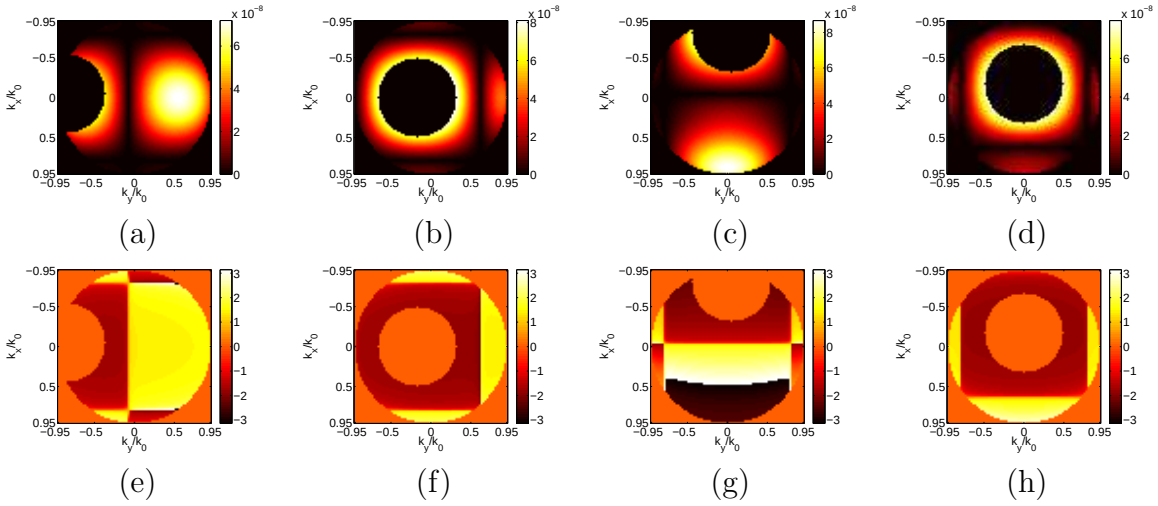

Figure C.2 : *Modulus (first line) and phases (second line) of the theoretical field in the Fourier space, polarizers in* $\widehat{\boldsymbol{h}}\widehat{\boldsymbol{h}}$ *mode. Samples diameter* 200 *nm, height* 150 *nm. (a) and (e)* $\theta_l = 55°$, $\phi_l = 0°$, *TE polarization; (b) and (f)* $\theta_l = 9°$, $\phi_l = 0°$, *TE polarization; (c) and (g)* $\theta_l = 54°$, $\phi_l = 90°$, *TM polarization; (d) and (h)* $\theta_l = 10°$, $\phi_l = 90°$, *TM polarization.*

An agreement between the measured data set with simulated ones within NA is visible.

C.2 Samples with diameter 150 nm

The $\widehat{\boldsymbol{h}}\widehat{\boldsymbol{h}}$ data set of sample with diameter 150 nm is presented in Fig. C.3.

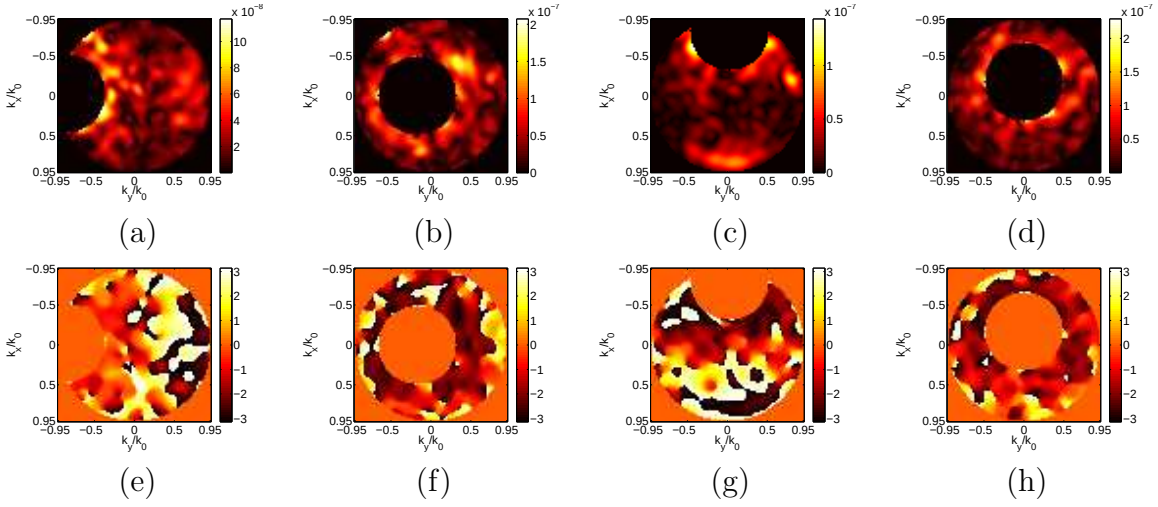

Figure C.3 : *Modulus and phases of the data set in the Fourier space, obtained by off-axis holography, polarizers in* $\widehat{\boldsymbol{h}}\widehat{\boldsymbol{h}}$ *mode. Samples diameter* 150 *nm, height* 150 *nm. (a) and (e)* $\theta_l = 55°$, $\phi_l = 0°$, *TE polarization; (b) and (f)* $\theta_l = 9°$, $\phi_l = 0°$, *TE polarization; (c) and (g)* $\theta_l = 54°$, $\phi_l = 90°$, *TM polarization; (d) and (h)* $\theta_l = 10°$, $\phi_l = 90°$, *TM polarization.*

We usually compute the theoretical diffracted field by CDM technique, in Fig. C.4, to have a preliminary comparison,

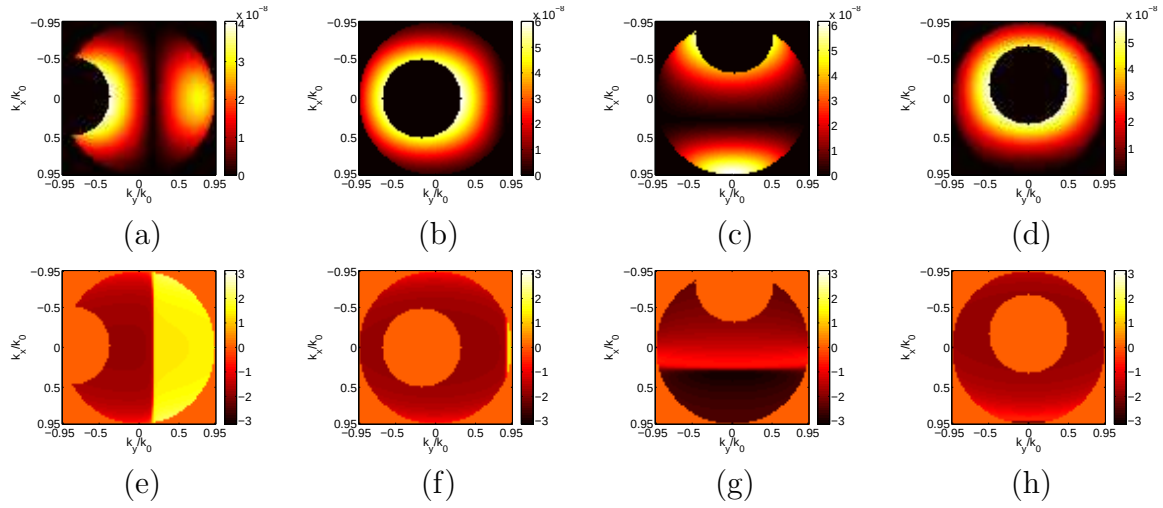

Figure C.4 : *Modulus (first line) and phases (second line) of the theoretical field in the Fourier space, polarizers in* $\widehat{\boldsymbol{hh}}$ *mode. Samples diameter* 150 *nm, height* 150 *nm. (a) and (e)* $\theta_l = 55°$, $\phi_l = 0°$, *TE polarization; (b) and (f)* $\theta_l = 9°$, $\phi_l = 0°$, *TE polarization; (c) and (g)* $\theta_l = 54°$, $\phi_l = 90°$, *TM polarization; (d) and (h)* $\theta_l = 10°$, $\phi_l = 90°$, *TM polarization.*

we continue to think that although there are lot of noise, a roughly consistency between the measured information and the theory is exsit.

Appendix D

The measured four groups of data set to retrieve the vectorial scattered fields

D.1 Samples with diameter 200 nm

The detected amplitude and phase of scattered far field of sample with diameter 200 nm, in Fourier domain, are presented as follows in Figs. D.1, D.2, D.3 and D.4.

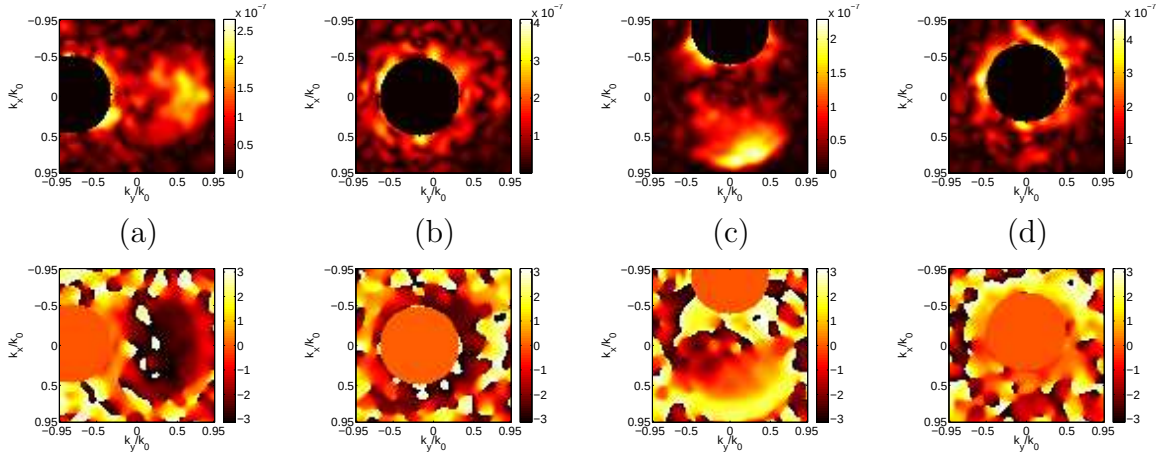

Figure D.1 : *Modulus and phases of the data set measured by* $\widehat{\boldsymbol{v}}\widehat{\boldsymbol{d}}_1$ *mode, in Fourier domain, off-axis holography method, respectively. Samples diameter* 200 *nm, height* 150 *nm. (a) and (e)* $\theta_l = 55°$, $\phi_l = 0°$, *TM polarization; (b) and (f)* $\theta_l = 9°$, $\phi_l = 0°$, *TM polarization; (c) and (g)* $\theta_l = 54°$, $\phi_l = 90°$, *TE polarization; (d) and (h)* $\theta_l = 9°$, $\phi_l = 90°$, *TE polarization.*

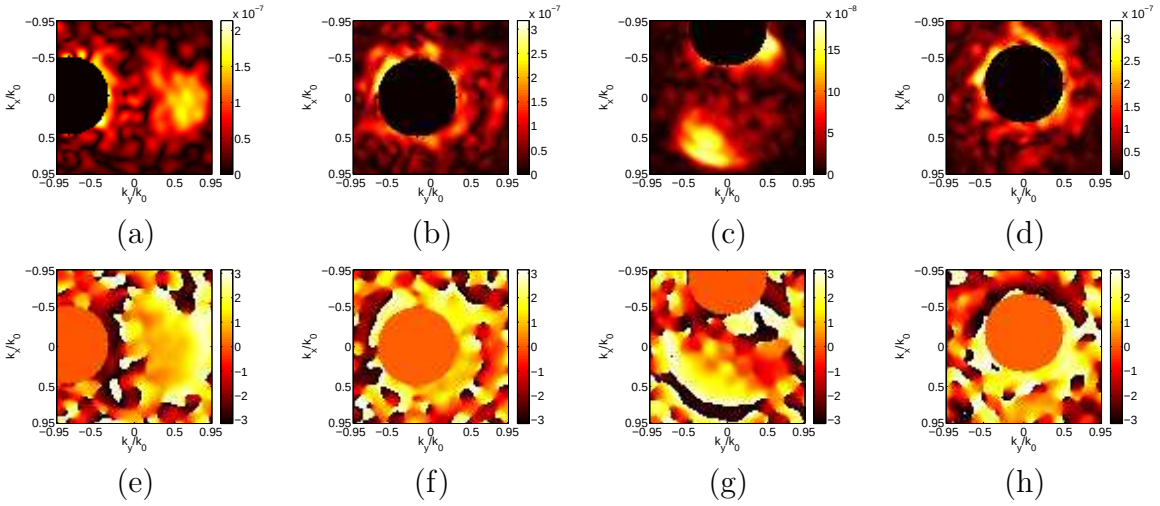

Figure D.2 : *Modulus and phases of the data set measured by* $\widehat{\boldsymbol{v}}\widehat{\boldsymbol{d}}_2$ *mode, in Fourier domain, off-axis holography method, respectively. Samples diameter* $200nm$*, height* $150nm$*. (a) and (e)* $\theta_l = 55°$*,* $\phi_l = 0°$*, TM polarization; (b) and (f)* $\theta_l = 9°$*,* $\phi_l = 0°$*, TM polarization; (c) and (g)* $\theta_l = 54°$*,* $\phi_l = 90°$*, TE polarization; (d) and (h)* $\theta_l = 9°$*,* $\phi_l = 90°$*, TE polarization.*

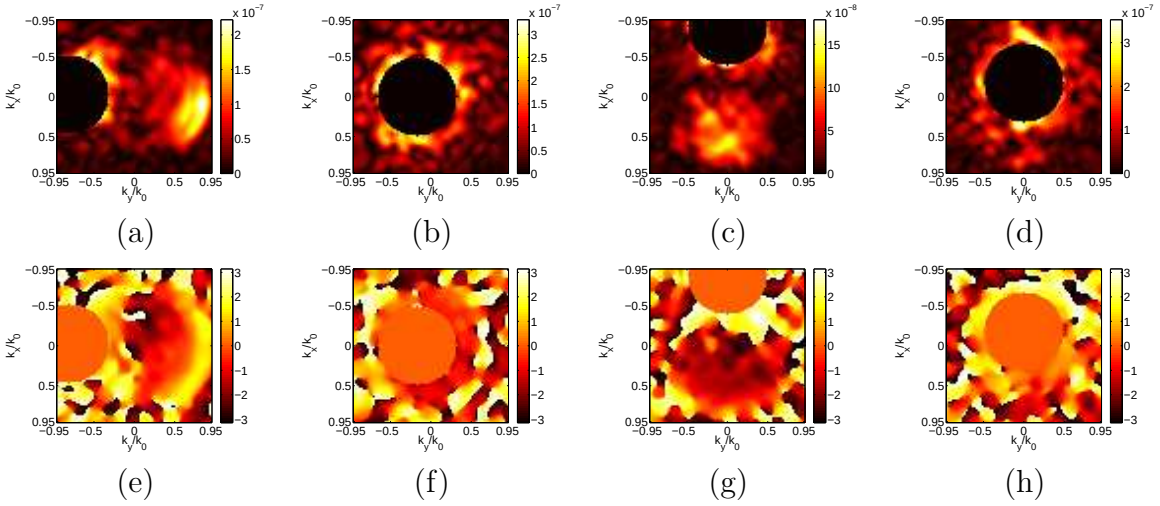

Figure D.3 : *Modulus and phases of the data set measured by* $\widehat{\boldsymbol{h}}\widehat{\boldsymbol{d}}1$ *mode, in Fourier domain, off-axis holography method, respectively. Samples diameter* 200 *nm, height* 150 *nm. (a) and (e)* $\theta_l = 55°$*,* $\phi_l = 0°$*, TM polarization; (b) and (f)* $\theta_l = 9°$*,* $\phi_l = 0°$*, TM polarization; (c) and (g)* $\theta_l = 54°$*,* $\phi_l = 90°$*, TE polarization; (d) and (h)* $\theta_l = 9°$*,* $\phi_l = 90°$*, TE polarization.*

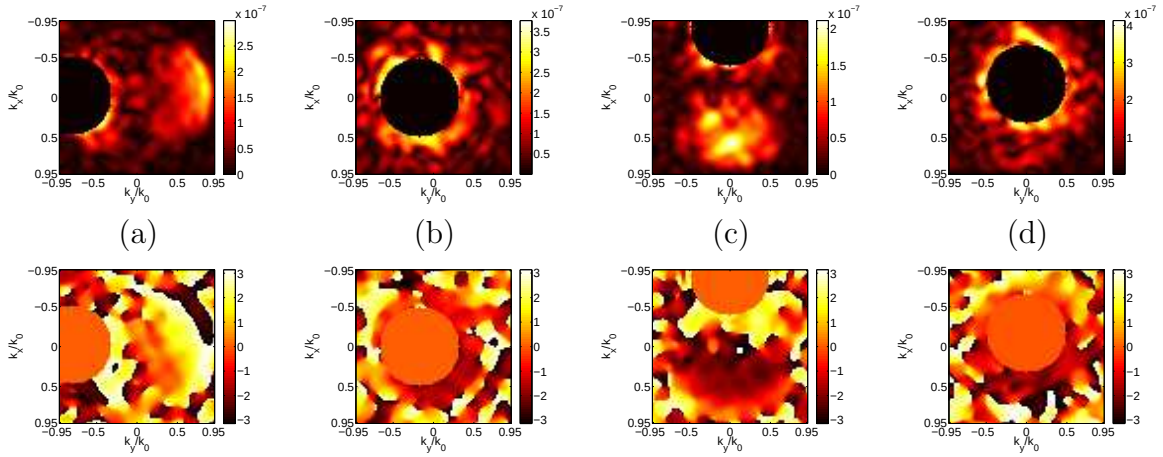

Figure D.4 : *Modulus and phases of the data set measured by* $\widehat{\boldsymbol{h}}\widehat{\boldsymbol{d}}_2$ *mode, in Fourier domain, off-axis holography method, respectively. Samples diameter* 200 *nm, height* 150 *nm. (a) and (e)* $\theta_l = 55°$, $\phi_l = 0°$, *TM polarization; (b) and (f)* $\theta_l = 9°$, $\phi_l = 0°$, *TM polarization; (c) and (g)* $\theta_l = 54°$, $\phi_l = 90°$, *TE polarization; (d) and (h)* $\theta_l = 9°$, $\phi_l = 90°$, *TE polarization.*

D.2 Samples with diameter 150 nm

The following four Figs. D.5, D.6, D.7 and D.8, present the measured scattered fields of sample with diameter 150 nm, under four different polarizers positions conditions.

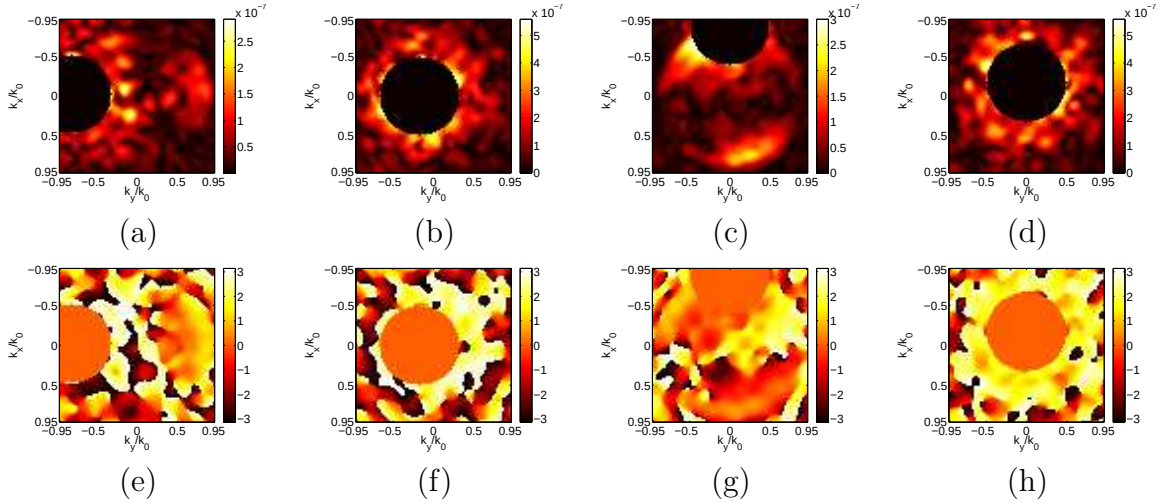

Figure D.5 : *Modulus and phases of the data set measured by* $\widehat{\boldsymbol{v}}\widehat{\boldsymbol{d}}_1$ *mode, in Fourier domain, off-axis holography method, respectively. Samples diameter* 150 *nm, height* 150 *nm. (a) and (e)* $\theta_l = 55°$, $\phi_l = 0°$, *TM polarization; (b) and (f)* $\theta_l = 9°$, $\phi_l = 0°$, *TM polarization; (c) and (g)* $\theta_l = 54°$, $\phi_l = 90°$, *TE polarization; (d) and (h)* $\theta_l = 9°$, $\phi_l = 90°$, *TE polarization.*

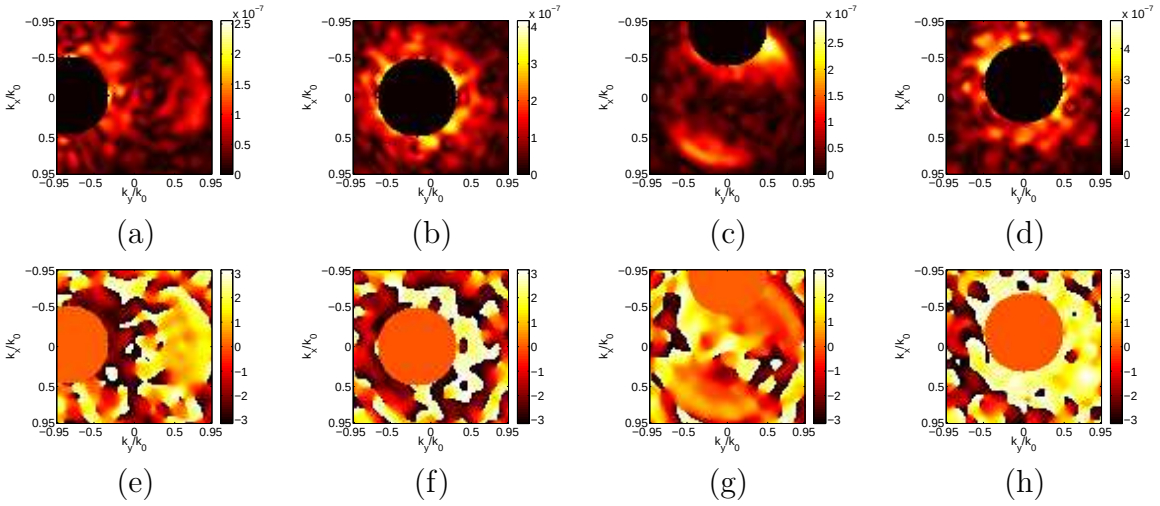

Figure D.6 : *Modulus and phases of the data set measured by* $\widehat{\boldsymbol{v}}\widehat{\boldsymbol{d}}_2$ *mode, in Fourier domain, off-axis holography method, respectively. Samples diameter* 150 *nm, height* 150 *nm. (a) and (e)* $\theta_l = 55°$, $\phi_l = 0°$, *TM polarization; (b) and (f)* $\theta_l = 9°$, $\phi_l = 0°$, *TM polarization; (c) and (g)* $\theta_l = 54°$, $\phi_l = 90°$, *TE polarization; (d) and (h)* $\theta_l = 9°$, $\phi_l = 90°$, *TE polarization.*

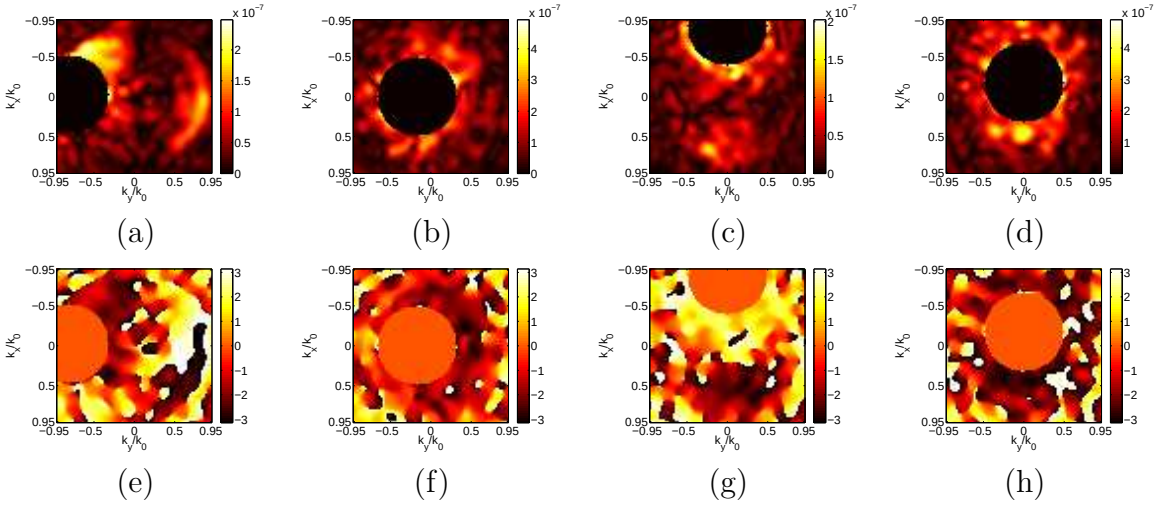

Figure D.7 : *Modulus and phases of the data set measured by* $\widehat{\boldsymbol{h}}\widehat{\boldsymbol{d}}_1$ *mode, in Fourier domain, off-axis holography method, respectively. Samples diameter* 150 *nm, height* 150 *nm. (a) and (e)* $\theta_l = 55°$, $\phi_l = 0°$, *TM polarization; (b) and (f)* $\theta_l = 9°$, $\phi_l = 0°$, *TM polarization; (c) and (g)* $\theta_l = 54°$, $\phi_l = 90°$, *TE polarization; (d) and (h)* $\theta_l = 9°$, $\phi_l = 90°$, *TE polarization.*

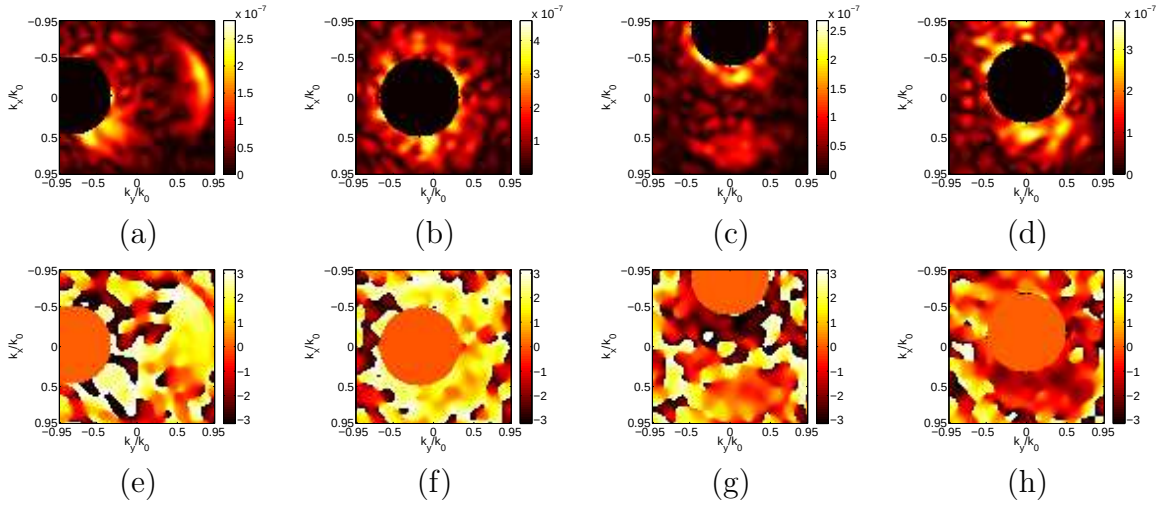

Figure D.8 : *Modulus and phases of the data set measured by* $\widehat{\boldsymbol{h}}\widehat{\boldsymbol{d}}_2$ *mode, in Fourier domain, off-axis holography method, respectively. Samples diameter* 150 *nm, height* 150 *nm. (a) and (e)* $\theta_l = 55°$, $\phi_l = 0°$, *TM polarization; (b) and (f)* $\theta_l = 9°$, $\phi_l = 0°$, *TM polarization; (c) and (g)* $\theta_l = 54°$, $\phi_l = 90°$, *TE polarization; (d) and (h)* $\theta_l = 9°$, $\phi_l = 90°$, *TE polarization.*

Bibliography

[1] G. Binnig, and H. Rohrer, "Scanning tunneling microscopy," IBM J.O.R.D **30**, 4 (1986).

[2] C.J. Chen, "Introduction to scanning tunneling microscopy ," Oxford University Press, New York (1993).

[3] D.A. Bonnell and B.D. Huey, "Scanning probe microscopy and spectroscopy: Theory, Techniques, and Applications," 2nd ed., Wiley-VCH, New York, (2001).

[4] E. Betzig and J.K. Trautman, "Near-Field Optics: Microscopy, Spectroscopy, and Surface Modification Beyond the Diffraction Limit," Science, **257**, 189–195 (1992).

[5] F. Zenhausern, Y. Martin, and H.K. Wickramasinghe, "Scanning Interferometric Apertureless Microscopy: Optical Imaging at 10 Angstrom Resolution," Science, **269**, 1083–1085 (1995).

[6] L. Salomon, F. Grillot, A.V. Zayats, and F. de Fornel, "Near-Field Distribution of Optical Transmission of Periodic Subwavelength Holes in a Metal Film," Phys. Rev. Lett., **86(6)**, 1111–1113 (2001).

[7] N. Fabre, L. Lalouat, B. Cluzel, X. Mélique, D. Lippens, F. de Fornel, and O. Vanbésien, "Optical Near-Field Microscopy of Light Focusing through a Photonic Crystal Flat Lens," Phys. Rev. Lett., **101**, 073901-1–073901-4 (2008).

[8] G. Binnig, C.F. Quate, and C. Gerber, "Atomic force microscope," Phys. Rev. Lett. **56**, 930–933 (1986).

[9] M. Tortonese, R.C. Barrett, and C.F. Quate, "Atomic resolution with an atomic force microscope using piezoresistive detection," Appl. Phys. Lett. **62**, 834–836 (1993).

[10] F.J. Giessibl, "Advances in atomic force microscopy," Rev. Mod. Phys. **75**, 949–983 (2003).

[11] H. Butt, B. Cappella, M. Kappl, "Force measurements with the atomic force microscope: Technique, interpretation and applications," Surf. Scie. Repo. **59**, 1–152 (2005).

[12] S.T. Hess, T.P.K. Giriajan, and M.D. Mason, "Ultra-high resolution imaging by fluorescence photoactivation localization microscopy," Biop. Jour. **91** 4258–4272 (2006).

[13] T.J. Gould, V.V. Verkhusha, and S.T. Hess, "Imaging biological structures with fluorescence photoactivation localization microscopy," Natu. Prot. **4** 291–308 (2009).

[14] R. Henriques, and M.M. Mhlanga, "PALM and STORM: What hides beyond the Rayleigh limit?," Biot. Jour. **4** 846–857 (2009).

[15] B. Huang, S.A. Jones, B. Brandenburg,and X. Zhuang, "Whole-cell 3D STORM reveals interactions between cellular structures with nanometer-scale resolution," Natu. Meth. **5** 1047–1052 (2008).

[16] M.J. Rust, M. Bates, and X. Zhuang, "Sub-diffraction-limit imaging by stochastic optical reconstruction microscopy (STORM)," Natu. Meth. **3** 793–796 (2006).

[17] X. Zhuang, "Nano-imaging with STORM," Natu. Phot. **3** 365–367 (2009).

[18] E. Wolf, "Three-dimensional structure determination of semitransparent objects from holographic data," Opt. Commun. **1**, 153–156 (1969).

[19] I. Yamaguchi and T. Zhang, "Phase-shifting digital holography," Opt. Lett. **22**, 1268–1270 (1997).

[20] U. Schnars and W. Jptner, "Digital Holography," 164 (2005).

[21] V. Lauer, "New approach to optical diffraction tomography yielding a vector equation of diffraction tomography and a novel tomographic microscope," J. Microsc. **205**, 165–176 (2002).

[22] O. Haeberlé, A. Sentenac, H. Giovannini, "An introduction to diffractive tomographic microscopy," Modern research and educational topics in microscopy, **2**, 956–967, (2007).

[23] W. Choi, C. Fang-Yen, K. Badizadegan, S. Oh, N. Lue, R.R. Dasari and M.S. Feld, "Tomographic phase microscopy," Nature Methods **4**, 717–719 (2007).

[24] J. Savatier, P. Bon, D. Marguet, and S. Monneret, "Correlative microscopy of living cells between fluorescence and quantitative phase imaging with a high resolution wavefront sensor," Biop. Jour. **100**, 356a (2011).

[25] B. Rappaz, P. Marquet, E. Cuche, Y. Emery, C. Depeursinge, P. Magistretti,"Measurement of the integral refractive index and dynamic cell morphometry of living cells with digital holographic microscopy Magistretti," Opt. Expr. **13**, 9361 (2005).

[26] M. Lambert and D. Lesselier, "Binary-constrained inversion of a buried cylindrical obstacle from complete and phaseless magnetic fields," Inve. Prob. **16**, 563–576 (2000).

[27] B. Simon, M. Debailleul, V. Georges, V. Lauer and O. Haeberlé, "Tomographic diffractive microscopy of transparent samples," Eur. Phys. J. Appl. Phys. **44**, 29–35 (2007).

[28] S. Alexandrov, T. Hillman and T. Gutzler,D.D. Sampson "Synthetic Aperture Fourier Holographic Optical Microscopy," Phy. Rev. Lett **97**, 1–4 (2006).

[29] A. Neumann, Y. Kuznetsova, and S. Brueck, "Imaging interferometric microscopy," Opt. Express **16**, 15886–15891 (2008).

[30] V. Mico, Z. Zalevsky, P. García-Martnez, and J. García,"Synthetic aperture superresolution with multiple off-axis holograms," J. Opt. Soc. Am. A **23**, 3162–3165 (2006).

[31] K. Belkebir and A. Sentenac, "High resolution optical diffraction microscopy," J. Opt. Soc. Am. A **20**, Issue 7, 1223-1229 (2003).

[32] G. Maire, J. Girard, F. Drsek, H. Giovannini, A. Talneau, K. Belkebir, P. C. Chaumet, and A. Sentenac, "Experimental inversion of optical diffraction tomography data with a nonlinear algorithm in the multiple scattering regime," J. Modern Optics **57**, 746 (2010).

[33] P. C. Chaumet, K. Belkebir and A. Sentenac,"Experimental microwave imaging of three-dimensional targets with different inversion procedures," J. Appl. Phys. **109**, 034901 (2009).

[34] P. C. Chaumet, A. Sentenac, and A. Rahmani, "Coupled dipole method for scatterers with large permittivity," Phys. Rev. E **70**, 036606 (2004).

[35] S.S. Joel, A.S. Stanley, and W.D. Michael, "The diffraction barrier in optical microscopy," www.microscopyu.com/articles/superresolution/diffractionbarrier.html

[36] M.W. Davidson, "Resolution," www.microscopyu.com/articles/formulas/formulasresolution.html

[37] E. Mudry, P. C. Chaumet, K. Belkebir, G. Maire and A. Sentenac, "Mirror-assisted tomographic diffractive microscopy with isotropic resolution," Opt. Lett. **35**, 11, 1857–1860, (2010).

[38] S. Vertu, J. Flügge, J.J. Delaunay, and O. Haeberlé, "Improved and isotropic resolution in tomographic diffractive microscopy combining sample and illumination rotation," Cen. Eur. J. of Phy. **9**, 11, 969–974, (2011).

[39] F. Charrière, A. Marian, F. Montfort, J. Kuehn, T. Colomb, E. Cuche, P. Marquet, and C. Depeursinge, "Cell refractive index tomography by digital holographic microscopy," Opt Lett. **31**, 2, 178–180 (2006).

[40] C. W. Mccutchen, "Generalized aperture and the three-dimensional diffraction image," J. Opt. Soc. Am. **54**, 240–242 (1964)

[41] A. Mortimer, and W.D. Michael, "Numerical aperture and resolution," http://www.olympusmicro.com/primer/anatomy/numaperture.html

[42] G. itold and O. Wolfgang, "Tomographic imaging of photonic crystal fibers," Opt Lett. **32**, 14, 1977–1979 (2007)

[43] M. Debailleul, B. Simon, V. Georges, O. Haeberlé, and V. Lauer, "Holographic microscopy and diffractive microtomography of transparent samples," Meas. Sci. Technol **19**, 074009 (2008).

[44] Y. Sung, W. Choi, C. Fang-Yen, K. Badizadegan, R.R. Dasari, and M.S. Feld, "Optical diffraction tomography for high resolution live cell imaging," Opt. Express **17**, 266–277 (2009).

[45] M. Kim, Y. Choi, C. Fang-Yen, Y. Sung, R.R. Dasari, M.S. Feld, and W. Choi, "High-speed synthetic aperture microscopy for live cell imaging," Opt. Lett. **36**, 148–150 (2011).

[46] M. Kim, Y. Choi, C. Fang-Yen, Y. Sung, K. Kim, R.R. Dasari, M.S. Feld, and W. Choi, "Three-dimensional differential interference contrast microscopy using synthetic aperture imaging," Jou. of Bio. Opt. **17(2)**, 026003-1–026003-6 (2012).

[47] S. Vertu, J.J. Delaunay, I. Yamada, O. Haeberlé, "Principles of computerized tombgraphic imaging," IEEE Press. (1998).

[48] A.C. Kak and M. Slaney, "Diffraction microtomography with sample rotation: influence of a missing apple core in the recorded frequency space," Cen. Eur. Jou. of Phy. **7(1)**, 22–31 (2012).

[49] F. Charrière, N. Pavillon, T. Colomb and C. Depeursinge, T.J. Hegera, E.A.D. Mitchella, P. Marquet and B. Rappaz, "Living specimen tomography by digital holographic microscopy: morphometry of testate amoeba," Opt. Express **14(16)**, 7005–7013 (2006).

[50] R. Fiolka, K. Wicker, R. Heintzmann, A. Stemmer, "Simplified approach to diffraction tomography in optical microscopy," Opt. Express **17**, 12407–12417 (2009).

[51] Z. Wang, D.L. Marks, P.S. Carney, L.J. Millet, M.U. Gillette, A.Mihi, P.V. Braun, Z. Shen, S.G. Prasanth, and G. Popescu, "Spatial light interference tomography (SLIT)," Opt. Express **19(21)**, 19907–19918 (2011).

[52] M. Sarmis, B. Simon, M. Debailleul, B. Colicchio, V. Georges, J.J. Delaunay, O. Haeberlé, "High resolution reflection tomographic diffractive microscopy," J. M. Optics. **57(9)**, 745 (2010).

[53] B. Simon, M. Debailleul, A. Beghin, Y. Tourneur and O. Haeberlé, "High-resolution tomographic diffractive microscopy of biological samples," J. Biophoton. **3(7)**, 462–467 (2010).

[54] M. Debailleul, V. Georges, B. Simon, R. Morin, and O. Haeberlé, "High-resolution three-dimensional tomographic diffractive microscopy of transparent inorganic and biological samples," Opt. Lett. **34(1)**, 79–81 (2009).

[55] Y. Sung and R.R. Dasari, "Deterministic regularization of three-dimensional optical diffraction tomography," J. Opt. Soc. Am. A **28**, 1554–1561 (2011).

[56] W. Thomson, Philos. Mag. **23** 252–255 (1887)

[57] M.F. Atiyah, "Resolution of singularities and division of distribution," Comm. Pure Appl. Math. **23**, 145–150 (1970)

[58] K. Creath, "Phase-shifting speckle interferometry," Appl. Opt. **24**, 3053–3058 (1985)

[59] V.I. Arnol'd, "Remarks on the stationary phase method and Coxeter numbers," Russian Math. Surveys , **28**, 19–48 (1973)

[60] F.W.J. Olver, "Asymptotics and special functions,", Acad. Press (1974)

[61] A.N. Varchenko, "Newton polyhedra and estimation of oscillating integrals," Funct. Anal. Appl , **10**, 175–196 (1976)

[62] T. Nomura, B. Javidi, S. Murata, E. Nitanai, and T. Numata, "Polarization imaging of a 3D object by use of on-axis phase-shifting digital holography," Opt. Lett. **32**, 481–483 (2007)

[63] I. Yamaguchi, T. Matsumura, and J. Kato, "Phase-shifting color digital holography," Opt. Lett. **27**, 1108–1110 (2002)

[64] J. Kato, I. Yamaguchi, and T. Matsumura, "Multicolor digital holography with an achromatic phase shifter," Opt. Lett. **27**, 1403–1405 (2002)

[65] F. Le Clerc, M. Gross, and L. Collot, "Synthetic-aperture experiment in the visible with on-axis digital heterodyne holography," Opt. Lett. **26**, 1550–1552 (2001)

[66] S. Tamano, Y. Hayasaki, and N. Nishida, "Phase-shifting digital holography with a low-coherence light source for reconstruction of a digital relief object hidden behind a light-scattering medium," Appl. Opt. **45**, 953–959 (2006)

[67] I. Yamaguchi, T. Ida, M. Yokota, and K. Yamashita, "Surface shape measurement by phase-shifting digital holography with a wavelength shift," Appl. Opt. **45**, 7610-7616 (2006)

[68] P. Guo and A. J. Devaney, "Digital microscopy using phase-shifting digital holography with two reference waves," Opt. Lett. **29**, 857–859 (2004)

[69] P. Carré, "Installation et utilisation du comparateur photolectrique et interf rentiel du bureau international des poids et mesures," Metrologia **2**, 13–23 (1966).

[70] J.H. Bruning, D.R. Herriott and J.E. Gallagher, D.P. Rosenfeld, A.D. White and D.J. Brangaccio, "Digital wave-front measuring interferometer for testing optical surfaces and lenses," Appl. Opt. **13**, 2693–2703 (1974).

[71] Z. Wang, L. Millet, M. Mir, H. F. Ding, S. Unarunotai, J. Rogers, M.U. Gillette, G. Popescu, "Spatial light interference microscopy (SLIM)," Opt. Exp. **19**(2), 1016–1026 (2011)

[72] O. Haeberlé, K. Belkebir and H. Giovannini and A. Sentenac, "Tomographic diffractive microscopy:basics, techniques and perspectives," J. of Mod. Optics **57**, 686–699 (2010).

[73] J. Primot and L. Sogno, "Achromatic three-wave (or more) lateral shearing interferometer," J. Opt. Soc. Am. A, **12**, 2679 (1995).

[74] J. Zou, A. Sautivet, J. Fils, L. Martin, K. Abdeli, C. Sauteret, and B. Wattellier, "Optimization of the dynamic wavefront control of a pulsed kilojoule/nanosecond-petawatt laser facility," Appl. Opt. **47(5)**, 704–710 (2008).

[75] P. Bon, G. Maucort, B. Wattellier, and S. Monneret, "Quadriwave lateral shearing interferometry for quantitative phase microscopy of living cells," Opt. Exp, **17(15)**, 13080–13094 (2009).

[76] R. V. Shack and B. C. Platt, "Production and use of a lenticular Hartmann screen," J. Opt. Soc. Am. **61**, 656 (1971).

[77] J. Primot, "Theoretical description of Shack-Hartmann wave-front sensor," Opt. Comm, **222**, 81–92(2003).

[78] J. Primot and N. Guerineau, "Extended Hartmann test based on the pseudoguiding property of a Hartmann Mask completed by a phase chessboard," Appl. Opt. **39(31)**, 5715–5720 (2000).

[79] G. Maire, F. Drsek, J. Girard, H. Giovannini1, A. Talneau, D. Konan, K. Belkebir1, P.C. Chaumet, and A. Sentenac, "Experimental demonstration of quantitative imaging beyond Abbes limit with optical diffraction tomography," Phys. Rev. Lett. **102**, 213905–213908 (2009).

[80] J. Girard, G. Maire, H. Giovannini, A. Talneau, K. Belkebir1, P.C. Chaumet, and A. Sentenac, "Nanometric resolution using far-field optical tomographic microscopy in the multiple scattering regime," Phys. Rev. A **82**, 061801(R) (2010).

[81] E.N. Leith, J. Upatnieks, and K.A. Haines, "Microscopy by Wavefront Reconstruction," J. Opt. Soc. Am. **55**, 981–985 (1965).

[82] U. Schnars and W. Jptner, "Direct recording of holograms by a CCD target and numerical reconstruction," Appl. Opt. **33**, 179–181 (1994)

[83] U. Schnars, "Direct phase determination in hologram interferometry with use of digitally recorded holograms," J. Opt. Soc. Am. A **11**, 2011–2015 (1994)

[84] M. Gross, M. Atlan, E. Absil, "Noise and aliases in off-axis and phase-shifting holography," Applied Optics 4**7(11)**, 1757–1766(2008)

[85] T. M. Kreis, W. P. O. Juptner, and J. Geldmacher, "Principles of digital holographic interferometry," SPIE, 3478:45, July (1988).

[86] M. Marim, E. Angelini, J.C. Olivo-Marin, and M. Atlan, "Off-axis compressed holographic microscopy in low-light conditions," Opt. Lett, **36(1)**, 79–81 (2011).

[87] Y. Pu and H. Meng, "Intrinsic speckle noise in off-axis particle holography," J. Opt. Soc. Am. A **21**, 1221–1230 (2004)

[88] T. Colomb, P. Dahlgren, D. Beghuin, E. Cuche, P. Marquet, and C. Depeursinge, "Polarization Imaging by Use of Digital Holography," Appl. Opt. **41**, 27–37 (2002)

[89] E. Cuche, F. Bevilacqua, and C. Depeursinge, "Digital holography for quantitative phase-contrast imaging," Opt. Lett. **24**, 291–293 (1999)

[90] J. H. Massig, "Digital off-axis holography with a synthetic aperture," Opt. Lett. **27**, 2179–2181 (2002)

[91] P. Massatsch, F. Charriére, E. Cuche, P. Marquet, and C. Depeursinge, "Time-domain optical coherence tomography with digital holographic microscopy," Appl. Opt. **44**, 1806–1812 (2005)

[92] P. Marquet, B. Rappaz, P.J. Magistretti, E. Cuche, Y. Emery, T. Colomb, and C. Depeursinge, "Digital holographic microscopy: a noninvasive contrast imaging technique allowing quantitative visualization of living cells with subwavelength axial accuracy," Opt. Lett. **30**, 468–470 (2005)

[93] F.M. Kahnert, "Numerical methods in electromagnetic scattering theory," J. Quant. Spectrosc. Radiat. Transf. **775**, 79–80, (2003).

[94] P. EM, and P. CR, "Scattering and adsorption of light by non-spherical dielectric grains," Astrophy J **186**, 705–714, (1973).

[95] A. D. Yaghjian, "Electric dyadic Green's functions in the source region," Proc. IEEE, **68**, 248–263, (1980)

[96] A. D. Yaghjian, "A delta-distribution derivation of the electric field in the source region," Electromagn., **2**, 161–167, (1982)

[97] W.S. Weiglhofer, A. Lakhtakia, B. Michel, "Maxwell Garnett and Bruggeman formalisms for a particulate composite with bianisotropic host medium," Microw. Opt. Technol. Lett. **15**(4), 263–266, (1998).

[98] A. Lakhtakia, "Selected Papers on Linear Optical Composite Materials," SPIE Press. **20**, (1996)

[99] A. Lakhtakia, "Electromagnetic Fields in Unconventional Materials and Structures," Wiley-Interscience. (2000)

[100] W. S. Weiglhofer, A. Lakhtakia, "Introduction to Complex Mediums for Optics and Electromagnetics," SPIE Press. (2003)

[101] P.C. Chaumet, A. Rahmani, F. de Fornel, and J.P. Dufour, "Evanescent light scattering:The validity of the dipole approximation," Phys. Rev. B **58**, 2310–2135 (1998)

[102] P.C. Chaumet, and M. Nieto-Vesperinas, "Coupled dipole method determination of the electromagnetic force on a particle over a flat dielectric substrate," Phys. Rev. B **61**, 14119–14128 (2000)

[103] P.C. Chaumet, A. Rahmani, and G.W. Bryant, "Generalization of the coupled dipole method to periodic structure," Phys. Rev. B 67, 165404–165408 (2003)

[104] P.C. Chaumet, K. Belkebir, and R. Lencrerot, "Three-dimensional optical imaging in layered media," Opt. Exp. **14**, 3415–3426 (2006)

[105] P. C. Chaumet, K. Belkebir, and A. Sentenac, "Three-dimensional subwavelength optical imaging using the coupled dipole method," Phy. rev. B **69**, 245405–245411 (2004)

[106] P.C. Chaumet, K. Belkebir, "Three-dimensional reconstruction from real data using a conjugate gradient-coupled dipole method," Inv. Problems **25**, 024003–024020 (2009).

[107] E. Mudry, P.C. Chaumet, K. Belkebir, and A. Sentenac, "Electromagnetic wave imaging of three-dimensional targets using a hybrid iterative inversion method," Inv. Problems **28**, 065007–065023 (2012)

[108] W. C. Chew and Y. M. Wang, "Reconstruction of two-dimensional permittivity distribution using the distorted Born iterative method," IEEE Trans. Med. Imaging, **9**, 218 (1990).

[109] N. Joachimowicz, C. Pichot, and J. P. Hugonin, "Inverse scattering: An iterative numerical method for electromagnetic imaging," IEEE Trans. Antennas Propag, **39**, 1742 (1991).

[110] A.G. Tijhuis, "Born type reconstruction of material parameters of an inhomogeneous, lossy dielectric slab from reflected-field data," Wave Motion, **11**, 151 (1989).

[111] A.G. Tijhuis, K. Belkebir, A. Litman, B.P. de Hon, "Theoretical and computational aspects of 2D inverse Profiling," IEEE Trans. Geosci. Remote Sens, **39**, 1316 (2001).

[112] R.E. Kleinman and P.M. van den Berg, "A modified gradient method for two dimensional problems in tomography," J. Comput. Appl. Math, **42(17)**, (1992).

[113] R.E. Kleinman and P.M. van den Berg, "An extended range modified gradient technique for profile inversion," Radio Sci, **28**, 877 (1993).

[114] K. Belkebir, S. Bonnard, F. Pezin, P. Sabouroux, M. Saillard, "Validation of 2D inverse scattering algorithms from multi-frequency experimental data," J. Elect. Waves and App, **14**, 1637–1667, (2000).

[115] K. Belkebir, A.G. Tijhuis, "$Modified^2$ gradient and modified Born method for solving a two-dimensional inverse scattering problem," Inverse Problems, **17**, 1671–1688, (2001).

[116] Y. Ruan, P. Bon, E. Mudry, G. Maire, P.C. Chaumet, H. Giovannini, K. Belkebir, A. Talneau, B. Wattellier, S. Monneret, and A. Sentenac, "Tomographic diffractive microscopy with a wavefront sensor," Opt. lett, **37(10)**, 1631–1633 (2012)

[117] K. Belkebir R.E. Kleinman and C. Pichot, "Microwave imaging location and shape reconstruction from multifrequency scattering data," IEEE Trans. Microw. Theory Tech, **45** 469–476 (1997)

[118] K. Belkebir, P.C. Chaumet and A. Sentenac, "Superresolution in total-internal reflection tomography," JOSA A, **22(9)**, 1889–1897, (2005).

[119] W.H. Press, S.A. Teukolsky, W.T. Vetterling and B.P. Flannery, "Numerical recipes: The art of scientific computing," Cambridge University Press, (1986)

[120] E. Mudry, K. Belkebir, J. Girard, J. Savatier, E. Le Moal, C. Nicoletti, M. Allain and A. Sentenac, "Structured illumination microscopy using unknown speckle patterns," Nature Photonics, **6**, 312, (2012).

Résumé

La microscopie tomographique (MTD) est une technique d'imagerie récente qui reconstruit la carte de permittivité tri-dimensionnelle de l'objet sondé avec une résolution accrue par rapport à la microscopie plein champ classique. Elle consiste à illuminer l'objet avec un faisceau laser sous différents angles d'incidence successifs, et à détecter à la fois en amplitude et en phase son champ diffracté imagé dans un microscope. Cette technique a jusqu'à présent été appliquée avec succès au cas des objets tri-dimensionnels uniquement pour de faibles contrastes d'indices de réfraction (habituellement inférieurs à 5.10-2), pour lesquels les approximations linéaires de calcul du champ diffracté sont valides. Ainsi un important champ d'application reste inaccessible à cette nouvelle technique.

Pour s'affranchir de ces limitations, nous présentons dans ce manuscrit les résultats obtenus en couplant un dispositif de MTD à un algorithme d'inversion sophistiqué, basé sur une modélisation rigoureuse de l'interaction onde-matière. Plusieurs configurations ont été appliquées dans le dispositif pour effectuer la mesure de phase. Des techniques classiques comme l'interférométrie à décalage de phase où l'holographie numérique hors axe, mais aussi pour la première fois en tomographie optique un capteur de front d'onde basé sur l'interférométrie à décalage multi-latéral. Cela conduit à une grande simplification du système et le rend compatible avec les architectures classiques de microscope plein champ, ainsi qu'avec des sources bon marché comme des diodes laser ou des LEDs. Notre algorithme d'inversion non-linéaire a été comparé à la procédure d'inversion linéaire classique basée sur l'approximation de Born pour reconstruire en 3D la carte de permittivité de petits objets en résine déposés sur substrat de silicium. Nous montrons que contrairement à l'inversion linéaire, notre approche restitue avec succès la permittivité et la géométrie 3D des objets avec environ 20 angles d'illuminations, même pour une résolution latérale à la limite de Rayleigh, à savoir 400 nm dans notre dispositif. Le nombre d'illuminations est ainsi diminué de plus d'un facteur 10 en comparaison des résultats usuels en inversion linéaire, ce qui peut être exploité pour accélérer le temps d'acquisition. L'extension axiale typique de 125 nm de nos objets est de plus retrouvée de manière satisfaisante, grâce à la modélisation de l'interaction entre les objets et le substrat réfléchissant, contrairement à l'approche linéaire. Enfin, le dispositif a été amélioré pour effectuer des mesures résolues en polarisation à la fois pour l'illumination et la détection, ce qui a permis d'améliorer la résolution transverse au-delà de la limite de Rayleigh.

Mots clés: tomographie optique; microscopie de phase; algorithmes d'inversion;

Resume

Tomographic diffractive microscopy (TDM) is a recent imaging technique that reconstructs the tri-dimensional permittivity map of the probed sample with an increased resolution compared to conventional wide-field microscopy. It consists in illuminating the sample with coherent collimated light under different successive incidence angles, and detecting both in amplitude and phase its scattered field imaged through a microscope set-up. This technique has until now been applied successfully to tri-dimensional samples only in the case of weak refractive index contrasts (usually below 5.10-2) where linear approximations to calculate the scattered field are valid. As a result, an important field of applications is still out of reach of this new imaging tool.

To go beyond these limitations, we present in this manuscript the results obtained by coupling a TDM set-up to a sophisticated inversion algorithm based on a rigorous modeling of the wave-sample interaction. Different configurations have been used in the set-up to perform the phase measurement. Classical ones like phase-shifting interferometry and off-axis holography, and also for the first time in tomography applications a wavefront sensor based on quadri-wave lateral shearing interferometry. This leads to a dramatic simplification of the system and makes it compatible with common wide-field microscopes and low cost light sources like laser diodes and LEDs. Our dedicated non-linear inversion algorithm has been compared to the standard linear inversion based on the Born approximation for the 3D reconstructions of the permittivity maps of small resin objects deposited on a silicon substrate. We show that contrarily to the linear inversion, our approach retrieves successfully the permittivity and the 3D geometry of the objects with about 20 illumination angles, even when reaching lateral resolutions at the Rayleigh limit, which is of 400 nm in our set-up. The number of illuminations is thus decreased by a factor of more than 10 compared to usual results obtained with the linear inversion, which can be used to increase the speed of the acquisition. The typical 125 nm axial extent of our objects is moreover satisfactory retrieved by the non-linear algorithm, thanks to the modeling of the interaction between the objects and the reflective substrate, contrarily to the linear approach. Lastly, the set-up has been ameliorated to perform polarization resolved measurements for both the illumination and the detection, which has permitted to improve the transverse resolution beyond the Rayleigh limit.

Key words: optical tomography; phase microscopy; inversion algorithms;